PROCEEDINGS OF THE SECOND ANNUAL ADVANCED POLYMER COMPONENTS SYMPOSIUM. VOL. III.
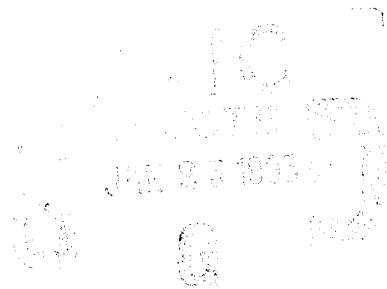
John J. Rusek

PHILLIPS LABORATORY
OLAC PL/RKCP
Edwards AFB CA 93523–5000

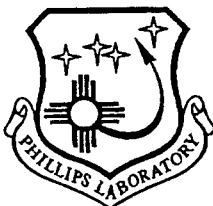July 1992

Interim Report

19950123 048

PHILLIPS LABORATORY
Propulsion Directorate
AIR FORCE MATERIEL COMMAND
EDWARDS AIR FORCE BASE CA 93524–7001

NOTICE

FOREWORD

The report has been reviewed and is approved for release and distribution in accordance with the distribution statement on the cover and on the SF Form 298.

DR. JOHN J. RUSEK
Project Manager

STEPHEN L. RODGERS
Chief, Emerging Technologies Branch

RANNEY G. ADAMS
Public Affairs Director

INDEX
AUTHORS

TABLE OF CONTENTS
Volumes 1–3

Volume 1

Volume 2

REPORT DOCUMENTATION PAGE	Form Approved OMB No 0704-0188

1. AGENCY USE ONLY (LEAVE BLANK	2. REPORT DATE July 1992	3. REPORT TYPE AND DATES COVERED Interim

4. TITLE AND SUBTITLE

Proceedings of the Second Annual Advanced Polymer Components Symposium

6. AUTHOR(S)

John J. Rusek

5. FUNDING NUMBERS

C:

PE: 62302F

PR: 5730

TA: 00R9

7. PERFORMING ORGANIZATION NAME(S) AND ADDRESS(ES)

Phillips Laboratory
OLAC PL/RKFE
Edwards AFB CA 93523-5000

8. PERFORMING ORGANIZATION REPORT NUMBER

PL-TR-92-3018

9. SPONSORING/MONITORING AGENCY NAME(S) AND ADDRESS(ES)
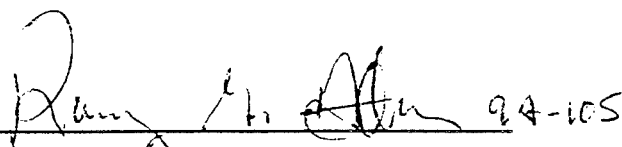
10. SPONSORING/MONITORING AGENCY REPORT NUMBER

11. SUPPLEMENTARY NOTES

COSATI CODE(S):21/06; 21/08/01; 21/09/01; 21/08/02; 21/09/02; 07/05; 07/06

12a. DISTRIBUTION/AVAILABILITY STATEMENT

Distribution approved for public release; Distribution is unlimited.

12b. DISTRIBUTION CODE

A

13. ABSTRACT (MAXIMUM 200 WORDS)

Advanced propulsion concepts rely on advanced propulsion materials. The Phillips Laboratory is aggressively pursuing advanced polymeric materials for use in Solid, Liquid, and Nuclear propulsion component applications. Traditional composite materials have high specific strengths, but suffer from high cost and labor intensive processing. The APC program is currently exploring thermotropic liquid crystal polymers; these materials have high specific strength and can be economically processed by traditional high volume routes such as injection molding and blow molding. Applications envisioned for these materials include rocket nozzles, pressure cases, propellant tanks and conduits, nuclear propulsion containment, fairings, high pressure tanks and orbit-processed habitats for interplanetary voyages. These proceedings contain the papers given at the Second Annual Advanced Polymer Components Symposium, which was held at the United States Air Force Academy at Colorado Springs CO.

14. SUBJECT TERMS

Liquid Crystal Polymers; Liquid Propulsion Synchrotron Radiation; Advanced Materials; Solid Propulsion; Neutron Diffraction; Thermotropic Polyester; Nuclear Propulsion; Polyester Synthesis

15. NUMBER OF PAGES

16. PRICE CODE

17. SECURITY CLASSIFICATION OF REPORT	18. SECURITY CLASSIFICATION OF THIS PAGE	19. SECURITY CLASSIFICATION OF ABSTRACT	20. LIMITATION OF ABSTRACT
Unclassified	Unclassified	Unclassified	SAR

Volume 3

Contrasting Shear-Flow Behavior of Tumbling and Flow-Aligning Nematics

P.T. Mather*, D.S. Pearson, and R.G. Larson[†]

Materials Department, U.C. Santa Barbara, CA 93106
[†]AT&T Bell Laboratories, Murray Hill, NJ 07016

Abstract

Monodomain samples of small-molecule nematic 5CB and 8CB were subjected to shearing flow in an instrument equipped with optical microscopic observation. The torsional shearing geometry was used with circular glass disks which were treated homeotropic (normal) director orientations. We found that increasing the angular velocity of the moving disk from zero, the director configuration in the cell was different for the two materials. Most remarkable was the observation that, while the director stays in the shearing plane for 5CB, the director rotates out of the shearing plane to an orientation nearly orthogonal to the shearing direction for 8CB. At high rotation speeds, disclinations of strength $|s|=1/2$ and $|s|=1$ were created in both 5CB (α_3 negative) and 8CB (α_3 positive). The disclination density averaged over the cell gap, ρ_A=length/area, was measured using image analysis techniques. We compare the two materials based on measured disclination density and its dependence on experimental conditions.

I. Introduction

Liquid crystalline materials in shear flow are known to exhibit disclination production[1,2]. Disclinations are line defects across which the preferred molecular orientation (the director) of the nematic changes abruptly. Even quiescent samples of nematic liquid crystals are characterized by copious quantities of disclination lines and this optical characteristic is referred to as the "threaded texture"[3]. This texture, unlike the "Schlieren" texture of thin samples, consists of a multitude of disclination lines in the form of loops and interconnections. The lines usually have core strengths of 1 ("thicks") or 1/2 ("thins") with the relative populations depending, in the static case, on ratios of elastic constants for the particular material and temperature. Here we have adopted the nomenclature originally due to Nehring[4]. The difference between these defects is the severity of the director distortion around their backbone - their core structure. The core structure metric is the strength[5] which for thicks is ±1 and for thins is ±1/2. For a review on the static properties of liquid crystals see, e.g., Kleman[6] or Saupe[7].

The threaded texture can be coarsened to a "monodomain", a sample free of disclinations, by using either field[8] or surface alignment[9] methods. Here we are concerned

with the creation of disclinations in such disclination-free samples with imposition of a shearing flow.

It is generally believed that the presence of disclinations modifies a material's rheological behavior[10], particularly the elasticity (storage modulus, normal stress differences, etc.) but also the viscosity (region I behavior). The mechanism by which these material properties are affected by disclinations or the presence of texture is largely unknown. One possibility is that the Frank elasticity associated with director curvature may become significant relative to molecular elasticity when the density of disclinations is large. Alternatively, the role of disclinations in LCP rheology may be through the macroscopic director randomization they cause.[11,12] This would cause the macroscopic properties to be an average over a length scale much larger than the average distance between disclinations. While some theoretical support exists for the former[13], parallel superposition experiments[14] suggest support for the latter. In addition to the rheological motivation for studying disclinations under flow, the expected influence of defects trapped in solid polymeric liquid crystals on mechanical behavior provides still further motivation.

The "threaded" texture has been observed for many years in flowing liquid crystals, but a satisfactory understanding of their production has remained elusive. One school of thought is that nematics of the *tumbling* type should be candidates for disclination production[10] because of their propensity for various flow instabilities[15]. Indeed, optical observations during shearing flow of tumbling nematics have shown production of disclinations[2,16]. Here, *tumbling* refers to the rotation of the average molecular orientation with time due to a non-vanishing viscous torque density. Materials for which the viscous torque density does vanish for a particular director orientation are called *flow aligning*. Most small-molecule liquid crystals are of this type. In fact, shear flow of a flow aligning nematic, MBBA, has also been shown to produce disclinations[1]. It is therefore unclear whether or not there is a connection between the tumbling phenomenon and disclination production.

While it is straightforward to determine which shear flow class (*tumbling* vs. *flow aligning*) a particular small molecule nematic belongs to, only a few polymers have been classified in this way. Most small-molecule liquid crystals are *flow aligning;* however, it is beginning to appear that many polymeric liquid crystals are *tumbling*. For rod-like liquid crystals (as opposed to disk-like), the classification is reduced to the determination of the sign of one of the Leslie parameters, α_3. The principal reason that few polymeric liquid crystals have been classified in terms of their flow type is that planar alignment is much more difficult to achieve due to their typically high viscosity.

The goal of this research is to determine the correlation between *tumbling* and disclination production in shear flow by comparing the shear flow behavior of small-molecule nematics possessing similar chemical structure, but of differing sign of α_3. As a framework for their comparison, we monitor the director orientation qualitatively using polarizing microscopy and measure the density of disclinations (projected length/area) present in each material under varying flow conditions.

II. Experimental Method

Materials

5CB and 8CB (4,4'-n-pentylcyanobiphenyl and 4,4'-n-octalcyanobiphenyl) were purchased from BDH and used as received. The optical[17], elastic[18,19], and viscous[20,21] properties have been measured as functions of temperature. 5CB has the phase sequence: **k** 22.4°C **n** 34.5°C **i**, while 8CB has an additional smectic-A phase: **k** 20.5°C **a** 33.3°C **n** 40.1°C **i**. The existence of the smectic phase in 8CB is believed to affect the dynamics of the nematic phase through the renormalization of one of the Leslie viscosities[22,23].

Flow Cell

We have constructed a torsional shear cell, shown schematically in figure 1, which is mounted in a thermostated environment and enables optical observations using conventional light microscopy[24]. The bottom disk is fixed to a rotational bearing table using a retaining ring and the table is connected to a DC servo motor rotating in a controlled steady mode using feedback from the motor tachometer. The top plate is separated from the bottom disk and made parallel by manipulation with a kinetic mount consisting of three micrometers, each with .5 μm resolution, configured as a tripod. Parallelism is obtained by zeroing the micrometers of the tripod with the top and bottom plate in intimate contact. The cell is filled by lifting the top plate/tripod jig, pouring a predetermined quantity of liquid crystal in the middle of the bottom disk, and replacing the top plate. The sample thickness is then adjusted, if necessary, until the liquid crystal meniscus meets the disk edge.

The temperature of the samples is controlled using foil heaters (aluminum on Kapton™) above and below the cell, each with a radial slot for optical access. Power to the heaters (Lambda LLS6018) is regulated using PID control (Eurotherm 808) with J-type thermocouple sensing. A guard heater is placed at the cell periphery to prevent heat loss at the edge. This guard heater consists of water circulated from a thermostated bath (Fisher 9000) through copper tubing embedded in an aluminum ring. Temperature

uniformity is confirmed by checking that the nematic/isotropic transition occurs throughout the cell with a .1 °C temperature jump. The actual temperature is also calibrated with this transition.

Each disk is optically flat (<λ/4) and approximately 43 mm in diameter. The disk surfaces are treated to obtain homeotropic alignment using the standard method of lecithin deposition[9]. The disks is secured to its aluminum mounting using simple retaining springs which apply force on the beveled edge of the disk.

Optical Microscopy

Optical observations are made with a modified NIKON polarizing microscope. Flowing samples can be observed along the radial heater slits which extend from the cell center to the edge. The optical components were mounted on a single-axis translation stage. Focusing is achieved through manipulation of the optics above the sample, rather than the sample itself, using a modular focus mount (NIKON). Video imaging is achieved using a CCD camera (Sony CCD Iris) connected to a monitor (Sony GVM1300), VCR (JVC BR-3200U), and frame grabber (Matrox MVP-AT). The flow cell was designed to allow integration with the translating microscope. Samples were illuminated with light from a tungsten source which is polarized.

To measure disclination density, light was polarized normal to the shear plane. With this polarization state, disclinations of both "thick" and "thin" types appear optically similar. Our method of disclination density measurement relies on the intensity contrast between the disclination lines and the background nematic fluid. The aperture below the condensing lens was adjusted to maximize this contrast. The illuminated sample is viewed with a low power objective lens (5x or 10x) and no analyzer is used.

Image Processing

Threaded images are analyzed to determine the line length per unit viewing area. The observed length is the sum through the objective depth of focus of all length in the viewing area as projected on a horizontal plane. To compute this length a simple image processing algorithm, described next, is implemented. 8-bit raw images are converted to 1-bit, or binary, using an intensity threshold selected so as to separate the dark disclination lines from the brighter background. Binary images are next dilated, to correct for imperfect threshold selection, and finally thinned such that the remaining image consists solely of lines one pixel wide. This thinned image is used to calculate the disclination line length. By measuring the viewing area and the length/pixel using a calibration slide (NIKON Objective Micrometer), the length/area can be computed. To obtain statistically

meaningful disclination densities, we have found that many images from samples under identical conditions must be made and averaged. In all of our experiments, the depth of focus is large enough to observe all of the disclinations present through the gap.

Experiments

Our experimental goals include answering the following: (1) Why do disclinations form in shear flow? (2) What controls the density of disclinations? and (3) How do the answers to (1) and (2) differ for flow-aligning and tumbling nematics. A motivating observation is found in the work of Wahl and Fischer[25], where it was observed that after prolonged shear of MBBA, disclinations were produced. As mentioned previously, the intrinsic stability of this material in shear flow makes this observation of shear-flow-induced disclinations puzzling.

Investigating the origin of disclination production necessarily involves "scouting" experiments which are qualitative in nature. For this purpose, we employ the methods of rheological microscopy in which we visualize director dynamics under shear flow using optical microscopy. Because disclinations have been found to appear upon increasing the applied shear rate or Er, we monitor the samples in torsional shear flow under conditions of increasing rotation speed. Various optical configurations are used and will be explained as the results are described.

To answer the question of what controls the density of disclinations, we have measured the disclination density, as described above, under a wide range of conditions. We also make qualitative observations, using microscopy, of the mechanisms by which the disclination density changes. In this manuscript, we focus solely on the disclination density measurements.

III.   Results and Discussion

5CB

The creation of disclinations in 5CB features interesting hysteresis behavior. When the rotation speed is ramped "slowly" from rest, disclinations do not appear until a critical rotation speed (for a given gap thickness) is reached. Once this critical condition is met, disclinations appear in large quantities, first near the cell edge, then quickly spreading radially throughout the cell. The fact that the cell fills radially with disclinations indicates that there is hysteresis, in that shear rates *lower* than the critical shear rate (edge shear rate at the transition) support disclinations. Further increase of the rotation speed gradually increases the disclinations at each radial position. When the rotation speed is decreased, the disclination density decreases, as expected, but significant numbers of disclinations remain even below the threshold observed during the previous ramp. Shown in figure 2 are disclination density measurements, ρ_A=length/area, for increasing (●) and decreasing (O) shear rate, viewed near the cell edge (r=16.75 mm) showing the dramatic level of hysteresis present.

If the step-size of the rotation speed ($\Delta\dot{\theta}$) used in the ramp is increased, the critical shear rate for disclination creation is decreased as shown in the inset to figure 2. This indicates that the instability is affected by the amplitude of noise (transient director response to a step in shear rate) present. The effect of noise was not investigated further, but a systematic study would likely consist of superposition of random noise of varying amplitude on the motor control signal and observing the dependence of the transition point on the relative amplitude of the noise.

At this point, the meaning of the observed quantity, ρ_A, requires some discussion. The length of disclination lines, L, observed using a given objective lens with a depth-of-focus, d_f, includes the contour length of disclinations within the field of view, projected on a horizontal (velocity-vorticity) plane, and summed over the depth of focus. Two regimes of interpretation exist with respect to the relative magnitude of d_f and the width, $\overline{\lambda}$, of the disclination density distribution across the gap. For $d_f<\overline{\lambda}$, the observed length, L, can be interpreted as the volumetric disclination density, ρ_V, calculated as $L/(A \cdot d_f)$, where L is the observed length and A is the field of view. For $d_f>\overline{\lambda}$, ρ_V is unknown unless an additional measurement of $\overline{\lambda}$ is made. In this case, only $\rho_A \equiv L/A$, here termed the area-based disclination density, is reported. In the instances that the relative magnitudes of d_f and $\overline{\lambda}$ are unknown as in figure 2, it is appropriate to report ρ_A with the understanding that the quantity may be modified if further measurements indicated that $d_f<\overline{\lambda}$. The disclination density data reported below was taken using a 5x objective lens for which d_f was measured to be 760±10μm, when used without condensed sample illumination. Therefore,

since all of our sample thicknesses were smaller than this, h<d_f, all measurements made with this lens yield the area-based disclination density, ρ_A. Later, we will report measurements of the distribution of disclination density across the gap which utilize the 20x objective lens, enabling measurement of ρ_V with vertical resolution.

We now present the results of a systematic investigation of the dependence of disclination density on shear rate and radial position. Shear rate sweeps during which ρ_A is measured yield curves which depend on the radial position in the cell. To gather data in this form, the observation radius is swept for a range of rotation speeds. This procedure was used to minimize long settling times which are necessary due to a long response time of disclination density to a change in shear rate. The dependence of ρ_A on radial position suggests that curvature effects are important.

An example plot showing a manifestation of the radial dependence of disclination density is shown in figure 3. Here, ρ_A is plotted versus shear rate where the data was obtained using a radial sweep (open symbols) at a fixed rotation speed $\dot{\theta} = .15$ rad/sec and rotation rate sweep (filled symbols) at a fixed radius of 16.5 mm. The disclination density is larger at smaller radial positions than would be expected based on shear rate alone. The effects of shear rate, radius, and gap thickness on disclination density are reflected in the an empirical relationship which we now develop. It is first necessary to discuss the dimensional analysis of the problem. Several dimensional quantities in these experiments exist: radial position (r), axial position (z), gap thickness (h), shear rate ($\dot{\gamma}$), and disclination density (ρ_A). From this set, four dimensionless quantities can be constructed: $\tilde{r} = r/h$, $\tilde{z} = z/h$, $Er = (\gamma_1/K_3)\dot{\gamma}h^2$, and $\tilde{\rho}_A = \rho_A h$. Here, Er represents the Ericksen number which, in the usual sense, is a measure of the relative influence of hydrodynamic and elastic stresses. In defining Er, the choice of the material constants is somewhat arbitrary and we chose the twist viscosity ($\gamma_1 = \alpha_3 + |\alpha_2|$) and the bend elastic constant, K_3. The bend elastic constant is used because deviations of the director from the homeotropic boundary conditions are met with resistance due to bend elastic torque. At any rate, all experiments were performed at a given temperature, 32.5 °C, where the material constants are fixed, so the appropriateness of our selection is not tested. Additionally, other choices would yield a (η/K) ratio of the same order of magnitude.

Given this simple dimensional analysis, one expects the general relationship:

$$\tilde{\rho}_A = f(Er, \tilde{r}). \qquad (1)$$

It is recalled that in the measurement of ρ_A, the axial position, z, is effectively averaged

over and therefore $\bar{z}$ does not appear in equation 4.1. Finally, the dimensional analysis implies that plots of $\tilde{\rho}_A$ vs. Er should superpose for fixed $\bar{r}$.

Data was gathered for a range of thicknesses, including 150, 250, 300, and 400 μm. An example scaled plot for $\bar{r} = 30$ appears in figures 4, where superposition of data for fixed $\bar{r}$ is obtained. Also, a power-law dependence (solid line) of ρ_A on Er emerges with the parameters of the power law containing the dependence of ρ_A on $\bar{r}$.

Power law fits were performed on data from samples of four thicknesses: 150, 250, 300 and 400 μm, and with $\bar{r}$ ranging from 14 to 117. With the power-law expressed as,

$$\rho_A h = \alpha(\bar{r}) Er^{\beta(\bar{r})}. \tag{2}$$

The dependence of α (filled symbols) and β (open symbols) on $\bar{r}$ is shown in figure 5. From this figure, one can identify three regions within the torsional shear cell: (I) the inner region, $\bar{r} < 20$, within which disclination density is negligible, (II) a transition region $20 < \bar{r} < 70$, where the dependence of disclination density on $\bar{r}$ is greatest, and (III) an outer or "local scaling" region, $\bar{r} > 90$, where disclination density depends only on Er. In the local scaling regime, region (III), we find that $\alpha \rightarrow 7.5 \cdot 10^{-3}$, and $\beta \rightarrow 0.635$.

8CB

8CB forms roll cells above a critical Ericksen number and disclinations are nucleated from this roll cell structure. At a fixed Ericksen number above the threshold for roll cell formation, the density of disclinations increases with time, so much so that the phase grating caused by the roll cells is virtually unobservable. A further increase in Er leads to a marginal increase in disclination density. As with 5CB, the density of disclinations remains significant when Er is lowered past the threshold for their formation on increasing Er. Shown in figure 6 is an example of the hysteretic behavior of disclination density where ρ_A is plotted as a function of shear rate for a 400 μm sample. The large overshoot and undershoot observed following the threshold for disclination formation is accompanied by the observation that the transition occurs locally, at first, with disclinations being created in large quantities within a narrow range of radial positions. As Er is further increased, the region of disclinations localized to a small range of radial positions suddenly spreads out to encompass most of the cell. It is at this point that the disclination density suddenly drops significantly. Still further increase in Er, and passage of time, returns the measured disclination density to the steady state curve which

is measured for decreasing Er. The exact shape of the curve for increasing Er depends on the ramping rate, with the overshoot and undershoot being eliminated for very small ramping rates.

For 8CB, plots of disclination density, ρ_A, versus applied shear rate, $\dot{\gamma}$, feature curves which depend on the sample thickness, as shown in figure 7. In general the levels of disclination density in 8CB are larger than in the case of 5CB over a similar range of shear rate. In contrast with 5CB, however, data from various thicknesses and radial positions superpose when plotted as $\rho_A h$ vs. Er, indicating a lack of explicit dependence of disclination density on the radial position. Figure 8 show a plot of dimensionless disclination density, $\rho_A h$, versus Er for several gap thicknesses (250[$\triangle$], 300[$\lozenge$], 350[$\bigcirc$], and 400[$\square$] μm) along with region III 5CB data (∇). Much information can be extracted from this figure; however, the most striking feature is the contrast in magnitude of disclination density between the two materials. *The density of disclinations in 8CB is an order-of-magnitude higher than in 5CB.*

For all thicknesses of 8CB studied, with the exception of 250 μm, we find a cross-over in scaling behavior from a power-law exponent of 0.5 for Er<2000 to a larger value tending toward 1.0 for Er>2000. We regard this cross-over in exponents as an indication that the behavior of disclinations in the shear flow of 8CB changes from 2-dimensional at low Er to 3-dimensional at high Er. This is peculiar, considering the large thicknesses of the samples and in light of the absence of an exponent cross-over for the *smallest* sample thickness, 250 μm, which has an exponent near 1.0 for the full range of Er investigated. Consistent with this observation, however, is the dependence of the width of the disclination density distribution on Er. In figure 9 we plot the width of the distribution of disclinations (determined to be the width at 1/5 height) as a function of Er for 8CB samples of thickness 400($\bigcirc$) and 250($\bullet$) μm. We find that coincident with the cross-over from 2D to 3D behavior of the 400 μm sample is the occurrence of saturation of the distribution width. The 250 μm sample, on the other hand, possessed distribution widths comparable to those of the 400 μm sample for 3D behavior for Er values below the cross-over. This is consistent with the observation that no 2D to 3D cross-over behavior is observed for this thickness. The relevance of the distribution width to the scaling dimensionality will be addressed in the section that follows.

Table 1 below summarizes the observed scaling behavior demonstrated in figure 4.0, from the formula $\rho_A h = \alpha \cdot Er^{\beta}$. The following section will attempt to explain the observed scaling behavior within the framework of "Marrucci Scaling".

Table 1: Power-law parameters for 8CB and 5CB

	α	β
8CB - 2D	0.149	0.5
8CB - 3D	$3.24 \cdot 10^{-3}$	1.0
5CB (free)	$7.41 \cdot 10^{-3}$	0.635
5CB (fixed)	$2.14 \cdot 10^{-2}$	0.5

Scaling Behavior

We now check for agreement between our disclination density data and "Marrucci scaling"[26], in which it is assumed that there exists a limiting value of the texture-based Ericksen number, $Er_{tex} \sim \dot{\gamma}a^2 \approx Er_{sat}$, which should be considered a material property. Here, Er_{tex} is a measure of the ratio of hydrodynamic stresses to elastic stresses from Frank elasticity due to the presence of "texture" characterized by a length scale, a. As described by Burghardt and Fuller[27], nematics may respond to any attempt to raise the local (textural) Ericksen number through increased shear stress by decreasing the characteristic length scale by creating defects. The parameter varied in the experiments is Er_{gap}, which uses the cell thickness as the length scale. The two Ericksen numbers are related,

$$Er_{tex} \cdot \frac{h^2}{a^2} = Er_{gap}. \tag{3}$$

One can define a two-dimensional texture length scale $a^{(2)} = 1/\rho_A$, which could be interpreted as the lateral spacing between disclination cores, leading to:

$$Er_{tex} \cdot (\tilde{\rho}_A)^2 = Er_{gap}, \tag{4}$$

where $\tilde{\rho}_A = \rho_A h$. This 2D version of Marrucci scaling then predicts:

$$\tilde{\rho}_A = \sqrt{Er_{gap}/Er_{tex}}. \tag{5}$$

This gives a slightly weaker Er_{gap} dependence compared with our findings in the local scaling limit of 5CB where and exponent of 0.635 was found, but shows good agreement with the 8CB data for Er<2,000. In both cases we can calculate Er_{tex} from α $(=Er_{tex}^{-1/2})$, fixing β at .5 for the 5CB case. Doing this, we find $Er_{tex} \sim 2,200$ for 5CB, while for 8CB

$Er_{tex}\sim50$. The latter is in agreement with the numerical simulation study of Burghardt and Fuller[27] on transient flow of tumbling nematics.

In an analogous fashion, one can define a 3-dimensional texture length scale such that $\rho_V = 1/\left(a^{(3)}\right)^2$, recalling that ρ_V is the volumetric disclination density. The right-hand side of this expression may be interpreted as the number of disclination cores per unit area of the gradient-vorticity plane. In the limit of large Er, we expect the disclinations to fill the gap such that $\rho_V = \rho_A/h$. In this limit, our definition of $a^{(3)}$ reads $\rho_A = h/\left(a^{(3)}\right)^2$, leading to the prediction,

$$\tilde{\rho}_A = \frac{Er_{gap}}{Er_{tex}}. \tag{6}$$

This agrees with our 8CB data for Er>2000, and for the entire Er range for the 250 μm 8CB sample. We note that a scaling exponent of 1.0 is also predicted for the case where the disclinations do not completely fill the gap, but fill a fraction of the gap, $\lambda = m \cdot h$, where λ is the width of the distribution and m<1. For the simple case of a uniform distribution, $\rho_V = \rho_A/mh$, and we find the prediction

$$\tilde{\rho}_A = m \cdot \frac{Er_{gap}}{Er_{tex}}. \tag{7}$$

We have observed that the distribution of disclinations across the gap for both materials is approximately Gaussian with a width-at-half-height, in the case of 3D 8CB, of 0.333·h. Finally, we find from the 3D 8CB data that $Er_{tex} \approx 100$.

Inspection of the raw ρ_A measurements indicates a range $5 < \rho_A < 35$ mm^{-1} corresponding to an average spacing between projected disclinations (l_{bp}) in the range $25 < l_{bp} < 200$ μm. In an order of magnitude sense, one can estimate the vertical spacing (l_v) and lateral spacing (l_h) between neighboring disclinations. l_h is estimated to be l_{bp}, from 25 to 200 μm, while l_v is on the order of 50-60 μm ($\lambda_{WHH}/2$). Therefore, the nearest-neighbor core-core interactions are roughly isotropic. However, since core-core interactions are long ranged ($F \sim d^{-1}$), an assessment of the total forces that a test disclination line feels must account for many-body interactions. Although a given disclination feels an isotropic force field from its nearest neighbors, the total force it feels may be highly anisotropic due to the planar contribution from the pseudo-infinite flat sea of other disclinations. Here we have neglected hydrodynamic forces.

In the limit of very large anisotropy, 2D behavior is expected. For 5CB we argue that for the range 500<Er<5000, disclinations feel forces which are highly anisotropic, being larger horizontally than vertically. Because we detect a cross-over from 2D to 3D scaling in 8CB samples (except for 250 μm) on increasing Er, the increasing disclination density itself may be the cause of the cross-over. At very low Er, disclinations are localized at the sample mid-plane due to the symmetry of the image forces from the bounding disks. As the disclination density is increased with increased Er, the disclinations pack near the mid-plane until the density become large enough that the disclinations begin to pile-up about the mid-plane. If the disclinations pile up to an extent equal or larger to the screening length of the core-core interaction forces, then the force on a test disclination is rendered isotropic and 3D scaling is expected.

IV. Concluding Remarks

Our experiments revealed some important aspects of disclination production in sheared nematics, including,

(1) Observation of disclinations in a nematic liquid crystal cannot be used to classify the material as a tumbling liquid crystal,
(2) Shear flow creates roughly ten times the density of disclinations in 8CB in comparison to 5CB, and
(3) The scaling of disclination density with Ericksen number under goes a transition from 2D to 3D under certain conditions.

Future work in this area will focus on the creation of disclinations in polymeric liquid crystals (PLC's).
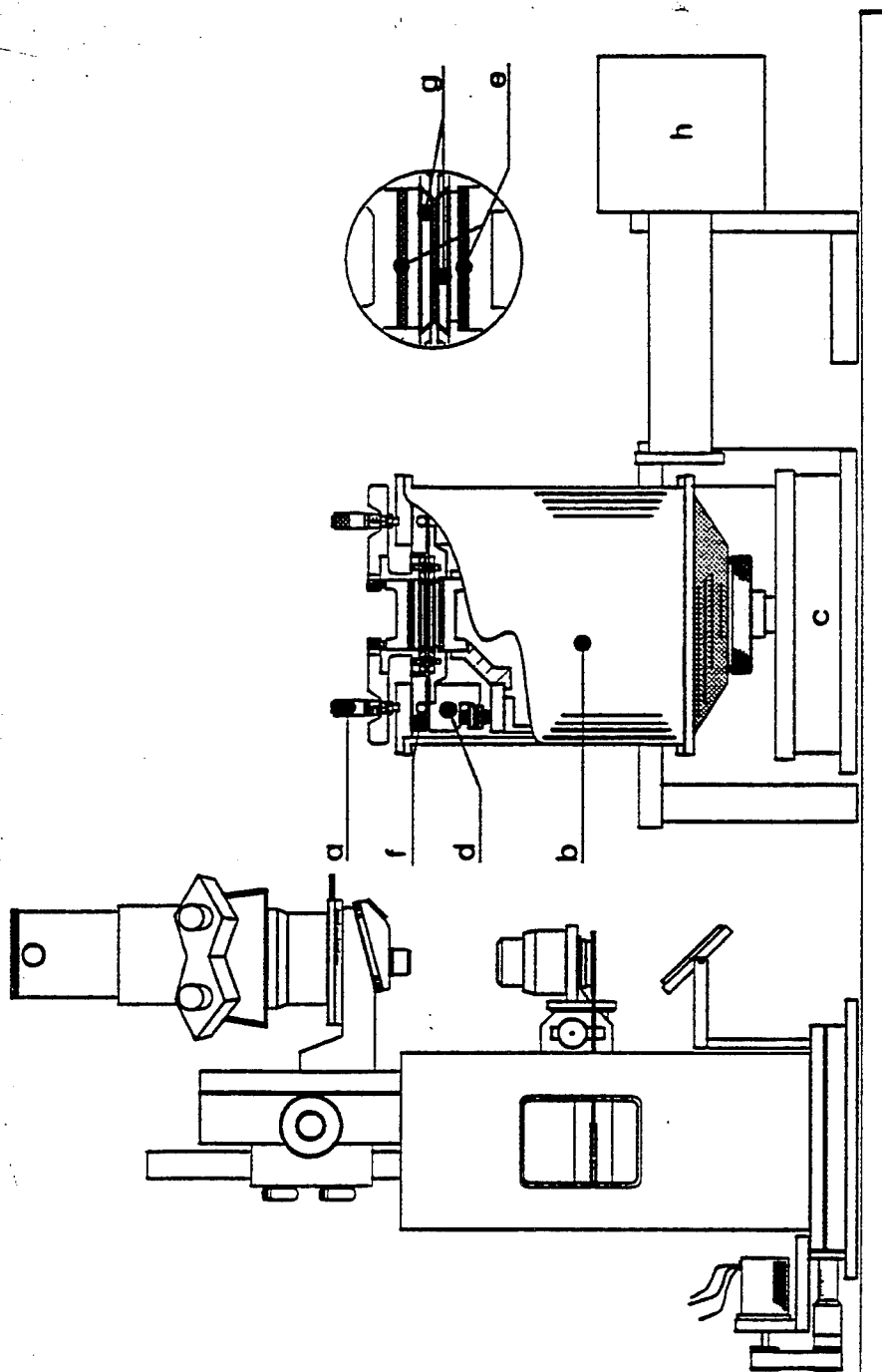
Figure 1 Schematic drawing of the apparatus, (a) kinematic mount consisting of three micrometers equally spaced on a bolt circle and set in recessed mounts, (b) outer support cylinder which transfers torque and normal force to: (c) strain-gauge transducer (Rheometrics Inc.), (d) rotary bearing table (RollerTrac VT, Master Machine Tools), (e) foil heaters (Heater Designs, Inc.) backed by glass insulators (Macor®, Corning Glass) and topped with copper disks, (f) guard heater using heating water from a circulation bath.
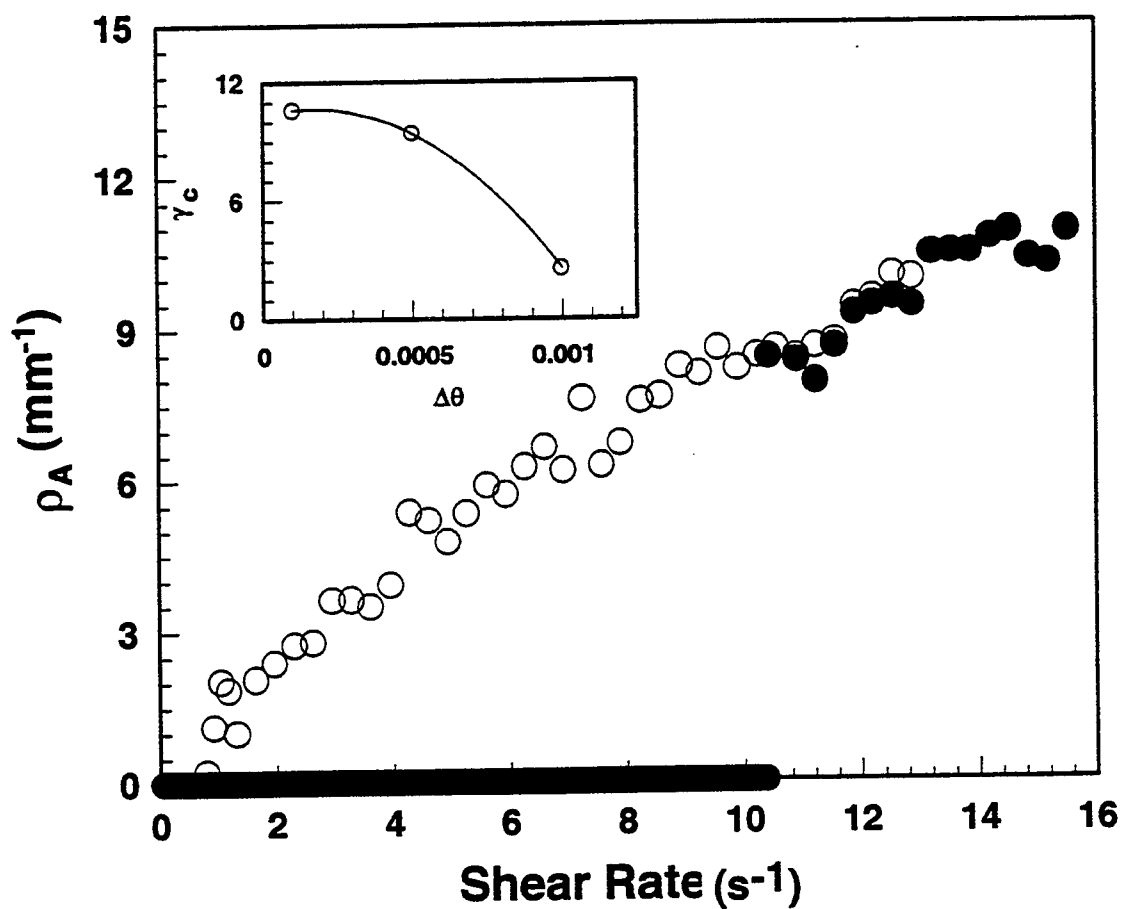
Figure 2: Hysterisis of scaled area-based disclination density in 5CB for h=250 μm. Closed symbols are for rising shear rate and open symbols are for decreasing shear rate.
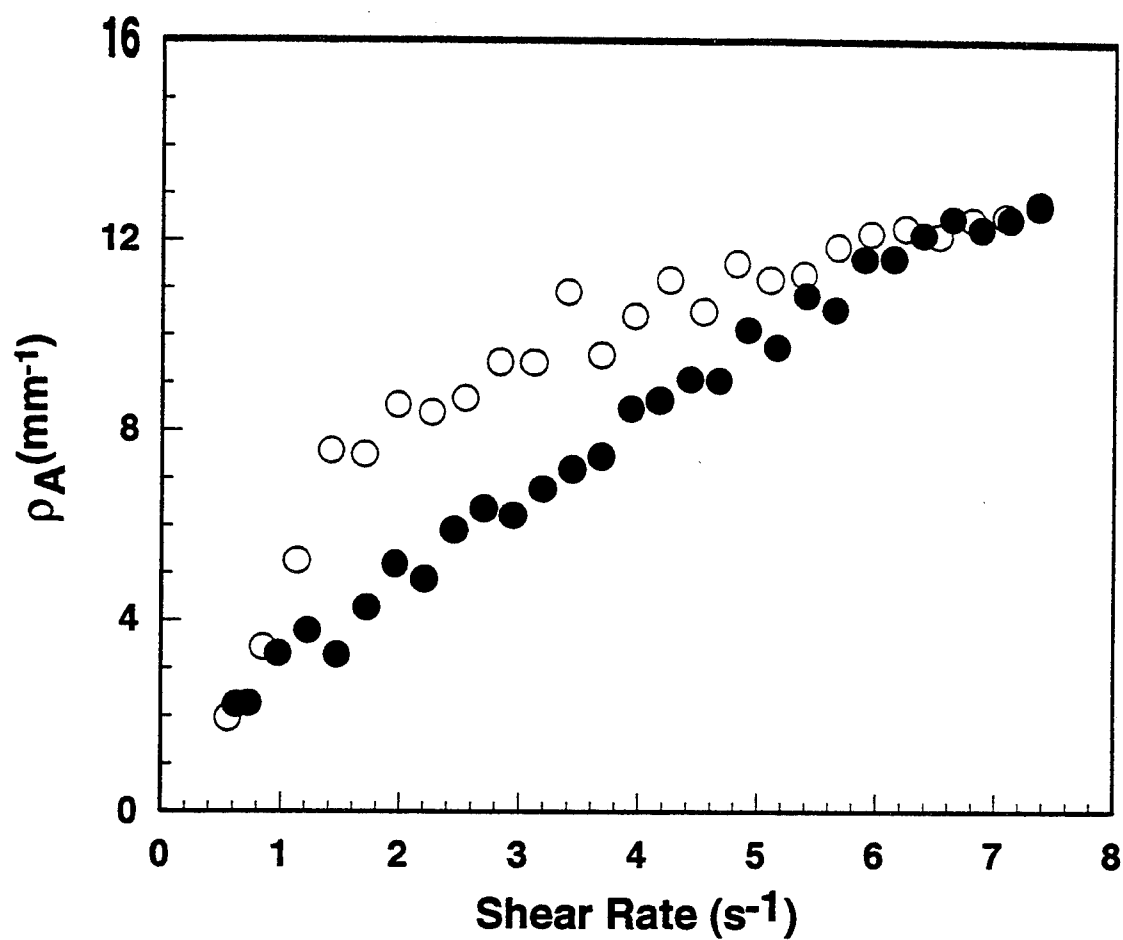
Figure 3: Disclination density ρ_A vs. shear rate for 5CB obtained using a radial sweep (open symbols) at fixed rotation speed (.15 rad/sec) and with a rotation speed sweep at fixed radial position of 16.5 mm. Sample thickness is 335 µm.
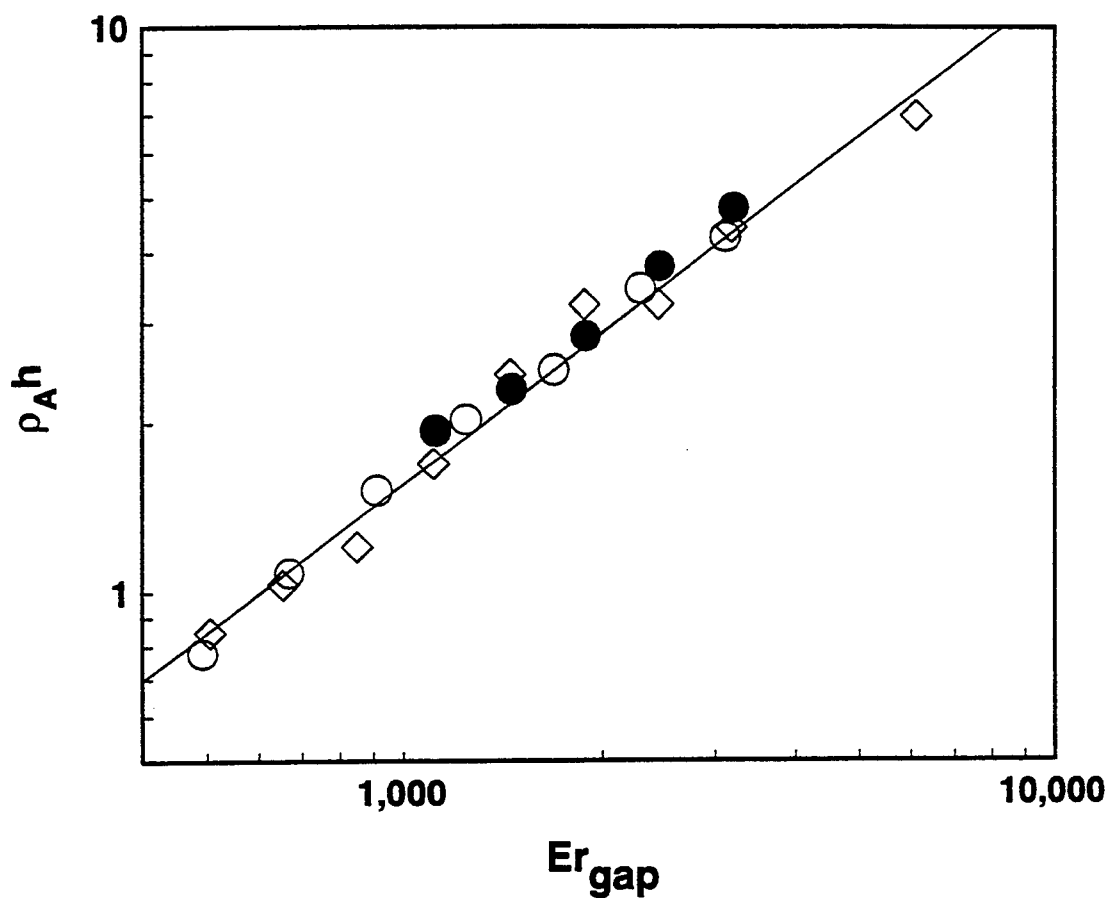
Figure 4: Dimensionless disclination density $\rho_A h$ vs. Er_{gap} for 5CB at 32.5 °C and $\bar{r} = 30$ for gap thicknesses of 250 μm (O), 300 μm (•), and 400 μm (◊). The solid line represents a power law fit to the 400 μm data.
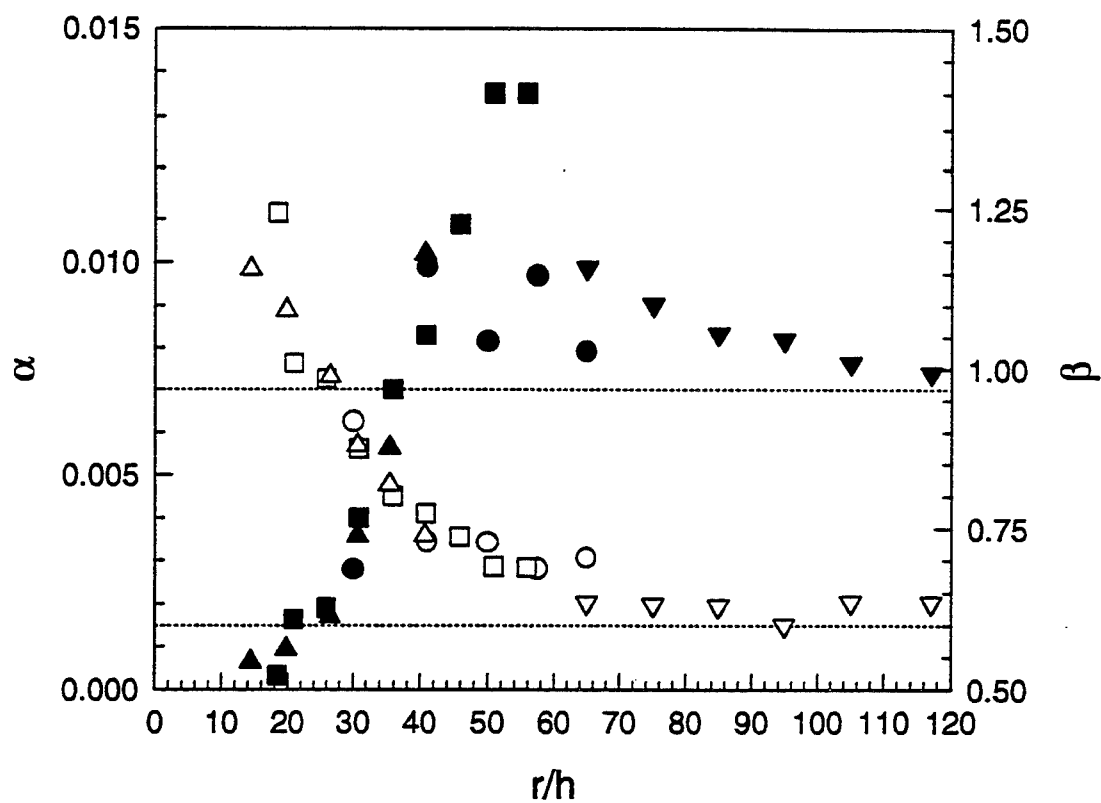
Figure 5: Pre-exponential factor, α (filled symbols), and exponent, β (open symbols), vs. r̃ =r/h for 150 μm (∇), 250 μm (O), 300 μm (•), and 400 μm (Δ).
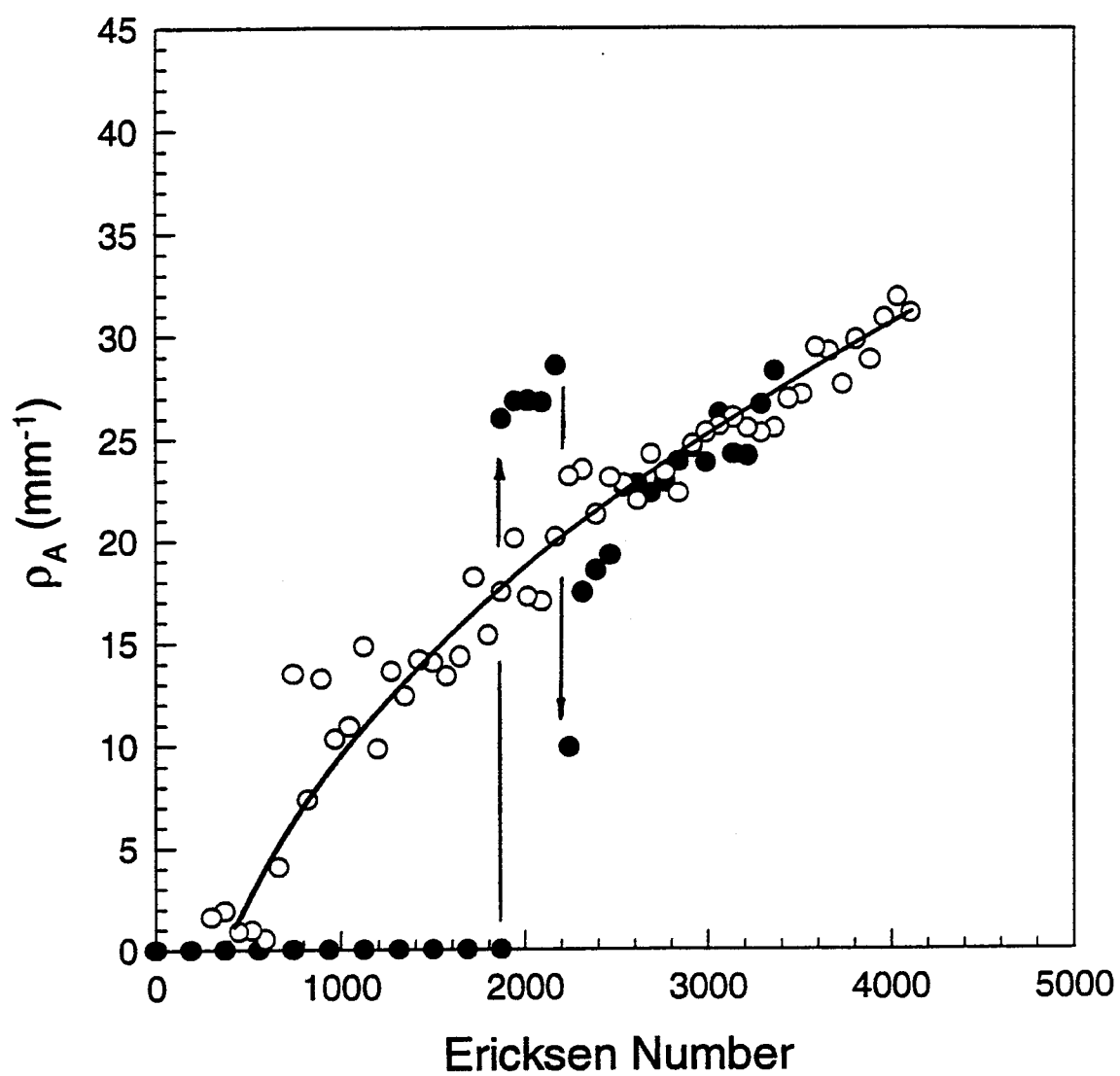
Figure 6: Hysterisis of area-based disclination density for h=400 μm. Closed symbols are for rising Er and open symbols are for decreasing Er.
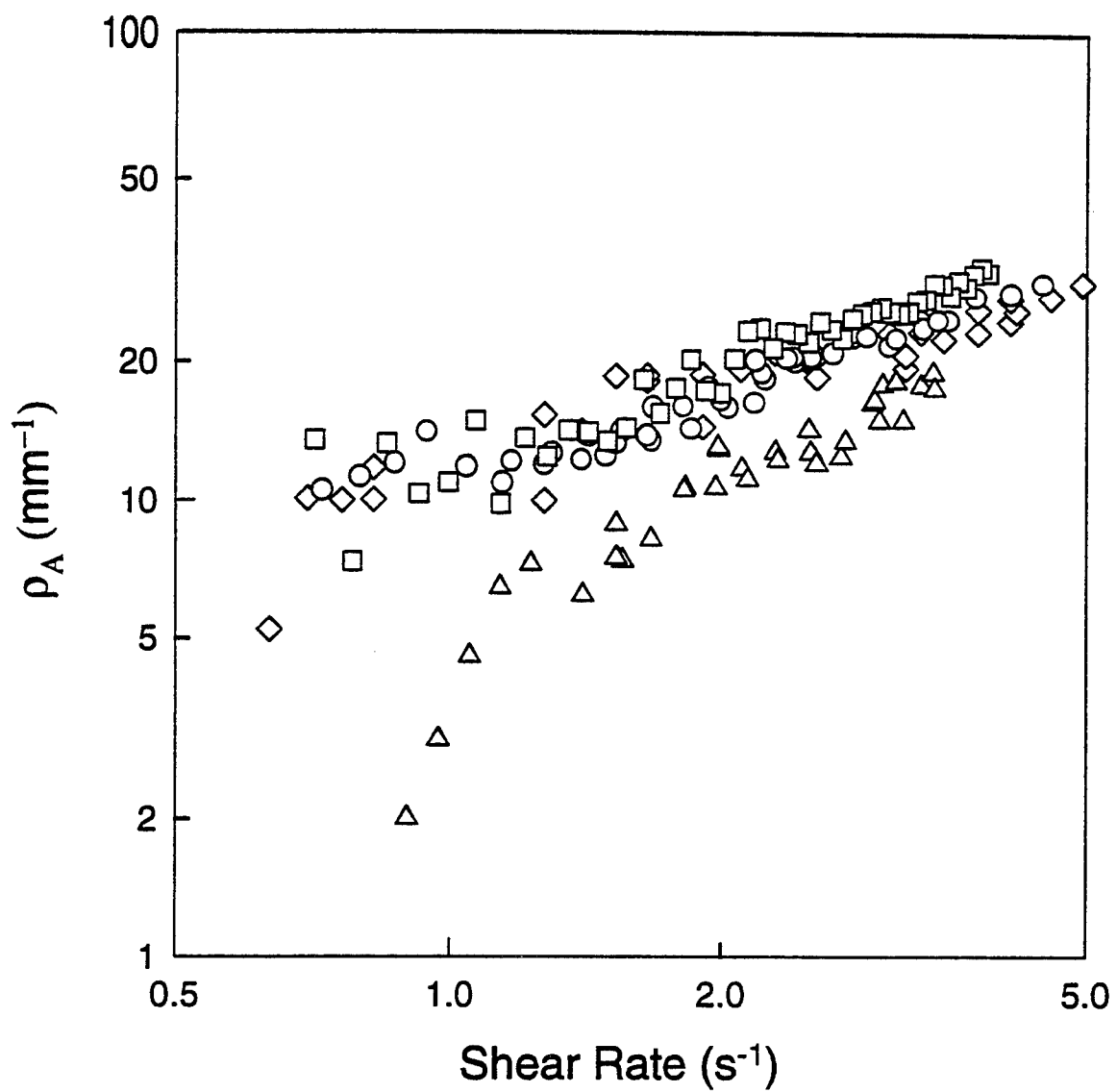
Figure 7: Raw plot of disclination density versus shear rate for three sample thicknesses h=250 μm(Δ), 300 μm(◊), 350 μm(O),400 μm(□).
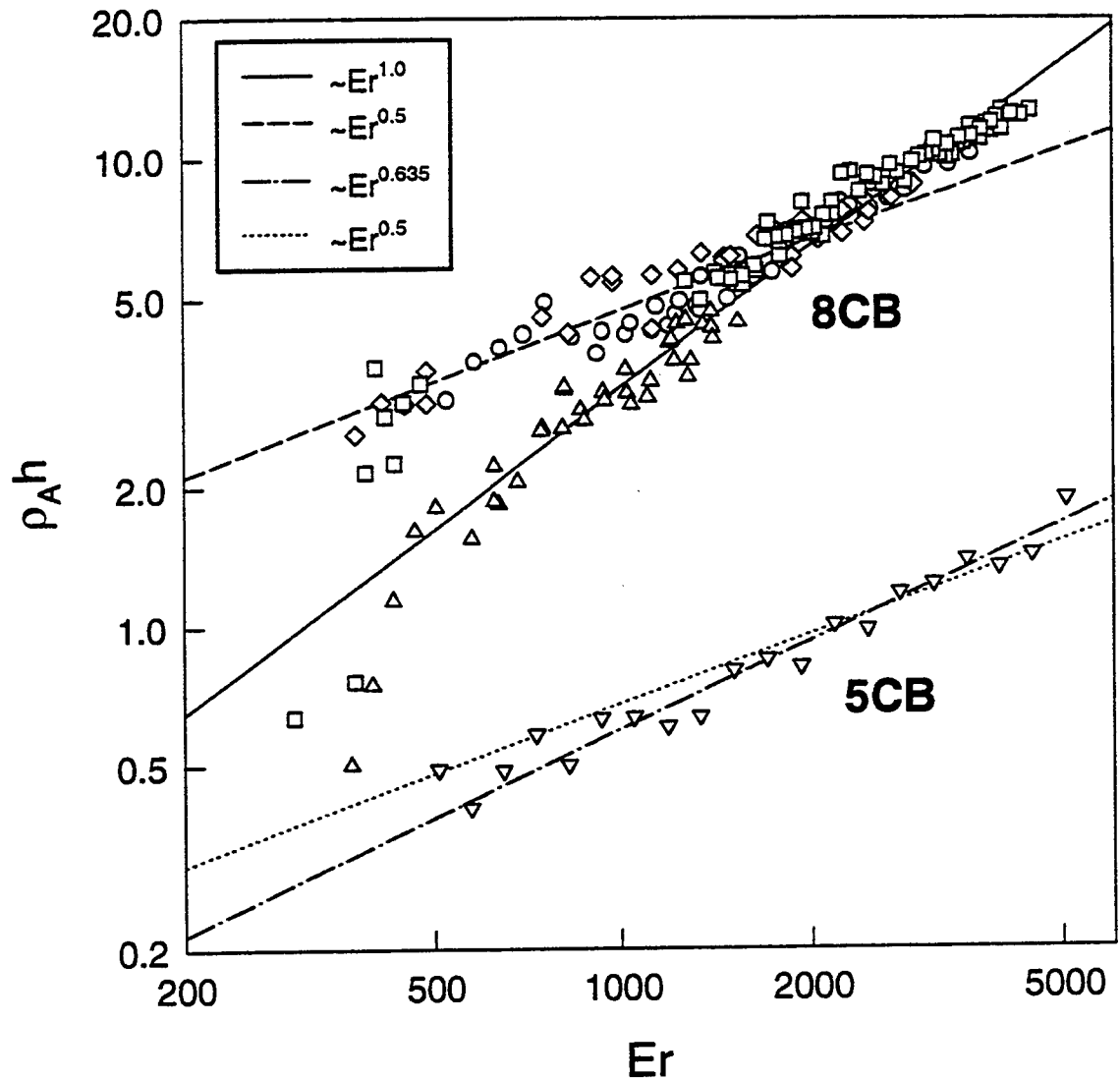
Figure 8: Dimensionless disclination density vs. gap Ericksen number for three sample thicknesses h= 250(△), 300(◊), 350(O), and 400 (□) μm. The solid line represents a best fit of the data (except 250 μm) with the exponent fixed at 1/2 (2D scaling) while the single dashed line is the best fit the exponent fixed at 1 (3D scaling). Also shown are the results for 5CB in the local-scaling limit (r/h=117) for comparison.
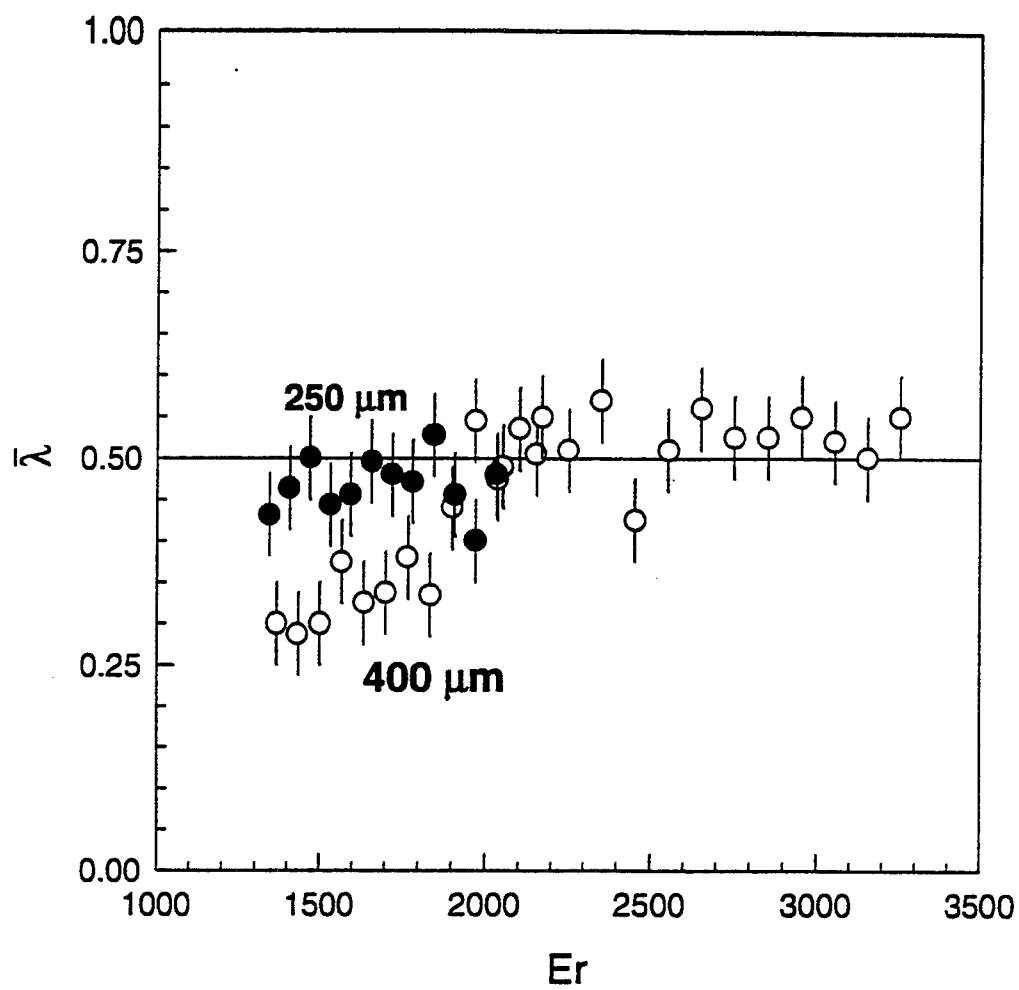
Figure 9   Dependence of λ, the average thickness of the disclination-containing slab, on Ericksen number.

References

1   D.J. Graziano and M.R. Mackley, "Disclinations Observed During the Shear of MBBA", *Mol. Cryst. Liq. Cryst.*, 1984, v106, 103-119.

2   P.E. Cladis, S. Torza, "Flow Instabilities in Couette Flow in Nematic Liquid Crystals", Colloid and Interface Science, 1976, v4, 487-499.

3   D. Demus and L. Richter, *Textures of Liquid Crystals*", Verlag Chemie, New York, 1978

4   J. Nehring, "Calculation of the Structure and Energy of Nematic Threads", *Phys. Rev. A*, v7, n5, 1973, 1737-1748.

5   P.G. DeGennes, The Physics of Liquid Crystals, 1985.

6   M. Kléman, "Defects in Liquid Crystals", *Rep. Prog. Phys.*, 1989, v52, 555-654.

7   A. Saupe, "Disclinations and Properties of the Directorfield in Nematic and Cholesteric Liquid Crystals", *Mol. Cryst. Liq. Cryst.*, 1973, v21, 211-238.

8   M. Srinivasarao, PhD Dissertation, Carnegie Mellon University, 1990.

9   J. Cognard, "Alignment of Nematic Liquid Crystals and Their Mixtures," *Mol. Cryst. Liq. Cryst.*, Suppl.1, 1985.

10 G. Marrucci and F. Greco, "Flow Behavior of Liquid Crystalline Polymers", *Adv. Chem. Phys.*, v86, 1993, Wiley.

11 R.G. Larson, M. Doi, "Mesoscopic Domain Theory for Textured Liquid Crystalline Polymers", *J. of Rheology*, 1991, v35, n4, 539-563.

12 G. Marrucci and P.L. Maffetone, "Nematic Phase of Rodlike Polymers. II. Polydomain Predictions in the Tumbling Regime," *J. Rheol.*, 1990, v34, n8, 1231-1244.

13 W.R. Burghardt, "Oscillatory Shear Flow of Nematic Liquid Crystals", *Journal of Rheology*, 1991, v35, n1, 49-62.

14 P. Moldenaers, J. Mewis, "On the nature of viscoelasticity in polymeric liquid crystals", Jo. *Rheology*, 1993, v37, n2, 367-380.

15 E. Dubois-Violette, G. Durand,E. Guyon,P. Manneville, P. Pieranski, "Instabilities in Nematic Liquid Crystals", *Solid State Physics Suppl. 14*, 1978, 147-208.

16   C. Gähwiller, "Temperature Dependence of Flow Alignment in Nematic Liquid
        Crystals", *Phys. Rev. Letters,* 12 June 1972, v28, n24, 1554-1556.

17   P.P. Karat and N.V. Madhusudana, "Elastic and Optical Properties of Some 4'-n-
        Alkyl-4-Cyanobiphenyls", *Mol. Cryst. Liq. Cryst.,* v36, 1976, 51-64.

18   P.P. Karat and N.V. Madhusudana, "Elastic and Orientational Order in Some 4'-n-
        Alkyl-4-Cyanobiphenyls: Part II", *Mol. Cryst. Liq. Cryst.,* v40, 1977, 239-245.

19   S. Morris, P. Palffy-Muhory, D.A. Balzarini, "Measurements of the Bend and
        Splay Elastic Constants of Octyl-Cyanobiphenyl", *Mol. Cryst. Liq. Cryst.,*
        v139,1986, 263-280.

20   H. Kneppe, F. Schneider, N.K. Sharma, "Rotational Viscosity γ_1 of Nematic
        Liquid Crystals", *J. Chem. Phys.,* v77, n6, 1982, 3203-3208.

21   H. Herba, A. Szymanski, A. Drzymala, "Experimental Test of Hydrodynamic
        Theories for Nematic Liquid Crystals", *Mol. Cryst. Liq. Cryst.,* v127,1985, 153-
        158.

22   C.R. Safinya, E.B. Sirota, R.J. Plano, "Nematic to Smectic-A Phase Transition
        under Shear Flow: A Nonequilibrium Synchrotron X-Ray Study", *Physical Review
        Letters,* 15 April 1991, v66, n15, 1986-1989.

23   R.F. Bruinsma, C.R. Safinya, "Landau Theory of the Nematic Smectic-A Phase
        Transition under Shear Flow," *Phys. Rev. A,* 1991, v43, n10, 5377-5404.

24   P.T. Mather and D.S. Pearson, *manuscript in preparation.*

25   J. Wahl, F. Fischer, "Elastic and Viscosity Constants of Nematic Liquid Crystals
        from a New Optical Method", *Mol. Cryst. Liq. Cryst.,* 1973, v22, 359-373.

26   Marrucci, G., "Rheology of Liquid Crystalline Polymers," *Pure Appl. Chem.,*
        1985, v57, 1545-1552.

27   W.R. Burghardt, G.G. Fuller, "Transient Shear Flow of Nematic Liquid Crystals:
        Manifestations of Director Tumbling", *Journal of Rheology,* 1990, v34, n6, 959-
        992.

WILEY ORGANICS
AND
ORGANIC TECHNOLOGIES

CONTENTS

HISTORY

FROM OHIO STATE UNIVERSITY TO CHEMICAL SAMPLES COMPANY

Wiley Organics has a unique background in the manufacture of organic research and development compounds. In 1951, Vincent G. Wiley joined the American Petroleum Institute's project at Ohio State University, then directed by Dr. Kenneth W. Greenlee. The project was sponsored by the American Petroleum Institute for the purpose of producing pure hydrocarbons in order to gain a better understanding of the relationship between molecular structure and fuel octane numbers. Over the life of the project, from 1938 to 1963, over 350 pure hydrocarbons were synthesized for the engine testing program and for the standard samples program at Carnegie Technical Institute, in conjuction with the National Bureau of Standards for the certification of pure hydrocarbons. In 1962, the hydrocarbon lab was moved to Oklahoma State University. Since neither Ken Greenlee or Vincent Wiley were interested in moving to Oklahoma, and since they believed the market would support a private enterprise, they founded Chemical Samples Company. They built new research and development laboratories for the manufacture of hydrocarbons and related compounds in 1963. By 1969, Chemical Samples Company had published a catalog listing of over 1800 research chemicals and their molecular structures. Chem-SampCo pioneered in the market by certifying the purity and identity of almost all of the 1800 research chemicals which they manufactured and sold. They quickly gained international recognition as the world's largest supplier of pure hydrocarbons, supplying the petroleum industry with analytical standards for the identification of petroleum components.

CHEM SAMP-CO'S EXPERIENCE MAKING PHEROMONES

Because of years of experience in manufacturing of specific complex molecules requiring multiple-step synthesis, Chemical Samples Company had required the expertise necessary for the production of commercial quantities of pheromones, the sex attractant compounds critical to the mating process of insects. ChemSampCo was the first company to successfully scale-up the manufacture of these complex compounds.

CHEMSAMPCO IS SOLD TO ALBANY INTERNATIONAL

ChemSampCo became a world leader in the production of pheromones by 1978. They were instrumental in supplying pheromones for the control of the Pink Boll worm cotton pest in Arizona and California. Potential foreign markets also included those in Egypt, Brazil and Israel. Albany International was ChemSampCo's largest customer and they were committing millions of dollars to the development of new feild application systems each year for many different insect pests. Albany International felt they would strengthen their market postion by the purchase of ChemSampCo. This purchase was completed in 1978, at which time Albany International was projecting a very rapid expansion of the pheromone technology throughout the world. These projections required a large expansion of the chemical production facilities.

NEW ALBANY INTERNATIONAL PRODUCTION PLANT IS BUILT

A new $10 million facility was built on the west side of Columbus, Ohio specifically for the manufacture of pheromones. The plant was designed and built under the direction of Vincent G. Wiley, as general manager, And David B. Wiley, as project manager. David went on to become plant manager. The plant was operational in late 1979, and successfully began manufacturing commerial quantities of several pheromones.

WILEY FAMILY BUYS BACK RESEARCH CHEMICALS BUSINESS

In 1980, Albany International made a decision to sell the research organics business to the Wileys. Subsequently, the Wileys left and started Wiley Organics with the catalog inventory, small scale synthesis and distillation equipment, and experience. In July, 1981, Wiley Organics leased a 13,000 square foot warehouse and moved in over 30,000 bottles, cans, and drums of the valuable organic inventory used to support the fine chemicals business. The largest production equipment, at that time, had only 25 gallons capacity. By 1985, Wiley Organics had increased its production capacity to include 200, 300, 800, and 1800 gallon production vessels, with associated purification/distillation columns up tp 1800 gallon batch capacity.

NEW PLANTS IN COSHOCTON AND NEWARK PURCHASED

As demand for Wiley Organic's services and products grew, an intensive search for a larger plant facility was begun. In the fall of 1986 a 50,000 square foot facility was located in Coshocton, Ohio. Refurbishment of the plant was begun in February 1987 and in June the first distillation column was brought on stream. By the fall of 1987 reaction vessels of 2000 and 4000 gallons capacity had been put in place, in addition to reboilers of 1200, 2200, and 10,000 gallons feeding 40 to 50 foot, high efficiency, packed columns of up to 20" in diameter. In 1989 another facility was purchased in Newark, Ohio and brought on stream by a newly created division of the company, Organic Technologies. The Organic Technologies unit has focused on pharmaceutical and polymer intermediates as well as other custom synthesis and distillation work. Wiley Organics now has production capabilities for tonnage volumes of a number of specialty custom products. The larger facilities now available have allowed greater diversification and economies of scale to be realized. They also have allowed accelerated development of a number of proprietary products and processes along with greater capabilities for custom product development services for other major manufacturers.

TECHNOLOGY AND SERVICES

ORGANIC SYNTHESIS

Wiley Organics has experience in the synthesis of over 1000 organic compounds by various routes. This expertise makes the organization especially well suited for custom organic synthesis and process development. They are experts in Grignard-type reactions, as many of the hydrocarbons they manufacture start with one or more Grignard steps. In fact, the company may well have run more different Grignard reactions than virtually any other domestic company. They are experts in all types of liquid ammonia reactions, and perform oxidations, low pressure and high pressure hydrogenations, high temperature vapor-phase reactions, halogenations, and a variety of specific condensation reactions.

DISTILLATION AND PURIFICATION

Over the years, Wiley Organics has developed an exceptional capability in fractional distillation, routinely producing compounds of 99.9% purity from the lowest to the highest molecular weight hydrocarbons. Separations of compounds with boiling point differentials of only one degree Celsius are feasible. Pressure distillations as high as 65 psi, and vacuum distillations down to .01 mm are performed. Wiley Organics also frequently does custom distillation for customers who have been unable to purify a product by conventional means or who need a quntity not suited to the customers existing equipment. Their experience with azeotropic distillations and extractive distillations, enable them to achieve purification in difficult cases.

MONOMERS AND POLYMERS

Wiley Organics has been synthesizing and developing purification processes for specialty monomers for about ten years. The company has participated collaboratively in the development of new liquid crystalline polymer (LCP) systems and/or monomers for the same. Currently, programs to supply developmental quantities of monomers for polyimides, high temperature thermosets are underway.

EQUIPMENT

Wiley Organics is proficient in the utilization, design, and installation of practically all types of process equipment used in the chemical industry, including glass and stainless steel equipment with capacities up to 4,000 gallons, distillation equipment of all types including highly efficient 120+ theoretical plate columns, wiped film evaporators. Reaction vessels of up to 4000 gallons (15,000 liters) are currently operational.

CUSTOMERS

Wiley Organics' customers encompass nearly all major institutions involved in advanced chemical research and development; included would be virtually all the major universities with programs in advanced chemistry, all the major petroluem companies and those pharmaceutical and chemcial manufactures involved in basic research and product development relying on petroleum-based starting materials and intermediates. A large number of their catalog items are also supplied to the major domestic fine chemical resellers such as Aldrich Chemical Company, ICN-K&K Laboratories and Pfaltz & Bauer. Large foreign customers include Fluka, Jannsen and Tokyo-Kasai.

HYBRID SOUNDING ROCKET DEVELOPMENT
AT THE UNITED STATES AIR FORCE ACADEMY

Capt. M. C. Lydon
Capt. R. J. Simmons
United States Air Force Academy

Abstract

The United States Air Force Academy (USAFA) has developed a LOx-HTPB (Liquid Oxygen-Hydroxyl Terminated Polybutadiene) powered sounding rocket. USAFA has proven the use of hybrid rockets as a forgiving instrument to teach the fundamentals of aerospace system engineering at the undergraduate level. A rocket motor has been designed which will deliver 1000 lbs. of thrust for 10-15 seconds and power the vehicle to approximately 20,000 ft. The rocket will be recovered via parachute and system performance will be recorded with an onboard data acquisition system. The main subsystems have been tested successfully and a launch is expected this summer.

I. Background

USAFA has been involved in hybrid research since 1989. During the last four years the Academy has developed the capability to fire 2.5 in diameter gaseous Oxygen powered hybrid rocket motors. In 1991 the Academy launched a small GOx-HTPB rocket designed by a systems engineering class offered by the Department of Astronautics. It was the first Department of Defense land-based hybrid rocket launch. During the two years that followed the successful first launch, a team of cadets and officers designed and built a larger and more powerful rocket, dubbed Chiron (see fig 1).

The overriding goal of the research effort is to give the students 'hands on' experience in design, test, integration and operation of an aerospace vehicle. A hybrid rocket was chosen as the research subject due to its inherent safety and the renewed interest shown by NASA and industry in the technology in recent years.

The research goals were also very broad, to fly a multi-port sounding rocket to an altitude of 30,000 ft and recover it safely. This paper will describe the rocket's sub-systems, design constraints and design choices that were made during the process. It will discuss the performance modeling and test results, and draw a conclusion as to the efficacy of this type of program in the undergraduate environment.

II. Propulsion

Chiron is powered by a three-port HTPB and liquid oxygen hybrid rocket motor (see fig 2). The motor is 6 inches in diameter and 42 inches long. It is designed with a two inch pre-combustion chamber and a four inch post-combustion chamber. To test a multi-port motor, three pie-shaped ports were designed with a Plexiglas web-stiffener in the walls between the ports.

The test motor cases were made of 6061 aluminum with 1/2" flanges welded on each end. The flight motor is constructed of stainless steel to minimize the possibility of motor case burn through. Insulation on the chamber walls is provided by unburned HTPB.

The motor was designed early in the program using Netzer's model for hybrid combustion [1]. The original model used was

$$r = a \, Gox^{.8} \qquad 1.$$

where $Gox = \dfrac{\dot{m}_{ox} + \dot{m}_{fuel}}{A}$ a is an empirically determined regression constant and r is regression rate in inches per second, and A is the port cross sectional area.. Academy research with the 2.5 in motors, and recent industry experiments, indicate a more accurate model of hybrid regression rate is

$$r = a \, G^{.5} \qquad 2.$$

where $G = \dfrac{\dot{m}_{ox}}{A}$. An internal study using Eq. 2 as the model indicates the motor will produce approximately 1000 lbs of thrust for 15 seconds. This prediction will be verified in the next test.

The oxidizer feed system is a simple regulated blowdown system using helium (He) as a pressurant (see fig. 3). The helium is stored in a commercially available SCUBA tank at 3000 psi.

The system is activated by a solenoid valve below the He tank. Opening the valve allows the gas to pass to the regulator and then to the LOx tank. The regulator reduces the He pressure to approximately 900 psi.

The LOx tank is a welded 1/8" aluminum tank designed and built by Dave Crisalli of Rocketdyne. It holds 30 lbm of LOx, and is insulated with a water heater tank blanket.
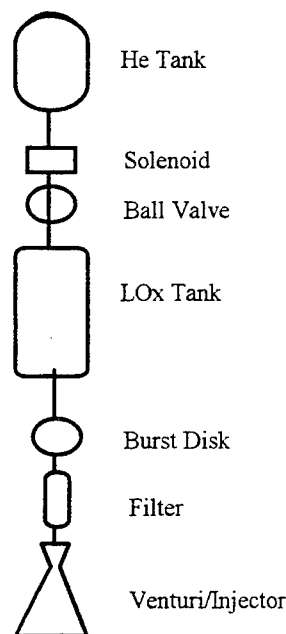
Fig. 3 Chiron LOx Feed System

Below the LOx tank fill port is the burst disk system. Burst disks were chosen over a solenoid valve due to simplicity, LOx compatibility and low cost. In retrospect, a valve would have been simpler and less expensive. Home made burst disks were used on a number of early system blowdown tests and were notorious for not bursting at a predictable pressure. Thus, commercial burst disks were acquired, at an exorbitant cost. Acquiring a LOx solenoid valve would have saved weeks of time and hundreds of dollars and will be a priority for next semester. Line pressure is isolated from the combustion chamber through the use of a cavitating venturi welded to the injector. The injector is a simple shower head non-impinging injector with a three clustered orifice pattern designed to inject an equal amount of LOx down each port. The injector is made of 302 stainless steel, has 27 orifices, each with a diameter of .0406 in and a vaporization length of 4.17% of the combustion chamber length.

The LOx feed system looks like the proverbial "camel designed by committee", because it was designed by three groups of students over four

semesters. The concession is that the parts are very inexpensive, readily available from any valve and fitting distributor or simple to build in the Academy machine shop.

Below the combustion chamber is a convergent-divergent graphite nozzle coated with silicon-carbide. The nozzle was designed using an axisymmetric method of characteristics computer model to design a bell-shaped nozzle set for perfect expansion at 16,500 ft .

III. Structure

The rocket structure is composed of six separate load bearing shroud segments. These segments house the combustion chamber, liquid oxygen tank, gaseous helium tank, data collection, main chute, and drogue chute (see fig 1). The structure was designed to bear the launch, flight, and recovery loads predicted by computer modeling, while having a minimum safety factor of 1.50. The inner diameter of the vehicle, 8.25 inches, was selected to house the largest tank.

Two structural loads are experienced during powered flight. The first is an axial load of approximately 1,000 lbf created by vehicle thrust. This load is the smaller of the flight loads and did not size any of the structural members. The next design load is created by a five degree side slip angle at maximum dynamic pressure. Max Q occurs at 1,100 ft/s at 10,000 ft MSL; this creates a load of roughly 1,250 lbf on each fin. This load condition required that both the fins and the combustion chamber shroud be 0.19 inches in thickness to avoid shroud failure and tear through of bolts.

The final design loads are experienced during the opening of the drogue and main chutes. Since little was known about the opening sequence when the skin was designed, a maximum of 10 g's was assumed for the opening of both chutes. Since the rocket is stable, deployment of the drogue after apogee will cause the vehicle to transition from a nose down to a nose up attitude. This considerable bending moment required the remainder of the shroud segments to be 0.10 inches thick. Main chute deployment was assumed to create a purely axial load.

The construction material was selected to minimize total vehicle weight. Several different materials were investigated including various aluminums, steels, and super alloys. Calculating the skin thickness to bear the required loads is an iterative process. First, a skin thickness is guessed; the vehicle weight and center of gravity are

398

calculated. With this information, chute opening loads, moments, and the necessary skin thickness can then be determined. This process continues until the skin thickness converges to the minimum required.

Of the materials investigated, Al 7075-T6 was selected for a low overall vehicle weight and availability at reasonable prices. It should be noted that very few seamless tubes greater than six inches in outer diameter can be purchased in any metal without paying sizable die fees. Therefore, the vehicle is made of rolled sheet aluminum with a bolted seam.

A semi-monocoque structure was selected to minimize fabrication complexity and maintain a reasonable weight. In this design, nine bulkheads and five shroud connections are placed throughout the 20.5 ft length to minimize buckling of the skin.

A finite element analysis of the vehicle was accomplished to determine the load at which the structure buckled and calculate stress concentrations that the initial static analysis could not predict. The finite element analysis determined that a load of 2350 lbf applied perpendicular to the centerline at the base of the nose cone would buckle the vehicle. This equates to approximately 7.6 g's of drogue opening shock, so the opening sequence was modified accordingly. The rocket is predicted to fail at approximately 50,000 lbf of axial load, which is well above any expected flight loads.

Two ports are located in the structure; one in each tank shroud section. These ports allow for final plumbing assembly, oxygen tank charging, and oxygen bleed immediately prior to launch. Each port interface is non-sparking to minimize fire hazard once the oxygen tank is charged.

To minimize the vehicle deadweight, lighter materials will be used to build a larger next generation rocket with composite tanks, body, and combustion chamber. A goal of the next class will be to reduce the deadweight fraction to 25%.

IV. Recovery

The recovery system is designed to return the rocket to earth within a defined landing area and without any significant system damage. These two basic requirements and the need to have a reliable, repeatable system drove the design of the current two stage recovery system.

The design began by attempting to make a one-stage recovery system (drogue and main deployed at the same altitude) satisfy the system constraints. Unfortunately, little information was readily available on opening forces and terminal velocities for a variety of chutes, deployment sequences, altitudes, and vehicle weights. To find this information, a computer program was written based on the Pflanz method [2]. Parameters such as line stretch time and inflation time were better estimated with the aid of a master rigger at the Academy [3]. The computer simulation for a five foot diameter, zero porosity, spherical drogue chute from an apogee of 27,000 ft MSL is tabulated below.

Δt (s)	Alt. (ft)	V_{ls} (ft/s)	G's
0.0	27000	105	0.7
6.7	26000	209	2.9
10.7	25000	303	6.2
13.6	24000	388	10.5

where: Δt = elapsed time since apogee
V_{ls} = velocity at line stretch

Table 1 *Opening Shock as a Function of Time*

This data shows that the rocket would fail if the chutes were deployed more than ten seconds after apogee. It was decided that at least the drogue chute would need to be deployed slightly after apogee with the aid of an apogee detection circuit (to be discussed later). Furthermore, the zero porosity drogue chute was modified with capped vent holes to decrease opening shock while maintaining the same decent rate.

A second computer simulation was created to determine the predicted landing footprint of the rocket under parachute. This code calculated the footprint of the vehicle accounting for two standard deviations in wind velocity, wind direction, flight path angle, and launch azimuth. The most valuable lesson learned from this code is the strong correlation between footprint size altitude at which the main was deployed. Figure 4 shows the footprint for a launch from Fort Carson, Co to a 27,000 foot apogee. This simulation accounts for standard winds in the month of June with two standard deviations on winds at various altitude blocks and +/- 2.0 degrees of azimuth and flight path angle. All altitudes are AGL.

This simulation vividly illustrates that a single stage recovery system is not acceptable because deployment of the main at apogee would require a range at least 16 mi. from east to west. Our impact rage is half that size so the main must be deployed below 15,000 ft AGL. An altitude of

10,000 ft AGL was selected for main deployment to provide adequate tracking time.

Finally, the main opening shock was investigated to determine if any damage is likely to occur to sensitive data collection systems. If main deployment caused too high a load, the drogue could be increased in size to decrease its terminal velocity. However, increasing drogue size would increase drogue opening shock. Main opening was investigated at 500 ft increments for drogue chutes from 4 to 6 ft in diameter. Results for a 10,000 ft deployment are summarized in Table 2 .

Dia (ft)	V_{td} (ft/s)	G's
4.0	188	8.1
5.0	150	5.3
5.5	137	4.5
6.0	125	3.8

where: V_{td} = terminal velocity. under drogue at 10,000 ft AGL.

Table 2 *Main Opening with Various Drogues*

The main chute opening shock is based on a standard C-9 opening sequence. Based on this data, the C-9 opening time was increased to eliminate possible chute damage; the current design has an opening shock of 3.5 g's for a five foot drogue. A five foot diameter drogue was selected for its reasonable loads from both drogue and main deployment.

The deployment of the two stage system begins at apogee. A commercially purchased apogee detector signals that static pressure is increasing and the drogue should be deployed. Logic within the system eliminates premature chute deployment from an increase in static pressure during supersonic flight. After apogee is determined, the nose cone is separated from the vehicle with a large spring compressed between two kick plates. The drogue chute is pulled from the nose cone then inflates. The rocket, with nose cone attached, falls until below 10,000 ft AGL. The spring and kicker plates return to Earth under their own chute.

At 10,000 ft an Automatic Activation Device (AAD) senses the corresponding barometric pressure and pulls the main chute release pin. The drogue chute then removes the main from the body tube and its storage bag. Once the main chute inflates, the nose cone and drogue chute will rest on the apex of the main. The vehicle will descend in this configuration until ground impact at a velocity of 21 ft/s.

To back up the apogee detector, a second AAD is in line with the drogue chute release pin. If the apogee detector fails to function properly, the AAD will be used to deploy the drogue 3,000 ft after apogee. This requires that the apogee prediction model is run on the launch date with the most recent thrust and weight data as well as current atmospheric temperatures.

V. Test Results

The propulsion system test program used a building block approach to gear up for the flight configuration motor test. Three separate test phases were conducted over the course of the semester, including LOx feed system blowdown tests, shroud free motor fire and flight configuration motor fire.

All propulsion system tests were conducted on a test stand built by the Academy in an uninhabited area north of the campus. The test stand is 18 ft tall on a 4 ft by 8 ft concrete pad (see fig 5). The motor is vertically stacked and exhaust is diverted by a duct on to the splash pad. For the blowdown tests and the first two hot fire tests, the system was stacked without the shroud by bolting each tank assembly to the stand separately.

The blowdown tests were conducted using liquid nitrogen (LNi). LNi's properties are very similar to LOx but without the fire hazard of working with oxygen. In these test the LOx feed system was stacked on the test stand down to the injector (fig 5). Pressure data was taken in below the regulator and at the injector face. The blow down test goals were as follows: test the LOx feed system for leaks and cryogenic compatibility, gaining experience loading the tanks and using cryogenic materials and characterizing the ability of the blowdown system to provide the motor with the design oxidizer flow rate.

Due to various failures that cropped up, four separate blowdown tests were required. Lessons learned from the test series included: home made burst disks were not reliable for use in our system, the system was not mass flow limited in any of the fittings and provided 10 seconds of LNi and a He purge of about 4 seconds. One shortfall in the system design was that there was no accurate way of determining the fluid level in the tank. This problem was never solved and will be a priority for next semester.

The next phase of the test program was a motor test fire without the shroud (see fig 6). This was accomplished so as to not endanger the $10,000 shroud in a cataclysmic test failure, and to keep the test as simple as possible. The test goals were to

ignite the motor, verify the feed system performance and data acquisition system. Ignition was to be accomplished using three Thermalite ignitor wires in parallel. The LOx tank was to be partially filled for a 4-5 second burn.

The nozzle was another experiment in low cost rocketry. Due to budget constraints, a single graphite nozzle was purchased. Concern about erosion over the three tests and a flight, and the risk of using the $1000 chunk of graphite on the first test, inspired the milling of a laminated oak nozzle by the machinist at the Academy. Since the test set-up did not allow thrust data to be acquired, a high performance nozzle was not needed. It was believed the wood would ablate slowly enough to survive a five second test fire.

The difficulty of determining the LOx tank level caused a change in plan. With frustration levels high, the decision was made to attempt the test by filling the tank to the top to make sure enough LOx was in the tank to give a valid test.

Pressure data for Test 1 is shown in fig 7. The engine burned for 17 seconds instead of the design 10 second. The nozzle throat ablated to the wall by 10 seconds, as can be seen in rapid decrease in combustion chamber pressure. Due to the longer than anticipated burn, the HTPB burned down to the aluminum and caused a combustion case burn-through (see fig 8). The large pressure spikes shown in the chart are assumed to be caused by transmission interference in the lines.

Though not a complete success, the test validated the design goals or gave enough data to effect a re-design. The motor exhibited smooth combustion with no bad startup transients. The thickness of the HTPB insulating fuel on the outer wall of the combustion ports and pre and post-combustion chambers was too thin. This was increased 1/2" on the chamber walls and approximately 1 " in the pre and post combustion chamber. The design chamber pressure of 300 psi was not achieved. A greater than anticipated pressure drop across the venturi/injector assembly is the suspected cause. The regulated pressure was stepped up to compensate. The inherent safety of hybrid rockets was shown by the burn through; when the LOx was depleted the fire went out, and no explosion occurred. The final lesson learned was that oak may make a nice table or a roaring fire, but shouldn't be used in a rocket nozzle.

Test 2 was configured similar to the first test except for a change in the ignitor wire configuration. Following a test failure due to the ignitors failing to light, a single wire configuration, stapled in a circular pattern around the pre-combustion chamber was adopted.

Pressure data from test 2 is shown in fig 9. As can be seen in the data, the major discrepancy is a two second delay in ignition. The ignitor was burning but did not light the HTPB. A series of ignitor wire configuration tests is planned to solve this problem. Another problem which occurred was the cracking of the graphite nozzle, the cause of the crack is being investigated. A third note is that again the oxidizer flow rate was lower than desired; a combustion chamber pressure of only 200 psi was achieved. Design changes to increase the chamber pressure are being investigated.

The recovery system was also extensively tested. The test series was performed as follows:
1. Pin-spring-pusher plate test. The pull force required to pull the pin out of the spring and fire the spring was quantified.
2. AAD-Pin-Spring tests. The AAD was wired into the system to test the capability of the AAD to pull the pin
3. Parachute deployment test. The drogue/main parachute and bag assemblies were dropped from the academy UV-18 jump plane, to test the inflation rates and configuration of the parachutes
Two recovery system tests are to be accomplished:
1. Apogee detector-AAD test. The Apogee detector will be wired to the AAD and put into a barometric chamber to test the detectors ability to activate the AAD.
2. Recovery system drop test. The recovery system including AAD, drogue and main parachutes, and spring plate assembly will be dropped from the UV-18 to test the entire recovery section.

The recovery system testing building block approach will give a high confidence that the system will work on the first launch.

V. Cost

For a program like Chiron, cost is one of the over riding design drivers. Normal DOD/NASA contractors such as Martin or General Dynamics have been bypassed in favor of smaller, more flexible contractors such as Dangerous Dave's Handmade Composite Stuff (nose cone), Vulcan Systems (motor) or Adept rocketry (apogee detector).

An interesting source for low cost rocketry component suppliers has been the Tripoli Rocketry Magazine Advertisements. The underground high powered amateur rocket builders have a suprising array of companies catering to their needs.

A summary of the major cost items is shown in Table 3. As can be seen, nearly half of the budget went into the custom built shroud. Finding a supplier of extruded 8 inch diameter tube was impossible for less than tens of thousands of dollars. A more cost effective design method would have been to find a supplier of extruded aluminum at a given diameter and designing the tanks and plumbing around that constraint.

Part	Cost
Shroud Sections	$10,000
Graphite Nozzle	$1000
7075-T6 Aluminum	$2887
Nosecone	$275
Test Pad	$542
Fittings and Plumbing	$1624
He Tank	$360
LOx/LNi/He	$1547
Burst Disks	$512.8
Pour Motors	$2350
Total Cost Spr 93	$25,079

Table 3 *Parts Cost Breakdown (Some parts not included in table)*

Conclusions

The Chiron project has been a safe, effective and exciting method to teach students about the design and testing of an aerospace system. Over the past two years the students and faculty have developed the capability to design, test and fly small sounding rockets. The students have generated code and design techiques for such areas as propulsion, apogee predictions, parachute deployments and wind drift. A axisymetric nozzle design code was also written.

As a research project, the capability to flight test hybrid rockets, cheaply and with a quick turn around will be invaluable to the hybrid community. Small demonstrator rockets such as the Academy's will help prove the value and simplicity of the technology.

As with most experimental programs, Chiron is "over budget and over-weight". Unfortunately, the rocket size and weight is nearly 75 lbs over the predicted weight, this will impact the design goal of a 30,000+ ft apogee. The latest predicted apogee is between 15-20,000 ft. Even with the predicted shortfall, the Academy cadets have done an outstanding job, and on a shoe string budeget, to get this rocket in the air.

References

1. Wetzer D.W., "Hybrid Rocket Internal Ballistics", National Technical Information Service, Jan 1972, AD-754769

2. Knacke T.W., "Parachute Recovery Systems, Design Manual, Chapter 5", Defense Technical Information Center, AD-A183191, June 1987

3. Personal Conversation with Bill Wenger, 94th ATS, USAFA Parahute Training Squadron, Jan-May 1993

Vital statistics

Vehicle
Length: 17.62 ft
Diameter: 8.5 in
Weight: 260 lbs

Propulsion system
Thrust: 1300 lbf nominal
Duration: 10 sec
Fuel/Oxidizer: HTPB/LO$_x$
Chamber Pressure: 260 PSI

T + 50 sec
Apogee
Altitude 30,000 ft

Altitude 15,000 ft
Drogue chute deploys
Vehicle slows to 150 kts

T + 10 sec
burnout
max velocity 1,000 ft/sec

Altitude 5,000 ft
Main chute deploys
Vehicle slows to 20 ft/sec

T = 0 sec
5 "G" Liftoff
Begin recording data

Land and recover

Nosecone	SH5: Recovery	SH4: Flight Data	SH3: Helium Tank	SH2: LOX Tank	SH1: Propulsion

20.000   36.000   13.000   35.100   48.250   59.115

211.465

12/92

Fig 1 Chiron Sounding Rocket Overview
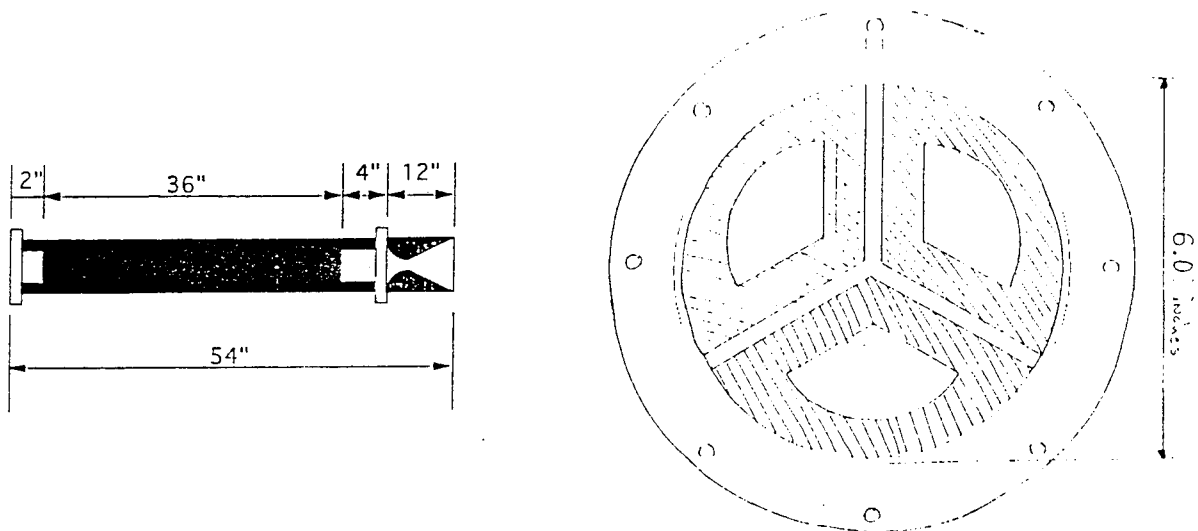
Fig 2 Motor Case Dimensions and Port Geometry

403
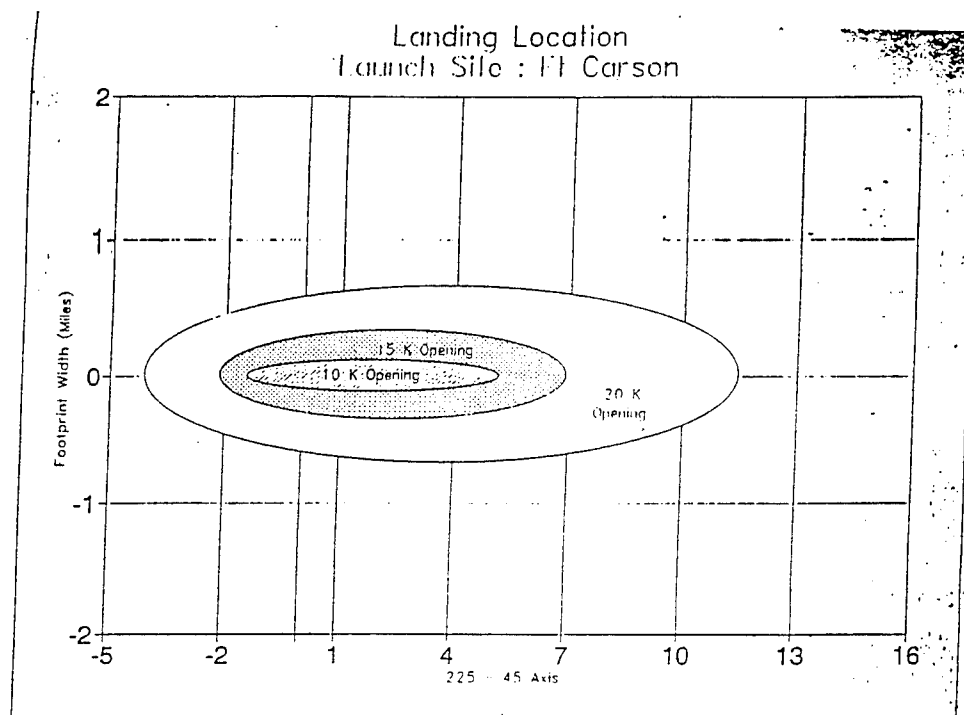
Fig 4 Landing Footprint as a Function of Main Deployment Altitude
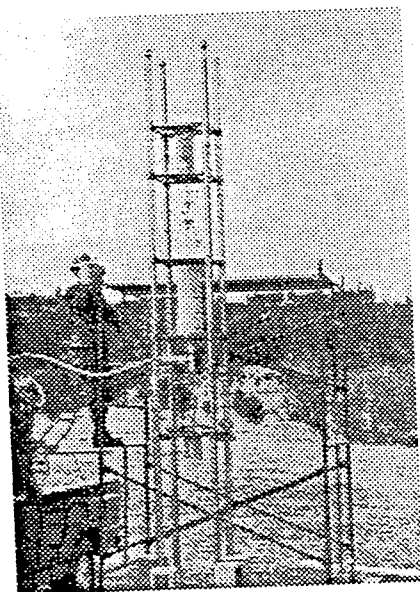
Fig 5 Test Stand
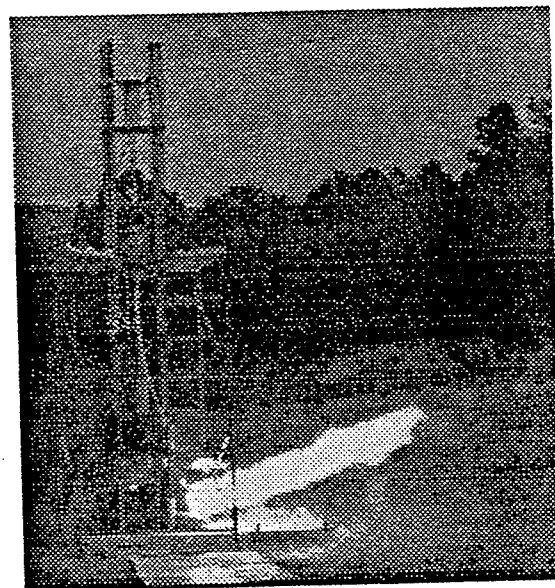
Fig 6 Static Test Fire
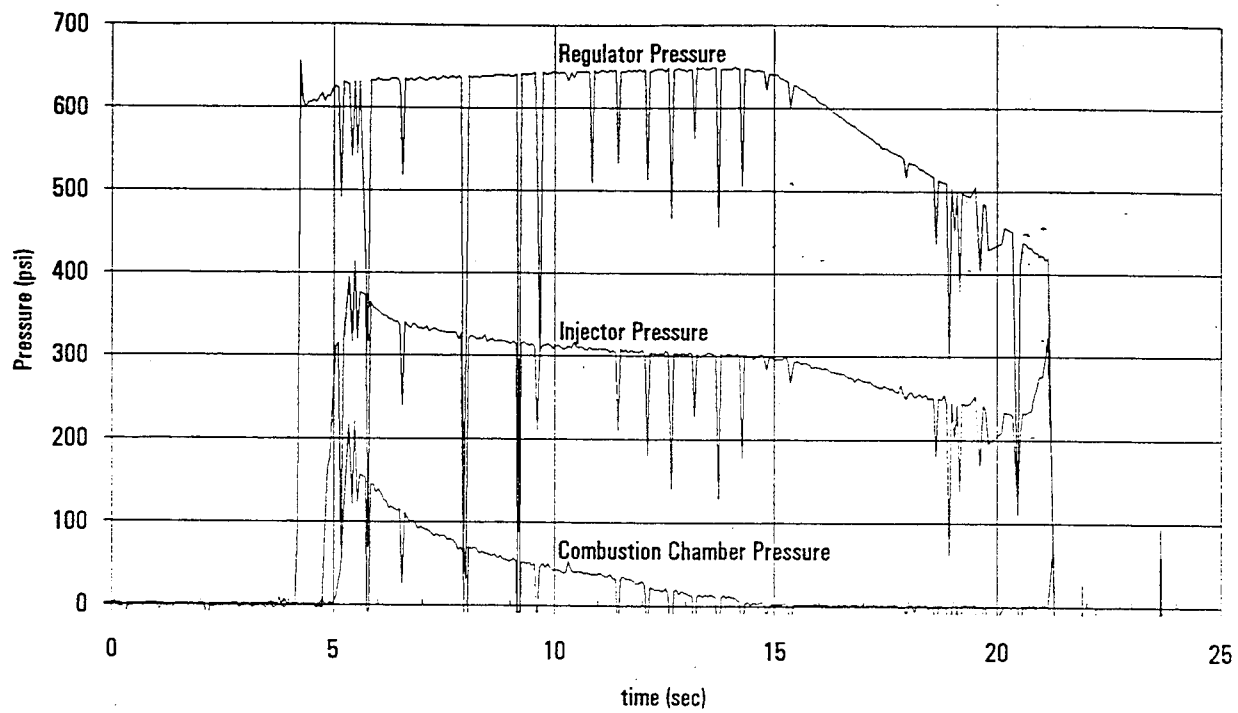
Fig 7 Static Test 1
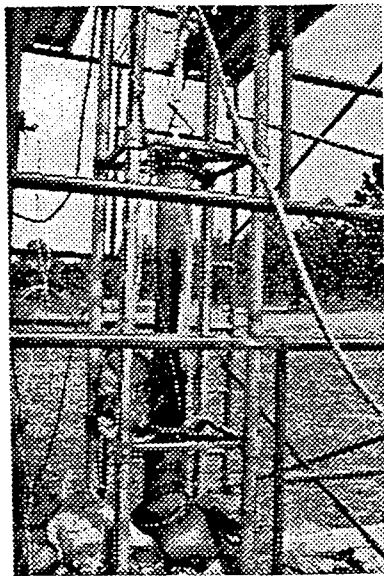
Fig 8 Motor Case Burn Through
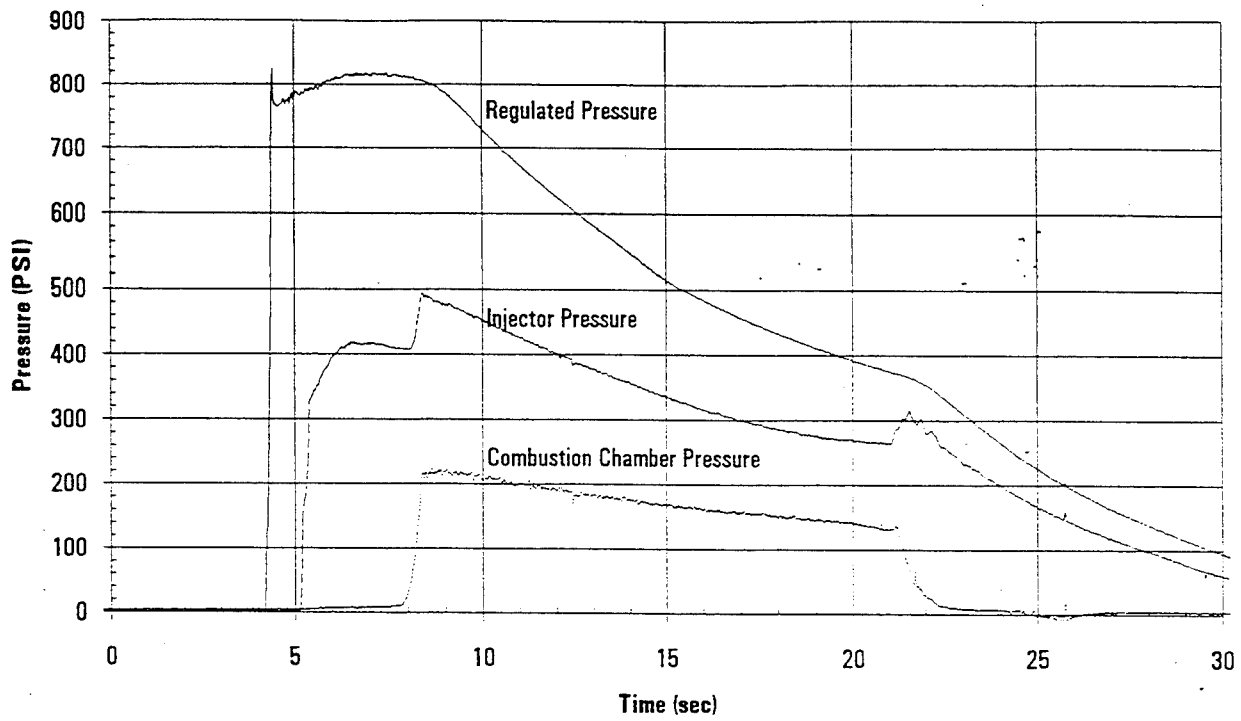
Fig 9 Static Test 2

Investigation of the Annealing Effects on DuPont HX-4000 Liquid Crystalline Polymer[*]

M. L. Lindauer[**]

S. Mall[***]

Department of Aeronautics and Astronautics
Air Force Institute of Technology
Wright-Patterson AFB, OH 45433

Abstract

Liquid crystalline polymer's unique high-temperature properties show great promise for high-temperature structural applications. To date little is known about their molecular behavior at elevated temperature or its effects on mechanical properties. DuPont HX-4000 appears to increase in strength and temperature resistance after some heating above its α transition temperature as a result of molecular interdigiting. However, excessive heating will decrease its strength. The rates at which these processes occur with respect to temperature and time at temperature is still unknown.

This research investigates the rates at which the material properties of DuPont HX-4000 change as a result of heat treating. Specimens of HX-4000 are annealed to different time and temperature specifications, then tensile tested. Ultimate strength, strain to fracture and modulus of elasticity are compared for each group of specimens. Further research will determine the rate of change in properties with respect to the annealing temperature, and the activation energies for microstructural changes will be calculated. The overall goal is to define these changes as a function of temperature by an Arrhenius equation.

---

[*] This paper was presented at the Second Annual Polymer Components Symposium, 13-17 September 1993, at the United States Air Force Academy, Colorado Springs, Colorado.

[**] Part-time graduate student, currently with the 4950th Test Wing, Wright-Patterson AFB, Ohio.

[***] Professor and Head, Department of Aeronautics and Astronautics, Air Force Institute of Technology, Wright-Patterson AFB, Ohio.

TABLE OF CONTENTS

TABLE OF FIGURES

TABLE OF GRAPHS

1.0 INTRODUCTION

During the last few decades, vast amounts of research have focused on developing high strength, high temperature polymers. A large group of liquid crystalline polymers (LCP) composed of semi-rigid rod-like molecules show promise to fulfill these requirements. When these materials are formed with a high shear process, such as fiber drawing and thin section injection molding, the molecules align into a highly ordered hierarchical fibrous microstructure. [1,2,3] This structure has very anisotropic properties which exploit the strength of polymers' covalent bonds along the molecules' backbones. It also allows very close packing with a high degree of hydrogen bonding between molecules. The result is a very stable structure that has impressive strength and stiffness in the fiber direction, very low thermal conductivity perpendicular to the fiber direction, excellent high temperature properties and the potential to customize mechanical properties with heat treating. Liquid crystalline polymers, including DuPont HX-4000, show great potential to fill many high strength and high temperature applications.

1.1 HISTORY OF LCP SCIENCE - Liquid crystalline polymers were unwittingly discovered as early as 1888 [4] when the botanist Friedrich Reinitzer noted that esters of cholesterol exhibit two melting points. He observed that this strange liquid showed iridescent colors and birefringence between these melting points. [5] In 1890, Otto Lehmann of Aachen University described these new materials as "Crystalline Liquids." [6] Research continued to spread throughout Europe over the next three decades to understand this liquid crystalline phase. Researchers eventually realized that there are several forms of the liquid crystalline phase. At Strasbourg in 1922, George Friedel defined the three forms of these liquid crystalline phases. To supplement the term "cholesteric," he coined the terms "*nematic*" and "*smectic*," from Greek roots, to describe different "*mesophases*" of these liquids. [7]

The first advances toward engineering materials came in the early 1920s when Staudinger suggested the possibility of long chain molecules. Then Vorlander of Halle began experimenting with increasing chain length. He synthesized rods of multiple benzene rings "para-linked" by ester groups. In 1923, he noted that the increasing chain length increased the transition temperatures of the resulting materials. The ultimate example of this was poly(p-benzamine) (PBA) which would char without softening. [8] For his work, Vorlander can be considered the father of Liquid Crystalline Polymers. [9]

410

The 1950s saw great progress in the science of liquid crystalline polymers. Onsager was the first to introduce Liquid Crystalline Polymer theory and explained the biphasic nature of solutions of rigid molecules in 1949. [10] Isihara [11] and Flory [12,13] further developed theories relating to the packing of rigid rod-like molecules. [14] Independently, in an effort to develop synthetic silk, Robinson documented the structure and phase equilibria of lyotropic solutions of polyglutamates. [15] These phase diagrams confirmed the work that Flory's model theoretically predicted.

Successful commercial products did not come until the 1960s. Ballard developed a method to spin fibers for lyotropic solutions of poly(γ-benzyl-L-glutamate) (PBLG) in 1958, but no commercial products were developed. [16] Finally, Kwolek and her team at DuPont developed the aromatic amide fiber named Kevlar, [17] which is spun from a solid lyotropic solution of 20% polymer in 99.8% pure sulfuric acid, then rinsed in a coagulating water bath. [18] With the prospect of marketable products, research into liquid crystalline polymers greatly broadened. Today there are many different products on the market in many different forms including a wide range of fiber products and moldable, thermotropic bulk materials, most notably Kevlar from DuPont, and the Vectra family of materials from Hoechst Celanese.

1.2 DESCRIPTION OF LCPs - Two basic types of molecules compose the majority of structural LCPs; smooth, semi-rigid rods and semi-rigid rods with side groups, sometimes called hairy rods. (Figure 1) Vectra is an example of the smooth, semi-rigid rod variety while Kevlar and HX-4000 are of the side group type.

Hoechst - Cenanese "Vectra" LCP Polyester

DuPont "HX-4000" LCP Polyester
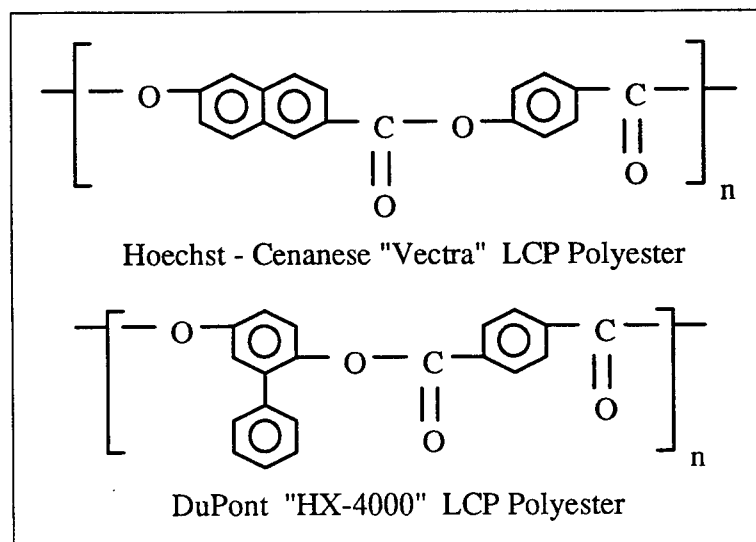
Figure 1 The chemical structures for the common semi-rigid rod LCP, Vectra, and for HX-4000, a semi-rigid rod LCP with side groups. [19]

Three major microstructural regions compose an injection molded LCP part: the skin, the fibrous intermediate region under the skin and the core at the center. (Figure 2) Each of these regions are suspected to have different microstructures relating to the environments within the injection mold. The skin of the injection molded part is usually rapidly quenched by the cold inner surface of the mold. In polymers, including LCPs, this often results in an amorphous, glassy structure on the surface of the resulting part. The thickness of this skin will vary depending on the relative temperature of the mold and the nature of the polymer. Under the skin is the fibrous intermediate region. This region is subject to the high shear rate of the laminar melt flow near the surface of the mold. It is suspected that this shear flow causes LCPs to align into their characteristic fibrous microstructure. (Figure 3) At the center of the part is the core. Less is known about the microstructure of this region than the others. Many suspect that in LCPs, these molecules do not align to a great degree, but exhibit somewhat random local crystallization and do not contribute their optimal strength.
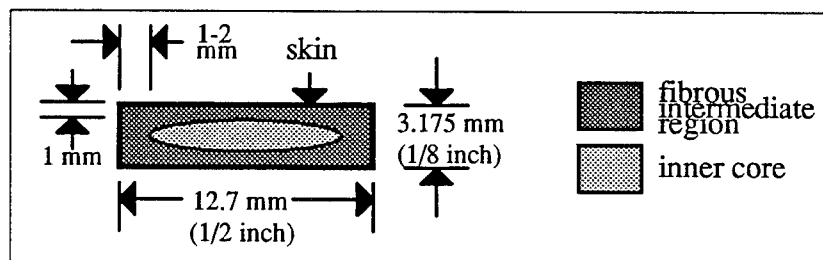
Figure 2 Cross-section of a DuPont HX-4000 specimen showing skin, fibrous intermediate region and inner core.

Many liquid crystalline polymers show changes in mechanical properties after exposure to high temperatures for extended periods of time. The high temperature allows the molecules to move and realign within the material. The temperature where these molecules become free to move is referred to as the materials' α transition temperature. [20] Under the proper conditions, they may further align into a more highly ordered, fibrous microstructure and possibly, in some materials, the side groups may interlock or interdigit. Often these microstructural changes significantly improve the strength of the material. Interdigiting is suspected to be a mechanism in Kevlar, DuPont HX-4000 and other materials with chemical side groups extending from each mer unit. However, neither these mechanisms nor their effects on mechanical properties are well understood.

The heat treating effects on the mechanical properties of these materials have not been extensively studied to date. Very little has been done to quantify these effects at the macroscopic level in engineering terms (stress, strain and modulus). The primary focus of research in this area has been to understand the materials' physical microstructures and

412

molecular behavior. This research is intended to quantify the effects of heat treating in DuPont HX-4000 in these engineering terms.
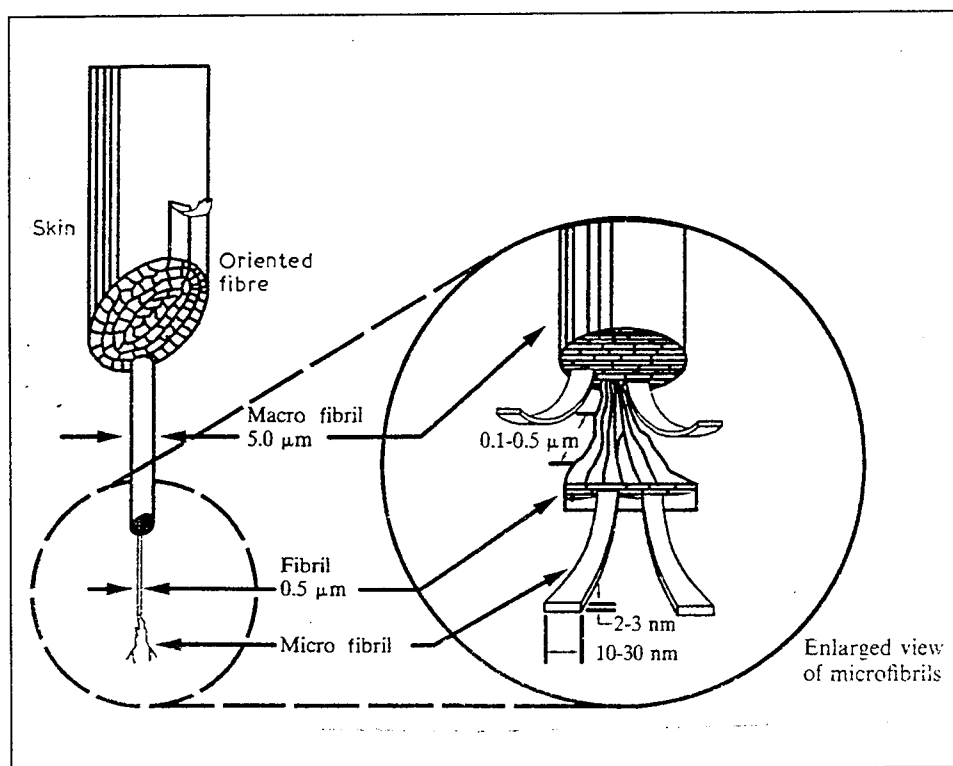
Figure 3 An expanded structural model is shown for the thermotropic and lyotropic LCPs, with more detail of the microfibril sizes, shapes and order. [21]

This paper presents initial findings from data collected to date from this research. More testing is necessary to support these initial findings and to derive any mathematical relationships. To date, only two annealing temperatures have been tested. This alone is not enough to draw any conclusions about the affects of annealing on HX-4000's mechanical properties. Another annealing temperature will be tested along with thermodynamic tests to support theories about HX-4000's microstructural changes.

2.0 OBJECTIVES

The goal of this research is to mathematically relate the changes in DuPont HX-4000 mechanical properties to the heat treating parameters. It is suspected that the mechanical properties of a liquid crystalline polymer change because, above the α transition temperature, the molecules further organize into the fibrous microstructure.

This reorganization is assumed to be similar to the diffusion of atoms, molecules and imperfections in other materials. Diffusion has been shown to relate to the thermal energy, or temperature, of the material by the Arrhenius equation:

$$\text{Rate} = c_0 \exp\left(\frac{-Q}{RT}\right)$$

where c_0 is a constant, R is the gas constant (1.987 cal/mol • K), T is the absolute temperature (K), and Q is the activation energy (cal/mol) required to allow the molecules to move. [22] Once armed with this information, the engineer could specify the optimum heat treating process for the desired mechanical properties.

This paper presents the data collected to date as part of this thesis research. These tests are designed to quantify the macroscopic effects of the annealing process on DuPont HX-4000. Three or four batches of annealed DuPont HX-4000 will be tested for tensile strength, strain and elastic modulus. Each batch of specimens will be annealed at a different temperature. Within each batch, groups of specimens will be annealed for different durations.

Other material tests will be performed to supplement the tensile test data. Elastic modulus will be measured with ultrasound. These "Sonic Modulus" tests should yield more reliable data than those obtained from the tensile tests, but the effects of possible modulus variation between the fibrous intermediate region and core regions are unknown. Thermo-mechanical Analysis (TMA), Thermo-gravimetric Analysis (TGA), Dynamic Mechanical Analysis (DMA) and Differential Scanning Calorimeter (DSC) will reveal valuable information about structural and phase transitions of the material and how they change with annealing. Finally, Scanning Electron Microscopy (SEM) of the fracture surfaces should illuminate various microstructures inside these specimens. All these tests should reveal microstructural changes related to the annealing process. Hopefully, these results will correlate with the tensile test results and reveal structural behaviors and explain the mechanical changes.

To date, two batches of specimens have been tensile tested: 300°C and 260°C. Annealing times ranged from non-annealed to 32 hours. Preliminary results indicate that longer annealing times are necessary to verify suspected trends. The next batch will be annealed at 220°C for up to 100 hours; an additional group will be annealed for 100 hours at 260°C to investigate trends in those data.

3.0 PROCEDURES

3.1 SPECIMEN PREPARATION - All specimens were injection molded ASTM D638-84 tensile specimens (Dog Bones) with neck dimensions of 12.7 x 3.175 x 76.2 mm (1/2 x 1/8 x 3 inches). The following processes were used by RTP company, Winona, Minnesota to mold them:

1.	Drying	Hopper dried, 3-4 hours, 121°C (250°F)
		Moisture Content to 0.015%
2.	Melt Temperature	337 - 354°C (640 - 670°F)
3.	Barrel Temperature	Typically a flat profile 335 - 349°C (635 - 660°F)
4.	Mold Temperature	77 - 149°C (170 - 300°F) [23]
5.	Fill Speed	Fast - less than 25 mm (1 inch) per second
6.	Screw Rotation/ Back Pressure	Minimum - only high enough to maintain uniform retraction. Upon screw retraction, the mold open cycle should begin, initiating a new cycle.
7.	Injection/Hold Pressures	5000 - 15,000 psi [24]

All heat treated (annealed) specimens were annealed using approximately the same process as follows:

1. Parts placed in furnace
2. Argon purge for 20 min
3. Heat applied for annealing time
   Slow Argon trickle
4. Heat removed, allow to cool
   Slow Argon trickle
5. Part removed when oven reached 160°C
   The 300°C batch was allowed to cool to 107°C

160°C was considered to be an adequate cooling temperature since that is the α transition temperature for HX-4000. It is assumed that no additional annealing occurs below 160°C. The observed variations in cooling time resulted from annealing different groups in different sized furnaces and starting with cold versus pre-heated furnaces. The effects of these variations will be discussed in RESULTS (section 4.1.2).

Fiberglass tabs were attached to the grip surface of most specimens to minimize damage from the tensile machine's grips. New grip teeth were installed into the test fixture between the 300°C and 260°C specimen tests. The new grips had very sharp,

pointed teeth that penetrated deeply into the specimens and caused them to split longitudinally, ruining them. The best remedy was to apply fiberglass tabs to all grip surfaces of the specimens. These tabs were easily attached to the roughened surfaces of the specimens with medium-viscosity cyanoacrylate adhesive and an accelerator. This process resulted in a very quick bond with greater than 1000 psi of shear strength -- more than adequate for these specimens. The fiberglass tabs eliminated failures resulting from grip damage.

3.2 EXPERIMENTAL PROCEDURE - All tensile tests were conducted at room temperature according to ASTM D638-84 except as described below. Specimens were annealed according to the following test matrix:

ANNEAL TEMP	ANNEAL TIMES (hr)						
260°C	0.0	2.3	4.2	7.0	12.0	20.5	36.5
300°C	0.0	10.5	15.5	18.0	23.5	31.5	43.0

figure 4

Tensile tests were conducted on a 110 kip MTS machine. Load and extension were digitally sampled approximately every one half to one MPa. Load was applied at a rate of 10 lbs per second. Even though ASTM D638-84 specifies strain control for tensile testing, load control was chosen because it better represents the design environment. Load control is the most common testing scheme used on the Air Force Institute of Technology laboratory for exotic material research. Although, while load control is more representative of the design environment, most other tensile testing uses strain control. The resulting data from this research does not correlate with other experimental data. [25] Further research will be necessary to compare results obtained here to those obtained elsewhere; however, the resulting correlation data should be useful to engineering applications in the future.

4.0 RESULTS

4.1 UNWANTED VARIABLES - Several variations in both specimen preparation and in the experimental procedure have resulted in undesired variables. With each iteration of the experiment, refinements limited further variations, but they must all be

considered. It is impossible to exactly determine the effects of these variations, but analysis of the results indicates they were not critical.

4.1.1 SUB-OPTIMAL MOLDING PROCESS - The first batch of specimens (later annealed at 300°C) were molded under constantly varying parameters. The molding process had not been refined before their manufacture, so injection parameters had to be constantly varied to obtain the best possible specimens. The melt temperature and injection speed varied from 371°C to 385 °C (700°F to 725°F) and from 25 to 35 mm/sec respectively. Additionally, the injection tool could only be heated to 68°C (155°F). From experience the best specimens come from molds heated between 107-149°C (225°F-300°F). [26] Most of these specimens could not be used due to obvious, visible flaws and inconsistencies.

All subsequent specimens were molded by RTP company, Winona, Minnesota, who specialize in molding exotic polymers. Their injection process (outlined in section 3.1) was uniform and produced very uniform specimens.

4.1.2 LONG AND VARIED POST-ANNEAL COOLING - Consistent annealing proved to be another challenge. The first batches of specimens were annealed in three different furnaces, normally used to heat treat large metal parts. The furnace controllers were very precise and accurate, but the cooling times were different for each furnace. It took from 6.0 to 7.5 hours to cool the specimens in the furnace from 300°C to 160°C, except one group which took 23 hours. All subsequent specimens were annealed in only one furnace; unfortunately, the shortest groups annealed at 260°C were annealed first, starting with a cold-soaked furnace. The resulting times to cool from 260°C to 160°C were short for the first group (1 hour) and got longer with each subsequent group. The cooling time for that furnace stabilized at about 4.5 hours. To remedy this variation all future batches will be annealed in the same furnace, with the longest annealing cycles first to thoroughly heat-soak the furnace.

The different cooling times had to be accounted for in this analysis. The chosen method was to add the cooling time to the annealing time to obtain a total duration of exposure to temperatures above 160°C. Subsequent mechanical properties were compared using this total annealing time and the maximum annealing temperature. This method yielded apparently good results with no noticeable correlation between the short cooling times and the resulting mechanical properties.

4.2 EXTERIOR APPEARANCE - Both batches of specimens manufactured to date have very different visual appearance. The first specimens, molded at Hill AFB,

Utah, were medium dark gray with a slight greenish tint. Many of these specimens had a worm-like pattern that coiled in the upper grip area (the injected end) and often extended through the neck. This "Worm Fill" appeared to be only a skin effect on most specimens, however in some, a "worm" of greatly degraded material, the thickness of the specimen, extended through the neck. All specimens that showed obvious visible flaws like this were rejected.

These specimens darkened noticeably after annealing at 300°C, even for the shortest duration annealing cycles. Many of these specimens were warped to some degree, and some appeared to be melted or degraded on the ends. Again, all specimens that had obvious visible damage were rejected.

The second batch of specimens, molded at RTP company, were much lighter gray in color with less obvious green tint. These specimens appeared to have thinner skin with well-behaved flow characteristics. Hair-like filaments could be raised on the surface when scratched and could be peeled several inches. This indicates that good fibrous crystallization was obtained even at the surface. Annealing at 260°C did not have any visible effects on these specimens. There was no discoloration and very little if any warpage. None of these specimens had to be rejected due to visible defects.

4.3 FRACTURE DESCRIPTION - Generally, much information about a material's microstructure can be gained by examining its fracture surfaces. In this research as well, visual inspection of the fractures and the number of invalid failures illustrate some important characteristics of injection molded HX-4000.

The specimens from both batches tested to date had similar physical structure. The exterior of each specimen looked glassy and showed evidence of injection flow. The first batch (300°C anneal) had a thick skin that often bubbled up from the underlying structure during the anneal. However, these flaws did not appear to affect the fracture or resulting mechanical properties. The later specimens (260°C anneal) had a much thinner skin which did not separate. Note that the higher temperature of the mold for these specimens resulted in better surface structure.

All specimens had a very distinct fibrous intermediate region under the skin with a similar color. This fibrous region appeared to be about 1 mm thick on the faces of each specimen and about 1 - 2 mm thick at the edges. (Figure 2) Its thickness was approximately the same regardless of the mold conditions or annealing temperature. It was visibly fibrous with a very irregular fracture surface, somewhat like a dry wood

fracture. Most fractures exhibited a layered appearance. (Figure 5) This region is very different from the core of the specimen.

At the center of each part was a core with a completely different appearance and fracture surface for all specimens. This core was a much lighter gray without the greenish tint of the exterior. Its fracture looked like satin and did not appear to be fibrous. Its fracture surface was smooth, tapered and regular with a blunt tip, usually pulled out from one side of the fracture. (Figure 5) The microstructure of this core appeared to be vastly different from that of the fibrous outer region and appeared to fracture independently. These differences were reflected in both their physical appearance and their fracture characteristics.
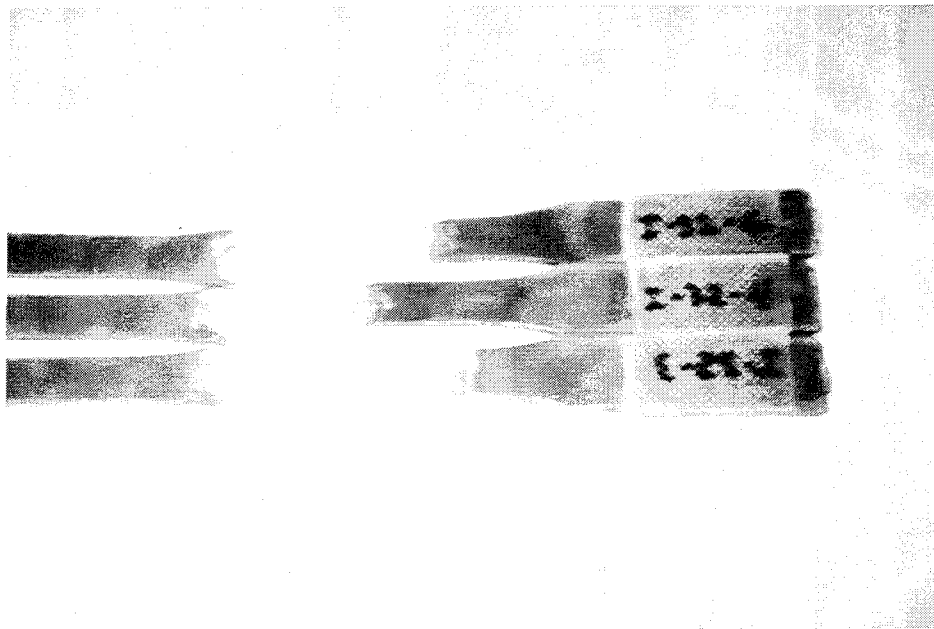
figure 5 Photos of typical fractures, a) fractures in the throat,
b) fractures in the fillet of the grip.

The majority of the specimens had similar fracture surfaces. The typical fracture surfaces resembled stair stepped pyramids in shape, like the end of a weathered wood plank. The core usually protruded 10 to 15 mm from one side of the fracture with the fibrous outer region tapering down from there. (Figure 5) The mating sides of the fracture usually fit snugly back together, characteristic of a brittle fracture. When the failures were in the fillet or the grip of the specimen, the protruding core tended to be lyre-shaped.

These fractures illustrate the different microstructures within the specimens and their apparently independent behavior.

The number of invalid failures of these specimens can also provide useful information. 60% of the specimens tested in this research fractured in the downstream or expanding fillet or grip relative to the injection flow direction. This is consistent with some other injection molded liquid crystalline polymers, such as Xydar. [27] The injection mold designer working with liquid crystalline polymers must avoid any feature that would cause a rapid decrease in flow pressure or shear according to C. Frank, an expert in liquid crystalline polymer molding. [28]
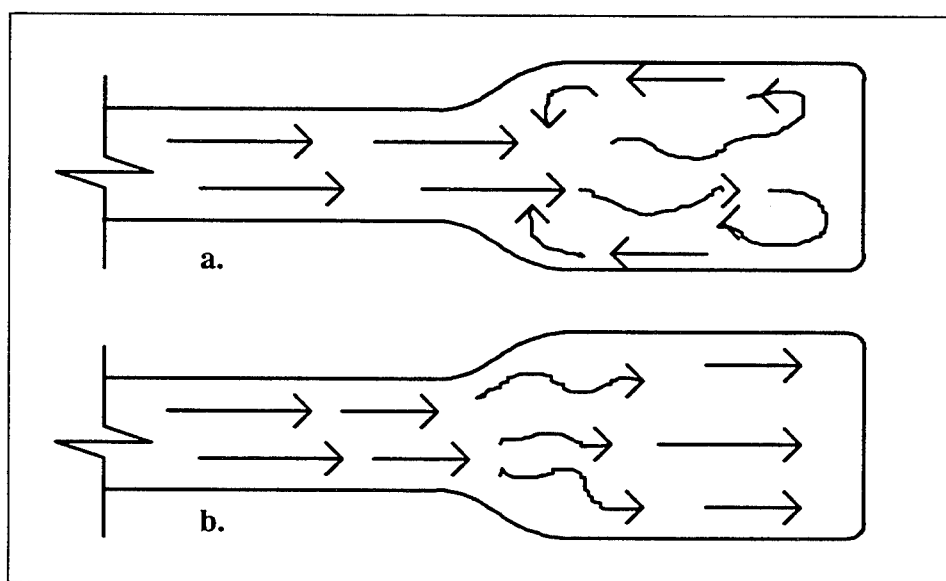
figure 6 Sketch of possible injection melt flow within the mold, a) backfilling into lower grip, b) turbulent flow in expanding fillet.

These weaknesses are probably caused by instability in the injection flow. The most likely explanation is that the viscous melt extrudes from the gage section, or throat of the mold, piles up in the grip area, then backfills into the fillet. (Figure 6) This scenario introduces two mechanisms which would both weaken the specimens. First, this does not provide the smooth shear flow necessary to orient the fibers through this region. Second, the knit line, or surface, between two meeting flow fronts is inherently weak. A less likely explanation is that slower flow in the expanding fillet and grip decreases injection flow shear rate near the mold surface. Turbulence in this flow field could also disrupt the desired fibrous structure and result in a thinner and possibly weaker fibrous region to support a load. The injection mold designer must be aware of these effects to avoid microstructure discontinuities and maintain stable injection flow to maximize the strength of the resulting parts.

Proper mold design, and gate location, orientation and type are critical in most injection mold applications. Flow direction and other characteristics around structural features can either introduce weaknesses or exploit a material's strength. Knit lines are a common source of weaknesses. Anisotropic materials like HX-4000 are even more sensitive to these injection phenomena since their strength depends on well aligned crystallization. The designer must take great care to engineer the melt flow as carefully as other design factors.

4.4 EXPERIMENTAL RESULTS - To date, 2 batches of specimens have been tested for a total of 98 tensile tests. These specimens were annealed at either 300°C and 260°C for varying annealing durations. The resulting mechanical properties were affected proportionally by each annealing process. Annealing at these temperatures, at least for the durations tested, actually weakened the specimens compared to the non-annealed ones. However, positive trends in the results indicate that there may be potential to improve the properties of the HX-4000 by heat treating.

STRENGTH vs ANNEAL TIME
(300 deg C)
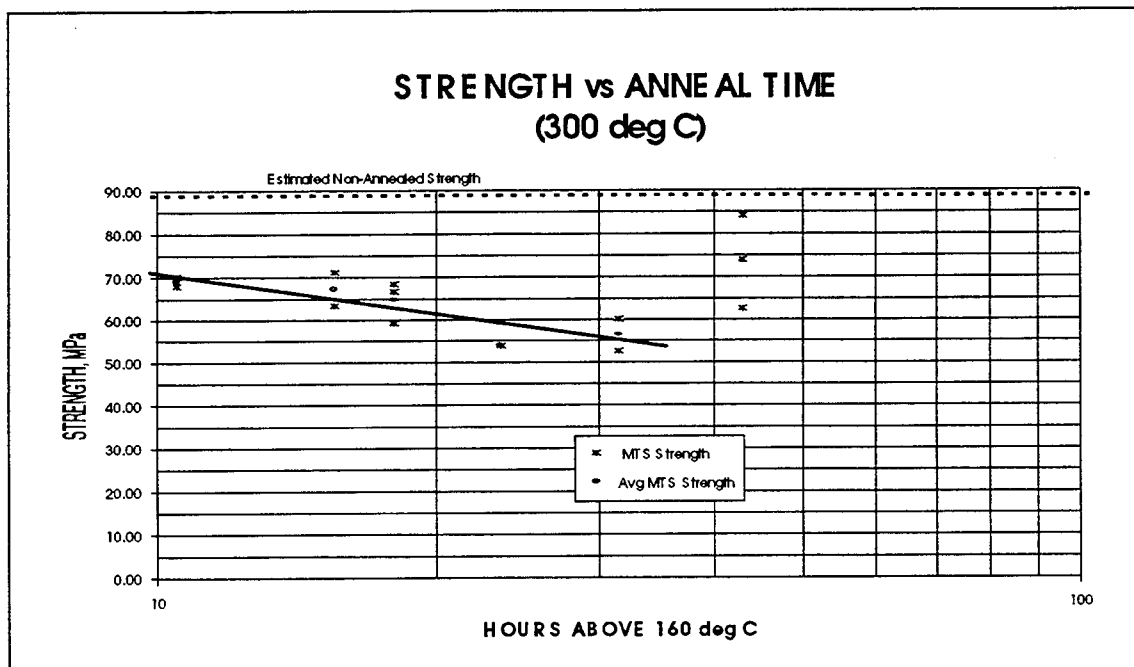
Graph 1

4.4.1 300°C ANNEAL - This temperature clearly diminishes the mechanical properties of HX-4000. The longer the specimens were exposed to this temperature, the weaker and more brittle they became. After 31.5 hours annealed above 160°C, their average ultimate strength decreased 32.5% to 56.4 from 83.5 MPa** at 300°C. (Graph 1) Much of the strength lost, resulted from the first 10.5 hours of annealing: 17.1% to 69.2 MPa. Likewise, their average strain at fracture decreased 42.1% (became more brittle) to

3239×10^{-6} from 5592×10^{-6}* mm/mm. (Graph 2) However, the initial strain after the first 10.5 hours was marginally greater than the non-annealed value, but well within the statistical scatter. There is no data below the 10.5 hour anneal, so this trend cannot be extrapolated. **Note that the non-annealed properties are only estimates; there were no successful tests of non-annealed specimens.

The change in properties due to annealing appeared to follow a logarithmic rate. When plotted on a semi-log scale, all strength data fell within approximately 10% of a straight line. (Graph 1) The strain data was more scattered than the strength data, but it also plotted very close to a line on the semi-log scale. There was significant scatter at one test point, but the averages at each point never strayed from the best straight line by more than 6%. (Graph 2) The logarithmic relationship is clear for these data with the exception on one test point not included above.

STRAIN vs ANNEAL TIME
(300 deg C)
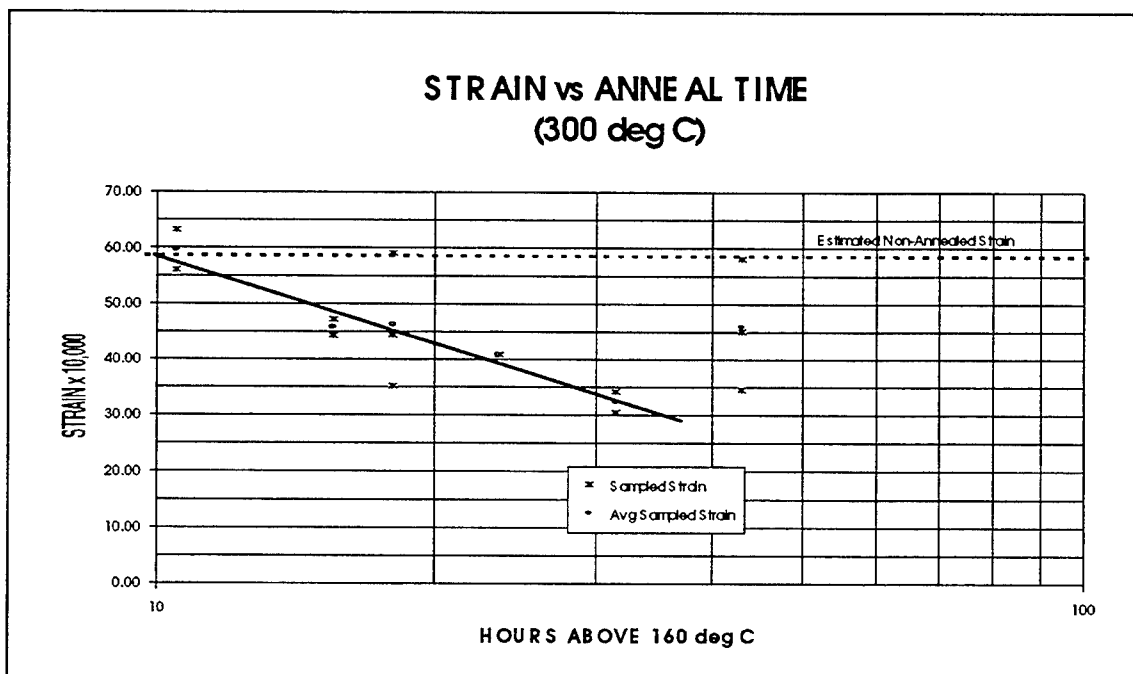
Graph 2

One group of specimens annealed at 300°C was much different from the others. These specimens were annealed in a very large furnace with a very large thermal mass. As a result, the specimens took 23 hours to cool from 300°C to 160°C following their 20 hour anneal time. This long cooling time allowed the material to react to the lower temperatures during cooling. In affect, this was like a very long anneal a lower than 300°C.

These specimens recovered much of their estimated non-annealed strength (Graph 1) and strain (Graph 2) compared to the others (88.1% and 82.1% of the non-annealed strength and strain, respectively). Their properties seemed to be unrelated to the other specimens except that they were still weaker and more brittle than the non-annealed benchmark. Perhaps the lower temperatures in the cooling cycle allowed the molecules to align into a more organized structure than the other annealed specimens. Whatever the mechanism, the long cooling time clearly enhanced the properties of this one group of specimens.

These results indicate that much of the strength lost in the 300°C anneal is recoverable. Permanent damage would indicate possible depolymerization during annealing. However, something happens at lower temperatures which positively affects the material. Perhaps at 300°C the material loses some of its hierarchical fibrous structure and randomizes or becomes more amorphous. The lower temperatures may allow it to recover its fibrous structure. The planned thermodynamic testing will be needed to help understand these mechanisms.

STRENGTH vs ANNEAL TIME
(260 deg C)
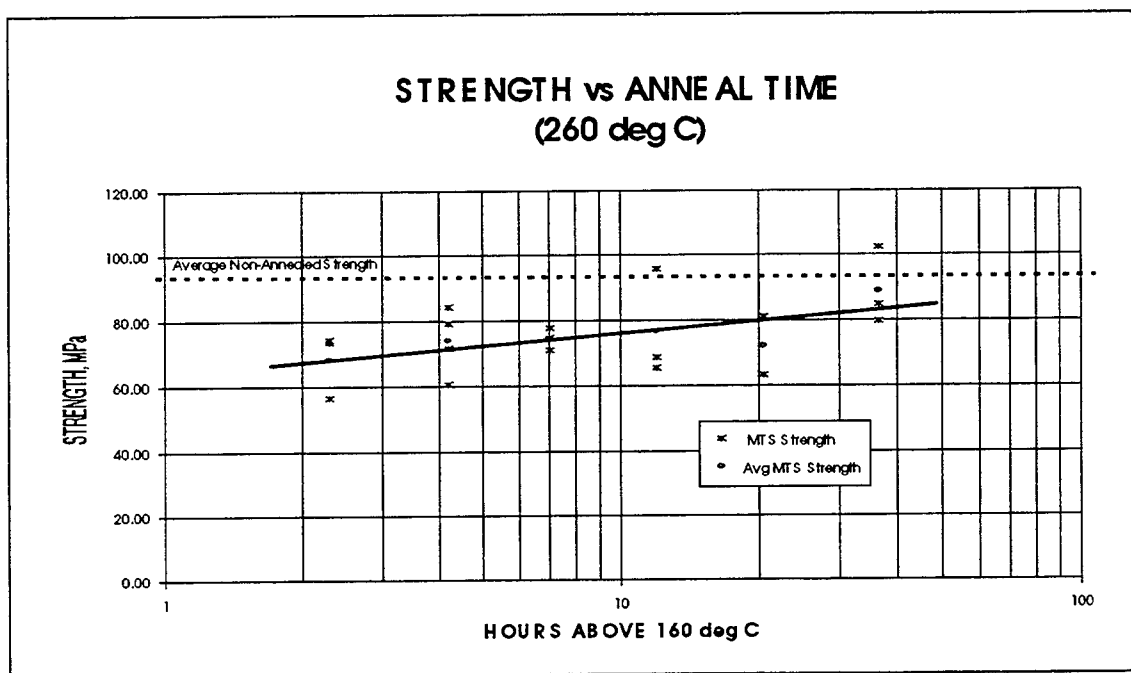
Graph 4

It is also important to note that there were no successful tests of the non-annealed specimens from this batch. Ten specimens were tested, and all of them broke in either the grip area or in the fillet. After only one hour of heat treating (four hours with cooling), the success rate jumped to 40%. This may indicate that annealing allows the structure to recover from the flow irregularities induced by the expanding cross section of the mold;

however, there was no trend in the successful test rates which would indicate further improvements. It does not appear that the mechanism responsible for this "healing" progresses any further after the initial annealing.

4.4.2 260°C ANNEAL - This annealing temperature shows that there is some potential to improve the mechanical properties of HX-4000 or at least not diminish its properties as much as 300°C. The specimens annealed at 260°C were not as strong as the non-annealed specimens, 26.9% of their strength was lost after 2.3 hours above 160°C (from 93.2 to 68.2 MPa), but their strength did increase to within 4.6% of their non-annealed strength, 88.9 MPa, with further annealing. (Graph 4) These data appear to reinforce the notion that annealing facilitates structural changes that may improve the material's properties. Similarly, elastic modulus for these specimens initially decreased 13.9% upon annealing (from 7380 to 6353 mm/mm), but seemed to improve as annealing durations increased (Graph 6). However, there is too much scatter in the strain (Graph 5) and modulus data (Graph 6) to draw any strong conclusions about these trends.

Graph 5
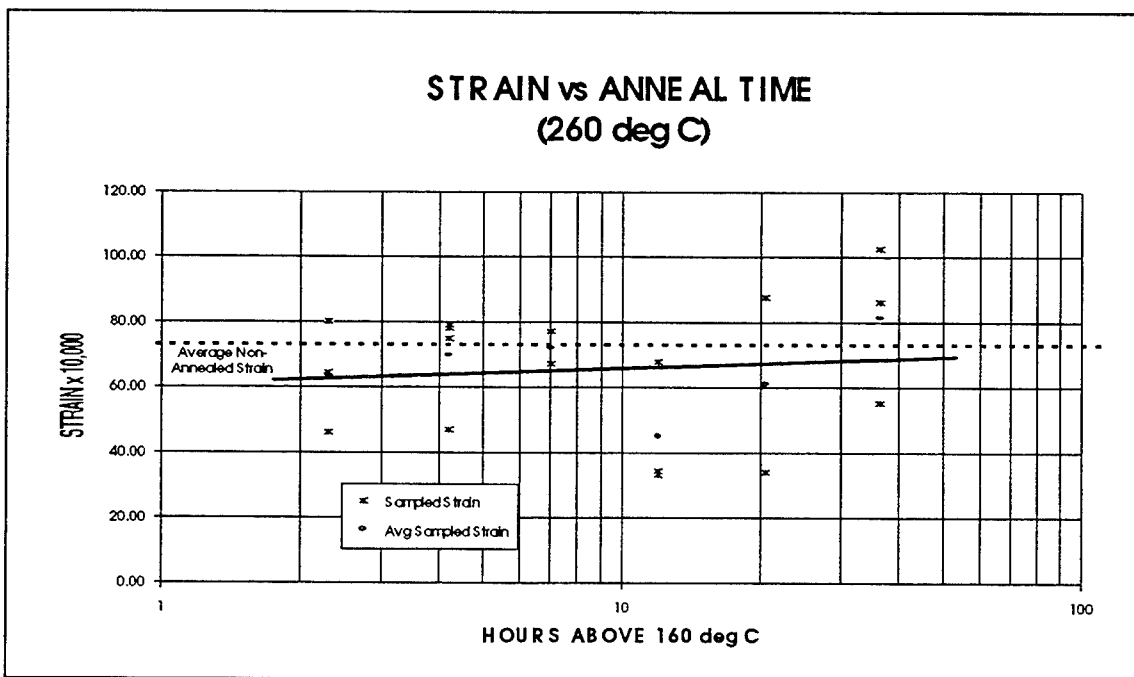
Again, the mechanical property changes appeared to follow logarithmic functions. While 80% of the valid strength data fit within 18% of a best fit line plotted on a semi-log scale, the averages at each test point were within 10%. There is more scatter in the modulus data, but they also indicate an increasing trend. The strain data are too scattered to conclude a relationship. While annealing at 260°C clearly had a detrimental effect on

424

these specimens for short annealing cycles, their ultimate strength did improve with time at a logarithmic rate after the initial decrease.

4.5 QUENCH EFFECT - One variable that could not be controlled precisely may have had some effect on the results: quench upon cooling. Most of the specimens annealed at 300°C were cooled in the furnace for approximately the same time. The variation from 6 hours to 7.5 hours cooling time did not reflect in the data. However, the 23 hour cooling time resulted in significantly different mechanical properties. As explained before, this could be due to favorable molecular reorganization at the lower cooling temperatures, but it could also have been spared any damage from a quench. In other words, a relatively rapid cooling time after annealing might have adversely affected the resulting mechanical properties.

Graph 6
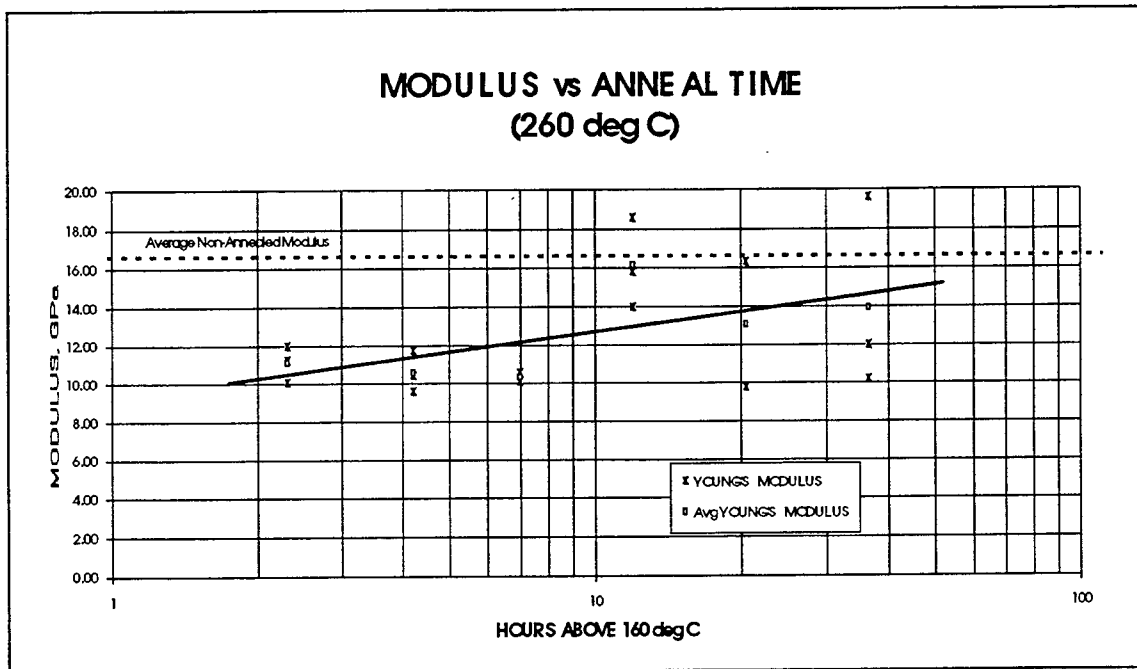
Likewise, the specimens annealed at 260°C may show the effects of quench. The first specimens to be annealed had very short cooling cycles corresponding to short annealing cycles. It is possible that the initial drop in strength could have been due to this quench effect. In that case, the property improvement observed at the longer annealing times could be partly attributable to less severe quench. This notion can not be supported by any known mechanism; additional tests should help to understand these phenomena.

4.6 EFFECT OF INVALID FRACTURES - The high number of invalid failures introduces some doubt that the valid test data reflects the true nature of this material.

60% of the 98 specimens failed in the downstream, expanding part of the specimen relative to the injection flow direction. It is known that such low pressure discontinuities should be avoided in injection mold design. If the specimens fractured in this acknowledged weak area, the true strength of the specimen can not be determined. How strong was the material in the gage length? It appears that the valid data presented in this research may reflect the weaker end of the strength distribution for this material.

A possible contribution to this high number of failures is the test method. Most tensile testing research is conducted according to ASTM D638-84 which specifies that specimens be pulled at a constant strain rate during tensile tests; this is called "strain control." These tests were conducted under "load control," loaded at a constant load rate regardless of strain, i.e. 10 pounds per second. This procedure introduces a relative shock to the specimen when strain rates increase, especially near fracture. In fibrous materials such as HX-4000, small fractures occur when individual fibers break, thus applying instantaneous shocks and higher strain rates. These shocks may be responsible for the high invalid failure rate.

The data in this paper cannot be correlated with other studies because of the different loading scheme. These specimens were not allowed the sustained plastic deformations normally associated with ductile metals. While a load dependent situation more accurately simulates the application environment, the resulting data does not correspond with other research.

5.0 CONCLUSIONS

Clearly this research is not yet complete. One or two more annealing temperatures must be tested as well as sonic modulus, TMA, TGA, DMA, DSC and SEM to learn as much as possible about the material changes that result from the annealing process. These tests will support the goal to mathematically relate these material changes to the temperature and duration of the annealing process on HX-4000.

Regardless of how preliminary this research is, some important understanding can be drawn from it. Mold design and fabrication processes are critical to make good parts with HX-4000 as with many other liquid crystalline polymers. The number of invalid failures of these specimens reinforces the importance of proper mold design. Low pressure and low shear rate regions in the melt flow, like rapidly expanding sections, must

be avoided since they create weak areas in the resulting parts. The injection molds must also be very hot to minimize the thickness of the amorphous skins. The fibrous microstructure of HX-4000 greatly contributes to its strength; therefore, thick amorphous skins are detrimental. Proper mold design and injection processes are important with all injection molding, but they are critical with HX-4000.

The annealing process is also critical to HX-4000, but ideal conditions are not yet obvious. It is clear, however, that 300°C is too hot to improve mechanical properties in HX-4000. This temperature caused parts to lose significant strength and become more brittle. It also caused these specimens to warp, sometimes severely. Mechanical property improvements were not obtained at 260°C either; however, they recovered some of their non-annealed mechanical properties. Hopefully, longer annealing cycles at 260°C or different annealing temperatures will produce some positive results.

6.0 RECOMMENDATIONS

It is already clear that some changes are necessary for further work in this area. First, tests should be conducted according to ASTM standards. The results from such testing can be directly compared to other research, and traditional analysis of the results will be meaningful. The results from these tests can not be directly correlated to other tests, and the stress-strain results are difficult to interpret. Second, straight tensile bars (or possibly ASTM D638-84 Type II "Dog Bones") should be used for tensile testing of HX-4000 versus the ASTM D638-84 Type I specimens used in this work. ASTM D638-84 recommends the Type II specimens when a material frequently fractures outside the desired gage length; however, the gage length in the Type II specimens are only half the cross-section area. These specimens may still experience failures since it appears that any expansion after a narrower sections would be inherently weak. Straight tensile bars would circumvent this problem altogether. The weakness caused by the expanding flair in the grip area wasted time, material and possibly lots of good data.

REFERENCES

1 C. SAWYER, and M. JAFFE, *J. Mater. Sci.* **21** (1986) 1897.

2 *Idem*, in "High Performance Polymers," edited by E. Baer and A. Moet (Carl Hanser, Germany, 1991) p. 56.

3 C. SAWYER and D. T. GRUBB, "Polymer Microscopy" (Chapman and Hall, London, 1987).

4 A. M. DONALD and A. H. WINDLE, "Liquid Crystalline Polymers" (Cambridge University Press, 1992) p. 1.

5 F. REINITZER, *Manatsch* **9** (1888) 421.

6 O. LEHMANN, *Z. Phys. Chem.* **5** (1890) 427.

7 G. FRIEDEL, *Ann. Physique* **18** (1922) 273.

8 D. VORLANDER, *Z. Phys. Chem.* **105** (1923) 211.

9 A. M. DONALD and A. H. WINDLE, "Liquid Crystalline Polymers" (Cambridge University Press, 1992) p. 2.

10 L. ONSAGER, *N.Y. Acad. Sci.* **51** (1949) 627.

11 A. ISIHARA, *J. Chem. Phys.* **19** (1951) 1142.

12 J. FLORY, *Proc. Roy. Soc.* **A234** (1956) 73.

13 *Idem*, in "Polymer Liquid Crystals", edited by A. Ciferri, W.R. Krigbaum and R.B. Meyer (Academic Press, New York, 1982).

14 C. SAWYER, R. T. CHEN, M. G. JAMIESON, I. H. MUSSELMAN and P. E. RUSSELL, *J. Mater. Sci.* **28** (1993) 225.

15 C. ROBINSON, *Trans. Faraday. Soc.* **52** (1956) 571.

16 D. G. H. BALLARD, *Courtaulds Ltd*, UK Patent BP 864, 962 (1058).

17 S. L. KWOLEK, *DuPont*, US Patent 3 600 350 (1971).

18 A. M. DONALD and A. H. WINDLE, "Liquid Crystalline Polymers" (Cambridge University Press, 1992) p. 84.

19 "Liquid Crystal Polymers," NMAB 453, MDA903-89-K-0078, National Academy of Science, February 28, 1990, p. 19.

20 D. E. KRANBUEHL, College of William and Mary, "Characterization, FDEMS Sensing and In Situ Process Monitoring During Cure of High Temperature Liquid Crystal Thermotropes" (Advanced Plymer Components Symposium, 1993).

21 C. SAWYER, R. T. CHEN, M. G. JAMIESON, I. H. MUSSELMAN and P. E. RUSSELL, *J. Mater. Sci.* **28** (1993) 235.

22 D. R. ASKELAND, "The Science and Engineering of Materials" (PWS-KENT Publishing Co, Boston, 1989) p. 118.

23 Use high temperature mold for good surface finish, thin wall and hard to fill sections. Use lower temperatures for complex parts with slicking problems.

24 J. NIELSEN, Technical Service, RTP co., Winona, Minnesota.

25 D. ELLIOT, Arkansas Technical University, "A Study of Thermotropic Liquid Crystalline Polymers" (Advanced Plymer Components Symposium, 1993).

26 *Inem*

27 C. FRANK, Advanced Composites Program Office, McClellen Air Force Base, California.

28 *Inem*

Appendix I

DATA TABLES

300 deg C ANNEAL

TEST POINT			MEASURED			DERIVED	
			U, STRENGTH		STRAIN	YOUNG'S MODULUS	
T ABOVE	COOL TIME	SAMPLE				PHYS (GPa)	SON (GPa)
160 deg C	hr	#	MPa	MPa (MTS)	micro in/in		
10.5	6.5	43	66.99	68.02	6,320		
10.5	6.5	83	68.37	70.30	5,601		
10.5	6.5	AVERAGE	67.68	69.16	5,961	#DIV/0I	#DIV/0I
15.5	7.5	91	62.00	63.44	4,430		
15.5	7.5	131	70.26	71.21	4,720		
15.5	7.5	AVERAGE	66.13	67.33	4,575	#DIV/0I	#DIV/0I
18	6	76	65.49	66.71	5,912		
18	6	121	58.20	59.29	4,441		
18	6	54	68.12	68.49	3,517		
18	6	AVERAGE	63.94	64.83	4,623	#DIV/0I	#DIV/0I
23.5	7.5	127	52.51	53.94	4,087		
23.5	7.5	AVERAGE	52.51	53.94	4,087	#DIV/0I	#DIV/0I
43	23	88	80.99	84.09	5,812		
43	23	75	70.96	74.02	3,454		
43	23	122	60.68	62.71	4,506		
43	23	AVERAGE	70.87	73.61	4,591	#DIV/0I	#DIV/0I
31.5	7.5	72	58.55	60.24	3,424		
31.5	7.5	79	49.70	52.58	3,054		
31.5	7.5	AVERAGE	54.12	56.41	3,239	#DIV/0I	#DIV/0I

300 deg C ANNEAL

TEST POINT			VAR FROM AVG / STANDARD DEVIATIONS				
			U, STRENGTH		STRAIN	YOUNG'S MODULUS	
T ABOVE	COOL TIME	SAMPLE	MPa	MPa (MTS)	micro mm/mm	PHYS (GPa)	SON (GPa)
160 deg C	hr	#					
10.5	6.5	43	-1.45%	-2.08%	6.03%	#DIV/0!	#DIV/0!
10.5	6.5	83	1.45%	2.08%	-6.03%	#DIV/0!	#DIV/0!
10.5	6.5	AVERAGE	2.06%	2.94%	8.53%	#DIV/0!	#DIV/0!
15.5	7.5	91	-6.26%	-5.78%	-3.17%	#DIV/0!	#DIV/0!
15.5	7.5	131	6.26%	5.78%	3.17%	#DIV/0!	#DIV/0!
15.5	7.5	AVERAGE	8.85%	8.18%	4.48%	#DIV/0!	#DIV/0!
18	6	76	2.54%	3.01%	27.87%	#DIV/0!	#DIV/0!
18	6	121	-9.10%	-8.67%	-3.94%	#DIV/0!	#DIV/0!
18	6	54	6.56%	5.66%	-23.93%	#DIV/0!	#DIV/0!
18	6	AVERAGE	8.13%	7.63%	26.13%	#DIV/0!	#DIV/0!
23.5	7.5	127	0.00%	0.00%	0.00%	#DIV/0!	#DIV/0!
23.5	7.5	AVERAGE	#DIV/0!	#DIV/0!	#DIV/0!	#DIV/0!	#DIV/0!
43	23	88	14.71%	14.69%	26.61%	#DIV/0!	#DIV/0!
43	23	75	-0.27%	0.16%	-24.76%	#DIV/0!	#DIV/0!
43	23	12?	-14.43%	-14.84%	-1.85%	#DIV/0!	#DIV/0!
43	23	AVERAGE	14.57%	14.77%	25.73%	#DIV/0!	#DIV/0!
31.5	7.5	72	8.25%	6.86%	5.71%	#DIV/0!	#DIV/0!
31.5	7.5	79	-8.25%	-6.86%	-5.71%	#DIV/0!	#DIV/0!
31.5	7.5	AVERAGE	11.66%	9.70%	8.08%	#DIV/0!	#DIV/0!

320 C ANNEAL

STRENGTH vs ANNEAL TIME
(300 deg C)

Estimated Non-Annealed Strength

| MTS Strength |
| Avg MTS Strength |

STRENGTH, MPa

90.00
80.00
70.00
60.00
50.00
40.00
30.00
20.00
10.00
0.00

10   100

HOURS ABOVE 160 deg C
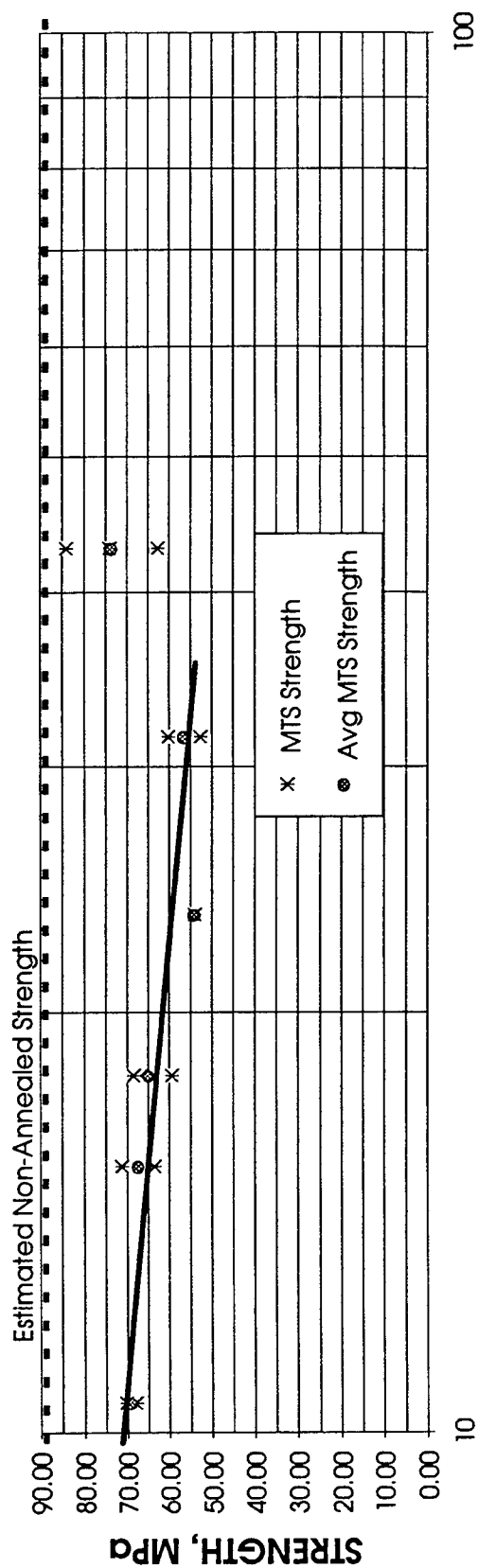
320 C ANNEAL

STRAIN vs ANNEAL TIME
(300 deg C)
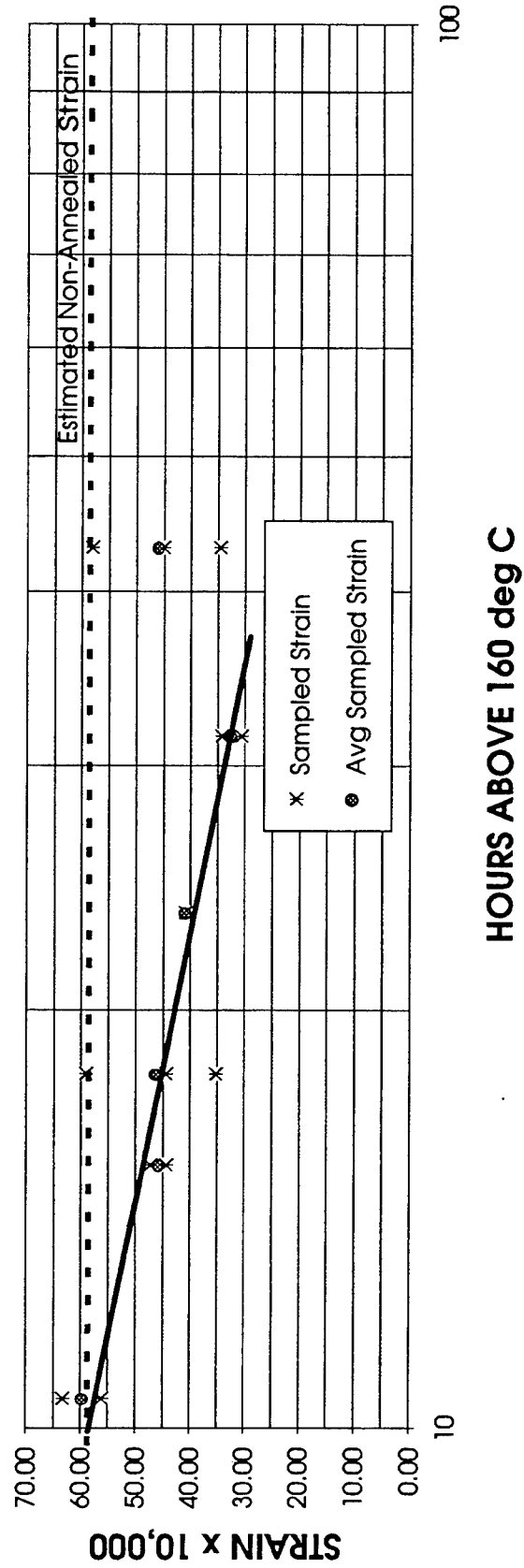
320 C ANNEAL

AVERAGE STRENGTH / STRAIN
vs ANNEAL TIME (300 deg C)

STRENGTH, MPa
STRAIN x 10,000

80.00
70.00
60.00
50.00
40.00
30.00
20.00
10.00
0.00

10

100

HOURS ABOVE 160 deg C

■ Avg Sampled Strength

⊗ Avg Sampled Strain
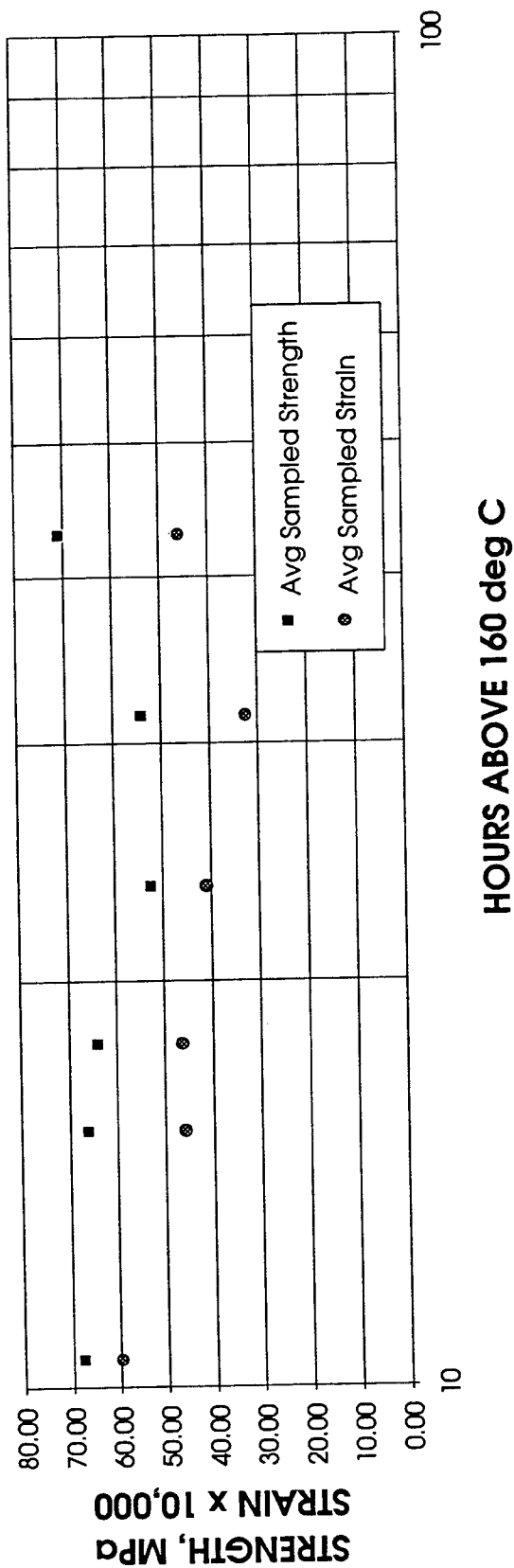
260 deg C ANNEAL

| TEST POINT | | | | DATA | | | | |
ANNEAL hr	T ABOVE 160 deg C	COOL TIME hr	SAMPLE FILE NAME	ULT STRENGTH MPa	MPa (MTS)	STRAIN micro mm/mm	YOUNG'S MODULUS PHYS (GPa)	SON (GPa)
0	0	0	1-0-1	98.62	99.35	6,460	16.50	
0	0	0	1-0-5	83.68	87.14	8,300	11.25	
AVERAGE	0			**91.15**	**93.25**	**7,380**	**13.88**	**#DIV/OI**
1	2.3	1.3	1-1-1	74.23	73.56	8,010	9.58	
1	2.3	1.3	1-1-2	71.64	74.34	6,430	10.50	
1	2.3	1.3	1-1-6	63.86	56.65	4,620	12.14	
AVERAGE	2.3			**69.91**	**68.18**	**6,353**	**10.74**	**#DIV/OI**
2	4.2	2.2	1-2-1	61.09	60.60	4,700	11.67	
2	4.2	2.2	1-2-2	70.65	71.66	7,490	9.67	
2	4.2	2.2	1-2-6	81.88	84.34	7,810	10.00	
2	4.2	2.2	1-2-7	77.14	79.32	7,920	10.00	
AVERAGE	4.2			**72.69**	**73.98**	**6,980**	**10.34**	**#DIV/OI**
4	7	3	1-4-2	68.54	71.02	6,710	9.92	
4	7	3	1-4-4	73.64	74.84	7,720	9.83	
4	7	3	1-4-8		77.85			
AVERAGE	7			**71.09**	**74.57**	**7,215**	**9.88**	**#DIV/OI**
8	12	4	1-8-2	68.06	68.72	3,320	18.33	
8	12	4	1-8-7	61.78	65.50	3,430	15.57	
8	12	4	1-8-8	92.65	95.60	6,780	13.25	
AVERAGE	12			**74.16**	**76.61**	**4,510**	**15.72**	**#DIV/OI**
16	20.5	4.5	1-16-3	63.11	63.27	3,410	16.33	
16	20.5	4.5	1-16-6	80.12	81.09	8,770	9.38	
AVERAGE	20.5			**71.62**	**72.18**	**6,090**	**12.86**	**#DIV/OI**
32	36.5	4.5	1-32-3	100.43	102.28	5,520	17.33	
32	36.5	4.5	1-32-4	78.65	79.72	10,250	11.36	
32	36.5	4.5	1-32-6	81.77	84.78	8,620	9.75	
AVERAGE	36.5			**86.95**	**88.93**	**8,130**	**12.81**	**#DIV/OI**

436

260 deg C ANNEAL

| TEST POINT | | | | VAR FROM AVG / STANDARD DEVIATIONS | | | | |
| ANNEAL | T ABOVE | COOL TIME | SAMPLE | U, STRENGTH | | STRAIN | YOUNG'S MODULUS | |
hr	160 deg C	hr	FILE NAME	MPa	MPa (MTS)	micro mm/mm	PHYS (GPa)	SON (GPa)
0	0	0	1-0-1	8.20%	6.55%	-12.47%	18.92%	#DIV/0!
0	0	0	1-0-5	-8.20%	-6.55%	12.47%	-18.92%	#DIV/0!
AVERAGE	0			11.59%	9.26%	17.63%	26.76%	#DIV/0!
1	2.3	1.3	1-1-1	-3.22%	-4.13%	21.32%	-10.80%	#DIV/0!
1	2.3	1.3	1-1-2	-6.36%	-2.86%	-2.61%	-2.23%	#DIV/0!
1	2.3	1.3	1-1-6	-17.05%	-26.44%	-30.03%	13.04%	#DIV/0!
AVERAGE	2.3			7.72%	14.66%	26.70%	12.07%	#DIV/0!
2	4.2	2.2	1-2-1	-20.21%	-22.26%	-24.40%	12.92%	#DIV/0!
2	4.2	2.2	1-2-2	-7.13%	-7.45%	20.47%	-6.43%	#DIV/0!
2	4.2	2.2	1-2-6	-7.13%	-7.45%	20.47%	-3.24%	#DIV/0!
2	4.2	2.2	1-2-7	-7.13%	-7.45%	20.47%	-3.24%	#DIV/0!
AVERAGE	4.2			12.38%	13.97%	21.93%	8.74%	#DIV/0!
4	7	3	1-4-2	-15.82%	-12.80%	-6.30%	0.46%	#DIV/0!
4	7	3	1-4-4	-9.35%	-7.90%	7.80%	-0.46%	#DIV/0!
4	7	3	1-4-8	-100.00%	-4.34%	-100.00%	-100.00%	#DIV/0!
AVERAGE	7			5.07%	4.59%	9.90%	0.64%	#DIV/0!
8	12	4	1-8-2	-7.01%	-8.71%	-36.41%	16.63%	#DIV/0!
8	12	4	1-8-7	-21.80%	-19.38%	-34.31%	-0.93%	#DIV/0!
8	12	4	1-8-8	15.37%	15.75%	29.85%	-15.69%	#DIV/0!
AVERAGE	12			22.00%	21.57%	43.61%	16.18%	#DIV/0!
16	20.5	4.5	1-16-3	-24.81%	-26.43%	-49.99%	27.03%	#DIV/0!
16	20.5	4.5	1-16-6	-4.27%	-5.44%	28.62%	-27.03%	#DIV/0!
AVERAGE	20.5			16.80%	17.46%	62.23%	38.23%	#DIV/0!
32	36.5	4.5	1-32-3	20.66%	20.29%	-23.51%	35.25%	#DIV/0!
32	36.5	4.5	1-32-4	-3.60%	-4.34%	42.03%	-11.34%	#DIV/0!
32	36.5	4.5	1-32-6	-0.69%	0.81%	19.45%	-23.91%	#DIV/0!
AVERAGE	36.5			13.55%	13.31%	29.55%	31.17%	#DIV/0!

STRENGTH vs ANNEAL TIME
(260 deg C)

STRENGTH, MPa

HOURS ABOVE 160 deg C

Average Non-Annealed Strength

✕	MTS Strength
⊗	Avg MTS Strength
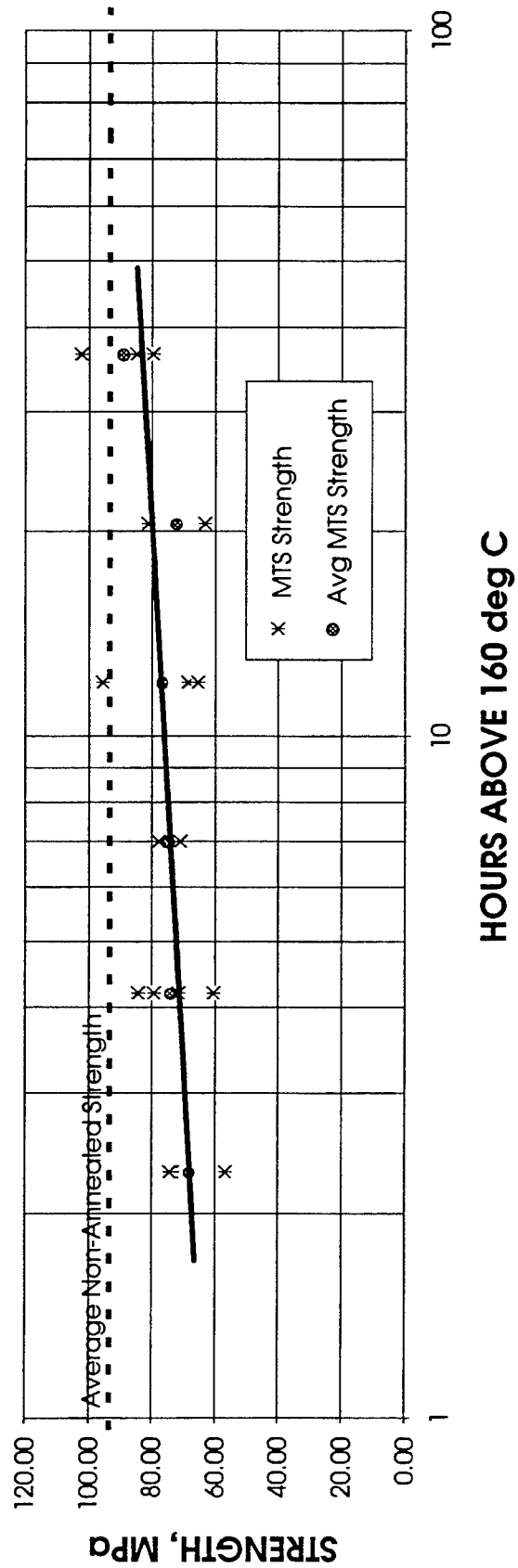
260 C ANNEAL

STRAIN vs ANNEAL TIME
(260 deg C)

MODULUS vs ANNEAL TIME (260 deg C)

HOURS ABOVE 160 deg C

MODULUS, GPa

Average Non-Annealed Modulus

× YOUNG'S MODULUS
□ Avg YOUNG'S MODULUS
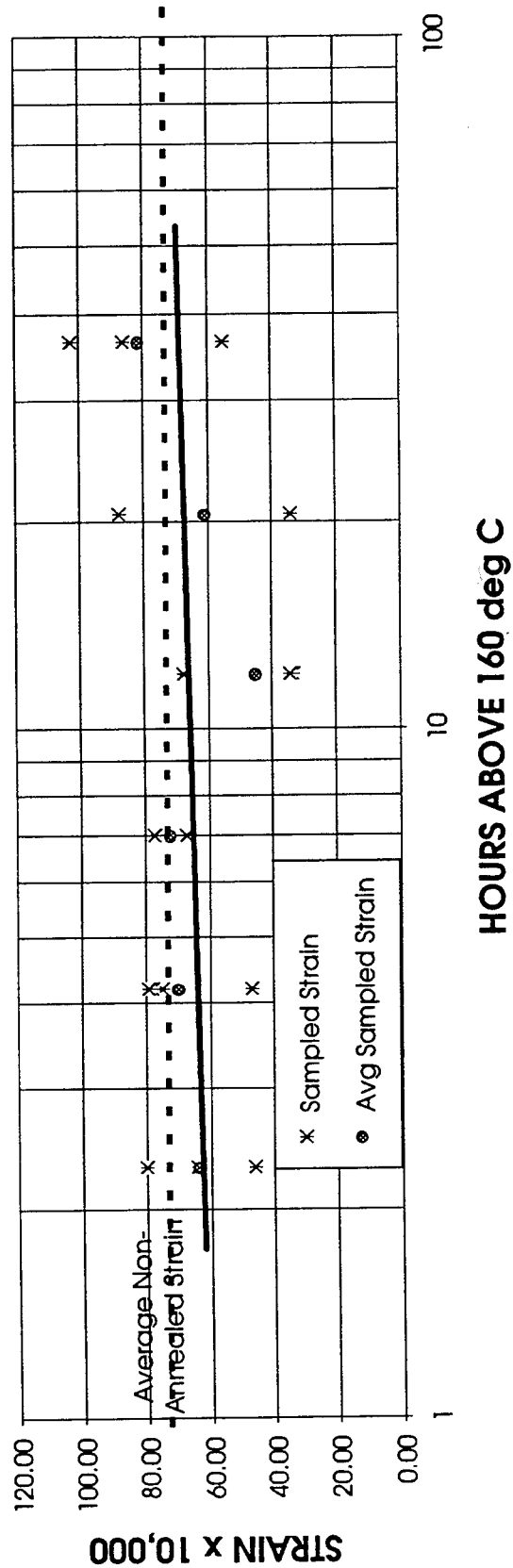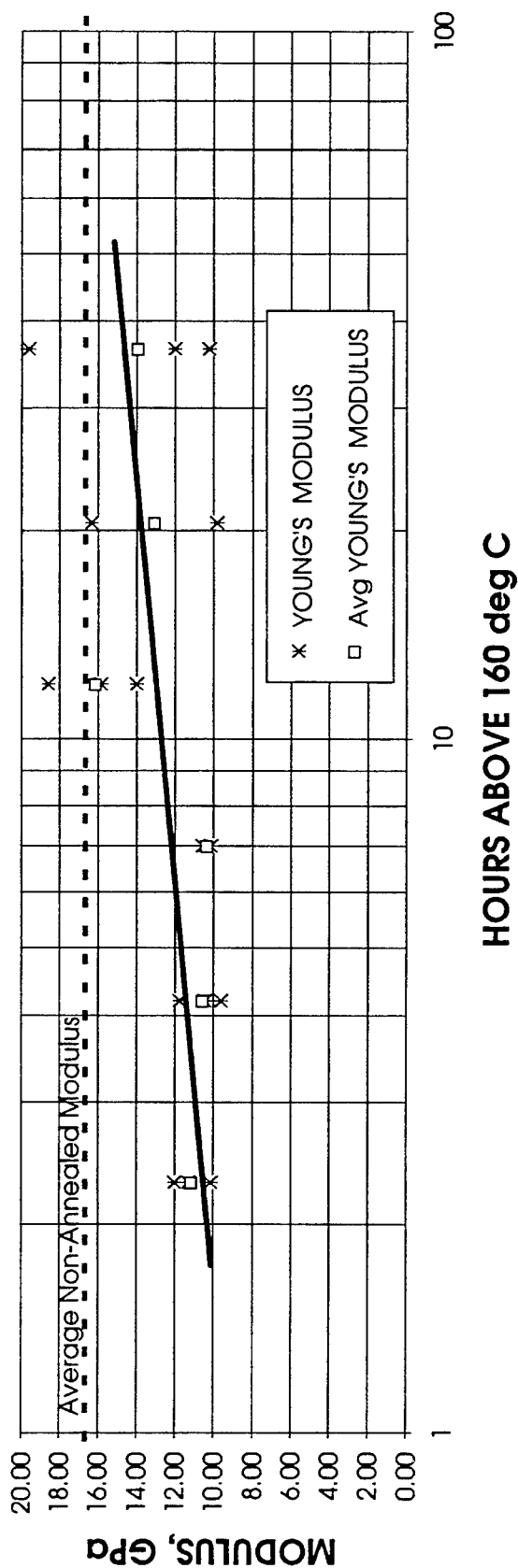
260 C ANNEAL

AVERAGE STRENGTH / STRAIN / MODULUS vs ANNEAL TIME (260 deg C)

Legend:
- ■ Avg Sampled Strength
- ⊗ Avg Sampled Strain
- ▲ Avg Measured Modulus

X-axis: HOURS ABOVE 160 deg C (1 to 100)

Y-axis: STRENGTH, MPa / STRAIN x 10,000 / MODULUS, GPa (0 to 90)
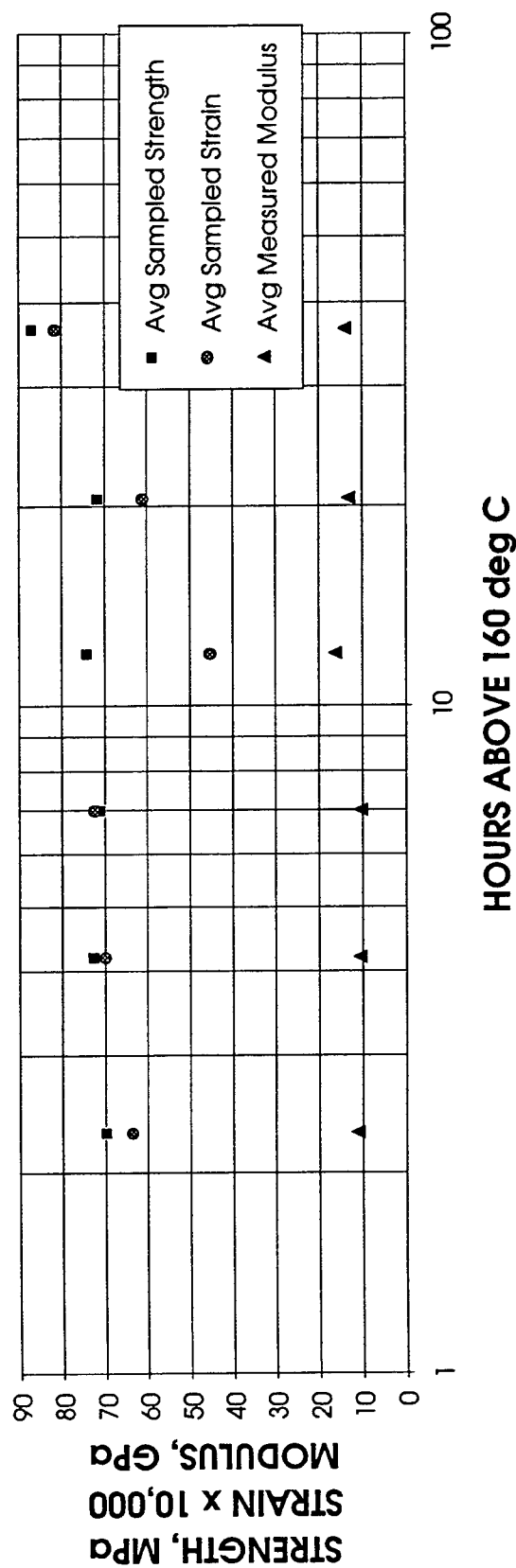
Appendix II

<u>STRESS-STRAIN DIAGRAMS</u>

STRESS vs STRAIN
NON-ANNEALED

443
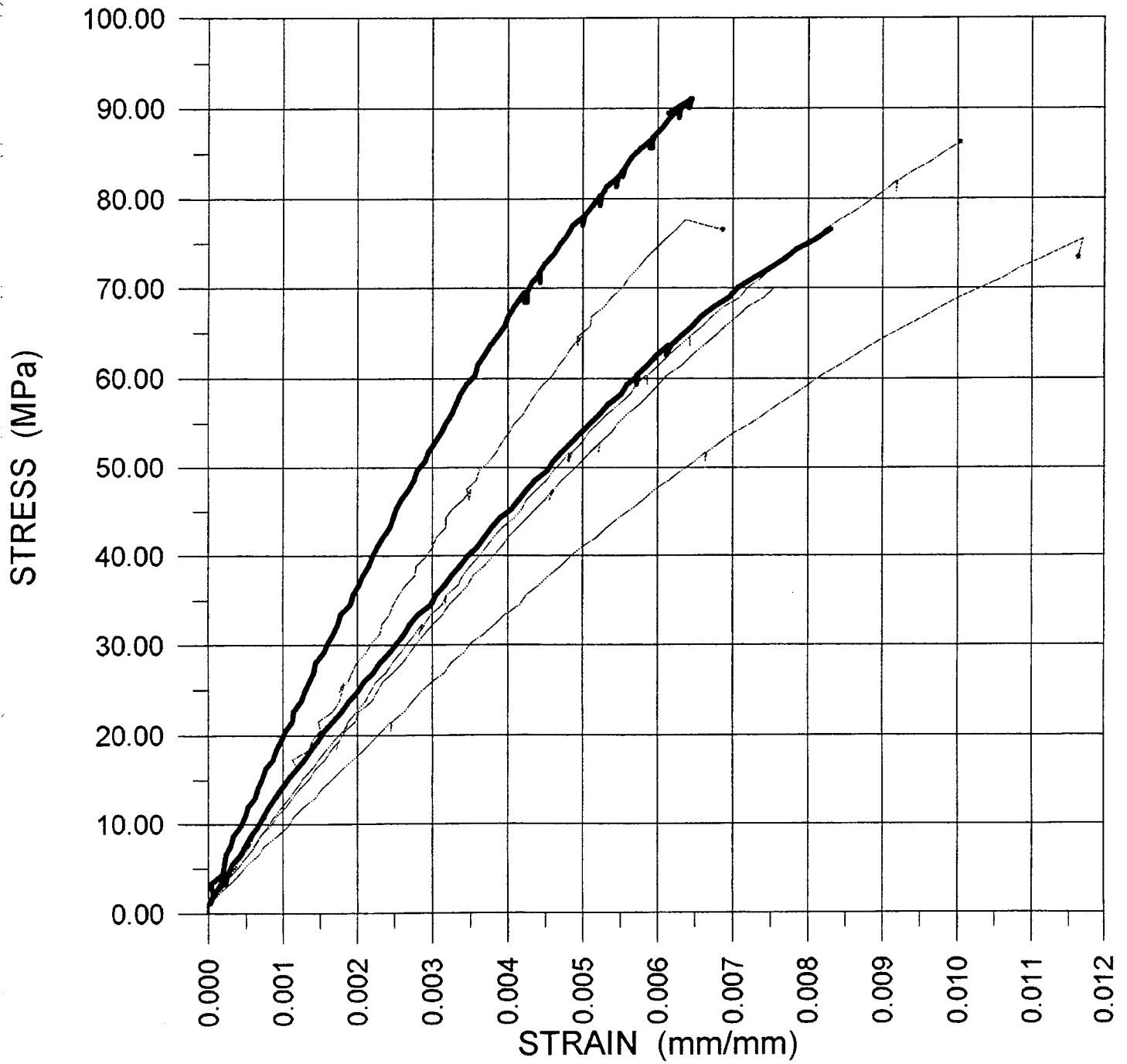
STRESS vs STRAIN
1 Hr ANNEAL @ 260 deg C
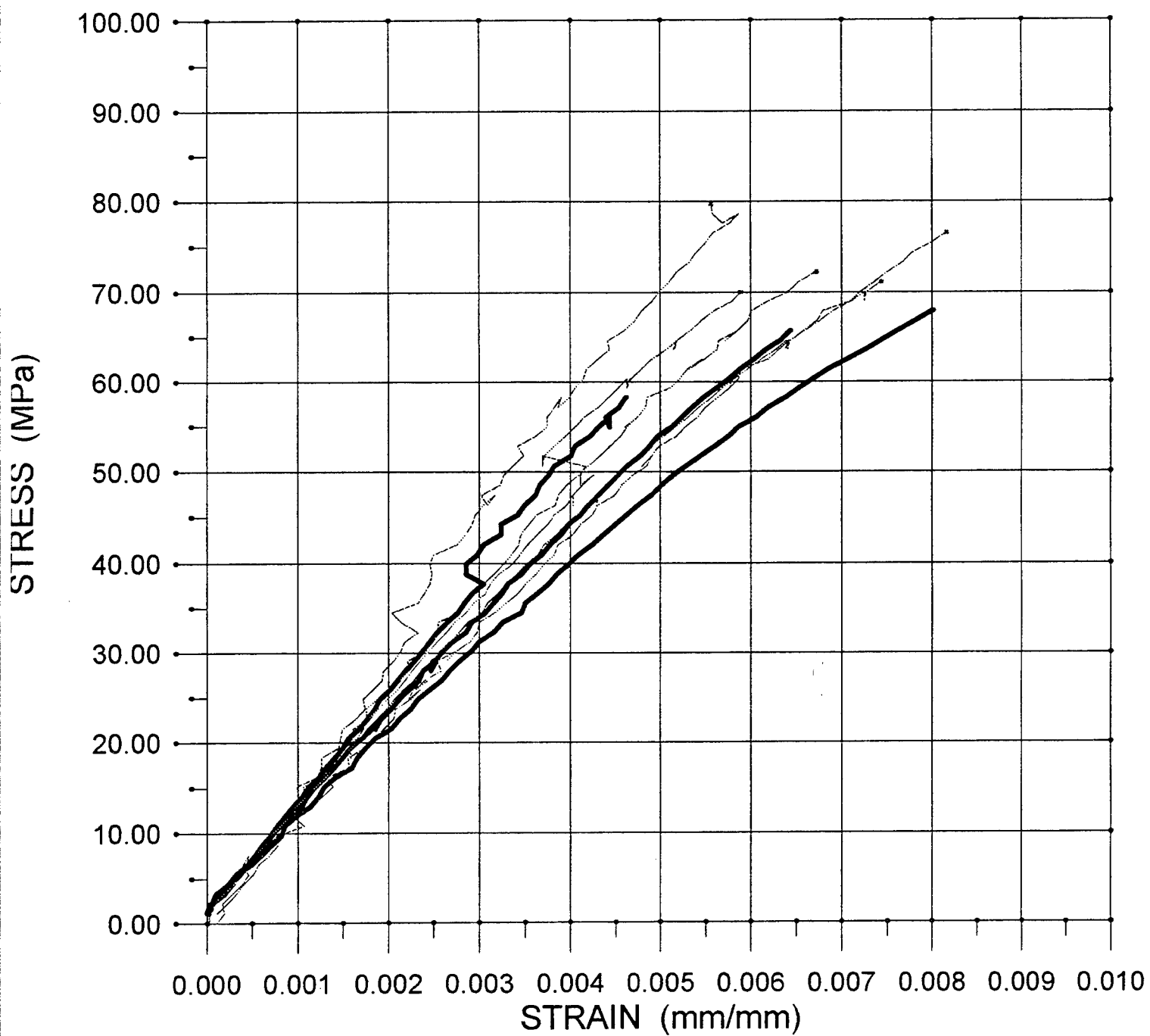
STRESS vs STRAIN

2 hr ANNEAL @ 260 deg C
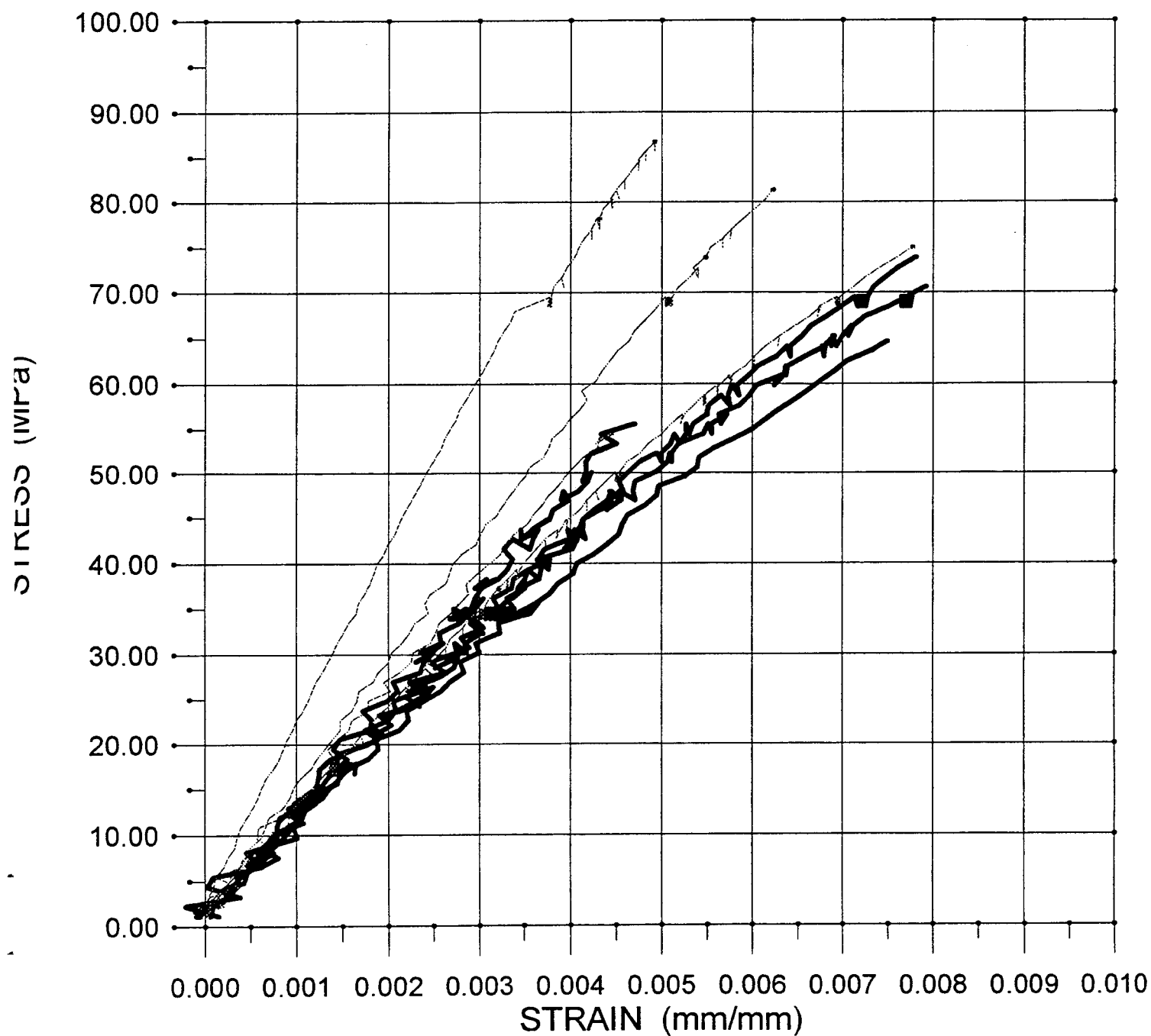
STRESS vs STRAIN
4 hr ANNEAL @ 260 deg C
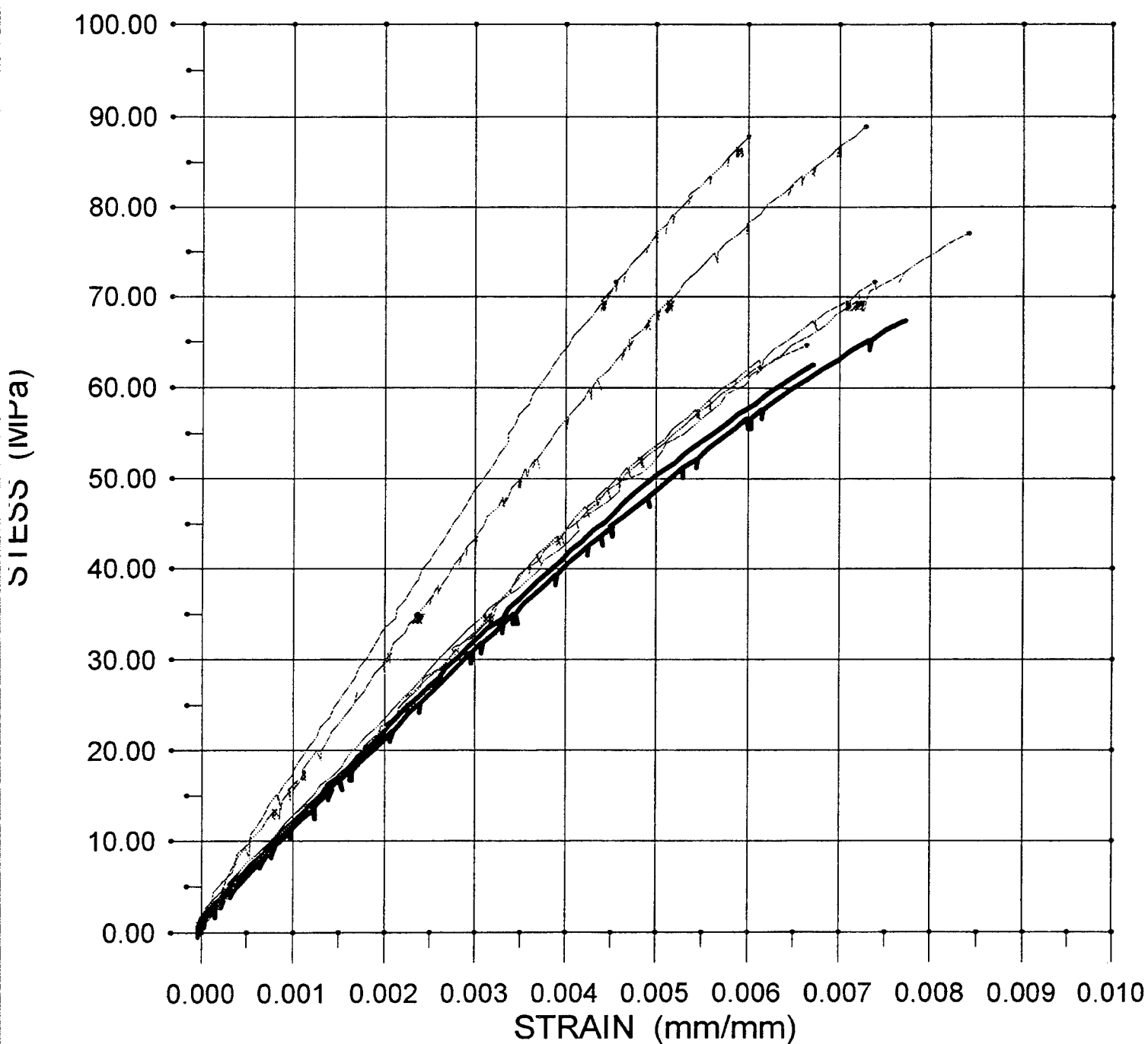
STRESS vs STRAIN
8 hr ANNEAL @ 260 deg C

STRESS (MPa) vs STRAIN (mm/mm)

447
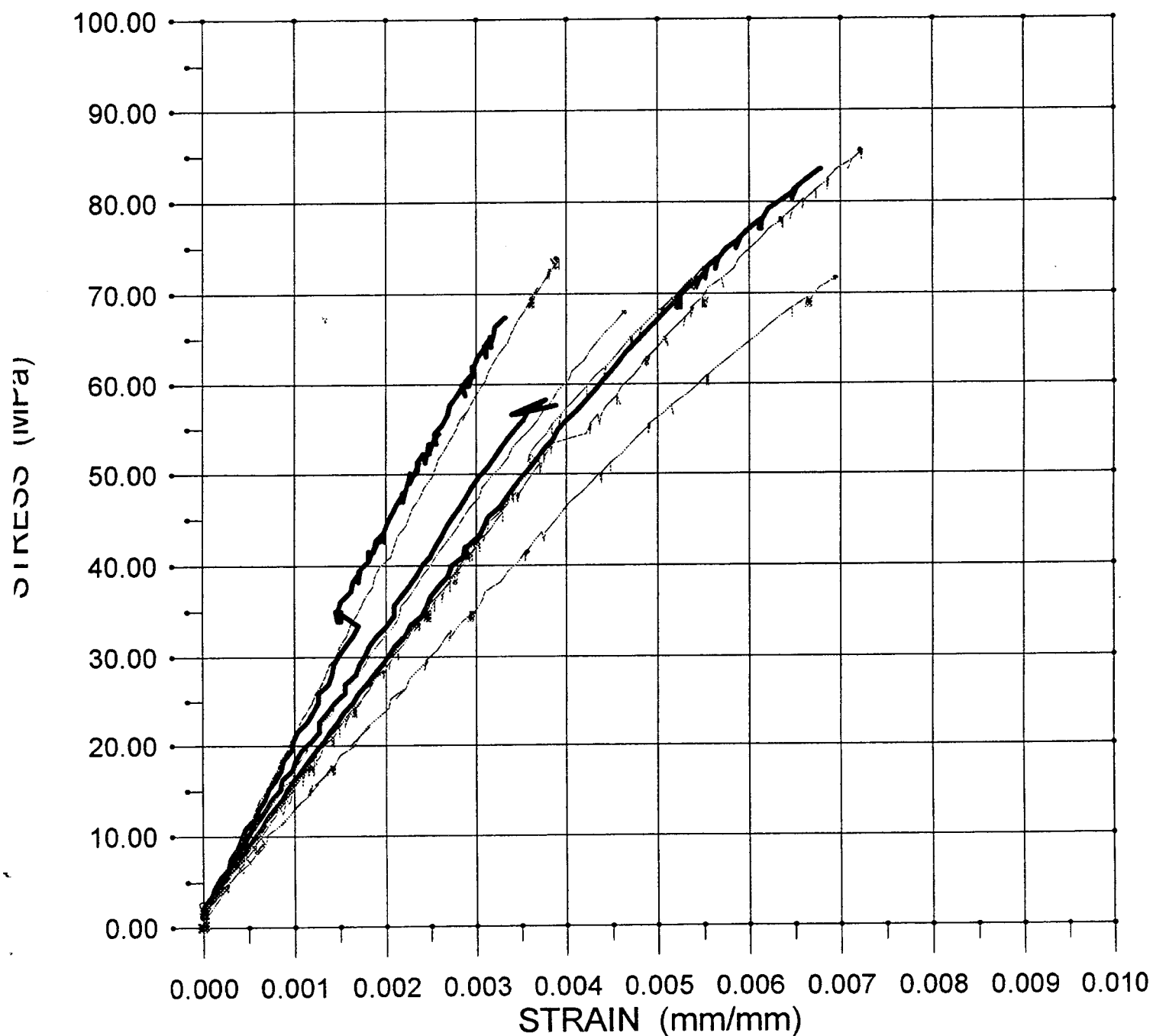
STRESS vs STRAIN

16 hr ANNEAL @ 260 deg C
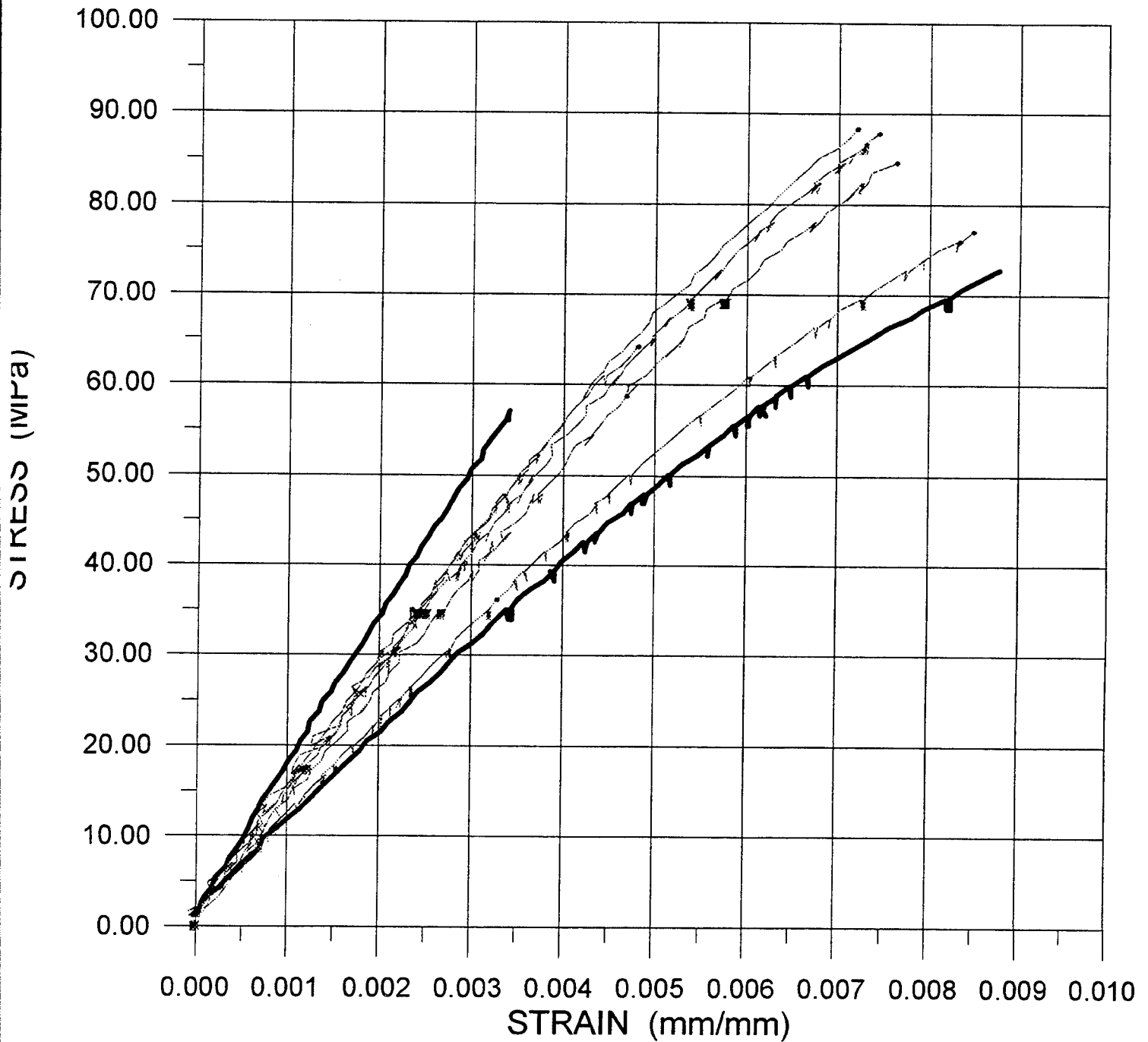
STRESS vs STRAIN
32 hr ANNEAL @ 260 deg C
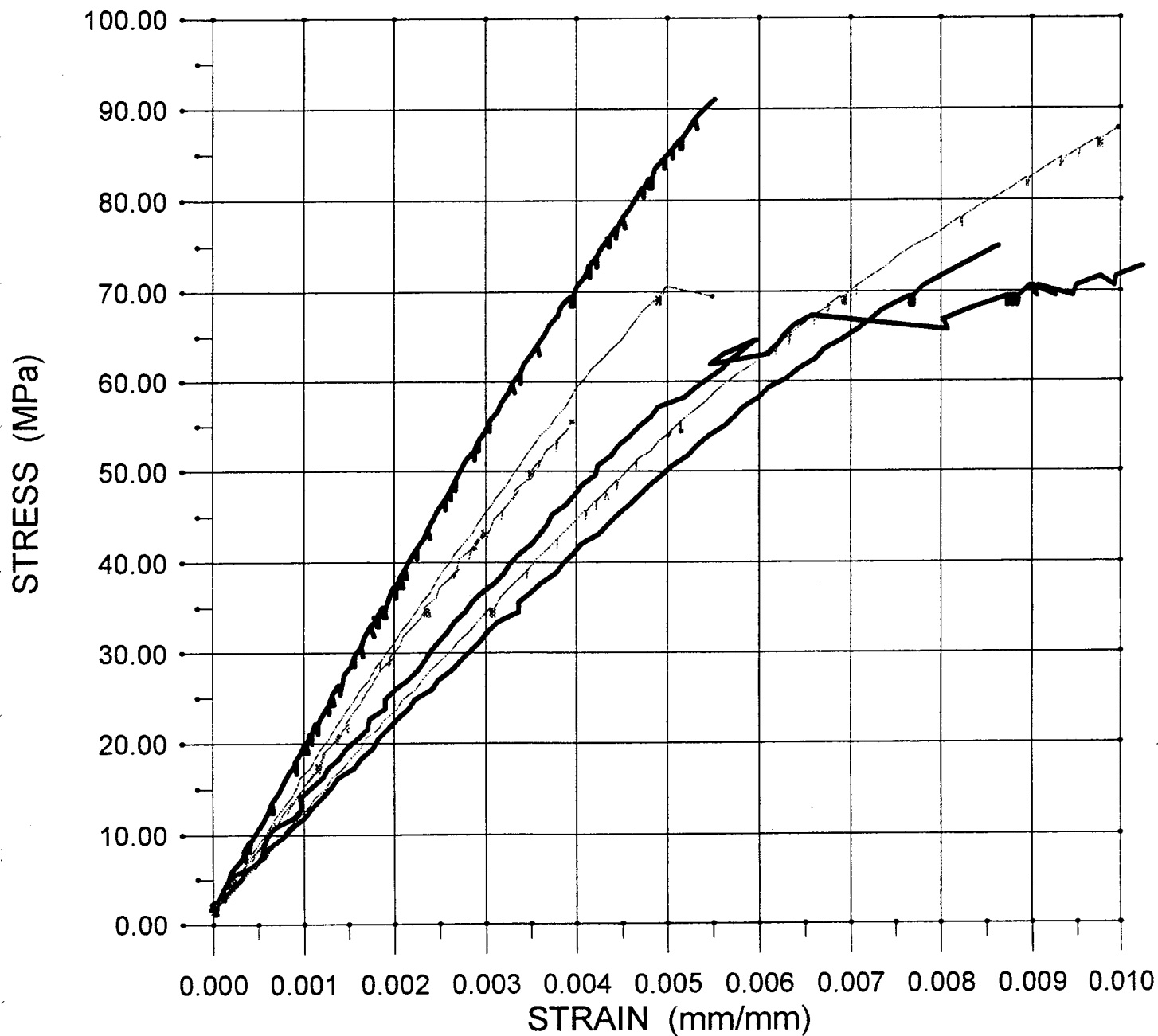
Appendix III

<u>TEST EQUIPMENT LIST</u>

TENSILE TEST EQUIPMENT: All tensile testing was accomplished in the mechanics laboratory of the Air Force Institute of Technology, Wright-Patterson AFB, Ohio.

	<u>DESCRIPTION</u>	<u>PART #</u>
Apparatus	MTS 110 kips Hydraulic Press	810
	MTS Hydraulic Grips	641.37
Controllers	MTS MicroConsole™	458.20
	MTS MicroProfiler™	458.91
	MTS DC Controller (load, strain)	458.11
	MTS AC Controller (head displacement)	458.13
Transducers	MTS 110 kips Load Cell	661.23C-01
	MTS Needle Extensometer (.5 in gage) with Ceramic Rods	632.53E-04
Other Equipment	Omega Solid State Temperature/Humidity Recorder	CT485 R5
	Zenith 248 Personal Computer (data collection)	

Advanced Polymer Processing
and
Mold Design

Christopher L. Frank

US AIR FORCE ADVANCED COMPOSITES PROGRAM OFFICE
SM-ALC/TIEC BUILDING 243
5201 Bailey Loop, McClellan AFB CA 95652-2514

ABSTRACT

An overview of processing methods and machinery required to mold Advanced Polymer Components (APC) is presented. Also the effects of mold design and process on the final product will be described.

INTRODUCTION

What most people think of when you mention plastics are toys or broken pens. These articles are made from commodity plastics that when compared to engineering plastics tend to be lower in cost and are often lower in strength as well. This lower strength will effect the performance of the resulting parts. Engineering plastics have enhanced structural properties and higher service temperatures. New advanced engineering polymers are challenging many traditional metal applications. With new materials being developed and introduced many applications that were previously out of reach for plastics can now be conquered. The possibilities seem to be limited only by your imagination.

What is injection molding? Injection molding is a manufacturing process widely accepted for high production of plastic parts. In general the type of plastic used in this process is thermoplastic, meaning that it can be reformed by the application of heat. The two key pieces of equipment required are 1. The mold or die as it sometimes referred to and 2. The injection molding machine. (fig. 1) The machine heats the plastic to its melting point by electrical and mechanical heating, this is done in the injection unit (fig. 2) with a rotating screw located inside the barrel. The machine then forces the molten plastic into the mold using the screw as a ram.
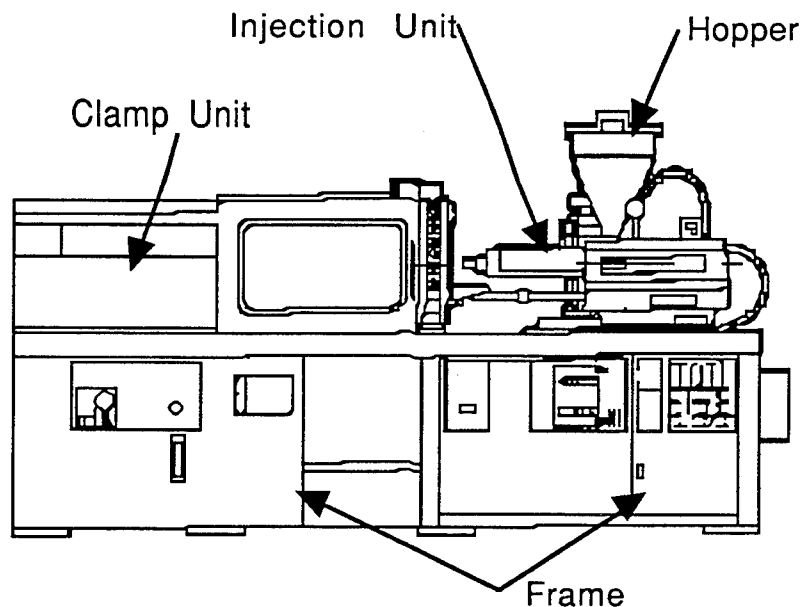
Figure 1

This force is sometimes very high (as much as 20,000 psi.) Therefore a large clamping force is required to keep the mold from opening or deforming while the plastic is being forced into the mold. The clamp section of the machine is designed to maintain uniform pressure on the mold to keep it closed and in place. (fig. 3)
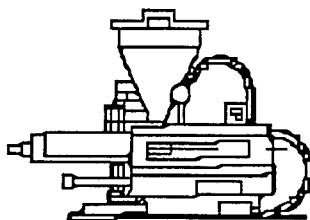
TYPICAL INJECTION UNIT
Figure 2

After the plastic is injected into the mold the clamping force keeps the mold closed until the plastic cools. The mold is then opened and the molded parts are removed by hand or by a mechanical ejection system. All of this happens each time a part is molded.
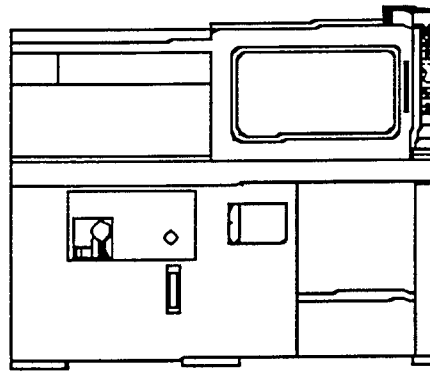
CLAMP SECTION OF MACHINE
Figure 3

The mold which defines the part, usually made of steel, this item must retain it's shape while being subjected to extreme pressures and temperatures. The mold is a nearly solid block of metal. In the center is a cavity which defines the shape of the part. The tool must withstand hundreds or thousands of cycles of opening and closing, heating and cooling during which it must maintain all the accurate dimensions.

Using this process, very intricate parts can be made, as thin as .010 of an inch with a high degree of detail. What really controls the intricacy of the part is the mold, of course the more detailed the part, the more detailed the tool and the more expensive it becomes. If the number of parts to be molded is small, aluminum can be used but if a large number of parts are required or the tool has sliding details or actions then steel is the only choice.

The most striking advantage of injection molding is repeatability over large numbers of parts and the detail that can be included in the primary process of molding. A good deal of details such as tabs, holes, and threads can be defined at molding thereby reducing the amount of post processing required. Also after the tooling is paid for the cost per part for manufacturing remains relatively low. Molds can be of three styles; Manual, Semi-automatic and Automatic Dies. The factors in determining style are quantity of job and cost. Manual dies are usually a single cavity and are put together and removed by hand. This is a time consuming operation. The mold has to be assembled and disassembled by hand, while the parts are cooling in the die. These dies are best suited to very short runs less than 25 parts. Typically these would run on a small prototyping

machine. Semi-Automatic dies are more cost effective. They require less manual operations and part production is faster. These dies require an ejection system and a sprue puller and are more expensive to build because of the mechanical operation involved. These dies are best suited to mid-range runs of more than 100 parts and up to thousands. Automatic dies are the most expensive die to build. These dies require ejection, sprue puller, runner system, heating and/or cooling system and usually more than one cavity (see fig. 4).
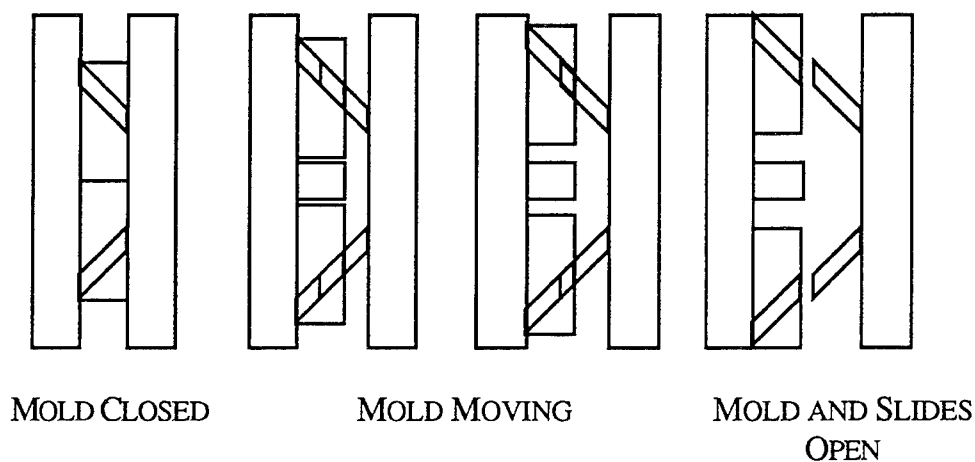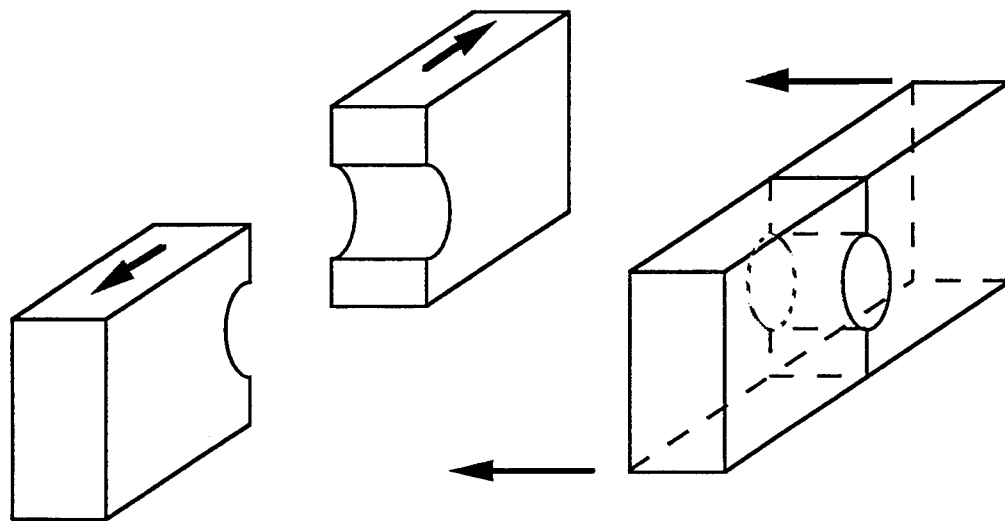
MOLD CLOSED   MOLD MOVING   MOLD AND SLIDES
                                            OPEN
MOVEMENT OF THE SLIDES IN AN AUTOMATIC MOLD
Figure 4

What are the limitations of this process? Not to be glib, but I would say only your imagination! Seriously, if we can fit it in a mold that will run on any of several DOD machines and the end application

temperatures and strengths are compatible with the chosen material almost any part can be molded.

PROCESSING

Once a mold for the motors was built, an injection molding process had to be developed using current commercial data, and information based on previous test results. The resulting molding process cycle produced acceptable parts and follows most of the manufacturers recommendations. A typical injection speed profile is shown below(fig. 5).
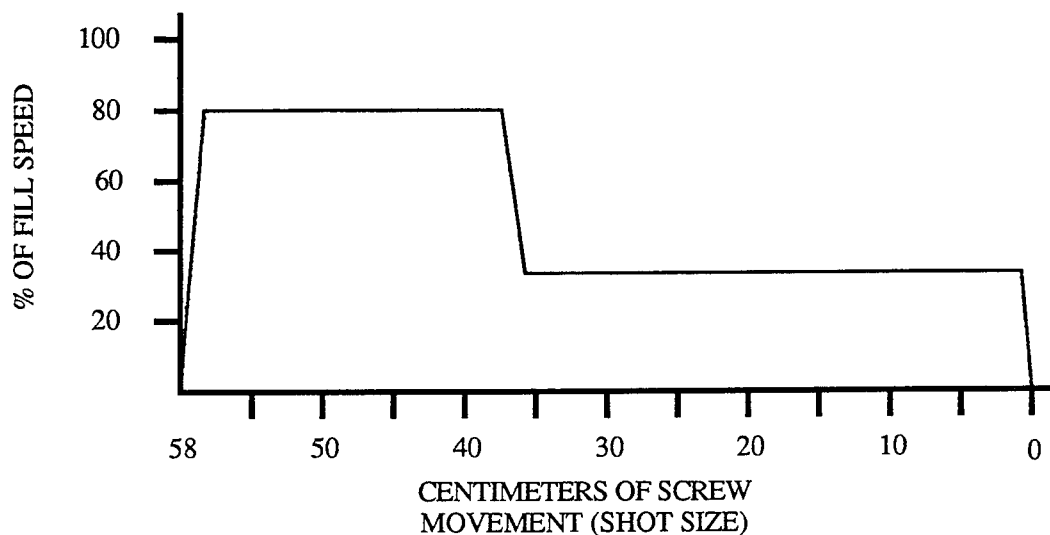
CENTIMETERS OF SCREW
MOVEMENT (SHOT SIZE)
Figure 5

THE RESULTS

Compared with typical injection molding runs, a very small number of articles (approx. 50 of each material) were produced. For this reason a fully developed process may not have been achieved. This may have resulted in the production of articles with less strength than was mathematically predicted. We felt that the drooling in the mold contributed to some of the lower test results. Due to those results new motors will be produced and new tests will be performed. In spite of this, the results remain quite impressive for a thermoplastic as are shown elsewhere in this report.

Without a doubt teamwork is a key element of any project. Doug Bennet, Richard Griffin and the others are very supportive of the projects we work on and often provide great insights for myself and

other engineers on machining and tooling. We couldn't ask for a better group of people to work with than these folks.

There is an additional process that is of interest to the APC group, stretch blow molding. In this process a preform is injection molded usually in the form of a test tube shape. (fig. 6)
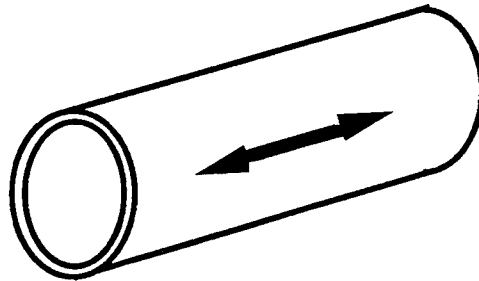
AN INJECTION MOLDED TUBE HAS LONGITUDINAL
ORIENTATION AND STRENGTH
Figure 6

The preform is then heated and blown to shape inside a larger tool stretching the tube like a balloon, thus producing the stretch in the hoop direction. (fig. 7) This process is currently used to produce 1 and 2 liter soda bottles out of PET material. Using LCPs it is hoped that this process could produce pressure vessels for fuel or gaseous storage.

STRETCHED/BLOWN
ALIGNMENT
STRENGTH

MOLDED ALIGNMENT
STRENGTH
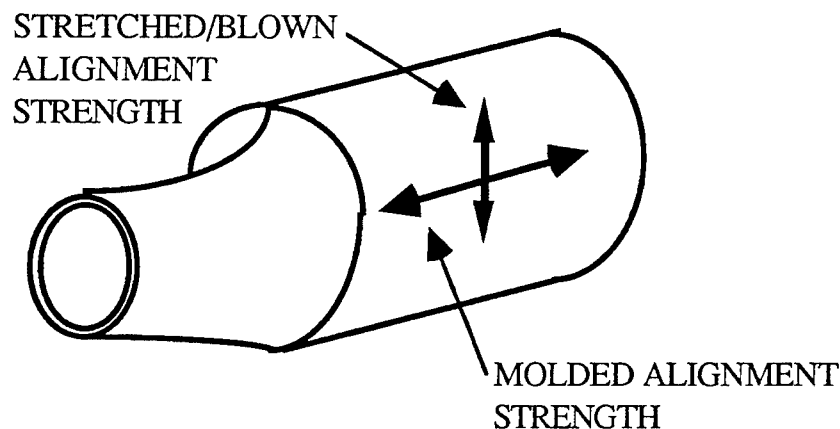
ONCE THE TUBE IS BLOWN THE RESULT IS HOOP AND
LONGITUDINAL ORIENTATION AND STRENGTH
Figure 7

DEPARTMENT OF THE NAVY

NAVAL AIR WARFARE CENTER
WEAPONS DIVISION
CHINA LAKE, CALIFORNIA 93555-6001

IN REPLY REFER TO:

3960
C2772/097
20 Oct 93

MEMORANDUM

From: Buck Guest, Composites & Plastics Section (Code C27721)
To: Alan Gehris, Solid Propulsion Branch (Code C2774)
Via: Head, Composites & Plastics Section (Code C27721)

Subj: FINAL REPORT OF PREDATOR MOTORCASE ADHESIVE BONDING SCREEN

Ref: (a) Memorandum, Guest to Gehris, Dated 27MAY93
(b) ASTM D 3165-91, Standard Test Method for Strength Properties of Adhesives in Shear by Tension Loading of Single-Lap-Joint Laminated Assemblies
(c) ASTM D 2093-84, Standard Practice for Preparation of Surfaces of Plastics Prior to Adhesive Bonding
(d) ASTM D 2651-90, Standard Guide for Preparation of Metal Surfaces for Adhesive Bonding
(e) MIL-A-8625, Cl. II, Ty. I, Anodic Coatings for Aluminum & Aluminum Alloys
(f) ASTM D 1002-72, Standard Test Method for Strength Properties of Adhesives in Shear by Tension Loading (Metal-to-Metal)
(g) ASTM D 3163-91, Standard Test Method for Determining Strength of Adhesively Bonded Rigid Plastic Lap-Shear Joints in Shear by Tension Loading

Encl: (1) Test Specimen Configuration
(2) PPA ASTM D 3039 Tensile Dogbone Data
(3) Hardman (Blue) PPA-PPA Tensile Shear Test Data (Unsupported)
(4) Loctite 414 PPA-PPA Tensile Shear Test Data (Unsupported)
(5) Shell Epon 828/Versamid #140 PPA-PPA Tensile Shear Test Data (Unsupported)
(6) Hysol 9340 PPA-PPA Tensile Shear Test Data (Unsupported)
(7) RF 1738 PPA-PPA Tensile Shear Test Data (Supported & Unsupported)
(8) RF 1738 Al-PPA Tensile Shear Test Data (Supported & Unsupported)
(9) Hysol 9309.3 PPA-PPA Tensile Shear Test Data (Supported & Unsupported)
(10) Hysol 9309.3 Al-PPA Tensile Shear Test Data (Supported & Unsupported)
(11) Hysol 9330.3 PPA-PPA Tensile Shear Test Data (Supported & Unsupported)
(12) Hysol 9330.3 Al-PPA Tensile Shear Test Data (Supported & Unsupported)

1. This work was a follow up to work previously completed and documented per ref. a. The previous work was a cursory screen designed to quickly screen two available adhesives: Resin Formulators RF-5160 and Dexter-Hysol EA-9394. The former was a one part urethane, the latter a two component epoxy. Results of the initial work was indeterminate due to adhesive curing temperatures, later found to be, incompatible with a live grain. This final work was more systematic in approach and application. It acted on some of the recommendations from the ref. a work. Additionally, the test specimen configuration was changed to that described by enclosure 1. Specimen configuration was changed to improve accuracy, repeatability and to hasten specimen production rates.

Subj: FINAL REPORT OF PREDATOR MOTORCASE ADHESIVE BONDING SCREEN

2. The adhesive screen had four objectives:

* Bond the compression molded phenolic nozzle into the aft end of the flight motorcase
* Bond the Al alloy forward closure into the case
* Demonstrate tensile shear strength in excess of 1700 PSI for Al & PPA substrates
* Demonstrate, via hydrostatic testing, motorcase breaking bonds

These objectives will be achieved without archaic use of cheater fasteners.

3. Success criteria included satisfying the 1.1 Mean Expected Operating Pressure MEOP (1595 PSI) hydrostatic test requirement or failure of the motorcase material, whichever was less.

4. Three adhesives were screened based on the following requirements:

* Demonstrate >1700 PSI in tensile shear
* Cure between room temperature-140°F
* Bond well to PPA & Al
* High elongation to failure, ~2%
* Demonstrate consistent bond performance as a function of variable bondline thickness

Four additional adhesives were tested because they were either cheap, available or fresh.

5. The major assumption made during this test was that bond performance between PPA adherends approximates that of PPA-phenolic adherends.

6. The adhesive candidates and cure conditions were as follows:

Adhesive	Chemistry	Cure Schedule
Hardman (Blue)	Urethane, 2 Component	Room Temperature
Loctite #414	Cyanoacrylate	Room Temperature
Shell Epon 828/Versamid #140	Epoxy	140°F, 2 Hours
Hysol 9340	Epoxy, 2 Part	Room Temperature
Hysol 9309.3	Epoxy, 2 Part	140°F, 2 hours
Hysol 9330.3	Epoxy, 2 Part	140°F, 2 hours
RF 1738-2	Urethane, 2 Component	140°F, 2 Hours

The last three adhesives, listed above, were of primary concern as they are high performance structural adhesives capable of meeting the adhesive requirements.

7. Test specimens were configured per ref. b, and illustrated by enclosure 1. While numerous joint configurations were referenced (ref. (f) & (g)), this joint was selected because it closely simulated the joint configuration of the predator motorcase. As such, it can be used to develop design allowables. Additionally, this joint allowed for rapid assembly and machining which was critical throughout the experiment. Bondline thickness was nominally set for 0.0045". This was set by simply using masking tape to establish the bondline. It worked well as it allowed for easy and rapid assembly. Final bondline thickness and variation was a function of the adhesive and was noted in each enclosure.

2

8. The adherends were prepared using ref. c and ref. d as a guide. Ref. d contains a callout for sulfuric anodizing, per ref. e, for non-clad Al adherends. This step was not completed as the Al forward closure did not receive a conversion coating. It was important the test joint configuration closely represent the actual service joint. Adherend preparation was the most time consuming part of the task as it required patience and spotless prep and assembly areas. All specimens were solvent wiped w/ 1,1,1-trichloroethane until the wiping rag remained clean. An abrasive blast treatment of all faying surfaces was next. The adherends were then treated to a hot soap and water scrub and rinse. At this point, the specimens were tested for a water break free surface. They were then oven dried @ 120°F for an hour. Subsequent to drying, numerous samples were randomly selected and again tested for water break. All passed, indicating the surface to be clean and chemically active.

9. Al adherends rapidly form an invisible oxide film which degrades adhesive bond performance. To minimize this, specimen assembly was completed within 2 hours (usually w/in 1 hour) of final preparation. Had the adherends been sulfuric anodized, oxidation would not be an issue. Specimens were assembled and machined using a locally manufactured assembly and machining jig. These shop aids greatly improved throughput and specimen quality.

10. Specimens were tested by the Metallic Material Section, Code C25471. They were tested at room temperature at a crosshead speed of 0.050"/minute. The specimens, where noted, were tested with an ASTM D 695 compression fixture clamped to the specimen, 1 in-lb at one end, zero clearance at the other end. The D 695 fixture was used to quantify the difference between apparent and true shear stress among specimens. The results of this test was significant and is discussed with the data.

11. To achieve baseline tensile properties, five injection molded tensile dogbones were tested. Results are listed as enclosure 2. These specimens were highly consistent as expected. Average tensile strength was ~43,000 PSI v 46,000 PSI per manufacturers data. Standard deviation among specimens was ~2.2%. Less confidence was placed in the modulus measurements, standard deviation among specimens was ~18%. Modulus was measured with an extensometer. It was possible that the knife edges may have moved slightly. Tensile modulus was ~5 MSI v 5.5 MSI per manufacturers data.

12. Hardman (Blue) urethane was tested PPA-PPA. As this adhesive was not of primary importance, only three specimens were tested. Test results were as expected and are listed as enclosure 3. Lap shear averaged ~2100 PSI with a low standard deviation of ~5%. Failure mode was ~50/50 cohesive and adhesive, respectively. Bondline thickness ranged from 0.010"-0.012".

13. Loctite 414 was tested and reported as enclosure 4. Three specimens were tested, PPA-PPA, for the same reason as para 12. It performed better than expected, lap shear values averaging ~2000 PSI. Standard deviation was wider, ~ 16%. Failure mode was ~75/25 cohesive and adhesive, respectively. Bondline thickness ranged from 0.0025"-0.005".

14. A mixture of Shell Epon 828 50% catalyzed w/ Versamid #140 was tested PPA-PPA. This adhesive did not perform nearly as well as expected based on previous experience. Shear strength, reported in enclosure 5, averaged 1100 PSI. Failure mode was an ideal 100% cohesive on two specimens and indeterminate on the third. Standard deviation was ~2.5%. Bondline thickness ranged from 0.010"-0.012". Previous experience with this adhesive predicted lap shear of ~3000-4000 PSI, depending on adherend composition.

15. Hysol 9340 was tested PPA-PPA and reported as enclosure 6. Lap shear, based on three specimens, averaged ~1400 PSI. Standard deviation was a close 2.3%. Failure mode ranged from 75-90 % cohesive. Bondline thickness varied from 0.005"-0.0075".

16. Resin Formulators #1738 was tested PPA-PPA, both supported with the ASTM D 695 fixture and unsupported. Five specimens were tested supported, three specimens unsupported. RF-1738 is composed of two low viscosity components which formed a thick gel immediately upon mixing. Resulting bondline thickness ranged from 0.014"-0.020". Test results are included as enclosure 7. Lap shear strength (supported) averaged ~2100 PSI w/ ~13% standard deviation. Failure mode was universally poor, 100% adhesive. This adhesive proved a disappointment, as it was highly recommended and previous positive experience w/ single component urethanes. The adhesive failure mode was largely responsible for the low lap shear values. Perhaps an alternate joint preparation schedule would allow this adhesive to perform to expectations. The adhesive performed poorly regardless of adherend composition. Lap shear strength (unsupported) also averaged ~2100 PSI w/ ~11% standard deviation. Failure mode was also 100% adhesive. Bondline thickness ranged from 0.010"-0.016". This adhesive was deselected from further consideration due to time constraints.

17. Resin Formulators #1738 was then tested Al-PPA, both supported with the ASTM D 695 fixture and unsupported. Five specimens were tested supported, three specimens unsupported. Test results are included as enclosure 8. Lap shear strength (supported) averaged ~1800 PSI w/ ~21% standard deviation. Failure mode was 100% adhesive. Bondline thickness ranged from 0.018"-0.021". Lap shear strength (unsupported) averaged ~1600 PSI w/ ~17% standard deviation. Failure mode was 100% adhesive. Bondline thickness ranged from 0.015"-0.021".

18. Dexter-Hysol 9309.3 was tested PPA-PPA and performed as expected. Supported specimens, with a one inch lap length, demonstrated adherend breaking bonds. The adhesive was stressed to ~ 3800 PSI when the adherends failed. Data spread among these specimens was ~1.3%. Bondline thickness varied between 0.0045"-0.005". The lap shear specimens were prepared before the tensile specimens were tested. From previous experience it was expected the tensile specimens would fail at 23,000-25,000 PSI, instead they failed at 43,000 PSI. The last three specimens were tested unsupported and clearly illustrated the difference in lap shear values between supported and unsupported specimens. The unsupported specimens failed at ~1300 PSI with a data spread of ~2.5%. Bondline thickness varied between 0.0045"-0.006". The supported specimens recorded lap shear averages in excess of 3x greater than unsupported specimens. The difference between the two sets of data was due to the difference between true and apparent shear. As the unsupported specimens were put in tension the adherends deformed out-of-plane. This resulted in a combination of non uniform shear, tensile (normal), cleavage and peel stresses introduced into the bondline, especially at the ends of the overlap. The joint failed largely as a result of excessive tensile stress in the adhesive, not shear stress. This data was reported as enclosure 9.

19. To follow up on the work described by para. 18, Dexter-Hysol 9309.3 was tested Al-PPA . These specimens were prepared w/ 0.5" lap to stress the adhesive to failure while maintaining adherend integrity. Thicker adherends if available, would serve the same function. Additionally, they would reduce the difference in (apparent) lap shear values between the supported and unsupported specimens due to reduced out-of-plane deformation. With the 0.5" lap length, the supported specimens were able to shear the adhesive. This data is reported as enclosure 10. Supported specimens demonstrated average lap shear values of ~4300 PSI with a standard deviation of ~5%. Bondline thickness varied from 0.0045"-0.010". Failure mode ranged from 25-

45% cohesive. Unsupported specimens demonstrated ~2800 PSI average lap shear with a wider data spread of ~8.6%. Bondline thickness varied from 0.0045"-0.011". Failure mode ranged from 25-40% cohesive.

20. Dexter-Hysol 9330.3 was tested PPA-PPA and also performed as expected. Supported specimens universally broke the motorcase material before the adhesive was stressed to ultimate. These specimens were also prepared before the tensile specimens were tested. The adhesive was stressed to ~ 3900 PSI when the adherends failed. Data spread among these specimens was ~1.3%. Bondline thickness varied between 0.004"-0.009". Specimen #5 demonstrated a wedge shaped bondline which varied from 0.004"-0.012". This was a workmanship error. Regardless, it still failed the motorcase material @ 3968 PSI. Specimens #6-#8 were tested unsupported and also illustrated the difference in lap shear values between supported and unsupported specimens. The unsupported specimens failed at ~1300 PSI with a data spread of ~6.2%. Bondline thickness varied between 0.006"-0.010". The supported specimens also recorded lap shear averages in excess of 3x greater than unsupported specimens. The difference between the two sets of data was explained in para. 18. This data was provided as enclosure 11.

21. Dexter-Hysol 9330.3 was tested Al-PPA . These specimens were prepared w/ 0.5" lap. Supported specimens demonstrated average lap shear values of ~4000 PSI with a standard deviation of ~4.7%. Bondline thickness varied from 0.006"-0.008". Failure mode was 100% adhesive for most specimens. Specimen #6 was substituted when specimen #5 was destroyed in machining. Two unsupported specimens, #7 &#8, demonstrated ~2800 PSI average lap shear with a data spread of ~1.7%. Bondline thickness varied from 0.0011"-0.015". Failure mode ranged 80-85% cohesive. This data was provided as enclosure 11. This completed the mechanical testing.

22. All references to standard deviations and coefficients of variation should be used only as an indicator of process control. The sample population was too small to be construed as hard statistical data.

23. Of the primary adhesives screened, two of them met or exceeded the objectives set forth in para. 2. These adhesives were both Dexter Hysol: EA 9330.3 & EA 9309.3.

24. To validate the experiment two flight motorcases were assembled for hydrostatic testing. One motorcase was prepared as net molded, the other was filament wound with two layers of S-2 glass tow wetted with Shell Epon 826. One layer was a hoop, the other an ~22° helical. The Epon 826 was catalyzed with 80-90 phr Nadic Methyl Anhydride and accelerated with 0.5 phr 2-Ethyl-4-Methyl Imidizole. The resin mixture was step cured culminating in a 250°F cure. EA 9309.3 was chosen to bond in both the phenolic nozzle and the forward closure. All components were prepared duplicating the process of the test coupons. Assembly was straight forward except for the glass wound case. The filament overwound case was cured at the glass transition temperature of the motorcase. Three to five pounds of winding tension caused deformation at the open end of the case resulting in a 0.007" out-of-round condition. This does not sound like much, but it meant the difference between scraping off the adhesive or having a liquid shim in lieu of a bondline. Additionally, significant disbonds were apparent, both visually and on x-ray, between the S-2 windings and the motorcase. The disbond, of ~0.009", was due to the high coefficient of thermal expansion (~1.2E-5 in/in/°F) of the motorcase material. Approaching the gelation temperature, the resin began to fuse which effectively locked the S-2 tows at a larger diameter. Upon cooling, the motorcase contracted resulting in disbonds between the case and windings. Assembling this case required machining the forward closure ~0.006" to eliminate an interference fit caused by the out-

of-round condition. Resulting bondlines for both cases ranged 0.007"-0.014". Nominal bond line for the nozzle end was 0.008" for both cases. The cases were instrumented with strain gages, installed in the test rig, LVDT's positioned and tested hydrostatically.

25. The S-2 glass wrapped case failed, due to rupture of the motorcase material, @ 1075 PSI. The net molded case failed, also due to rupture of the motorcase, @ 1094 PSI.

26. In summary, the Hysol EA 9309.3 achieved or exceeded each objective in this phase of the test program. The experiment demonstrated on two test articles that the bonded joint possessed sufficient margin to fail the motorcase material. The fact that the glass wrapped case failed at a slightly lower case load than the net molded case was statistically meaningless. However, the success criteria of satisfying the 1.1 MEOP requirement was not demonstrated.

27. The following actions are recommended for the next phase of the program:

*   Select a room temperature or low elevated (<160°F) cure resin to eliminate case distortion and disbonds, assuming a fiber overwrap is required at all

*   Rework mold core and cavity to incorporate pending configurational improvements

*   Conduct moisture & chemical resistance, durability and accelerated adhesive aging tests

*   Improve case performance to adequately test bonded joint integrity to 1.1 MEOP

BUCK GUEST

Copy to:

C2774 (Pritchard)
C2547 (Kline, Kauffman)
C2711 (Heumann)
C2891 (Sanford, Hicks)
Edwards, AFB (Dr. Rusek)
McClellan, AFB (Chris Frank)
Naval Surface Warfare Center (Rinco)

Test Specimen Configuration

* Based on ASTM D 3165-91

* Supported & Unsupported w/ ASTM D 695 Fixture

0.25"

0.0045" Nominal Bondline

0.75"

0.5"   PPA-to-PPA or PPA-Al Adherend

R3.0"

8.0"

.125
TYP

.031
TYP

.062

.250

1.000

.250
TYP

.125
TYP

.281 DRILL THRU
(4 PLACES)

.500
TYP

GR

GR

2.000

.062 R

TYP

2.750

ASTM D 695 Fixture

.500

.500

.250

1.500

463

Enclosure 1
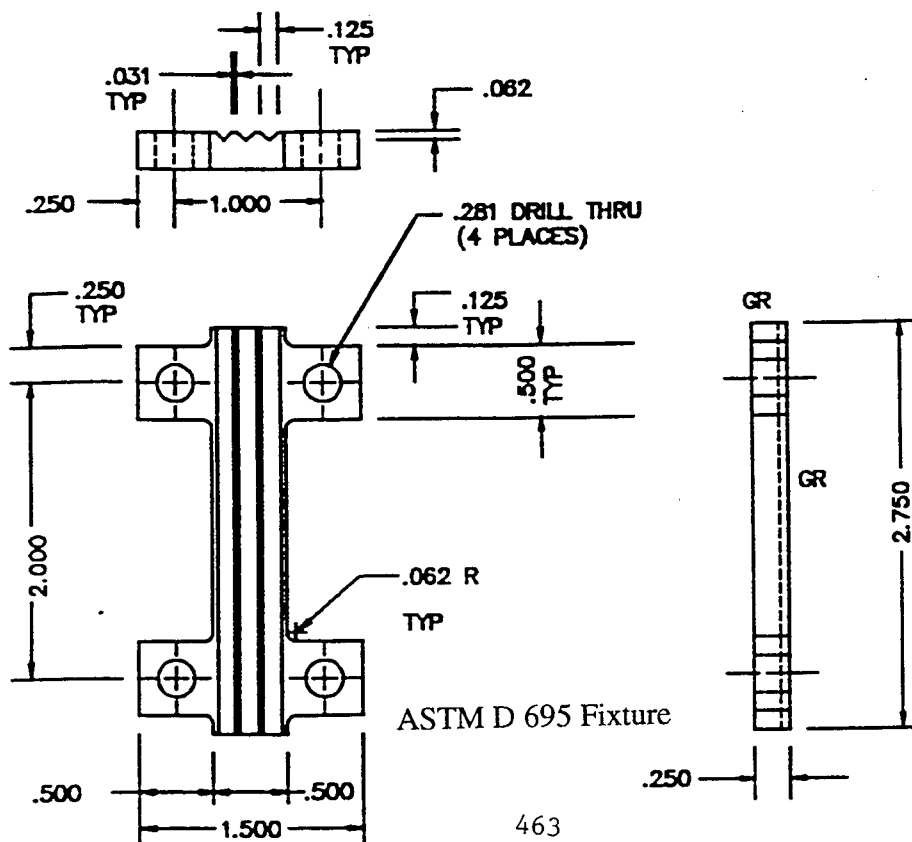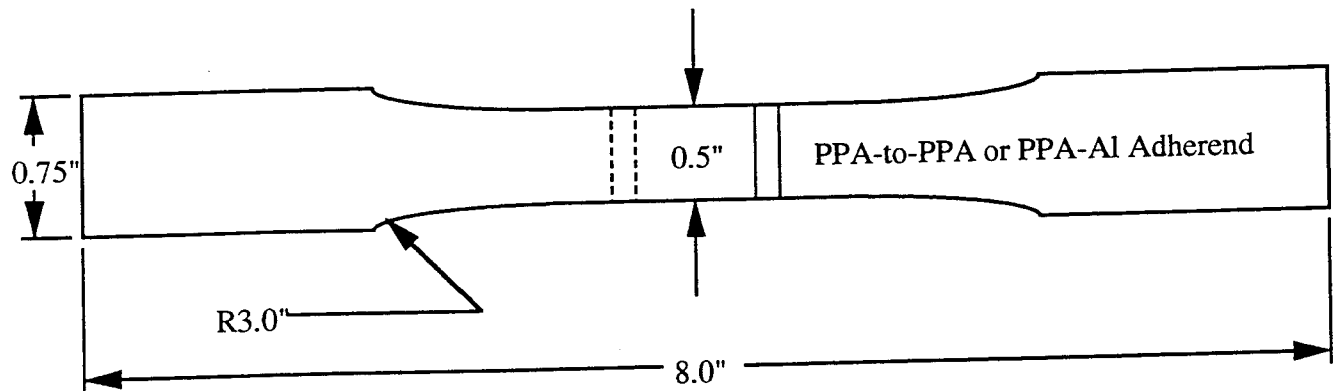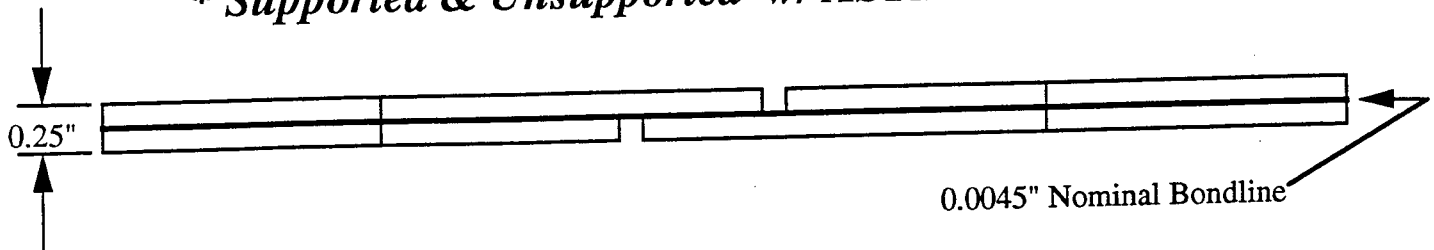
ADHEREND TENSION TEST RESULTS

REQUESTER   BUCK GUEST
  CODE   C27721
 PHONE   939-8897
   JO   1270803FYH
 MATERIAL   ADHEREND: PPA 40% CARBON FILLED INJECTION MOLDED
  DATE   8/16/93

TENSILE TEST RESULTS IN ACCORDANCE WITH ASTM D3039

SAMPLE	WIDTH INCHES	THICKNESS INCHES	AREA SQ IN	MAX LOAD LBS	MAXIMUM TENSILE STRENGTH PSI	DELTA LOAD LBS	DELTA STRAIN IN/IN	TENSILE MODULUS MSI
T-1	0.4910	0.1200	0.0589	2500	42,430	1000	0.0038	4.47
T-2	0.4915	0.1200	0.0590	2600	44,083	5000	0.0146	5.81
T-3	0.4915	0.1200	0.0590	2500	42,387	2000	0.0057	5.95
T-4	0.4920	0.1200	0.0590	2580	43,699	2000	0.0077	4.40
T-5	0.4910	0.1200	0.0589	2620	44,467	2000	0.0084	4.04

AVERAGE					43,413			4.93
STANDARD DEVIATION					956			0.88
COEFFICIENT OF VARIATION					2			18

C. F. KLINE JR.
C25471
939-1945

SHEAR BY TENSION OF SINGLE-LAP-JOINT TEST RESULTS

REQUESTER   BUCK GUEST
CODE   C27721
PHONE   939-8897
JO   1270803FYH
MATERIAL   ADHERENDS: PPA 40% CARBON FILLED INJECTION MOLDED
            ADHESIVE: HARDMAN BLUE, 2 PART URETHANE, ROOM TEMPERATURE OVERNIGHT CURE
DATE   8/16/93

PPA - PPA

SPECIFICATION: ASTM D3165

SAMPLE	BONDLINE THICKNESS INCHES	WIDTH INCHES	LENGTH INCHES	AREA SQ IN	MAX LOAD LBS	MAXIMUM SHEAR STRENGTH PSI	NATURE OF FAILURE % COHESIVE	% ADHESIVE
U-1	0.010	0.4975	1.0050	0.5000	1000	2,000	50	50
U-2	0.012	0.4960	1.0060	0.4990	1040	2,084	50	50
U-3	0.012	0.4980	1.0050	0.5005	1100	2,198	50	50
AVERAGE					1,047	2,094		
STANDARD DEVIATION					50	99		
COEFFICIENT OF VARIATION					5	5		

C. F. KLINE JR.
C25471
939-1945

REQUESTER   BUCK GUEST
    CODE   C27721
   PHONE   939-8897
      JO   1270803FYH
MATERIAL   ADHERENDS: PPA 40% CARBON FILLED INJECTION MOLDED
            ADHESIVE: LOCTITE SUPERBOND 414 CYANOACRYLATE ESTER, 1 PART, ROOM
                          TEMPERATURE OVERNIGHT CURE
    DATE   8/16/93

PPA - PPA

SPECIFICATION: ASTM D3165

SAMPLE	BONDLINE THICKNESS INCHES	WIDTH INCHES	LENGTH INCHES	AREA SQ IN	MAX LOAD LBS	MAXIMUM SHEAR STRENGTH PSI	NATURE OF FAILURE % COHESIVE	% ADHESIVE
414-1	0.0050	0.4980	1.0000	0.4980	1125	2,259	75	25
414-2	0.0025	0.4970	1.0020	0.4980	980	1,968	75	25
414-3	0.0040	0.4980	1.0070	0.5015	820	1,635	75	25
AVERAGE					975	1,954		
STANDARD DEVIATION					153	312		
COEFFICIENT OF VARIATION					16	16		

C. F. KLINE JR.
C25471
939-1945

ENCL (4)
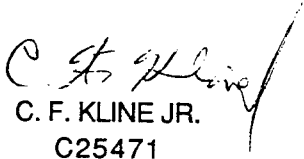
SHEAR BY TENSION OF SINGLE-LAP-JOINT TEST RESULTS

REQUESTER   BUCK GUEST
    CODE   C27721
    PHONE   939-8897
    JO   1270803FYH
    MATERIAL   ADHERENDS: PPA 40% CARBON FILLED INJECTION MOLDED
        ADHESIVE: SHELL EPON 828 EPOXY, CATALYZED WITH VERSAMID #140, 1:1 RATIO,
            CURE 140°F OVERNIGHT
    DATE   8/16/93

PPA - PPA

SPECIFICATION: ASTM D3165

SAMPLE	BONDLINE THICKNESS INCHES	WIDTH INCHES	LENGTH INCHES	AREA SQ IN	MAX LOAD LBS	MAXIMUM SHEAR STRENGTH PSI	NATURE OF FAILURE % COHESIVE	% ADHESIVE
828-1	0.012	0.5000	1.0000	0.5000	570	1,140	100	0
828-2	0.010	0.4980	1.0000	0.4980	540	1,084	?	?
828-3	0.012	0.4980	1.0050	0.5005	550	1,099	100	0

AVERAGE   553   1,108
STANDARD DEVIATION   15   29
COEFFICIENT OF VARIATION   3   3

C. F. KLINE JR.
C25471
939-1945

ENCL (5)

REQUESTER   BUCK GUEST
CODE   C27721
PHONE   939-8897
JO   1270803FYH
MATERIAL   ADHERENDS: PPA 40% CARBON FILLED INJECTION MOLDED
            ADHESIVE: HYSOL 9340, 2 PART EPOXY, 1:1 RATIO, CURE 140°F 2 HOURS
DATE   8/16/93

PPA - PPA

SPECIFICATION: ASTM D3165

SAMPLE	BONDLINE THICKNESS INCHES	WIDTH INCHES	LENGTH INCHES	AREA SQ IN	MAX LOAD LBS	MAXIMUM SHEAR STRENGTH PSI	NATURE OF FAILURE % COHESIVE	% ADHESIVE
9340-1	0.0075	0.4970	1.0000	0.4970	700	1,408	90	10
9340-2	0.0050	0.4980	1.0050	0.5005	710	1,419	75	25
9340-3	0.0070	0.4970	1.0000	0.4970	675	1,358	90	10
AVERAGE					695	1,395		
STANDARD DEVIATION					18	32		
COEFFICIENT OF VARIATION					3	2		

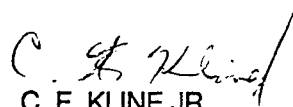C. F. KLINE JR.
C25471
939-1945

ENCL (6)

SHEAR BY TENSION OF SINGLE-LAP-JOINT TEST RESULTS

REQUESTER BUCK GUEST
CODE C27721
PHONE 939-8897
JO 1270803FYH
DATE 9/3/93
MATERIAL ADHERENDS: PPA 40% CARBON FILLED INJECTION MOLDED
ADHESIVE: RESIN FORMULATORS #RF 1738, 2 PART URETHANE, 1:2 RATIO,
CURE 140°F OVERNIGHT

PPA - PPA

**SPECIFICATION: ASTM D3165 AND USING ASTM D695 FIXTURE TO MAINTAIN
SAMPLE STRAIGHTNESS**

SAMPLE	BONDLINE THICKNESS INCHES	WIDTH INCHES	LENGTH INCHES	AREA SQ IN	MAX LOAD LBS	MAXIMUM SHEAR STRENGTH PSI	NATURE OF FAILURE % COHESIVE	% ADHESIVE
1738-1	0.017	0.4960	0.5080	0.2520	400	1,588	0	100
1738-2	0.017	0.4960	0.5130	0.2544	560	2,201	0	100
1738-3	0.014	0.4970	0.5060	0.2515	560	2,227	0	100
1738-4	0.016	0.4970	0.5060	0.2515	570	2,267	0	100
1738-5	0.020	0.4960	0.5080	0.2520	545	2,163	0	100
AVERAGE					527	2,089		
STANDARD DEVIATION					72	283		
COEFFICIENT OF VARIATION					14	14		

SAME AS ABOVE EXCEPT NO FIXTURE USED

SAMPLE	BONDLINE THICKNESS INCHES	WIDTH INCHES	LENGTH INCHES	AREA SQ IN	MAX LOAD LBS	MAXIMUM SHEAR STRENGTH PSI	NATURE OF FAILURE % COHESIVE	% ADHESIVE
1738-6	0.010	0.4960	0.4990	0.2475	460	1,859	0	100
1738-7	0.014	0.4960	0.5110	0.2535	585	2,308	0	100
1738-8	0.016	0.4950	0.5140	0.2544	565	2,221	0	100
AVERAGE					537	2,129		
STANDARD DEVIATION					67	238		
COEFFICIENT OF VARIATION					13	11		

C. F. KLINE JR.
C25471
939-1945

REQUESTER   BUCK GUEST
CODE   C27721
PHONE   939-8897
JO   1270803FYH

DATE   9/3/93
MATERIAL   ADHERENDS: PPA 40% CARBON FILLED INJECTION MOLDED
             AND 6061-T6 ALUMINUM
             ADHESIVE: RESIN FORMULATORS #RF 1738, 2 PART URETHANE, 1:2 RATIO,
             CURE 140°F OVERNIGHT

ALUMINUM - PPA

SPECIFICATION: ASTM D3165 AND USING ASTM D695 FIXTURE TO MAINTAIN SAMPLE STRAIGHTNESS

SAMPLE	BONDLINE THICKNESS INCHES	WIDTH INCHES	LENGTH INCHES	AREA SQ IN	MAX LOAD LBS	MAXIMUM SHEAR STRENGTH PSI	NATURE OF FAILURE % COHESIVE	% ADHESIVE *
A/P1738-1	0.020	0.4960	0.5080	0.2520	360	1,429	0	100
A/P1738-2	0.018	0.4960	0.5120	0.2540	590	2,323	0	100
A/P1738-3	0.021	0.4960	0.5090	0.2525	430	1,703	0	100
A/P1738-4	0.018	0.4960	0.5090	0.2525	515	2,040	0	100
A/P1738-5	0.020	0.4960	0.5030	0.2495	365	1,463	0	100

AVERAGE					452	1,792	
STANDARD DEVIATION					99	385	
COEFFICIENT OF VARIATION					22	21	

SAME AS ABOVE EXCEPT NO FIXTURE USED

SAMPLE	BONDLINE THICKNESS INCHES	WIDTH INCHES	LENGTH INCHES	AREA SQ IN	MAX LOAD LBS	MAXIMUM SHEAR STRENGTH PSI	NATURE OF FAILURE % COHESIVE	% ADHESIVE *
A/P1738-6	0.021	0.4960	0.5070	0.2515	470	1,869	0	100
A/P1738-7	0.015	0.4970	0.5110	0.2540	370	1,457	0	100
A/P1738-8	0.022	0.4960	0.5120	0.2540	350	1,378	0	100

AVERAGE					397	1,568	* FAILURES: ALUMINUM
STANDARD DEVIATION					64	264	TO ADHESIVE
COEFFICIENT OF VARIATION					16	17	

C. F. KLINE JR.
C25471
939-1945

REQUESTER   BUCK GUEST
CODE   C2891
PHONE   939-8897
JO   1270803FYH
MATERIAL   ADHERENDS: PPA 40% CARBON FILLED INJECTION MOLDED
            ADHESIVE: HYSOL EA 9309.3 N/A, 2 PART EPOXY, 100:22 RATIO, CURE 140°F OVERNIGHT
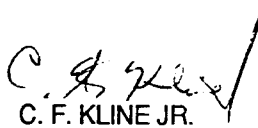DATE   8/19/93

PPA - PPA

SPECIFICATION: ASTM D3165 AND USING ASTM D695 FIXTURE TO MAINTAIN SAMPLE STRAIGHTNESS

SAMPLE	BONDLINE THICKNESS INCHES	WIDTH INCHES	LENGTH INCHES	AREA SQ IN	MAX LOAD LBS	MAXIMUM SHEAR STRENGTH PSI	NATURE OF FAILURE % COHESIVE	% ADHESIVE
9309.3-1	0.0045	0.4970	1.0060	0.5000	1930	3,860	ADHEREND FAILED IN TENSION	
9309.3-2	0.0050	0.4960	1.0040	0.4980	1880	3,775	ADHEREND FAILED IN TENSION	
9309.3-3	0.0045	0.4970	1.0040	0.4990	1920	3,848	ADHEREND FAILED IN TENSION	
9309.3-4	0.0050	0.4970	0.9960	0.4950	1870	3,778	ADHEREND FAILED IN TENSION	
9309.3-5	0.0050	0.4970	0.9940	0.4940	1920	3,886	ADHEREND FAILED IN TENSION	

AVERAGE   1,904   3,829
STANDARD DEVIATION   27   50
COEFFICIENT OF VARIATION   1   1

SAME AS ABOVE EXCEPT NO FIXTURE USED

SAMPLE	BONDLINE THICKNESS INCHES	WIDTH INCHES	LENGTH INCHES	AREA SQ IN	MAX LOAD LBS	MAXIMUM SHEAR STRENGTH PSI	NATURE OF FAILURE % COHESIVE	% ADHESIVE
9309.3-6	0.0050	0.4970	1.0010	0.4975	580	1,166	THESE THREE SAMLES DID NOT	
9309.3-7	0.0045	0.4970	1.0010	0.4975	670	1,347	PART COMPLETELY AND WERE	
9309.3-8	0.0060	0.4960	0.9970	0.4945	630	1,274	NOT EVALUATED	

AVERAGE   627   1,262
STANDARD DEVIATION   45   91
COEFFICIENT OF VARIATION   7   7

C. F. KLINE JR.
C25471
939-1945

REQUESTER BUCK GUEST
CODE C27721
PHONE 939-8897
JO 1270803FYH
MATERIAL ADHERENDS: PPA 40% CARBON FILLED INJECTION MOLDED
AND 6061-T6 ALUMINUM
ADHESIVE: HYSOL EA 9309.3 N/A, 2 PART EPOXY, 100:22 RATIO. CURE 140°F OVERNIGHT
DATE 8/26/93

ALUMINUM - PPA

**SPECIFICATION: ASTM D3165 AND USING ASTM D695 FIXTURE TO MAINTAIN
SAMPLE STRAIGHTNESS**

SAMPLE	BONDLINE THICKNESS INCHES	WIDTH INCHES	LENGTH INCHES	AREA SQ IN	MAX LOAD LBS	MAXIMUM SHEAR STRENGTH PSI	NATURE OF FAILURE % COHESIVE **	% ADHESIVE
A/P9309.3-1	0.0090	0.4960	0.5060	0.2510	1100	4,383	45	55
A/P9309.3-2	0.0100	0.4960	0.5020	0.2490	1030	4,137	30	70
A/P9309.3-3	0.0045	0.4960	0.5060	0.2510	1180	4,702	25	75
A/P9309.3-4	0.0060	0.4960	0.5010	0.2485	1050	4,225	25	75
A/P9309.3-5	0.0050	0.4960	0.5030	0.2495	1055	4,229	25	75
AVERAGE					1,083	4,335		
STANDARD DEVIATION					60	223		
COEFFICIENT OF VARIATION					6	5		

** COHESIVE FAILURE IN PPA

SAME AS ABOVE EXCEPT NO FIXTURE USED

SAMPLE	BONDLINE THICKNESS INCHES	WIDTH INCHES	LENGTH INCHES	AREA SQ IN	MAX LOAD LBS	MAXIMUM SHEAR STRENGTH PSI	NATURE OF FAILURE % COHESIVE **	% ADHESIVE
A/P9309.3-6	0.0045	0.4960	0.4910	0.2435	740	3,039	25	75
A/P9309.3-7	0.0110	0.4960	0.5090	0.2525	725	2,872	40	60
A/P9309.3-8	0.0100	0.4970	0.5030	0.2500	640	2,560	40	60
AVERAGE					702	2,823		
STANDARD DEVIATION					54	243		
COEFFICIENT OF VARIATION					8	9		

** COHESIVE FAILURE IN PPA

C. F. KLINE JR.
C25471
939-1945

REQUESTER BUCK GUEST
CODE C27721
PHONE 939-8897
JO 1270803FYH
DATE 9/3/93
MATERIAL ADHERENDS: PPA 40% CARBON FILLED INJECTION MOLDED
ADHESIVE: HYSOL 9330.3, 2 PART EPOXY, 100:33 RATIO,
CURE 140°F OVERNIGHT

PPA - PPA

SPECIFICATION: ASTM D3165 AND USING ASTM D695 FIXTURE TO MAINTAIN
SAMPLE STRAIGHTNESS

SAMPLE	BONDLINE THICKNESS INCHES	WIDTH INCHES	LENGTH INCHES	AREA SQ IN	MAX LOAD LBS	MAXIMUM SHEAR STRENGTH PSI	NATURE OF FAILURE % COHESIVE	% ADHESIVE
9330.3-1	0.0100	0.4960	1.0060	0.4990	1960	3,928	ADHEREND FAILED IN TENSION	
9330.3-2	0.0090	0.4960	1.0080	0.5000	1990	3,980	ADHEREND FAILED IN TENSION	
9330.3-3	0.0050	0.4960	0.9960	0.4940	1955	3,957	ADHEREND FAILED IN TENSION	
9330.3-4	0.0045	0.4960	1.0070	0.4995	1925	3,854	ADHEREND FAILED IN TENSION	
9330.3-5	0.004-0.012	0.4960	1.0060	0.4990	1980	3,968	ADHEREND FAILED IN TENSION	
AVERAGE					1,962	3,938		
STANDARD DEVIATION					25	51		
COEFFICIENT OF VARIATION					1	1		

SAME AS ABOVE EXCEPT NO FIXTURE USED

SAMPLE	BONDLINE THICKNESS INCHES	WIDTH INCHES	LENGTH INCHES	AREA SQ IN	MAX LOAD LBS	MAXIMUM SHEAR STRENGTH PSI	NATURE OF FAILURE % COHESIVE	% ADHESIVE
9330.3-6	0.006-0.010	0.4970	1.0040	0.4990	680	1,363	THESE THREE SAMLES DID NOT	
9330.3-7	0.0080	0.4970	1.0040	0.4990	600	1,202	PART COMPLETELY AND WERE	
9330.3-8	0.0090	0.4970	1.0030	0.4985	640	1,284	NOT EVALUATED	
AVERAGE					640	1,283		
STANDARD DEVIATION					40	80		
COEFFICIENT OF VARIATION					6	6		

C. F. KLINE JR.
C25471
939-1945

SHEAR BY TENSION OF SINGLE-LAP-JOINT TEST RESULTS

REQUESTER BUCK GUEST
CODE C27721
PHONE 939-8897
JO 1270803FYH
DATE 9/3/93
MATERIAL ADHERENDS: PPA 40% CARBON FILLED INJECTION MOLDED
AND 6061-T6 ALUMINUM
ADHESIVE: HYSOL 9330.3, 2 PART EPOXY, 100:33 RATIO,
CURE 140°F OVERNIGHT

ALUMINUM - PPA

SPECIFICATION: ASTM D3165 AND USING ASTM D695 FIXTURE TO MAINTAIN
SAMPLE STRAIGHTNESS

SAMPLE	BONDLINE THICKNESS INCHES	WIDTH INCHES	LENGTH INCHES	AREA SQ IN	MAX LOAD LBS	MAXIMUM SHEAR STRENGTH PSI	NATURE OF FAILURE % COHESIVE	% ADHESIVE
A/P9330.3-1	0.008	0.4950	0.5050	0.2500	1060	4,240	0	100
A/P9330.3-2	0.008	0.4960	0.5040	0.2500	950	3,800	0	100
A/P9330.3-3	0.007	0.4960	0.5070	0.2515	1060	4,215	0	100
A/P9330.3-4	0.007	0.4960	0.5050	0.2505	985	4,215	0	100
A/P9330.3-6	0.006	0.4960	0.5050	0.2505	995	3,932	0	100
						3,972	5	95
AVERAGE					1,010	4,032		
STANDARD DEVIATION					49	190		
COEFFICIENT OF VARIATION					5	5		

SAMPLE #5 NOT TESTED (IT WAS DESTROYED IN MACHINING)

SAME AS ABOVE EXCEPT NO FIXTURE USED

SAMPLE	BONDLINE THICKNESS INCHES	WIDTH INCHES	LENGTH INCHES	AREA SQ IN	MAX LOAD LBS	MAXIMUM SHEAR STRENGTH PSI	NATURE OF FAILURE % COHESIVE	% ADHESIVE
A/P9330.3-7	0.015	0.4950	0.5060	0.2505	720	2,875	20	80
A/P9330.3-8	0.011	0.4960	0.5070	0.2515	705	2,803	15	85
AVERAGE					713	2,839		
STANDARD DEVIATION					11	50		
COEFFICIENT OF VARIATION					1	2		

C. F. KLINE JR.
C25471
939-1945

474

Modern Ablatives. The Design, Development, and Application of Hybrid Polymers

Joseph D. Lichtenhan

Phillips Laboratory

(Emerging Technologies Branch, Rocket Propulsion Directorate)

Edwards AFB, California, 93524

The economic and environmental demands associated with modern rocket propulsion have forced scientists and engineers to make continued decreases in the manufacturing costs of systems, while simultaneously improving their performance, reliability, maintainability, and environmental acceptability. Consequently, this has pushed the existing materials technology to its critical performance limits and has antiquated a significant number of well established manufacturing processes and materials. Because space and rocket propulsion will remain a "mission critical" area for the Air Force and related agencies, a search for new materials and processes which can be used to either replace or retrofit those currently in application has been actively pursued by the DoD and its contractors. These new requirements have significantly affected the solid rocket propulsion community in terms of the acceptability of various ablative and insulative materials used in applications such as internal and external solid motor insulations, antenna windows, nozzles and throats.

The hybrid polymer applications program at the Phillips Laboratory is focused on the development of new classes of ablative materials to meet the current and future needs of rocket propulsion. This research is driven by the demand for ablative materials which offer low cost automatable processing, improved system reliability, design flexibility, environmentally acceptable technology, and improved ablation performance (reduced erosion rates).

This paper focuses on the development of internal ablative thermal insulation for solid rocket motors. Solid rocket motor insulation serves three main system functions: to position the propellant relative to the case and nozzle during system transport and operation, to control the amount of combustible propellant surface area during system operation, and to protect the motor case and payload from thermal damage.

During a motor firing, internal insulation is subjected to temperatures that may exceed 2000 °C and pressures of 1000 psi or greater. The insulation will experience a variety of operational stresses (compressive, tensile, shear) and a chemically oxidizing atmosphere with gas and particulate velocities that may range from Mach 0.1 to 10+.

A number of materials have been engineered to provide acceptable levels of thermal protection in such environments. The most widely used class of materials are elastomeric composites. These consist of a rubbery matrix (such as NBR, PI, EPDM, etc.) which has been reinforced with various fibers (asbestos, carbon, glass, PBI, etc.) and fillers (silica, coal, etc.). These composite elastomers derive their insulative behavior by producing decomposition gases and by the production of an insulative char layer which results from decomposition reactions between the residual polymer matrix, fibers and fillers.

The chars produced from such ablatives are structurally weak and susceptible to removal by mechanical erosion. To reduce mechanical erosion and aid in char retention, fibers are typically added to the virgin material. Provided that the char remains intact, it is still susceptible to removal via thermal and chemical ablation.

The composite-like nature of this class of ablatives also severely limits their processability and requires them to be pattern cut, and laid into place by hand. This not only significantly increases overall system production costs but also generates significant amounts of scrap material (as much as 50 %) that cannot be reused. Recently a number of environmental issues have become of concern regarding the disposal of hazardous scrap and the use of solvents and adhesives required to glue composite insulation to the motor case and propellant. Additional issues pertaining to the integrity of the material interfaces (traditionally called bondlines) between the case-insulation-propellant and regarding the performance, predictability, and durability of the insulative char have all served to lower customer confidence in the reliability of solid propulsion systems.

Recent advances in the synthesis of polymeric hybrid materials provides an opportunity to take advantage of a unique class of evolving materials which combine the favorable properties of both organic and inorganic substances (hence the term hybrid).[1] Hybrids show excellent potential as ablative materials because upon pyrolysis they can be converted into a ceramic char which may promise significantly increased resistance to oxidation and mechanical erosion than current char forming carbon based ablative materials (Figure 1).[2]

In addition to providing increased ablation resistance, polymeric hybrid materials can be designed to possess enhanced material processability and thereby facilitate the reduction of scrap-waste material. Hybrid polymers can potentially be cast, flame sprayed, extruded, or injection molded and if necessary, recast into a variety of forms. The processability of hybrid

[1] (a) Lichtenhan, J. D.; Vu, N. Q.; Carter, J. A.; Gilman, J. W.; Feher, F. J. *Macromolecules* 1993, *26*, 2141-2142. (b) "Thermoplastic Elastomer Blends Prepared from Polycarbosilane and Polysilastyrene Preceramic Polymers" Joseph D. Lichtenhan, Alan G. Bolf *Polymer Preprints* in press. (c) "Synthesis and Characterization of Polyhedral Oligosilsesquioxane Polymers Incorporating Transition Metals" Joseph D. Lichtenhan, Timothy S. Haddad *Polymer Preprints* in press.

[2] "Advanced Propulsion Materials: New Classes of Ablative Materials Based on Hybrid Silicon Polymers," Lichtenhan, J. D.; Haddad, T. S. 1993 Project Report, PL-TR -93-#; UDRI-TR-93-#.

polymers is obviously desirable from a manufacturing point of view and is more environmentally sound because of the recycling and solventless processing options.
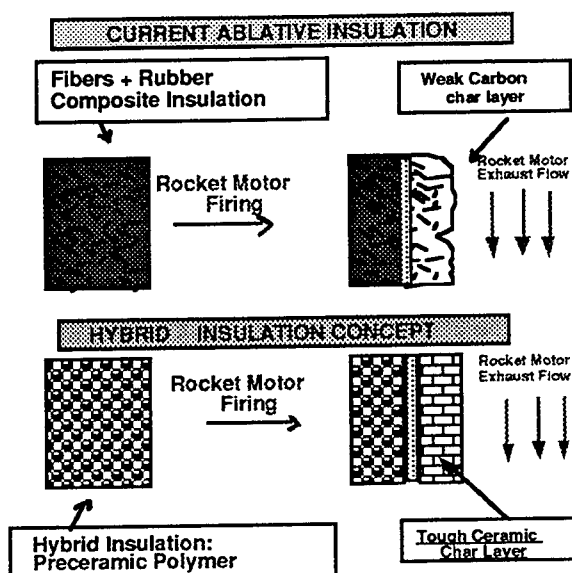

Figure 1. Conventional -Vs- hybrid materials as internal ablative solid rocket motor insulation.

The processability of polymeric hybrid materials coupled with their unique chemical compositions may also enable the design of compatible interfaces between the ablative insulation and the polymeric propellants used in solid rocket motors. This capability manifests itself in the potential for elimination of bondlines in solid rocket motor systems.[3] Considering that over half of the known solid rocket motor failures result from bondline / interfacial failures, the impact that hybrid materials may have on system reliability and performance would be considerable.[4]

We have approached the development of ablative hybrid insulations through the use of empirical ablation studies and experimental synthetic inorganic polymer chemistry.

3 (a) "Preliminary Investigation of a Graded Interface Between Solid Rocket Motor Propellant and Insulation," Joseph D. Lichtenhan, Tommy W. Hawkins, Kevin P. Chaffee. Proceedings of the High Energy Density Matter (HEDM) Contractor's Conference, T. L. Thompson ED., November 1993, PL-TR-93-3041, 450-453. (b) "Experimental Investigation into the Nature of a Graded Propellant/Insulation Interface in Solid Rocket Motors," Charles J. Noel, Joseph D. Lichtenhan. The Advanced Polymeric Components Symposium Proceedings 1993.
4 Unclassified data taken from both classified and unclassified documents supports that over half of all know solid rocket motor failures results from either failure of the insulation or from material failures at the propellant-insulation or insulation-case interfaces.

EMPIRICAL MODELING STUDIES

Empirical models useful for modeling and ultimately predicting the ablative performance of various materials are well known.[5] Predicting the ablative performance of carbon based systems has been the focus of most studies. This reflects the recent interest and largely successful efforts by the aerospace industry to replace metallic components in rocket and space vehicle propulsion systems with carbon composites. Consequently, a sound empirical and experimental foundation covering the performance of carbon-based ablatives exists to which we can compare the relative performance of the proposed hybrid materials.

The initial starting point in our empirical ablation studies has been to identify char compositions that will show more chemical and thermal stability than carbon in the solid rocket motor environment.[6] Table 1 contains the relative performance data for a series of silicon based chars, two forms of carbon char, and several more exotic char compositions. Note that the availability and cost of suitable precursors to the latter chars makes their development and application challenging.

Table 1. Theoretical values for various char compositions.

Char	Ave Eros Rate	Surface Temp	Surface Species[a]
ZrO_2	0.00 mil/sec	3271 K	ZrO_2
ZrC	0.00	3396	ZrC
AlN	0.03	3456	Al_2O_3
SiC	0.48	3133	Si
B_4C	0.82	3316	BN
C (pg)	0.96	3124	C
Si_3N_4	1.49	3328	Si
BN	2.01	3348	BN
C (ph)	2.63	3189	C
SiO_2	2.99	3398	SiO_2

ph = from phenolic precursors, pg = pyrolytic graphite, a = after a 30 sec exposure

---

[5] Acurex Corp., "Aerotherm Charring Material Thermal Response and Ablation Program" Aerotherm division (1987)

[6] Propellant used in this study was an HTPB based 88/19. Typical oxidizing exhaust species include: O_2, O, CO_2, OH, HCl,

The performance data represents the response of the char after exposure to a rocket motor environment with a chamber pressure of 1270 psi and a flame temperature of 3632 K for 30 seconds.[7] The erosion rates were determined by first calculating a non dimensional ablation rate that is based upon a chemical equilibrium between the surface species on the char with those in the exhaust gas stream.[8] Dimensional ablation rates were then calculated by determining the energy and mass balance at the surface of each char. Surface species, temperatures, and average erosion rates corresponding to the initial char compositions are listed in the table above.

Table 2. Material values for the theoretical char compositions.

Char	K^b	C$_p$^{a}	Density	Melt
C (ph)	0.227×10^{-3}	0.47	1.14 g/cc	3593 °C
SiO$_2$	0.225×10^{-3}	0.23	2.32	1704
ZrO$_2$	0.209×10^{-3}	0.16	5.75	2710
SiC	0.472×10^{-2}	0.31	3.22	2500
B$_4$C	0.441×10^{-2}	0.22	2.51	2470
Si$_3$N$_4$	0.375×10^{-2}	0.15	3.18	1900
ZrC	0.329×10^{-2}	0.08	6.66	3532
C (pg)	0.39×10^{-1}	0.38	2.22	3593
BN	0.292×10^{-1}	0.17	2.27	3000
AlN	0.265×10^{-1}	0.17	3.26	2235

ph = from phenolic precursors, pg = pyrolytic graphite, a = Btu/lb °F, b = Btu/sec ft °F

The data in Table 1 primarily represent chemical ablation rates and have not been corrected for any kinetic effects on the equilibrium nor have the values been corrected for material loss that would arise due to mechanical erosion or thermal ablation. Despite the potential for material loss from other ablative mechanisms, the erosion rates for C (ph) and C

---

[7] The A/A* was 51.0. Boundary layer conditions were as follows: Recovery Enthalpy = 1059.7 BTU/lb; Radiation Heating Rate = 608.3 Qradin Btu/ft^2 sec; Heat Transfer Coefficient = 0.1231.

[8] All values for the rate constants were taken from tabulated values listed in the JANNAF thermochemistry tables.

(pg) are within 5 % of that observed experimentally.[9] In general, surface reactions of the char with gas stream species in rocket motor exhaust are primarily responsible for the ablation of insulations in the low mach regions of a motor (head-end and side walls). Thermal effects on the erosion rate data listed above can "qualitatively" be assumed to increase if the melt transition of the char is lower than the calculated surface temperature. Table 2 contains a partial listing of the material properties for the chars.

The relative insulating performance of the chars listed above are shown in Figure 2. This plot shows the thermal profiles of each of the materials listed examined in this study. All compositions were thermally saturated at the end of a 30 second exposure so for comparative purposes only 10 second profiles are shown.
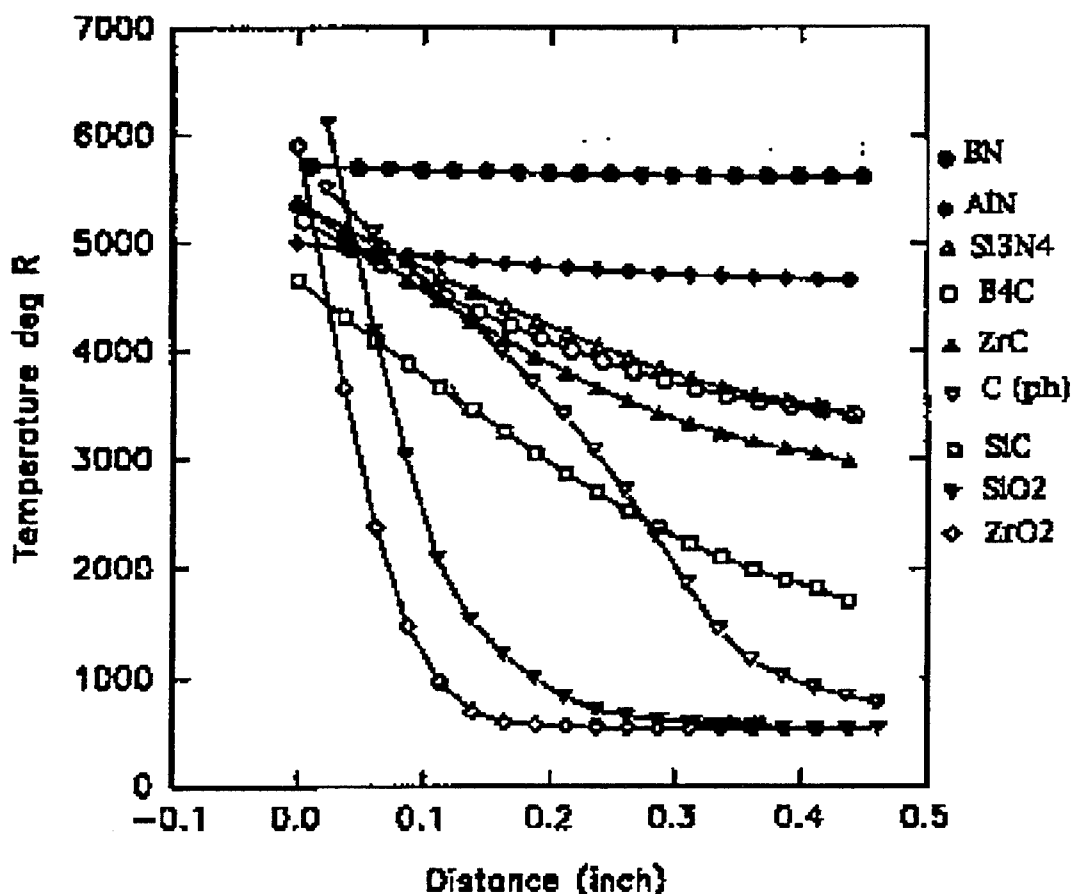

Figure 2. Thermal profiles for various char compositions.

---

[9] This is true only for material exposure in static or low mach region of a solid rocket motor.

The data in Figure 2 point out the importance that thermal conductivity values (K) for various char compositions will have on their insulative performance. In general as the value for the thermal conductivity of the char increases the thermal profile becomes flat. Thermal saturation of the char layer will likely not be desirable in hybrid ablatives for it may result in conversion of the remaining virgin material into char (see Figure 1). This could potentially place the rocket motor case or payload at risk from thermal damage.

Comparison of the predicted erosion rate data in Table 1 to the thermal profiles in Figure 2 provides a preliminary measure of guidance for the development of char producing ablative hybrid materials.[10] A ranking of the char compositions relative to the best overall combination of insulative capacity and erosion rate for exposures over 10 seconds would be as follows: ZrO_2, SiC, SiO_2, C. Missions requiring under 10 seconds of ablative insulation exposure may consider usage of ZrO_2, ZrC, SiC, SiO_2, C, B_4C, and Si_3N_4.

Combinations between various char compositions may also be useful in yielding ablatives that will satisfy engineering requirements. For example, creating an ablative composed of alternating layers of different char compositions could potentially take advantage of chars with low erosion rates while offsetting any undesirable high thermal conductivity through the use of a second more insulative material layer

Ablative materials on current propulsion systems like shuttle and on various ballistic missiles are over engineered to account for material loss that will occur during system operation. This necessary engineering consideration increases both the dead weight and volume of such systems. Reducing the inert component volume and improving ablative material efficiency would increase the available propellant volume and improve operational performance of rocket and space vehicle propulsion systems.

Additional studies are underway to advance our understanding of ablative hybrid materials. We are hopeful that at some point these studies will provide insights that will impact our synthetic efforts aimed at developing new classes of ablative materials.

---

[10] The ablative effects from gases produced upon conversion of the virgin material into the predicted chars will also contribute to the overall ablative performance The magnitude of such an effect for systems, and predicted ablation rates for the materials of interest here have not yet been verified experimentally.

POLYMERIC HYBRID MATERIAL SYNTHESIS

We are exploring two synthetic approaches toward the preparation of polymeric hybrid materials with thermoplastic elastomeric properties.[11] The first involves the synthesis of a new family of preceramic copolymers for which one can tailor the mechanical and thermal properties. This class of materials has been developed through the polymerization of appropriately functionalized inorganic polyhedra. Polyhedral oligosilsesquioxane (POSS) compounds have been employed as macromers in polymerizations with a variety of organic and inorganic comonomers (Figure 3).
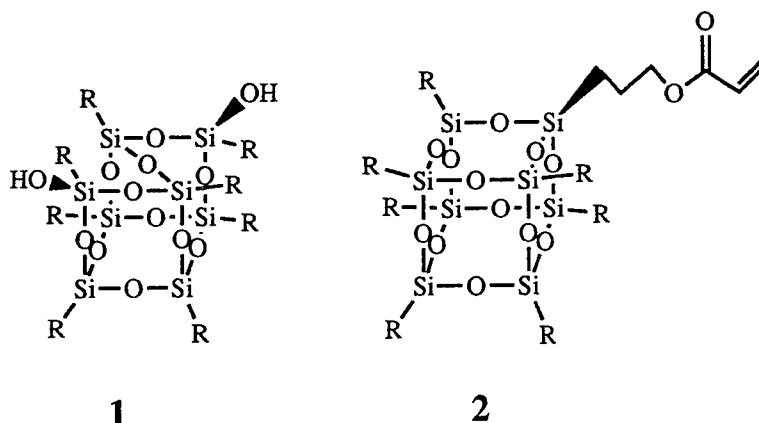
Figure 3. Polymerizable POSS Macromers

Using standard polymerization techniques and through variation of comonomeric reagents, the composition and properties of the resulting polymers can be rationally controlled (Figure 4). In general, the POSS segment acts as a hard (rigid) block in these linear polymeric systems.
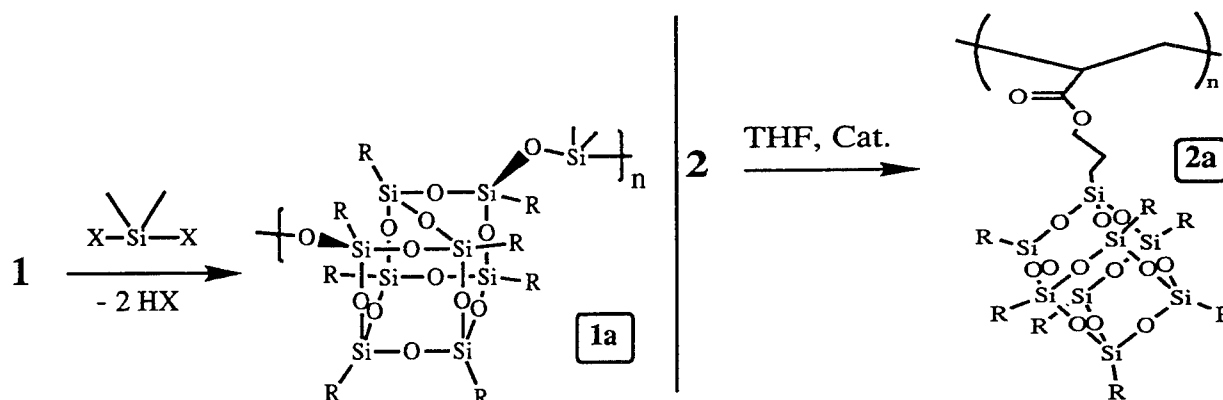
Figure 4. POSS-based Homopolymers.

---

[11] In general, desirable material properties for virgin ablatives include 5-30 % elasticity at low temperatures (-40 °F) and creep resistance at elevated temperatures (160 °F), tensile strengths from 750 -3000 psi. Specific requirements do vary with system.

POSS segments can enhance thermal stability, abrasion resistance, and alter a material's thermal and mechanical properties. In particular it can be used to promote TP and TPE behavior. POSS-based materials can also be cured via chemical or photochemical methods which serve to crosslink the POSS group. In linear polymeric systems POSS segments may also act as branch points and impart a material with composite like characteristics. This has been observed in the stress-strain curves of POSS-Siloxane copolymers (Figure 5).
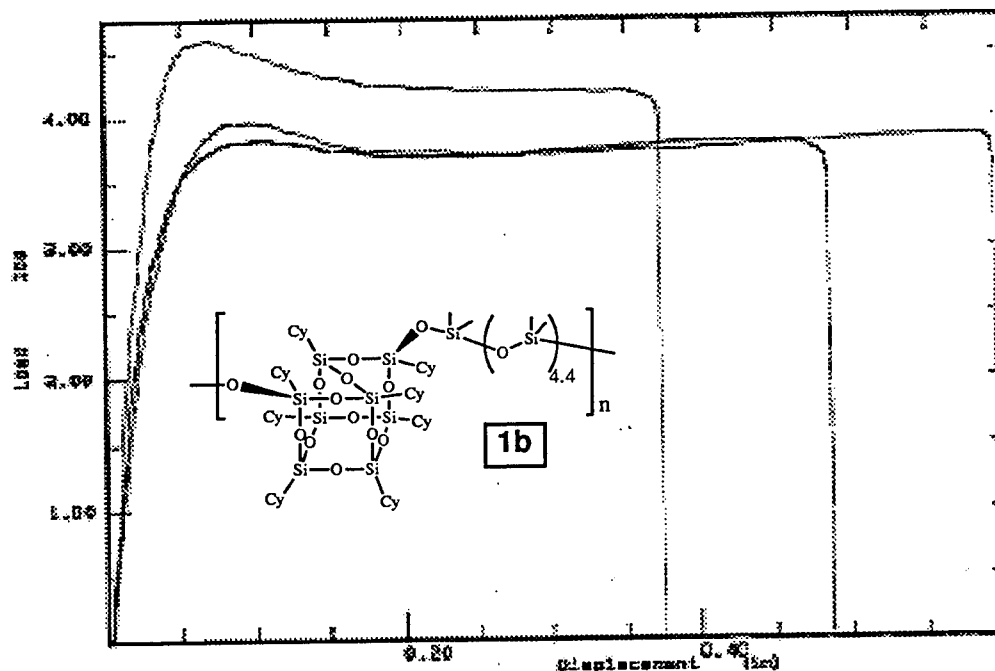

Figure 5. Plot of load -v- displacement for a POSS-Siloxane TPE copolymer.

The initial region of the curve represents elastomeric behavior (deformation to stress) of the material. The latter portion of the curves show that the material is undergoing increased strain without a significant amount of increase stress. Similar curves are observed for fiber or particulate reinforced composite materials. In POSS-based polymers this behavior has been attributed to the POSS group restricting the alignment of individual polymer chains within the stressed material thereby enabling the material to yield like a composite.

In addition to the above mentioned properties the POSS-based materials can also be converted into SiC based ceramics following pyrolysis at high temperatures. Typical char yields range from 50-70 % depending on the amount of POSS incorporation.

Our second approach toward developing ablative thermoplastic hybrid materials seeks to tailor the properties of commercially available preceramic materials (e.g. polycarbosilane,

polysilastyrene). The properties of commercial preceramics are not sufficient to allow their application as engineering plastics. In an attempt to modify the mechanical properties of these materials we have pursued blending PCS and PSS with engineering thermoplastics such as PEBAX (a polyether block polyamide rubber). The resulting blends have been shown to possess a tailorable range of mechanical properties and can produce SiC based ceramics at high temperatures (Table 3).

Table 3. Partial listing of properties for hybrid polymer-polymer blends.

Material	Pk. Stress	Brk. Strain	Yng. Mod.	Melt Temp.	Char Yld.
PEBAX / PCS					
80/20	2313 psi	7.0 in/in	1894 psi	118 C	18 %
50/50	733	0.67	8333	125	44
30/70	1022	0.10	46830	216	56
20/80	---	---	----	200	69
PEBAX / PSS					
80/20	2210	9.4	745	118	15
50/50	448	3.8	2253	110	43
30/70	280	5.9	5021	73	43
20/80	194	1.2	15530	52	50
PSS	---	----	----	148	79
PCS	----	----	----	199	74
PEBAX	2778	8.2	617	119	2.0

Both of the synthetic approaches outlined above have advantages which complement one another. The first approach is superior to the second because precise control over polymer architecture and material properties is possible. The primary advantages of the second approach are lower costs and the ready availability of large quantities of the raw materials. The preparation of hybrid materials from the two approaches and a comparison of their thermal properties and char yields to those of two current ablative insulations is shown below.

Table 4. Comparison of hybrid polymer properties to ablative insulations.

Material	Decomp. Temp.	Char Yld. (@1000 C)	Melt Temp.
EPDM Ins	200	26%	x- linked
POSS-1a	400	65	x- linked
TPE Ins	300 C	8 %	120 C
POSS-1b TPE	400	51	110
50/50 PCS Blend	380	44	125
50/50 PSS Blend	375	39	110

In addition to matching the melt transitions of the polymeric hybrids to those of conventional insulations, the hybrid systems also show enhanced decomposition temperatures and char yields.

Investigations are underway to further the development and application of polymeric hybrids as new ablative materials.

A PRELIMINARY INVESTIGATION INTO THE NATURE OF A GRADED PROPELLANT/INSULATION INTERFACE IN SOLID ROCKET MOTORS

Charles J. Noel

Associate Professor, Department of Textiles and Clothing
The Ohio State University, Columbus, Ohio

Joseph D. Lichtenhan
Phillips Laboratory (Rocket Propulsion Directorate)
Edwards Air Force Base, California

Abstract

Conventional solid rocket motors contain composite ablative internal insulation to protect the case and payload from potential thermal damage during firing. An adhesive material is used to bond the insulation to the propellant; this so-called bond line is considered to be a mechanically weak area in the rocket motor, and numerous failures in the firing of solid rocket motors are attributed to problems with this bond line. A new generation of solid rocket motors has been proposed in which the bond line is replaced by a graded interface between the propellant and insulation. The graded interface is achieved through the use of chemically similar thermoplastic elastomers (TPEs) as the binders in both insulation and propellant. In this concept, the propellant and insulation are co-extruded, and the graded interface is formed by shear or diffusional mixing of the molten materials as they emerge from the extruder side by side. An added advantage of this concept is that the use of TPE binders in both propellant and insulation eliminates the need for additional curing steps necessary when conventional materials such as urethanes are used. In this study the graded interface was simulated by shear mixing TPE based propellant (TP-T-3006, Thiokol) with hybrid insulation. Two different TPE binders (PEBAX-2533, a block copolymer of nylon 12 and poly(tetramethylene glycol) and Kraton D-1102, a styrene-butadiene-styrene triblock polymer) were evaluated in the insulations which were composed of a 50/50 blend of binder and either of two silicon-containing preceramic polymers, polycarbosilane (PCS) or polysilastyrene (PSS). The TPE propellant and the hybrid insulation were mixed at three different P/I levels, representing three points within the postulated composition continuum comprising the graded interface. The mixtures were characterized by measurement of physical properties (peak and break stress, peak and break strain, and Young's modulus), and thermal properties, using DSC, TGA, and TMA. Results obtained indicate the viability of the concept; properties tended to vary smoothly with composition, suggesting that a "seamless" interface between propellant and insulation could be achieved. Examination of microtomed surfaces of the P/I blends using reflected light photomicrography indicated that uniform blends of propellant and insulation were obtained. With PEBAX-2533 as the TPE, blends with PSS were easier to process than were blends with PCS. With PCS as the preceramic, Blends with Kraton D-1102 were easier to process than were blends with PEBAX-2533. The combination Kraton D-1102/PSS should be evaluated to complete the study.

INTRODUCTION

Conventional solid rocket motors contain composite ablative internal insulation to protect the case and payload from potential thermal damage during firing. This insulation consists of a variety of materials including heat resistant fibers such as asbestos, flame retardants and carbonaceous materials such as coal, held in a crosslinked binder such as vulcanized rubber or polyurethane. Conventional solid rocket propellants generally contain fuel, oxidizer, and catalyst dispersed in a crosslinkable polymeric binder which often contains plasticizer to reduce viscosity. Both insulation and propellant need to be cured to achieve crosslinking; these steps in the production process may require more than a week for completion for large rocket motors. Since the propellant and the insulation are chemically dissimilar, a layer of adhesive material is used to create a bond line between the two. Delamination at this bond line is reputed to be a major cause of solid rocket motor failure; structural integrity is lost if catastrophic unzipping of the bond line occurs under loads such as ignition pressurization, and this in turn leads to flame growth along the wall, with case burn through being the ultimate result (1,2).

A new generation of solid rocket motors has been proposed in which the bond line is replaced by a graded interface between propellant and insulation (3). The graded interface is achieved through the use of chemically similar thermoplastic elastomers (TPEs) as the polymeric binders in both the propellant and the insulation. In this concept, propellant and insulation are co-extruded, and the graded interface is formed by shear or diffusional mixing of the molten materials as they emerge from the extruder side by side. An added advantage of this system is that the use of TPE binders in both propellant and insulation eliminates the costly and time consuming curing steps needed for processing conventional propellants and insulations, which make use of thermosetting binders. TPEs may be defined as

materials which combine the processing characteristics of thermoplastics with the physical properties of vulcanized rubber (4). TPEs are comprised of block copolymers in a variety of forms; one of the blocks is a "soft" block with a glass transition temperature usually well below room temperature, and the other is a "hard" crystallizable block with a relatively high melting point. Properties of the TPE can be engineered by varying the nature, the arrangement, the molecular weights, and the relative amounts of the two blocks. Unlike vulcanized rubbers, TPEs are not crosslinked, but the aggregation of the hard blocks act as crosslinks at use temperatures. These associations disappear at elevated temperatures, enabling the material to be processed.

Nahlovsky, Hargis, and Raterman (5) reviewed the work done in various government, industry, and university laboratories to develop solid rocket propellants based on TPE binders, both inert and energetic. Their work concluded that polyethylene block copolymers which contained crystalline end blocks obtained by hydrogenation of low-vinyl polybutadiene and soft blocks obtained by hydrogenation of polyisoprene or high-vinyl polybutadiene would work well in this area. Palopoli et al.(6) report on the successful development of a solid rocket propellant using commercially available TPE binders. Propellants having up to 88% solids were obtained using Shell's Kraton D-1102, a triblock of the SBS type, where the hard end blocks are polystyrene and the soft middle block is polybutadiene. Over 250kg of a propellant designated TP-T-3006 was continuously processed on a twin-screw mixer/extruder in a demonstration of the feasibility of the concept. This propellant was selected as the TPE based propellant for use in this study.

Preceramic or hybrid polymers are a unique evolving class of materials which combine the favorable properties of both organic and inorganic substances (7). Upon pyrolysis, preceramic materials can be converted to a ceramic which is more resistant to oxidation and mechanical erosion than conventional char from organic based ablative systems. Two commercially available silicon-containing preceramic polymers are polycarbosilane (PCS) and polysilastyrene (PSS). Polycarbosilane is formally poly(methylene methylsilane) but in fact is slightly crosslinked. Polysilastyrene is a linear 1/1 copolymer of

dimethylsilane and methylphenylsilane, presumed to be more or less alternating. These two preceramics were both included in this study. Promising materials for future evaluation are hybrid polymers based on substituted polyhedral oligosilsesquioxanes (POSS) (7). These are currently unavailable in sufficient quantities for blending studies, but work is underway to scale up their production.

The purpose of this study was to characterize the graded interface which would be expected to form when molten TPE based propellants and insulations are co-extruded. The graded interface would be driven to form by either shear or diffusional mixing of the melts as they emerge side by side from an extruder or extruders. On one side of the graded interface, one would find 100% insulation and on the other, 100% propellant. Properly formed, the graded interface would consist of a continuum of blend levels, ranging all the way from 99P/1I to 1P/99I. It was decided to "sample" this continuum by preparing three different P/I blends at 75/25, 50/50, and 25/75 by mixing presoftened propellant with presoftened insulation in a high-shear mixer. A Morton-Thiokol propellant, TP-T-3006, was chosen as the propellant. No attempt was made to optimize an insulation formulation at this time; insulations evaluated were 50/50 blends of either of two preceramics (PCS or PSS) with either of two commercially available TPEs. PEBAX-2533 was selected because of its prior use in propellants, while Kraton D-1102 was chosen because it is the TPE used in the selected propellant. It was intended to evaluate four insulations, combining each preceramic with each TPE, but the Kraton/PSS combination could not be made because additional PSS could not be obtained from its original supplier. By the time an alternate supplier was identified, it was too late to include this insulation in this study. The work is planned to be completed when the new batch of PSS is received.

METHODOLOGY

Preparation of Insulation
The insulation materials used in this study were 50/50 blends of a TPE with a silicon-containing preceramic polymer. Two TPEs were used: PEBAX-2533 (Elf Atochem) is a block copolymer of nylon 12 (hard block) and poly(tetramethylene-

glycol) (soft block); Kraton D-1102 (Shell) is a SBS (styrene-butadiene-styrene) triblock polymer. Two silicon-containing preceramic polymers were also used: polycarbosilane (PCS) (Dow-Corning) and polysilastyrene (PSS) (Hüls). The materials were used as received from their suppliers. Blends were prepared by adding 50.0g TPE and 50.0g preceramic to 1000mL solvent (500mL dichloromethane ad 500mL tetrahydrofuran) in a 2.0L resin kettle. The mixture was allowed to stand for 60m; at this time the TPE was either dissolved (Kraton) or swollen (PEBAX). The resulting mix was heated to the boil while being stirred with a Ross high-shear emulsifier. Mixing continued for 60m, then the solution was poured into a Teflon coated dish (11"x 9"x 5/8") and the solvent was allowed to evaporate. When the material appeared to be dry, it was treated in a vacuum oven at 80°C overnight to remove residual solvent. The resulting sheets were cut into pellets for blending with propellant. Three 50/50 blends of TPE with preceramic were prepared: PEBAX/PCS, PEBAX/PSS, and Kraton/PCS. The fourth blend, Kraton/PSS, was not prepared because of difficulty in procuring additional PSS from Hüls; an alternate source was located and material has been ordered so that this blend will be prepared and evaluated in the near future.

Propellant

The propellant TP-T-3006 was used as received from Morton-Thiokol. The propellant contains 88% solids and 12% TPE binder system. The reported composition of the propellant is (6):

Solids:	Al	21.0%
	NH_4ClO_4	38.7%
	$NaNO_3$	28.1%
	Fe_2O_3	0.2%
Binder	Kraton D-1102	3.0%
	Shellflex 71	7.5%
	Endex 160	1.5%

Shellflex 71 (Shell) is a plasticizer, while Endex 160 (Shell) is a poly-α-methylstyrene filler. The propellant was cut into pellets to facilitate blending with insulation.

Preparation of P/I Blends

Blends of propellant and insulation were prepared using a quarter-pint Baker-Perkins mixer. Materials were preheated at 130°C for 30m prior to mixing. Blends of propellant and insulation

were prepared in 120g batches at three different levels, 75/25, 50/50, and 25/75, corresponding to three points in the hypothesized composition continuum comprising the graded P/I interface. For the 75/25 P/I blends, 90.0g preheated propellant was placed in the bowl of the mixer and was stirred alone for 30m at 130-135°C. The bowl was then lowered, the blades scraped down, and 30.0g preheated insulation was added. This was then mixed for an additional 30m at 130-135°C. At this time, the material in the bowl appeared to be homogeneous, so no further mixing was done. The blended material was cast into lab-scale slabs (4"x 3"x 0.18") using preheated Teflon molds. The 50/50 and 25/75 P/I blends were prepared in the same manner, except that in the case of the 25/75 blends, the insulation was added in three 30.0g increments with 15m mixing for each addition of insulation.

Characterization of Materials

Mechanical properties of the materials were measured using an Instron Series 1123 Tester equipped with Series IX Automated Materials Testing System 1.15. Testing was carried out at ambient conditions (23°C, 50%RH) using the JANNAF Standard Mini-Dog Bone Test. The 1.0" minibones were elongated at the rate of 1.0"/m. Data obtained included peak and break load, peak and break stress, peak and break strain, and Young's modulus. At least eight minibones were broken for each P/I blend.

Thermal properties were measured using a DuPont (TA) Thermal Analysis System, which included a DSC 912 module, a TGA 951 module, a TMA 2940 module, and a Model 2000 Thermal Analyst controller. Heating rates were 10°C/m for the DSC and TGA, and 3.0°C/m for the TMA. The TMA was operated with a 10g weight in the penetration probe mode, and a 2g weight in the expansion probe mode.

Scanning electron micrographs of materials were taken using an International Scientific Instruments Model CL6 equipped with a LaB_6 filament. Photomicrographs were taken using a Jennalumar research microscope equipped with the Datex-Man Automatic-2 photographic system, using both ASA 64 color film for slides and ASA 100 color print film.

RESULTS AND DISCUSSION

In this study, an effort was made to characterize the nature of the graded interface between propellant and insulation in solid rocket motors. The graded interface is postulated to form when the thermoplastic propellant and insulation are extruded side by side and the two melts are driven to mix by shear forces. The graded interface consists of a continuum of compositions ranging from 100% propellant on one side to 100% insulation on the other. To characterize this interface, mixes of propellant and insulation were made at the 75/25, 50/50, and 25/75 levels, representing three points within the composition continuum. The experiment was designed to evaluate for different insulations, made by blending either of two TPEs with either of two preceramics at the 50/50 blend level. The two TPEs were PEBAX-2533, a block copolymer of poly-(dodecanoic lactam) (nylon 12) and poly-(tetramethylene glycol), and Kraton D-1102, an SBS (styrene-butadiene-styrene) triblock copolymer. The two preceramics were poly-carbosilane (PCS) and polysilastyrene (PSS), which is a 50/50 copolymer of dimethylsilane and methyl-phenylsilane. Three of the four insulations were evaluated; the fourth, Kraton/PSS, will be evaluated in the near future to complete the study.

Before discussing the results of physical testing and thermal analysis, some qualitative observations regarding the processability of the P/I blends should be reported. All mixes were made at 130-135°C using a Baker-Perkins high-shear mixer operating at 50 rpm, with the exception of the 25/75 P/I blend with PEBAX/PCS as the insulation. This material could only be mixed at 30 rpm because its viscosity was apparently too high for the mixer. (One fuse was blown attempting to mix at 50 rpm.) After mixing, all P/I blends were hand cast into preheated Teflon molds by scooping a spatula full of material out of the bowl of the mixer, and spreading the material onto the mold. P/I blends at the 75/25 level were invariably easier to spread than either 50/50 or 25/75 blends; 50/50 blends were generally easier to spread than 25/75 blends. Blends containing Kraton/PCS insulation all spread easier than the corresponding blends containing PEBAX/PCS insulation. However, all the blends containing PEBAX/PSS insulation spread easier than *any* of the other blends, regardless of P/I blend level.

Preheated metal plates were then placed on top of the material in the mold to assist the material in filling the cavity in the mold. When cool, standard JANNAF mini-dog bones were cut from these molded slabs for physical testing. Since the minibones were all cut using a standard die, the length and width of all the minibones were close to being the same. Cross-sectional areas of the minibones were determined for the calculation of stress and modulus values. Since the widths of the minibones were fairly constant, most of the variation in the values of the calculated areas may be attributed to differences in the thicknesses of the individual specimens. Increased thickness and increased variability in thickness resulted when material was more difficult to spread. Table 1 shows the area measurements for the P/I blends as a function of blend level and composition. The data shown support the qualitative observations on processability; the thinnest minibones were obtained with P/I blends containing PEBAX/PSS insulation, and the area (and hence thickness) tended to increase with insulation content. The high coefficient of variation for the 50/50 P/I blend with PEBAX/PSS insulation is due to a bimodal distribution; five of the tested minibones had an average cross-sectional area of 0.0094 in^2 (0.35% C.V.), while the other four tested had an area of 0.0162 in^2 (1.84% C.V.).

The results obtained from the physical testing of materials are shown in Table 2. This table contains the results obtained for the P/I blends as well as the results obtained for the propellants and the insulations alone. The physical properties of solid rocket propellants most often reported in the literature are the Peak Stress, Break Strain, and Young's Modulus. These values are given in Table 2 along with values for Break Stress, Peak Strain, Peak and Break Load, and the ratios of Peak to Break Stress (PS/BS) and Peak to Break Strain (PE/BE). Examination of the data for the P/I blends shows that Peak and Break Load and Peak and Break Stress increase with increasing insulation content in every case, and that the values of Peak and Break Stress for these blends fall between the values obtained for the propellant and the pertinent insulation. Plots of Peak Stress vs. Insulation Content show a smooth increase from 0 to 100% Insulation in all three cases, with the measured values being below values calculated by use of an additive law of mixing for the two insulations containing PCS, and above those calculated values for the PEBAX/PSS insulation.

TABLE 1

CROSS-SECTIONAL AREA OF JANNAF MINI-DOG BONES FOR PHYSICAL TESTING

Insulation	P/I	Number	Area (in²)	Std. Dev. (in²)	C.V. (%)
PEBAX/PCS	75/25	8	0.0354	0.0029	8.21
	50/50	8	0.0302	0.0066	21.90
	25/75	9	0.0420	0.0078	18.59
Kraton/PCS	75/25	8	0.0349	0.0029	8.38
	50/50	8	0.0364	0.0010	2.78
	25/75	8	0.0355	0.0037	10.43
PEBAX/PSS	75/25	8	0.0122	0.0008	6.38
	50/50	9	0.0124	0.0036	29.25[a]
	25/75	10	0.0145	0.0016	10.68

[a]Bimodal distribution

The PEBAX/PSS insulation had the lowest Peak Stress of any of the three insulations studied. Peak Strain also increased with increasing insulation content in every case, as did Break Strain, with the single exception of the 50/50 P/I blend with PEBAX/PCS insulation. This composition reached its Peak Stress at a strain of 9.1% (0.091 in/in) but did not break until a strain of 158.7% was reached. Plots of Break Strain vs. Insulation Content show a smooth increase from 0 to 100% Insulation in all three cases, with the single exception noted above; the measured values were slightly below values calculated using a simple additive law of mixing for the compositions where the insulation contained PCS, but were far below these calculated values for blends containing the PEBAX/PSS insulation. The Young's Modulus data show no clear trend with increasing insulation content. The propellant itself, having 88% solids and only 12% TPE binder system (which is less than half polymer) showed low Young's Modulus (750 - 1325 psi). Of the materials tested, only the unblended TPE PEBAX-2533 showed a lower Young's Modulus (581 psi). When PCS is blended with PEBAX at the 50/50 level to form a hybrid insulation, the modulus increased tremendously, from 581 to 8333 psi, but when PSS is used with PEBAX, the modulus only increased from 581 to 2253 psi. The unblended TPE Kraton D-1102 had a higher modulus than the neat PEBAX (2132 vs. 581 psi); the Kraton/PCS insulation had the same modulus as the unblended Kraton (2175 vs. 2132 psi).

Whatever the modulus of the unblended insulation, the 75/25 P/I blends all had much higher modulus than the propellant alone. There was no further identifiable trend with increasing insulation content. For P/I blends with PEBAX/PCS insulation, Stayed high and fairly constant as insulation increased from 25 to100%. For P/I blends with Kraton/PCS insulation, modulus was lower than for the PEBAX/PCS blends, and appeared to decrease with insulation content over the same range. For P/I blends with PEBAX/PSS insulation, modulus values were comparable to those obtained with PEBAX/PCS, except for the 50/50 P/I blends, where the PEBAX/PSS composition had a lower modulus; there was no clear trend over the composition range. The modulus data showed a fair amount of scatter within the samples of 8 to 10 minibones. Coefficients of Variation for Young's Modulus ranged from 10.33% (50/50 P/I blend with Kraton/PCS) to 39.11% (75/25 P/I blend with PEBAX/PCS), and averaged 19.73% for all P/I blends tested. Svob (8) reports that it is common for the C.V. for Young's Modulus to approach 15%; many of the data reported here seem to show more scatter.

The ratios of peak stress to break stress (PS/BS) and peak strain to break strain (PE/BE), taken with the actual values of the stresses and strains, provide some information regarding the shapes of the stress-strain curves. The

TABLE 2

PHYSICAL PROPERTIES OF PROPELLANT/INSULATION BLENDS

Propellant : TP-T-3006
Insulation: 50/50 TPE/Preceramic

Sample	TPE/Preceram	Blend	Pk. Load (lb.)	Pk. Strs. (psi)	Pk. Strn. (in./in.)	Br. Load (lb.)	Br. Strs. (psi)	Br. Strn. (in./in.)	Yng. Mod (psi)	PS/BS	PE/BE
CJN001	PEBAX/PCS	75/25	3.85	109.6	0.039	2.075	58.8	0.272	7622	1.896	0.182
CJN002	PEBAX/PCS	50/50	7.11	238.5	0.091	5.162	173.1	1.587	7546	1.408	0.078
CJN003	PEBAX/PCS	25/75	12.46	298.1	0.307	10.558	251.5	0.369	5069	1.193	0.857
CJN004	Kraton/PCS	75/25	3.78	108.6	0.078	1.511	43.6	0.389	4043	2.778	0.211
CJN005	Kraton/PCS	50/50	7.21	197.9	1.498	6.239	170.8	1.716	3308	1.362	0.867
CJN006	Kraton/PCS	25/75	13.03	369.1	3.557	12.668	356.5	3.705	1786	1.036	0.961
CJN007	PEBAX/PSS	75/25	3.07	247.8	0.136	1.988	160.9	0.196	8686	1.531	0.708
CJN008	PEBAX/PSS	50/50	4.25	341.5	0.334	3.103	247.6	0.443	3427	1.382	0.764
CJN009	PEBAX/PSS	25/75	6.66	458.8	0.627	5.089	351.8	0.772	5912	1.325	0.814
CJN011	Kraton/PSS	75/25									
CJN012	Kraton/PSS	50/50									
CJN013	Kraton/PSS	25/75									

PHYSICAL PROPERTIES OF PROPELLANT, TPEs, AND TPE/PRECERAMIC BLENDS

		Blend	Pk. Load (lb.)	Pk. Strs. (psi)	Pk. Strn. (in./in.)	Br. Load (lb.)	Br. Strs. (psi)	Br. Strn. (in./in.)	Yng. Mod (psi)	PS/BS	PE/BE
TP-T-3006	(From Thiokol Report)			100				0.250	750		0.893
TP-T-3006	(From material as received)		2.48	93.1	0.144	2.16	81.2	0.162	1046	1.152	0.856
TP-T-3006	(From remixed material)		0.639	24.9	0.028	0.488	19.04	0.036	1325	1.332	
PEBAX-2533			49.39	3057	8.422	48.37	2996	8.539	581	1.022	0.986
PEBAX/PCS		50/50	13.22	816	0.558	11.87	733	0.674	8333	1.116	0.827
PEBAX/PSS		50/50	9.45	475	3.728	8.96	448	3.801	2253	1.053	0.962
Kraton D-1102			24.41	1199	6.987	23.76	1167	6.984	2132	1.028	0.986
Kraton/PCS		50/50	9.61	619	5.883	9.37	595	5.962	2175	1.025	0.986
Kraton/PSS		50/50									

491

PEBAX/PSS and Kraton/PCS insulations tended to reach maximum stress very close to their breaking points; this peak stress is only 2-5% higher than the break stress and is reached at an extension within 4%of the extension at break. This behavior is very similar to that of the two TPEs, and these two insulations have high break strains as do the two TPEs. By contrast, the PEBAX/PCS insulation has a peak stress nearly 12% higher than its stress at break, and reaches this at only 83% of its break extension, which itself is relatively low (67%). The TP-T-3006 propellant itself has a stress-strain curve similar in shape to that of the PEBAX/PCS insulation; peak stress is 15% greater than stress at break, and is reached at 89% break extension. The values for peak stress and break strain for the propellant are of course much lower for the propellant than for this insulation, as well as for the other two insulations, since most of the mass of the propellant (>95%) is not load-bearing. With 75/25 P/I blend ratio, and either PEBAX/PCS or Kraton/PCS insulation, peak stresses are 90-180% greater than stresses at break, and these peak stresses are attained at only 18-21% of break extension. The most unusual stress-strain curve was exhibited by the 50/50 blend of propellant with PEBAX/PCS insulation; the peak stress was 40% higher than the stress at break, and the peak stress was reached at an extension which was, on average, only 7.8% of the extension at break. By contrast the 50/50 P/I blend with Kraton/PCS insulation had a peak stress 36% higher than the break stress, but this was reached at 87% of break extension. At the 25/75 P/I blend levels the PS/BS and PE/BE ratios were similar to propellant for the PEBAX/PCS insulation, and similar to insulation for the Kraton/PCS insulation. For the PEBAX/PSS insulation, the PS/BS ratio was greater for the 75/25 P/I blend than for the propellant alone, then decreased steadily as insulation content increased from 25 to 100%. The PE/BE ratios showed the opposite behavior. Even at the 25/75 P/I blend level, both ratios were more similar to those of propellant than those of insulation.

The data in Table 2 point out that the propellant is not particularly heat stable. Data taken from reference 6 for peak stress, break strain and Young's modulus are reported in this table, as well as two sets of data obtained in the course of this study. Minibones were cut from slabs machined from bricks of propellant which had been stored at Edwards AFB for over one year.

Minibones were also cut from slabs which were cast from propellant given the same treatment as the P/I blends: preheated at 130°C for 30m, mixed alone for 30m at 130°C, then cast into preheated Teflon molds. Test results from these samples are also included in Table 2. The results obtained from the stored material suggest a slight deterioration in properties; peak stress for stored material was 93 psi compared to 100 psi reported in reference 6, break strain was 16% compared to 25%, and Young's modulus was 1046 psi compared to 750 psi. An increase in modulus is consistent with a decrease in elongation. In comparison to the stored material, the processed (remixed) material was badly degraded. Peak stress decreased from 93 to 25 psi, break strain decreased from 25 to only 3.6%, and modulus increased from 1046 to 1325 psi. The polymeric TPE binder may be undergoing slow degradation through contact with the propellant's oxidizers on storage; this degradation is accelerated by processing the propellant at elevated temperatures. It is recommended that a property profile over time be maintained for stored propellant to see how serious a problem this might be. The accelerated degradation upon heating is not a problem, since the graded P/I interface would be formed at the time the propellant is first extruded; it is not intended that previously formed propellant would be reprocessed in the co-extrusion model. In all property comparisons discussed above, values for stored propellant were used. Values reported above for all P/I blends may be lower than those which would actually be obtained in a graded interface, since the propellant component of the blend has undergone degradation. The TPEs in the insulations in the P/I blends could also possibly undergone some degradation during the long contact with the propellant's oxidizers during the mixing at 130°C.

To evaluate the uniformity of the blends obtained, scanning electron microscopy and reflected light photomicrography of microtomed surfaces were both used. The scanning electron micrographs taken at magnifications of 500-1250X were difficult to interpret. Uniformity appeared good but the field of view was so small that this was hard to judge. Particulate matter was visible in both surface and cross-sectioned specimens; the amount of particulates decreased with increasing insulation content in the blends. No evidence for or against phase separation could be inferred. Photomicrographs taken at about 75X

magnification taken using light reflected from microtomed surfaces showed the propellant and insulation to be well mixed, at least at the macro level. The aluminum particles in the propellant were clearly visible, as were large and small clear crystals of the ammonium perchlorate and sodium nitrate oxidizers. Tiny bright orange crystals, presumably of ferric oxide, could be seen in some fields of view. The aluminum particles and oxidizer crystals appeared to be uniformly distributed over each specimen viewed, and were definitely in proportion to the level of propellant in the blends. Based upon these qualitative observations, the conclusion was reached that the mixing procedure used did produce uniform blending of propellant and insulation.

The results obtained by thermal analysis are summarized in Table 3. This table includes results obtained by Thermogravimetric Analysis (TGA), and by Differential Scanning Calorimetry (DSC). The onset temperature determined by TGA represents the temperature at which the first evidence of weight loss was detected, while the onset temperature determined by DSC represents the temperature for the first clear deviation from the baseline. The decomposition temperature determined by TGA was obtained by constructing tangents to the initial and steepest portions of the weight-temperature curve, and determining the temperature of their intersection; this roughly corresponded to the temperature at which the specimen weight loss was 10%. The decomposition temperature determined by DSC was taken as the peak temperature of the first significant exotherm; usually there were additional exotherms at higher temperatures and these were generally smaller than the first. The glass transition temperatures determined by DSC were taken as the temperatures where baseline shifts occurred, representing a change in specimen heat capacity. Glass transition temperatures by Thermomechanical Analysis (TMA) and by Dynamic Mechanical Analysis (DMA) will be measured as will softening temperatures by TMA. Percent Char by TGA as reported in Table 3 was the weight of the residue after heating the specimen from room temperature to 1000°C at the rate of 10°C/m, expressed as a percentage of the original weight of the specimen.

The propellant TP-T-3006 showed first evidence of weight loss at 195°C, with rapid weight loss commencing at 242°C. By DSC, all samples containing any propellant showed a small but characteristic "signature" endotherm at 243°C, followed immediately by a significant exotherm apparently associated with decomposition. The hybrid insulations alone all exhibited higher temperatures for initial weight loss, compared to propellant, and much higher decomposition temperatures, by TGA. The two insulations made with PEBAX as the TPE had decomposition temperatures of 375-381°C while the Kraton/PCS insulation had a decomposition temperature of 443°C, by TGA. TGA decomposition temperatures for P/I blends with PEBAX/PCS insulation did not increase with increasing insulation content as expected, but TGA decomposition temperatures for P/I blends with both Kraton/PCS and PEBAX/PSS did increase with increasing insulation content. Residues from P/I blends with all three insulations, reported as % Char by TGA, tended to approach or exceed the values obtained for the insulations alone, and were always higher than the residue from the propellant alone. The residue from the propellant alone was a silvery gray powder; the residues from the P/I blends and the insulations alone were hard and sometimes brittle black ceramic-like material. Qualitative elemental analysis of these residues by EDAX showed that the residue from the propellant alone contained aluminum and oxygen, but no sodium or chlorine; residues from P/I blends contained aluminum, sodium, silicon, and oxygen, but no chlorine; and residue from insulations alone contained only silicon and oxygen. Since the propellant contains aluminum as fuel and both ammonium perchlorate and sodium nitrate as oxidizers, it was expected that its residue would consist of aluminum oxide and sodium chloride; the alumina was detected but the salt was not. The preceramic polymers in the hybrid insulations should convert to ceramic materials by pyrolysis and oxidation, yielding silicon oxide, silicon carbide, and silicon oxycarbide. The silica was detected, but the carbon derivatives were not.

Glass transition temperatures as determined by DSC were well below room temperatures, as would be expected for elastomeric materials. The values were determined by analysis of the DSC baseline in the temperature range from -150°C to 100°C. A shift in the baseline is indicative of a change in the heat capacity of the material being tested; this shift was very small in all cases where it was detected, and the shift was not detected every time. About one out of every

TABLE 3

THERMAL ANALYSIS OF PROPELLANT, INSULATION, AND P/I BLENDS

% Ins.	T-onset (TGA)	T-decom (TGA)	% Char (TGA)	Tg (DSC)	T-onset (DSC)	T-decom (DSC)
TP-T-3006/(PEBAX-2533/PCS)						
0	195°C	242°C	34.3	-92°C	243°C	300°C
25	171	246	43.1	-83	243	287
50	187	250	49.9	-69	243	284
75	168	238	46.9	-71	243	419
100	225	381	43.5	-67	327	425
TP-T-3006/(Kraton D-1102/PCS)						
0	195	242	34.3	-92	243	300
25	191	333	43.1	-104	243	315
50	180	398	42.8	-79	244	345
75	245	440	45.1	-78	245	354
100	238	443	38.5	-79	270	379
TP-T-3006/(PEBAX-2533/PSS)						
0	195	242	34.3	-92	243	300
25	197	266	37.1	-71	243	271
50	183	264	47.3	-91	243	270
75	226	356	42.1	-87	243	264
100	285	375	42.2	-66	235	409

six traces did not show a measurable base line shift. The DSC glass transition temperatures reported are the average of at least two detectable shifts. The values for the insulations were all lower than that for the propellant; values for the P/I blends showed no readily apparent trends with composition. Additional thermal characterization of these materials is being carried out, using both DMA, and TMA equipped with an expansion probe to determine glass transition temperatures, and TMA equipped with a penetration probe to determine softening temperatures. Both TMA and DMA make use of larger test specimens than are used in DSC (4-6mg), and may provide better measurements of glass transition temperatures than were obtained by DSC.

SUMMARY AND CONCLUSIONS

This study was undertaken to characterize the graded interface between propellant and insulation which is postulated to form when TPE-based propellant and insulation are co-extruded side by side in the making of the rocket motor of the future. The graded interface is driven to form by the shear forces present as the melts emerge from their extruder(s), and could be augmented by diffusional mixing of the melts. The graded interface is the material between 100% insulation on one side and 100% propellant on the other, having a continuously graded composition throughout. To characterize this interface, propellant and insulation were mixed at three different levels, 75P/25I, 50P/50I, and 25P/75I, representing a sampling of the interface's postulated composition continuum. Mixes were accomplished using a high shear mixer at elevated temperatures (130-135°C) where the TPE binders in both propellant and insulation exhibit thermoplastic behavior. The resulting P/I blends were evaluated using standard physical and thermal analysis tests. Four hybrid insulations, each a 50/50 blend of one of two TPEs with one of two silicon-containing preceramic polymers, were to be evaluated to demonstrate the effect of materials on the properties of the interface; because of the unavailability of one of the preceramics, only three were actually cone. The fourth will be evaluated in

the near future when additional preceramic is procured.

Photomicrographs taken using light reflected from microtomed surfaces indicated that the propellant and insulation were well mixed, at least at the macro level. Scanning electron micrographs showed no clear evidence of phase separation, but these were difficult to interpret. During mixing and casting of the mixed materials, it was noted that ease of processing of the blends followed the order:

(PEBAX/PSS) > > (Kraton/PCS) > (PEBAX/PSS)

and that within a given composition, processability decreased with increasing insulation content. Support for this qualitative observation was gained by examination of the minibones cut for physical testing; cross-sectional area differences in the minibones are largely due to thickness differences, and thinner test slabs are made from materials which are easier to process. It is recommended that measurements of viscosity and the viscosity-temperature relationship be made for these blends to quantify differences in processability. The striking improvement in processability shown by the P/I blends made with the PEBAX/PSS insulation over those made with insulations containing PCS may be due to the fact that PSS is a linear polymer, while PCS, although formally linear, is actually crosslinked to some extent. The presence of a network polymer in the melt would significantly increase viscosity and make processing more difficult.

Peak and break stress, peak and break strain, and Young's modulus were determined for the materials using standard JANNAF procedures. Peak and break stress and peak strain varied smoothly through the interface as did break strain with one exception; the 50/50 P/I blend with PEBAX/PCS insulation had an unusually high break strain. Young's modulus showed no clear trend with insulation content through the interface for any of the insulations, except that the modulus values for the 75/25 P/I blends were all higher than the modulus of the propellant itself, and that the moduli of the blends containing higher levels of insulation tended to move toward the moduli of the pertinent insulations. One point to keep in mind while examining the stress-strain data is that the TPE is the load-bearing material in the system. For the propellant, there is only 3.0% TPE by weight; this value increases to 14.8%, 26.5%, and 38.3% as the insulation level in the blends increases to 25%, 50% and 75%, respectively. The hybrid insulation contains 50% TPE.

The ratios of peak to break stress (PS/BS) and peak to break strain (PE/BE) were used to characterize the shapes of the stress-strain curves of the materials. For all the materials tested, stress reached a maximum value at a particular value of strain (extension), then decreased with further strain until the test specimen ruptured. The two TPEs used to make the hybrid insulations both achieved maximum stress at an extension very near the break strain, and this peak stress was only slightly higher than the break stress, i.e., PS/BS was slightly above 1.0 and PE/BE was slightly below 1.0. Two of the insulations (PEBAX/PSS and Kraton/PCS) behaved in a similar manner while the third (PEBAX/PCS) had a higher PS/BS and a lower PE/BE. The TP-T-3006 propellant alone had ratios similar to the PEBAX/PCS insulation, although the absolute values of the stresses and strains were naturally much lower for the propellant. The 75/25 P/I blends all showed much higher values of PS/BS and much lower values of PE/BE, compared to either propellant or insulation alone. This corresponds to the large increase in Young's modulus observed for these 75/25 blends compared to unblended propellant. At higher levels of insulation in the P/I blends, the PS/BS ratios tend to decrease and the PE/BE ratios tend to increase toward the values of the insulations, with the exception of the 50/50 P/I blend with PEBAX/PCS insulation, where peak stress was reached at very low extension, as noted above. These data indicate that the hybrid insulations tend to behave like the TPEs used to make them and that, for the most part, the behavior of the propellant/insulation blends becomes more rubber-like as the insulation content increases.

Decomposition temperatures measured by TGA tended to increase with increasing insulation content through the graded interface. Decomposition temperatures measured by DSC were lower for P/I blends than for either propellant or insulation when the blends contained insulations made with PEBAX, but increased with insulation content for blends made with the Kraton/PCS insulation. All the P/I blends exhibited the "signature" endotherm of the TP-T-

3006 propellant, at 243°C, by DSC. The presence of insulation in the blends increased the amount of residue or char remaining at 1000°C, by TGA, compared to propellant alone, and changed the nature of the residue from powder to ceramic.

One important observation made in this study is that the propellant itself is degraded by continued exposure to elevated temperatures (preheating and mixing at 130°C) and possibly by long term storage under ambient conditions. Properties measured on stored propellant showed slightly lower peak stress, lower break elongation, and higher Young's modulus than reported by the manufacturer. Propellant which was preheated to soften, then "mixed" alone showed much lower values for peak stress and break strain and higher values of modulus than the stored propellant. Slow degradation on storage is potentially a more serious problem than the more extensive degradation observed on heating, since it is expected that, in making solid rocket motors with graded interfaces, the propellant and insulation will be co-extruded as the propellant is formulated, and the motor will not be made by re-extruding softened previously formed propellant with molten insulation as was done in this study. It is recommended that a long term property-time profile be established for this propellant.

The work reported here demonstrates that fairly smooth transitions in most properties are observed in blends representing a sampling of the composition continuum postulated to occur in the formation of a graded interface between propellant and insulation, i.e., that the concept of a graded interface possesses validity. No information was developed concerning the actual dimension (thickness) of the graded interface; it is presumed that this dimension could be engineered and controlled by proper selection of materials and processing conditions. Further, no attempt was made in this study to develop an optimized formulation for the insulation to facilitate formation of the graded interface. In conventional solid rocket motors (having propellants based on thermoset binders rather than TPE binders), plasticizers are incorporated into the propellant formulations. On storage, these plasticizers migrate or diffuse from the propellant through the bond line into the insulation, changing the physical properties of both. This is reputed to be a major cause of failures in the firing of solid rocket

motors (1,2). Since the TPE-based propellant used in this study also contains plasticizer to provide proper viscosity for processing (6), it is proposed that an optimized formulation for a TPE-based hybrid insulation would also incorporate plasticizer for two important reasons. First, the driving force for the diffusion of plasticizer from propellant to insulation in solid rocket motors is the concentration gradient which exists between the plasticizer-rich propellant and the plasticizer-poor insulation. Incorporation of plasticizer in the insulation would reduce or even eliminate this gradient, and thereby minimize the extent of diffusion and the resultant property changes. Second, the presence of plasticizer in the insulation would reduce its viscosity and improve its processability, and would probably promote the shear mixing of propellant and insulation, aiding in the formation of the graded interface. It should also be possible to incorporate a higher loading of preceramic polymer in the insulation, giving higher char yields and improved insulation performance. Since plasticizer is incorporated at the 7.5% level in the TP-T-3006 propellant, if the insulation is formulated with 7.5% plasticizer the concentration gradient would be zero, and there would essentially be no plasticizer diffusion through the graded interface. Preceramic and TPE could be optimized to a total of 92.5%, providing the best compromise between processability and insulation performance, using standard statistical optimization procedures.

REFERENCES

1. Oberth, A.E. *Principles of Solid Propellant Development*, CPIA Publication 469, September 1987.

2. Schreuder-Stacer, H.L. and Stacer, R.G. *Bonded Interface Technology Development for Solid Rocket Motors*, Report AL-TR-89-082, September, 1991.

3. Lichtenhan, J.D., Hawkins, T.W. and Chaffee, K.P. *Preliminary Investigation of a Graded Interface Between Solid Rocket Motor Propellants and Insulations*, Phillips Laboratory Internal Report, July, 1993.

4. Holden, G. *Application of Thermoplastic Elastomers*, in Legge, N.R., Holden, G. and Schroeder, H.E., (Eds.) *Thermoplastic Elastomers*, Hanser Publishers, N.Y., 1987.

5.   Nahlovsky, B.D., Hargis, I.G. and Ratermann, A.L. *Thermoplastic Elastomer Development*, Report AL-TR-89-010, August, 1989.

6.   Palopoli, S.F., Hartwell, J.A. and Polleck, R.R. *TPE Propellant Development*, Report PL-TR-91-3096, June, 1992.

7.   Lichtenhan, J.D., Vu, N.Q., Carter, J.A., Gilman, J. W. and Feher, F.J., *Silsesquioxane-Siloxane Copolymers from Polyhedral Silsesquioxanes*, Macromolecules, 1993, *26*, 2141-2142.

8.   Svob, G.J. *Propellant Mechanical Properties Evaluation*, in Oberth, A.E., *op. cit.*

DESIGN AND ANALYSIS OF THE AIR FORCE ACADEMY SOLID BOOSTER

T. A. Elkins
U.S. Air Force - Phillips Laboratory
Edwards AFB, CA 93524-7190

ABSTRACT

The Advanced Polymer Components Initiative[1] (APC) of the Phillips Laboratory was structured to investigate the application of Liquid-Crystal Polymers (LCPs) to rocket propulsion systems. Small test articles all the way up to a full solid booster system were examined to test the material and structural properties of the LCPs and the feasibility of their application. This paper will discuss the Air Force Academy Solid Booster application, the design concerns that had to be addressed, the analyses involved, vehicle construction techniques, testing, and the results of the research[2].

BACKGROUND

In 1989 the director of the Air Force Astronautics Laboratory (now Phillips Laboratory) presented his vision for the future of rocketry -- an all non-metal rocket. That vision spawned a series of technology demonstration programs focusing on materials and concepts that would make that vision a reality. Among the programs was the Advanced Polymer Components Initiative (APC) headed by Dr. John Rusek. The APC program was a 4 year effort to investigate the properties and potential application of Liquid-Crystal Polymers (LCPs) to rocket propulsion systems. LCPs have numerous desirable properties which make them excellent candidates to satisfy the Space Program's need for strong, lightweight, inexpensive, high-temperature materials. Polymer characterization, synthesis, and tests of small injection-molded articles laid the groundwork for further investigation and a feasibility study.

APPROACH

The feasibility study looked at a direct metal-to-plastic replacement without taking into consideration the properties of the LCPs or the manufacturing considerations for molded plastics. For this study the simple geometry of the 2x4 motor case was selected. The 2x4 cases were injection-molded, propellant was cast into the case, and the propellant was ignited. The tests showed that the materials could withstand direct plume contact with flame temperatures of at least 5000°F for 1-2 seconds and that LCP pressure vessels could contain fairly high pressures on the order of 1000psi.

With the success of the 2x4 tests the members of the APC team began directing their attention to the Air Force Academy Booster. The AFA solid booster is an educational tool used by the Air Force Academy to aid the cadets in understanding rocket propulsion systems. The existing system consists of a paper/phenolic case, a separate paper/phenolic forward bulkhead, and a machined graphite nozzle (see Figure 1). The case and bulkhead are prepared by hand. The assembled booster system is inserted into a launch vehicle to provide the thrust needed to lift the vehicle, booster, guidance system, recovery system, and payload.

The primary goals of the research were to determine what components of the booster system, if any, could be replaced with LCP parts without compromising safety, reliability or performance. Additional goals to reduce the cost and labor involved in manufacturing the boosters were proposed. These goals and the results of the previous research and tests formed the framework for the design.

Figure 1. Technology Demonstration Articles For The APC Initiative
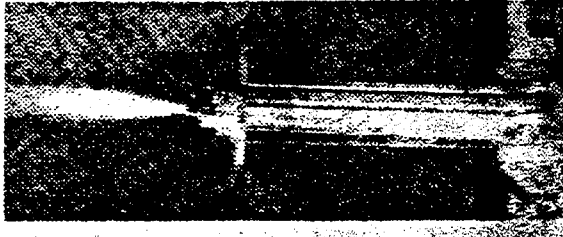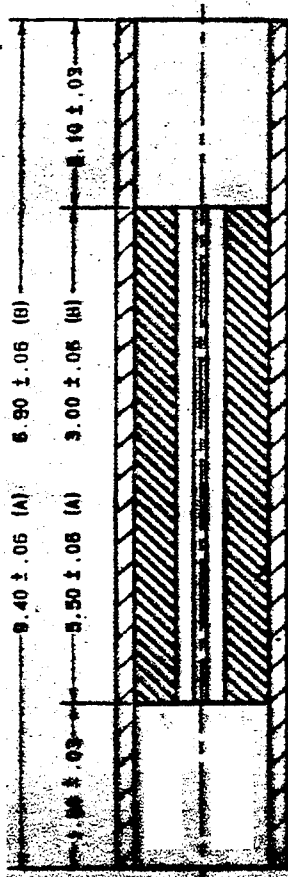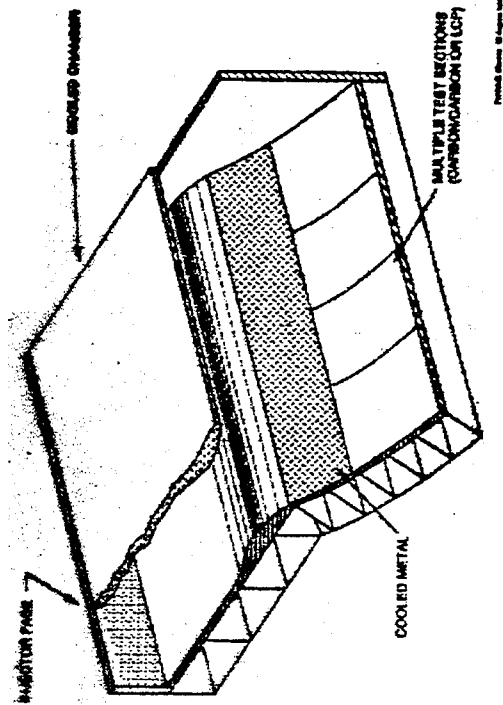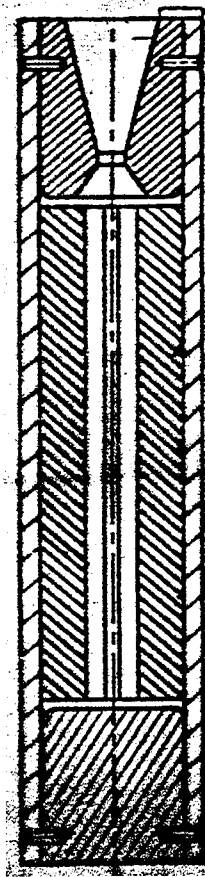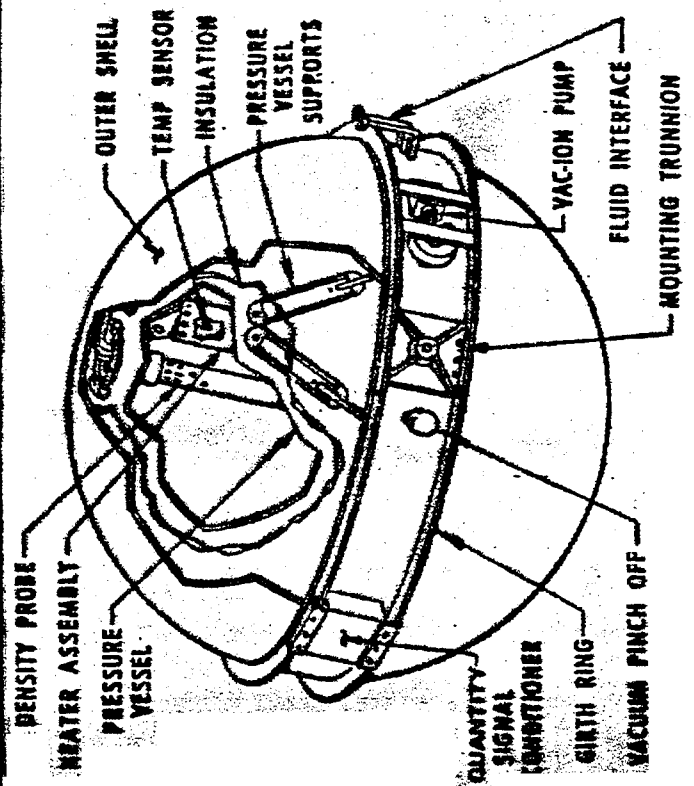
DESIGN ISSUES

MATERIAL LIMITATIONS

From the 2x4 study and other research it was determined that the LCP fibers, the source of the material's strength, form in the direction of molten flow due to the high shear fields within the mold. As a result the molded LCP material is highly anisotropic. Pressure vessels, like the booster's case, require sufficient hoop strength to handle the high pressures of the combustion process as well as longitudinal strength to combat the acceleration forces of the launch and boost phases. Previous research in the APC program revealed that material properties transverse to the molten flow were on the order of 50% of the properties in the flow direction. Other material characterization discovered a skin-and-core effect which produced highly oriented fibers along the skin of the molded part, and a more isotropic structure in the center of the part. The critical parts of the booster were designed to be as thin as possible to maximize the strength of the skin region while still maintaining structural integrity and manufacturability.

STRUCTURAL REQUIREMENTS

The booster system will be used by inexperienced cadets at the Air Force Academy in their study of rocket propulsion systems. For that reason the safety factors for the structural requirements are quite high, and this is a fairly small component which must fit inside a launch vehicle, so all of the structural members must fit in a compact volume. The existing system provides a performance benchmark that the new system must meet or exceed.

The propulsion system transfers its thrust to the main vehicle by pushing against a flat bulkhead inside the vehicle, requiring a flat surface on the forward end of the booster. The requirement for also having a hemispherical pressure dome in the same area poses a problem -- large volume changes in plastic parts can cause the plastic to warp and shrink, and an isotropic volume will form which considerably reduces the strength. A series of four ribs provides the flat surface as well as strengthens the forward pressure dome without compromising the overall material properties.

MANUFACTURING LIMITATIONS

Blow-molding an entire vehicle would provide the least expensive and strongest solution to the problem; the blow-molding process would produce a biaxially oriented part which would provide the proper hoop and longitudinal strength, the nozzle and forward dome would be integrated with the case to eliminate joints and seals, and the labor involved would be negligible. Blow molding, however, would have required a significant capital investment which was not a goal of the program, and the annoying technicality of not being able to cast the solid propellant into the case defeated the goal of reducing labor. It was decided that injection-molding, a well established manufacturing process, would yield the desired degree of reliability and producibility while remaining within a reasonable budget. It was decided that the forward pressure dome and case could be injection-molded as one piece, and the nozzle as a separate part.

Injection-molding cylindrical parts, such as the booster case and nozzle, requires that the parts be filled from end to end to prevent weld, or "knit," lines; however, as was mentioned above, the LCP fibers form in the direction of the flow within the mold. The resulting anisotropy prohibits the formation of hoop load-bearing members in cylindrical structures. From the 2x4 tests, though, it was shown that a LCP case with no hoop reinforcement could withstand pressures in excess of the operating pressures of the existing
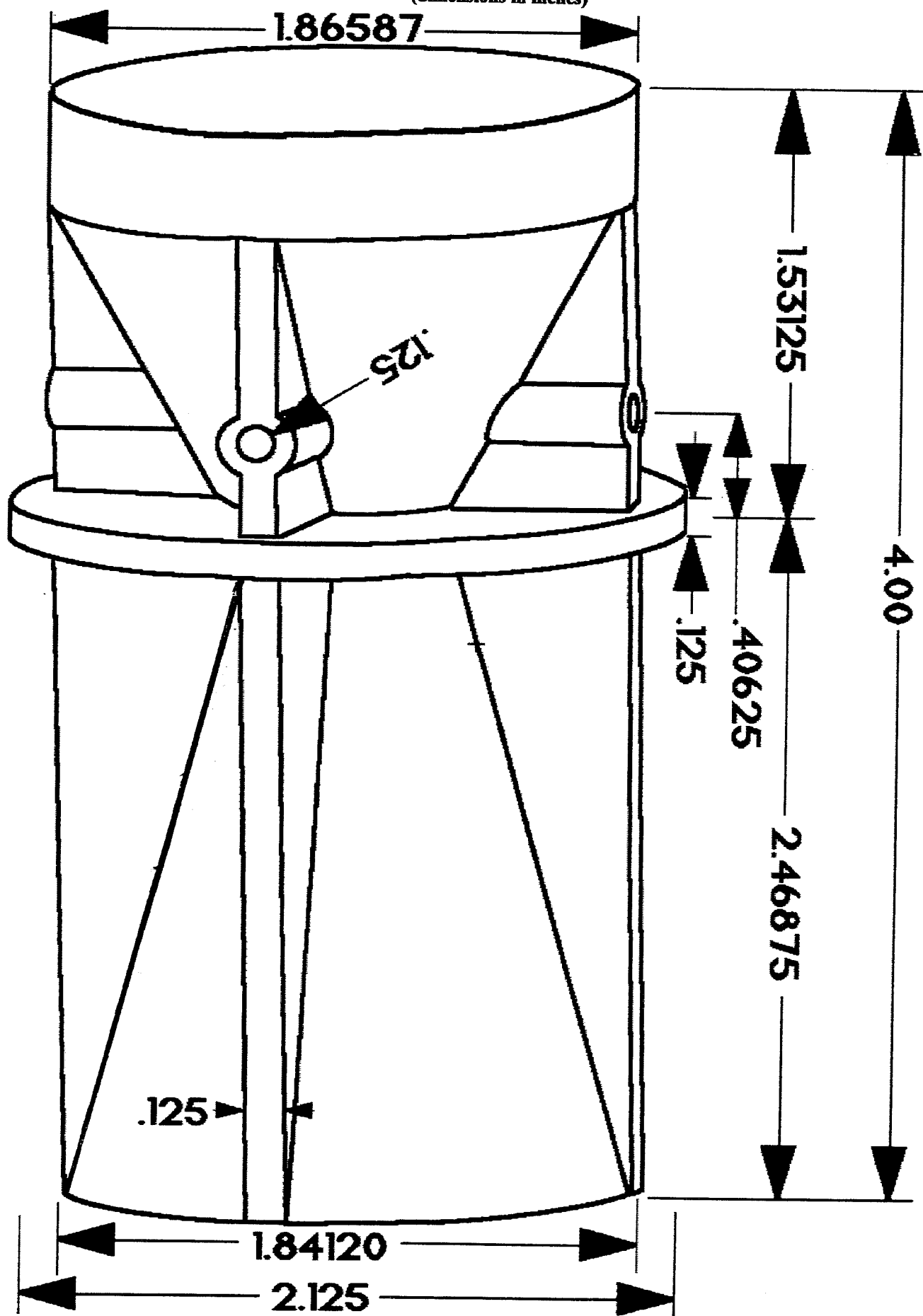
Figure 2. 3D Model Of The Initial Nozzle Design
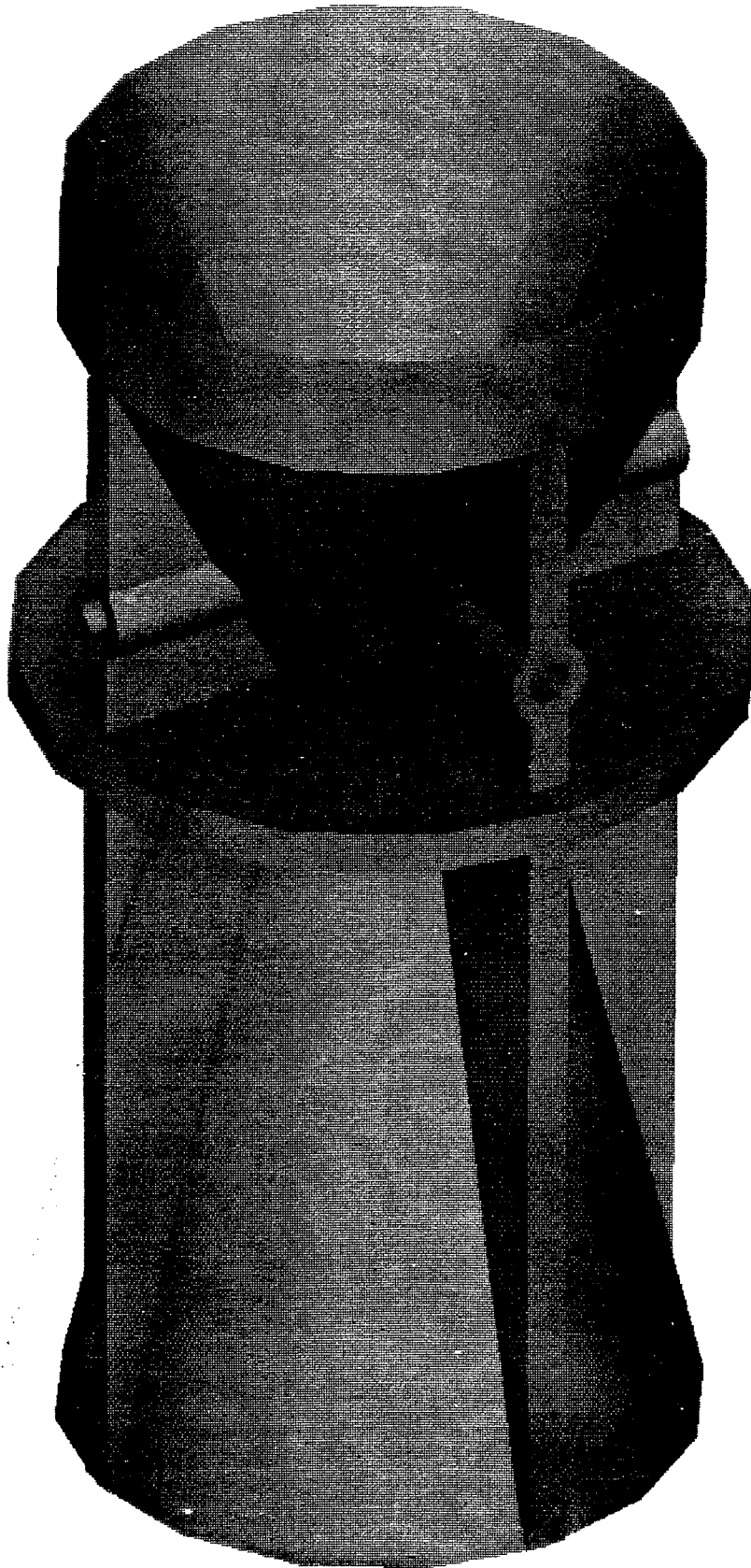
Figure 3. Initial Nozzle Design
(dimensions in inches)

1.86587

.125

1.53125

.125

.40625

4.00

2.46875

.125

1.84120

2.125

AFA booster system. Further reinforcement of the case would be desirable to increase reliability, but that was beyond the scope of the research. The converging-diverging shape of the nozzle provided an avenue for conquering the manufacturing limitation while maintaining the dimensional limits. External structural members (the longitudinal and circumferential ribs) provided the hoop load-bearing supports for the nozzle at the expense of manufacturing complexity (see Figures 2 & 3). Injecting the plastic from one end of the nozzle, though, would force the plastic to flow longitudinally through the supports, defeating the purpose of having the supports in the first place. The injection gate was moved to the throat of the nozzle to allow the plastic to flow properly through the nominal wall and force the flow to change direction at the support ribs, and no weld lines would be formed.

Plastics tend to shrink as they cool which can cause the molded part to shrink onto the tool preventing the part from being ejected from the mold. To avoid this problem parts with cavities are molded with an interior "draft angle" which provides a mechanism for shrinking parts to eject themselves from the mold core. The nozzle shape, by default, has interior angles so this was not a problem. The case, however, had to be designed with a draft angle, which caused a couple of problems:

1. The forward end of the nozzle inserts into, and must be flush with, the aft end of the case. The exterior of the nozzle was given the same draft angle as the interior of the case so that the nozzle would fit flush against the case when fully inserted.

2. The conical propellant geometry would alter the thrust profile. Various alternatives were considered and tested, including casting the propellant into a cylindrical tube which would slide into the case,

One method to reduce the costs involved in a research and development program is to identify multiple customers for the product, so additional applications of the AFA booster components were considered and incorporated into the design. Before any major capital investment was made, analyses on the design were performed.

ANALYSES

PRODUCIBILITY ANALYSIS

The 2x4 test, as well as the injection-molding team's experience, provided the knowledge necessary for manufacturing the booster case. The nozzle, however, required a more detailed analysis to determine if the part could be injection molded. A second reason for the producibility analysis was to determine if the nozzle could use the same mold base as the 2x4 motor case. The overall dimensions of the two parts are close enough that using the same mold base with different core and cavity pieces would make economical sense. A finite element model of the 2x4 mold's filling and cooling system were modeled and the nozzle model was inserted into place (see Figure 4). A filling and cooling analysis showed that the 2x4 mold base could be used to mold and cool the nozzle in about 16 seconds and that the molten plastic would flow through the structural members in the proper orientation (see Figures 5 & 6).

STRUCTURAL ANALYSIS

A 2-dimensional structural analysis was performed to see if the plastic nozzle could withstand the pressures of the environment. The pressure load and resulting mach profile were calculated using a 2D gas kinetics code (TDK) (see Figures 7-9). The analysis showed that the forward ribs would fail at the pin bosses due to a compressive load induced by the

Figure 4. Model Of The Nozzle With Filling And Cooling System

Figure 5. Part Cooling Analysis Results

Cooling Time (sec)

10.3
9.65
8.35
7.06
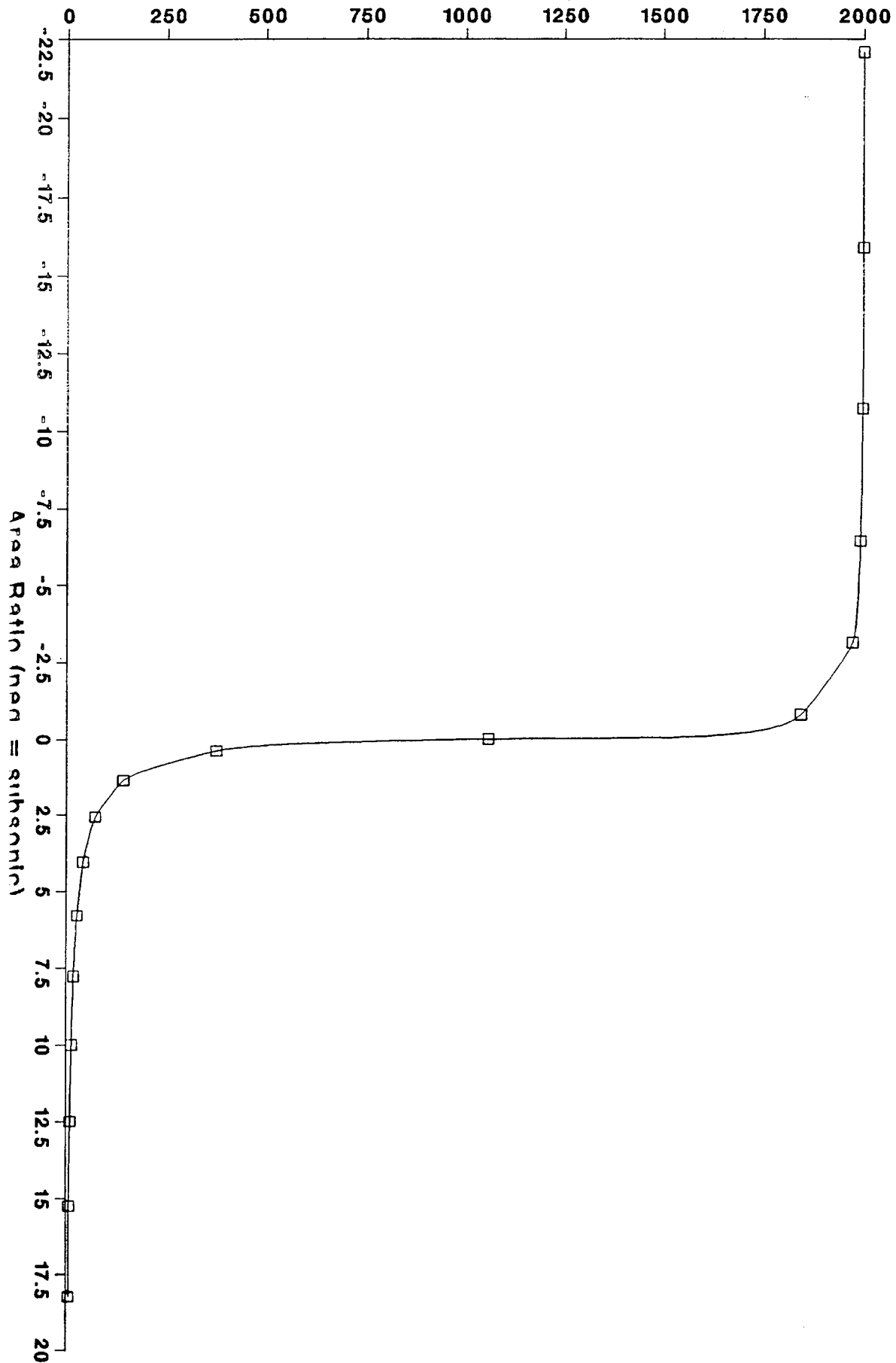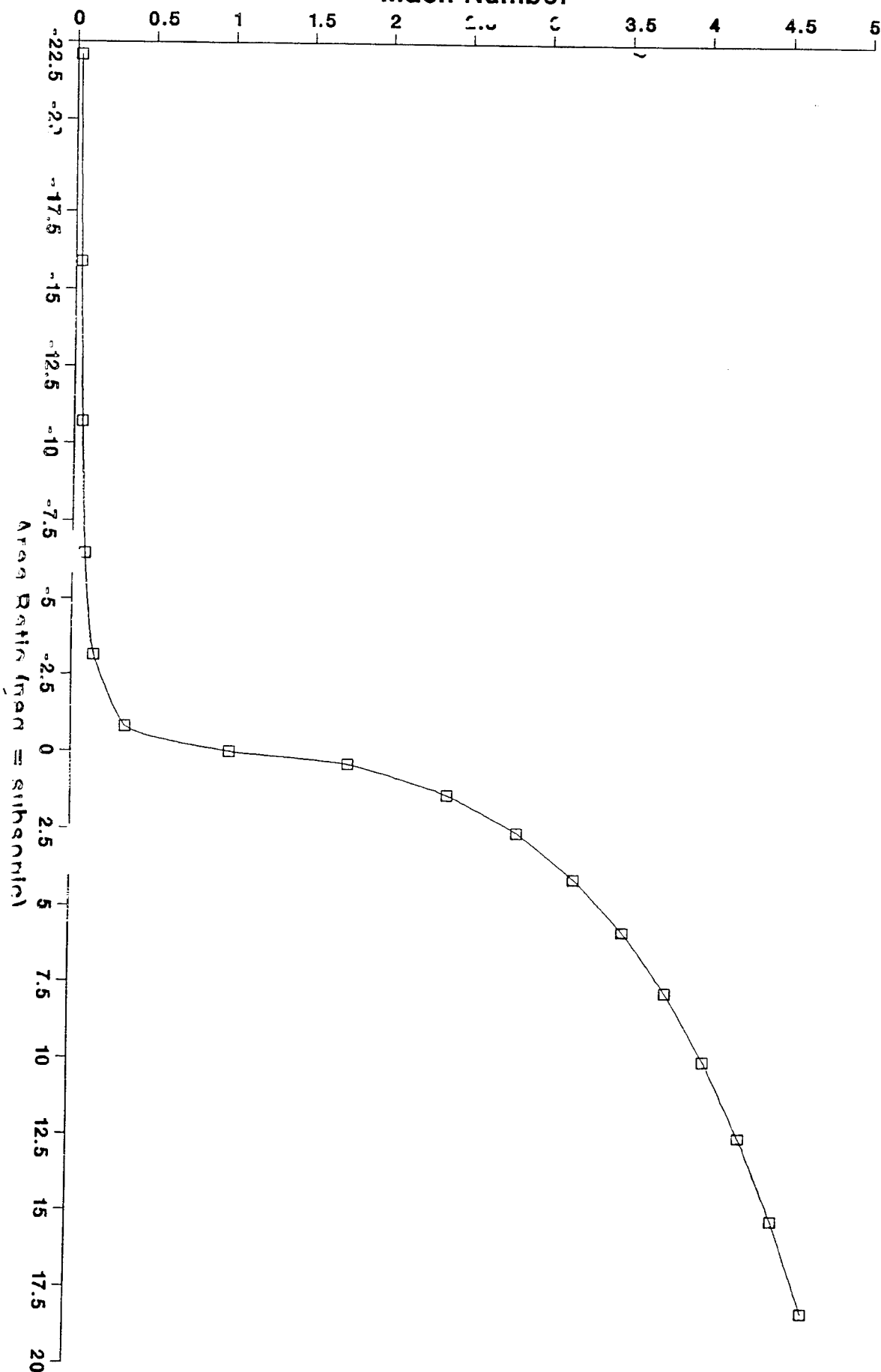5.11
1.87

Minimum : 1.87
Maximum : 11.60
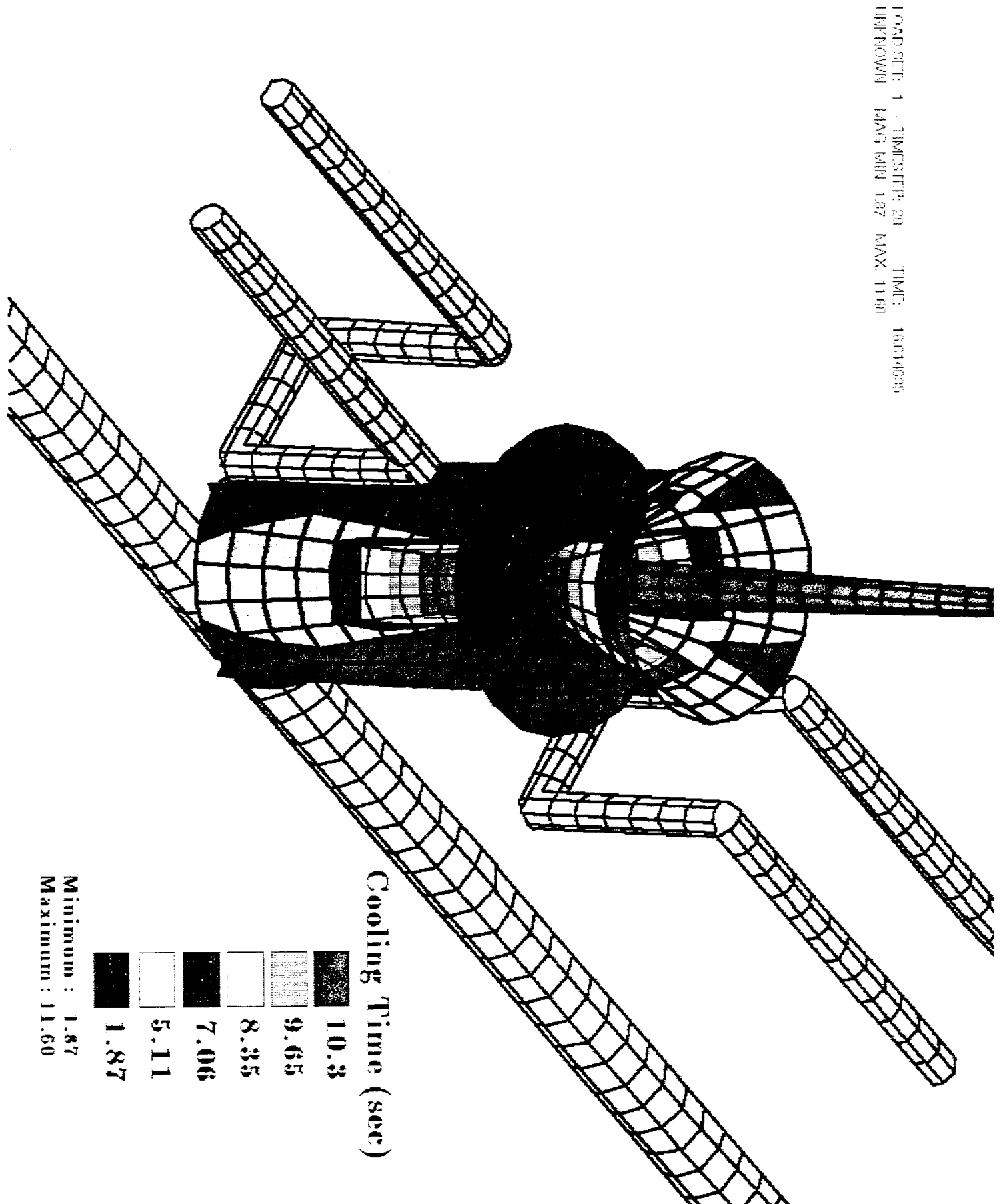
Figure 6. Mold Filling Analysis -- Checking Proper Flow Orientation
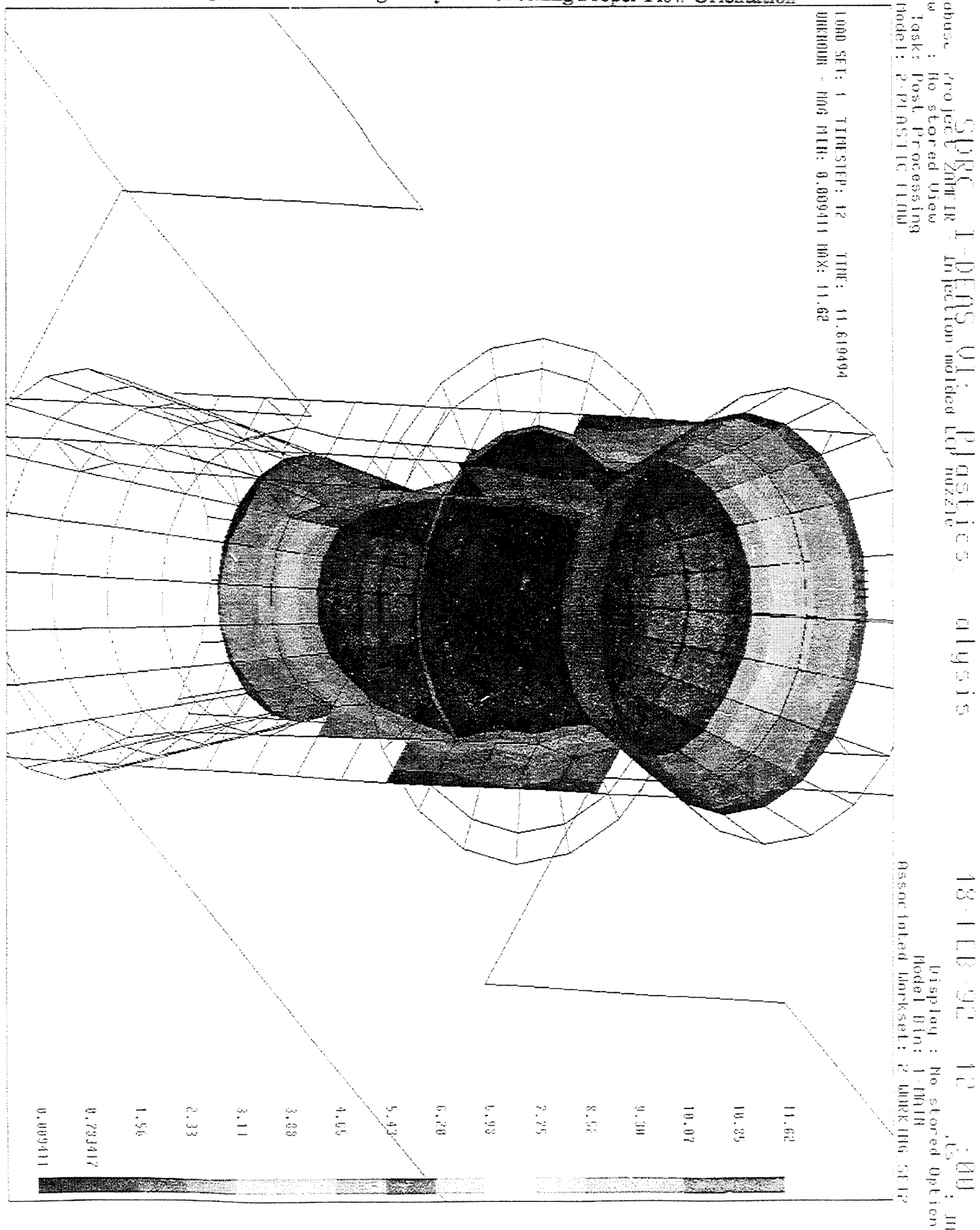
Pressure (PSIA)

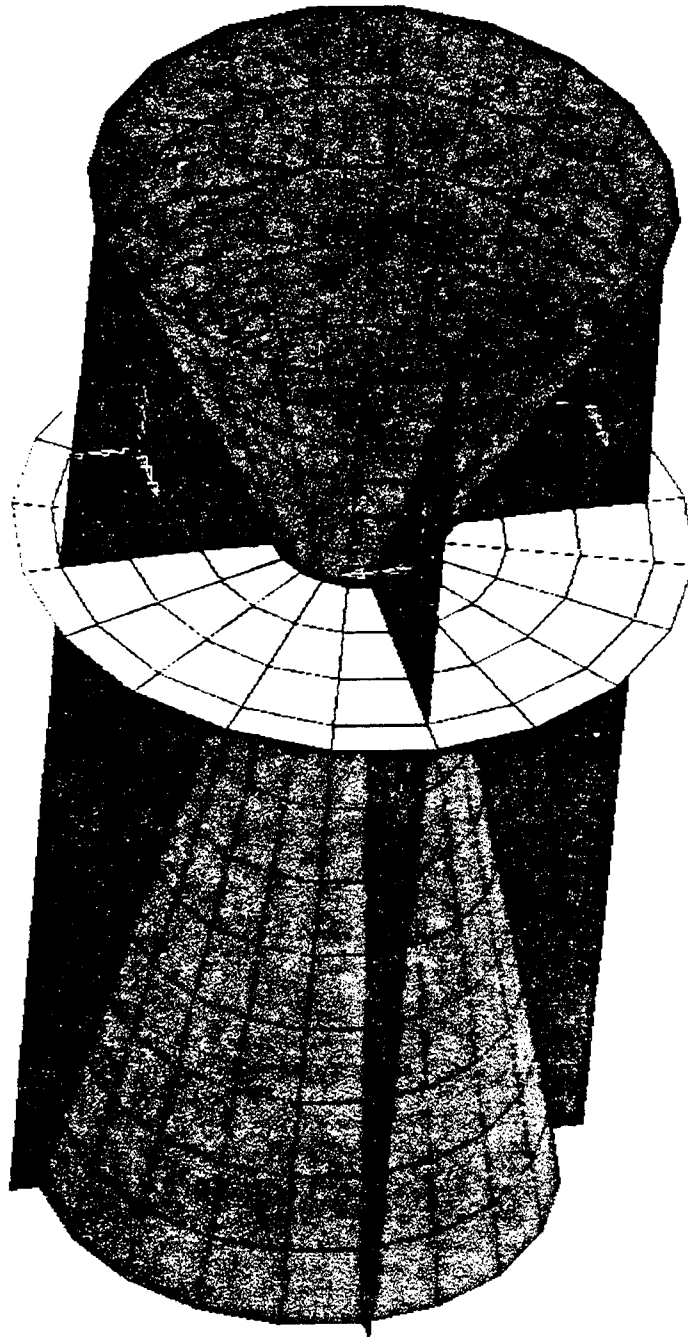LCP Nozzle static firing (GH2/Air) – ODE solution

ODE Pressure profile

Area Ratio (neg = subsonic)

Figure 7. Pressure Profile For Pc=2000psi

Figure 8. Expected Mach Profile For Nozzle @ Pc=2000psi

Figure 9. Finite Element Model Of Nozzle With Applied Pressure Load And Pin Restraints

Figure 10. Nozzle Displacement Results Of 2D Analysis

400.98

1190.02

2781.03

3576.54

5167.55

5963.05

6780.55

8349.56

9145.87

10736.08

11531.58 (psi)

Figure 11. Max. Principal Stress Results From 2D Analysis

511

Figure 12. Redesigned Nozzle With Additional Forward Rib
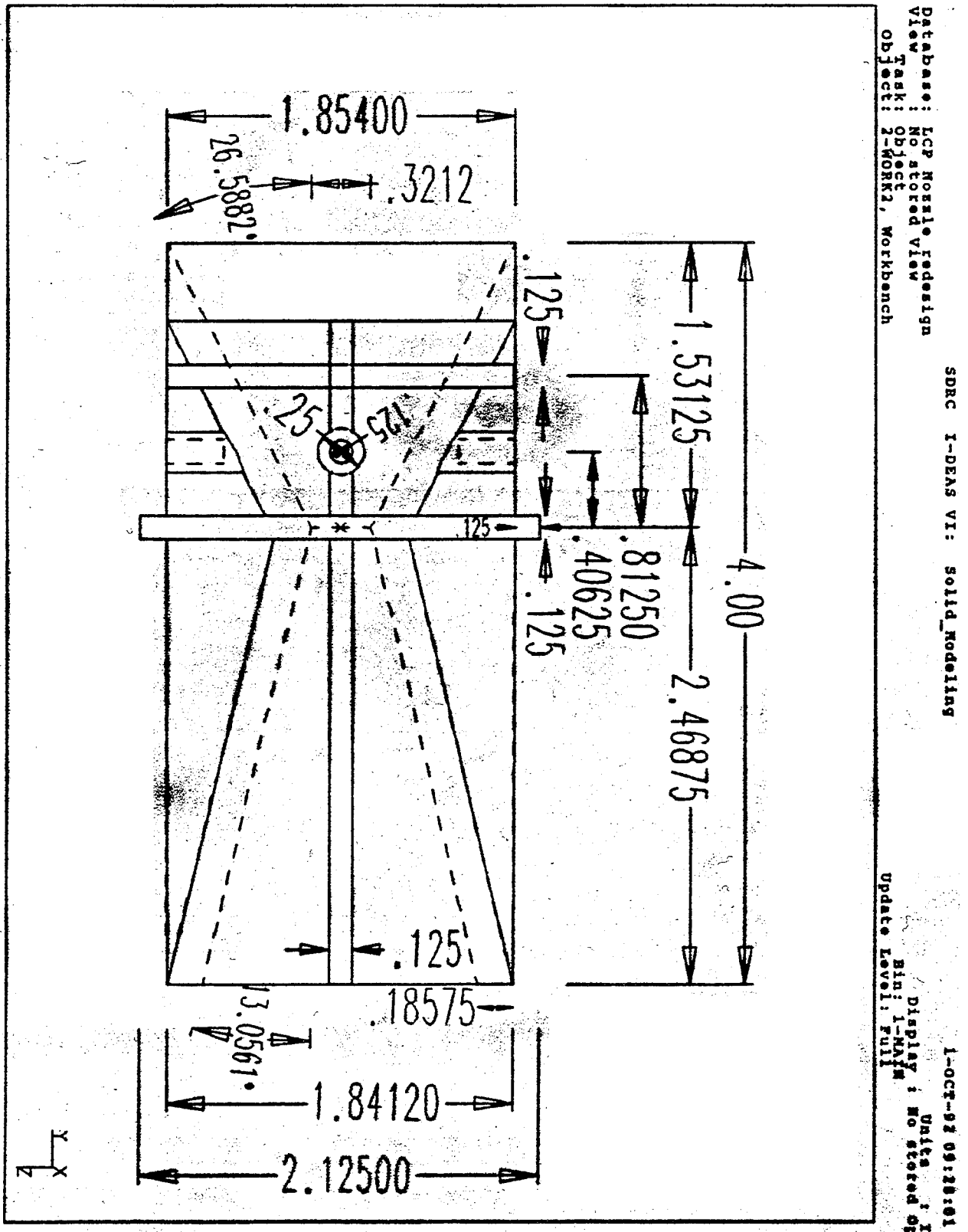
Figure 13. 3D Analysis — Pc=1000psi, No Extra Rib

Database: Structural Analysis of LLP Nozzle without forward support
View: RESULTS COMPARISON
Task: Post Processing
Model: 1-SOLID FE MODEL

Units   : IN
Display : No stored Option

Structural Analysis of LCP Nozzle without forward support

LOAD SET: 4 - GH2/AIR, PC=1000
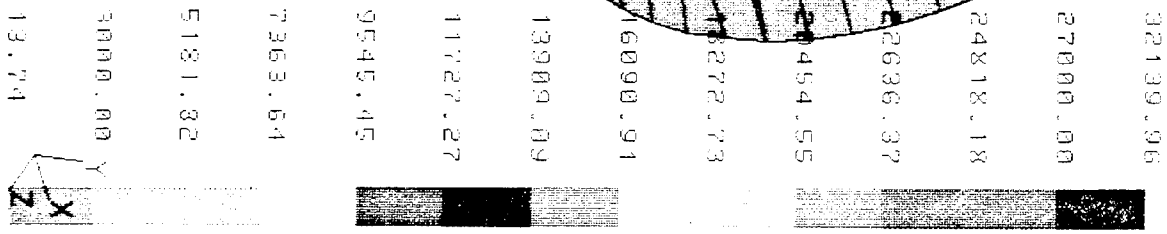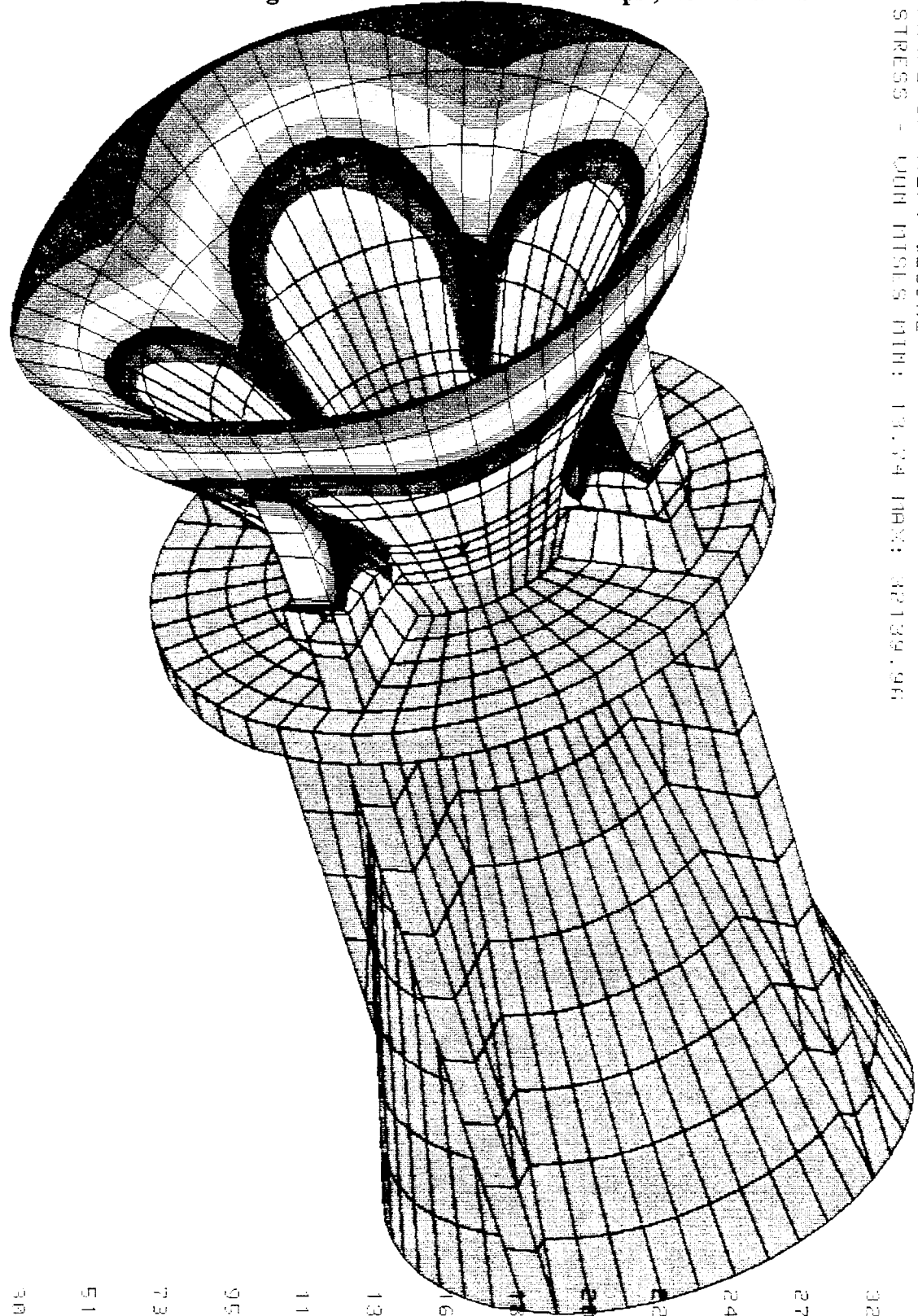FRAME OF REF: GLOBAL
STRESS - VON MISES MIN: 7.73 MAX: 16070.90

Model Bin: 1-MAIN
Model Bin: 1-MAIN
Associated Workset: 1-WORKING SET

29181.82
27000.00
24818.18
22636.37
20454.55
18272.73
16090.91
13909.09
11727.27
9545.45
7363.64
5181.82
3000.00
7.73

513

Figure 14. 3D Analysis — Pc=1250psi, No Extra Rib

SDRC I-DEAS VI: FE Modeling & Analysis   20-AUG-93 15:52:05

Database: Structural Analysis of LCP Nozzle without forward support
View   : RESULTS COMPARISON   Display : No stored Option
Task   : Post Processing   Units : IN
Model   : 1-SOLID FE MODEL   Model Bin: 1-MAIN
                                                                Associated Workset: 1-WORKING SET

          Structural Analysis of LCP Nozzle without forward support

LOAD SET: 3 - GH2/AIR, PC=1250
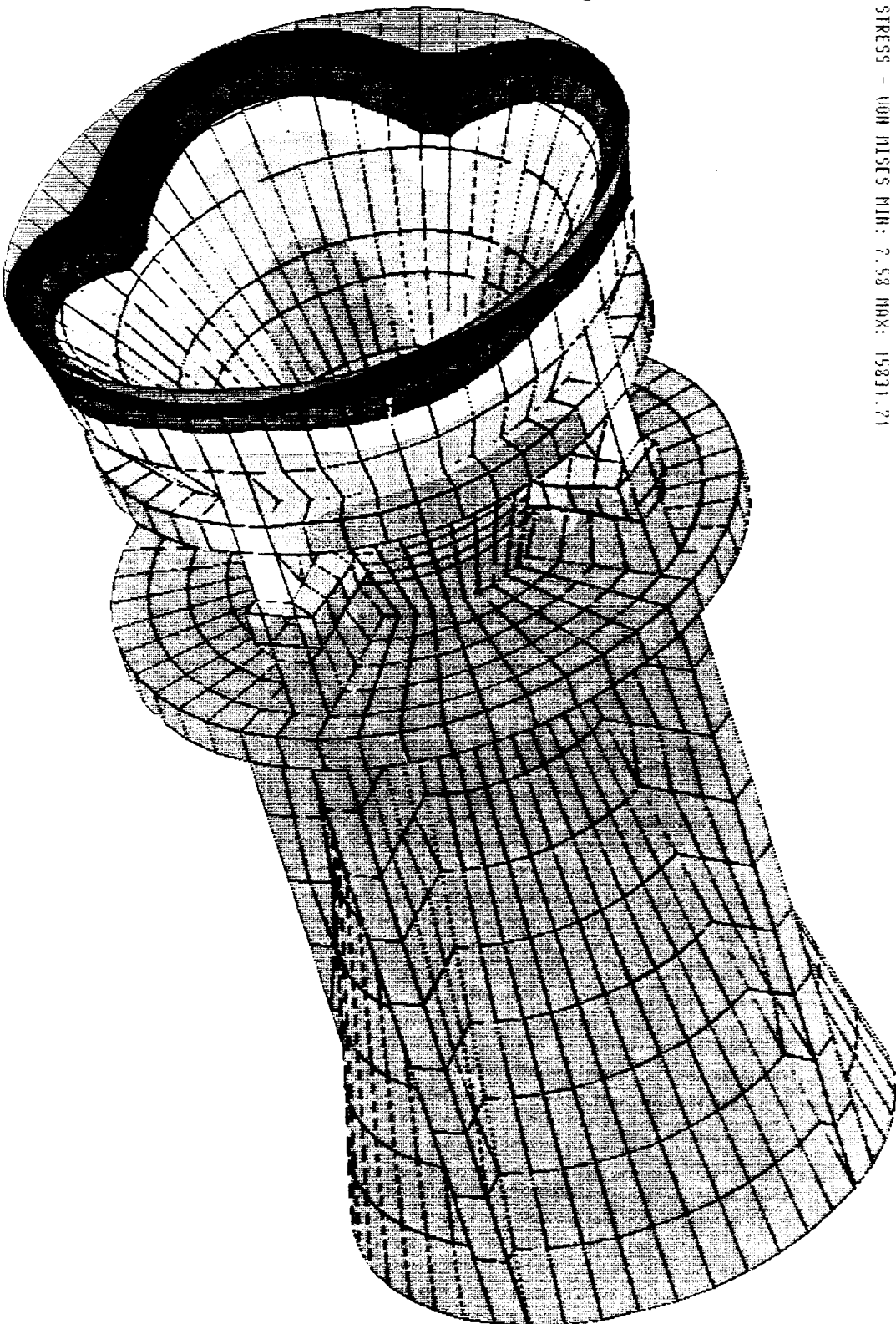FRAME OF REF: GLOBAL
STRESS - VON MISES MIN: 9.63 MAX: 20037.54

29181.82
27000.00
24818.13
26636.37
0454.55
8272.73
16090.91
13909.09
11727.27
9545.45
7363.64
5181.82
3000.00
9.63

Figure 15. 3D Analysis — Pc=1500psi, No Extra Rib

515

Figure 16. 3D Analysis — Pc=2000psi, No Extra Rib

Figure 16. 3D Analysis — Pc=2000psi, No Extra Rib

Figure 17. 3D Analysis — Pc=1000psi, With Extra Rib

SDRC I-DEAS VI: FE Modeling & Analysis   20-AUG-93   17:48:11

Database: 3D Model of the LCP Nozzle - by Tom Likins/RKAD   Units   : IN
View :   Display : No stored Option
Task: RESULTS COMPARISON   Model Bin: 1-MAIN
Model: Post Processing   Associated Workset: 1-WORKING_SET
Model: 1-SOLID FE MODEL

3D Model of the LCP Nozzle - by Tom Elkins/RKAD

LOAD SET: 4 - GH2/AIR, PC=1000
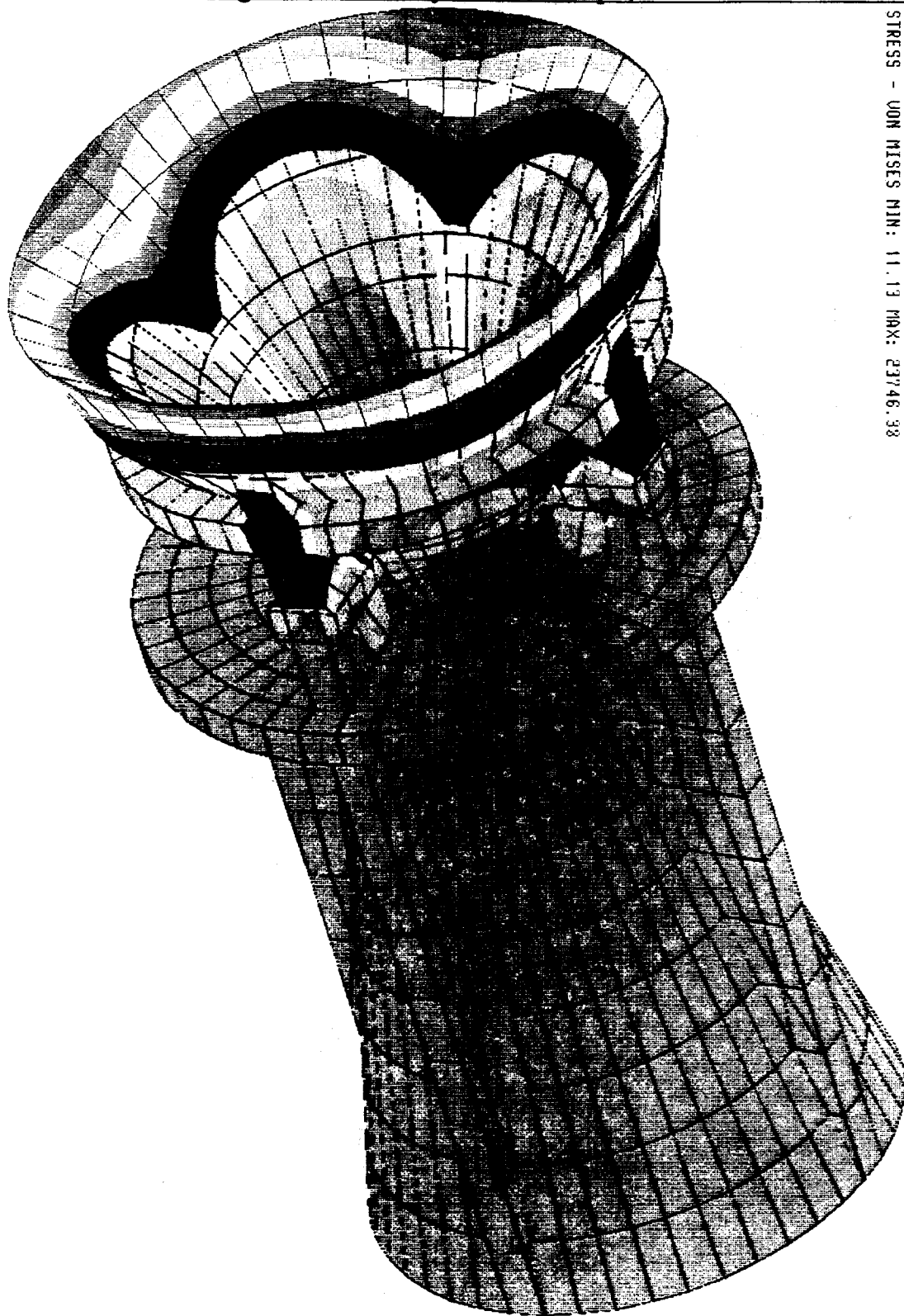FRAME OF REF: GLOBAL
STRESS - VON MISES MIN: 7.58 MAX: 15831.71

29131.36
27800.00
24818.18
22636.37
20454.55
18272.73
16090.91
13909.09
11727.27
9545.45
7363.64
5181.82
3000.00
7.58

517

Figure 18. 3D Analysis -- Pc=1250psi, With Extra Rib

Figure 19. 3D Analysis — Pc=1500psi, With Extra Rib

Database: 3D Model of the LCP Nozzle - by Tom Elkins/RKAD
View   : RESULTS COMPARISON   Units : IN
Task: Post Processing   Display : No stored Option
Model: 1-SOLID FE MODEL   Model Bin: 1-MAIN
                                                             Associated Model Workset: 1-WORKING SET1

3D Model of the LCP Nozzle - by Tom Elkins/RKAD

LOAD SET: 2 - GH2/AIR, PC=1500
FRAME OF REF: GLOBAL
STRESS - VON MISES MIN: 11.13 MAX: 23746.38

29181.82
27000.00
24818.18
22636.37
20454.55
18272.73
16090.91
13909.09
11727.27
9545.45
7363.64
5181.82
3000.00
11.13

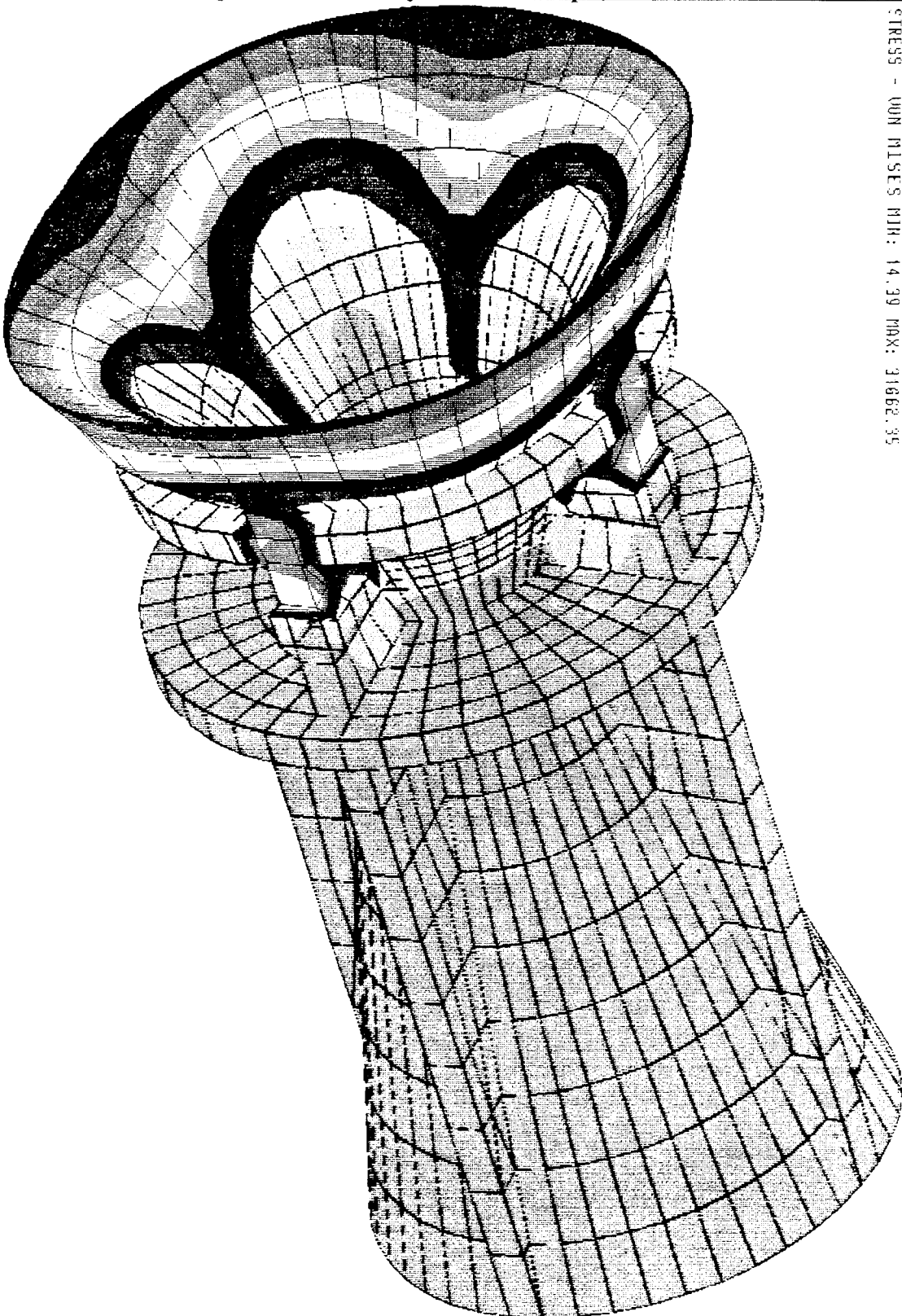**Figure 20. 3D Analysis — Pc=2000psi, With Extra Rib**

expected 2000psi chamber pressure against the inlet wall (see Figures 10 & 11). The ribs would buckle and fail at the pin bosses. The design was modified to include a second circumferential rib forward of the pin bosses to strengthen the inlet area and distribute the compressive load over the circumference (see Figure 12). In addition the second rib would provide another mating surface on which an epoxy could be applied to reinforce the seal between the nozzle and case. A 3-dimensional analysis with and without the second rib confirmed the corrective action (see Figures 13-20). With the analyses completed it was time to build and test the system.

CONSTRUCTION

To reduce the costs even further, all of the injection molding was performed at Hill AFB, and the ammonium perchlorate (AP) propellant was specially mixed and prepared at Phillips Lab - Edwards AFB. Several booster configurations were prepared and documented with the reduction of labor being the key. The following are the steps that were involved in building a test article.

1. The propellant cylinder could be inserted into the case and locked into place with a phenolic spacer, or, when a binder was applied to the inside of the case, the propellant could be cast directly into the case. The propellant geometry was simplified to a circular bore to improve safety and reduce labor (the old grain geometry required the students to cut slots in the grain with a hacksaw). The combination of a circular bore and the interior draft angle of the case generated a progressive burn profile.

2. The gate material was removed from the nozzle throat and the throat cleaned. The nozzle was inserted into the case and pinned with standard rivets. The nozzle/case interface was sealed with a urethane epoxy.

3. Simple igniters were made with a small piece of propellant wrapped with igniter wire and inserted about two-thirds of the way into the case.
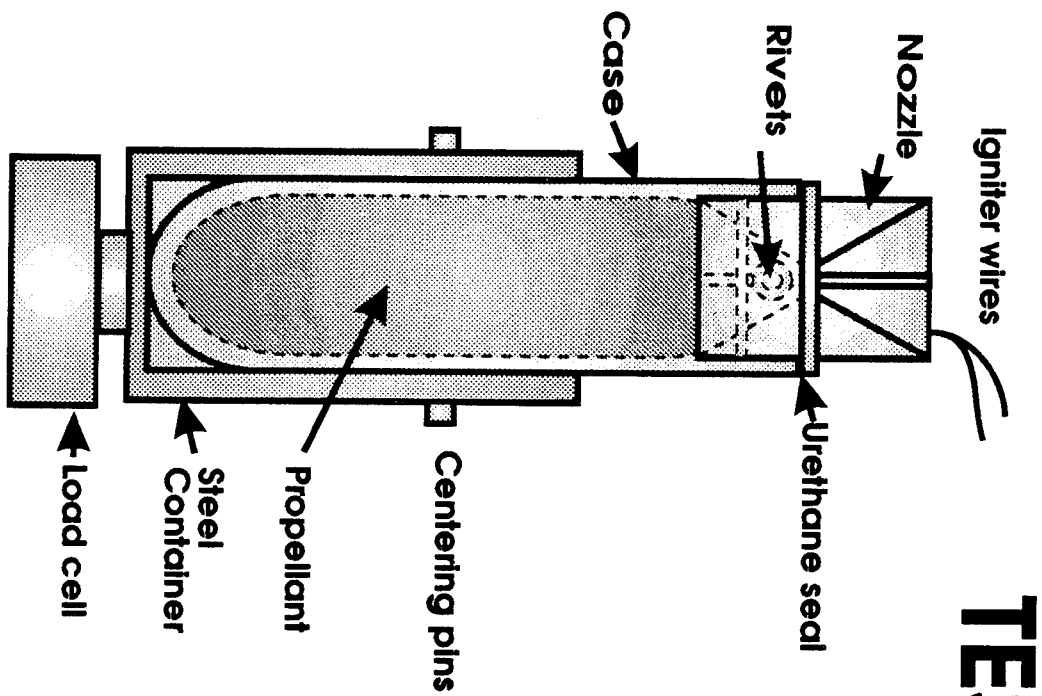
TESTING

(see Figure 21) The booster was inserted nozzle-up into a steel "cup" mounted to a load cell. Pins were used to center the booster in the container; however, the case expanded against the pins and ruptured. The early igniters clogged the throat, causing an overpressurization of the case and resulting in the failure of the pin bosses (as per the analysis). Initially the propellant tubes were cut into three segments; however, the segments shifted at the ignition pulse causing two failure modes:

1. The aft propellant segment was pushed into the throat. Cardboard from the segment was attached to the inlet area near the throat and the inlet was charred.

2. A structural-ballistic interaction occured causing the forward segment to deform and create an aerodynamic nozzle. Pressures above 16,000psi were recorded and the center and aft propellant segments showed no sign of burning.
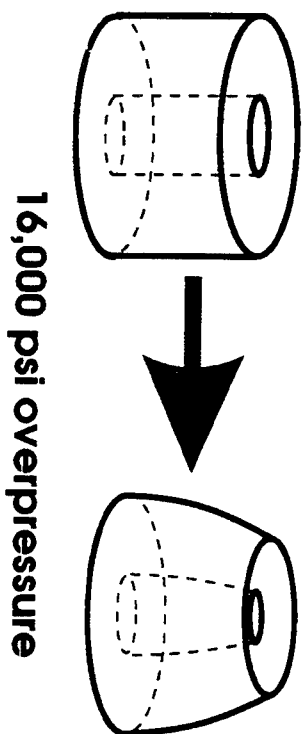
The segmented grain concept was replaced by a single tube with a phenolic spacer placed at the aft end to prevent the grain from moving into the nozzle. The next failure involved the burn-through of the nozzle which led to the use of a stainless steel insert to protect the inlet and throat areas. The stainless insert, however, vaporized indicating that the pressure and temperature at the throat were higher than expected.

Figure 21. Testing Apparatus And Failure Modes

TESTING

Igniter wires blocked throat

Propellant shift --> spacer

Centering pins ruptured case

Nozzle burn through --> inserts

Segmented grain ... SBI

16,000 psi overpressure

ADVANCED POLYMER COMPONENTS

Labels on apparatus:
- Igniter wires
- Case
- Rivets
- Nozzle
- Load cell
- Steel Container
- Propellant
- Centering pins
- Urethane seal

RESULTS

	Old Booster	New Booster
Case	Paper/Phenolic	LCP
Bulkhead	Paper/Phenolic	LCP integrated w/ case
Nozzle	Graphite	LCP
Manufacturing	By hand	Injection molded
Assembly Time	2+ hours	<5 minutes
Total Weight	351g	776g
Inert Weight	70%	37%
Thrust (Burn)	60lbf (.9sec)	41 - 209 lbf (1.88sec)
		125 lbf average
Cost	~$30	$5 - $10

CONCLUSIONS

- The research has shown that LCPs can be used as structural materials if the material properties and manufacturing limitations are examined and understood upfront. The design must answer the concerns of the metal-to-plastic replacement without compromising structural or performance requirements.

- Software tools exist that aid in the decision-making process before any capital investment is made. Simulation and analysis can be performed on nearly every step of the manufacturing and operation processes and can point out potential problems, alternative ways of doing things, and even optimize the manufacturing process to minimize costs and increase reliability.

- The injection-molding process is a well established process which lends itself well to mass production, pushing production costs down. The automation aspects of the industry reduces the labor involved in manufacturing and provides reproducibility to the system.

- As uses of the LCPs increase the cost of the raw material will drop, further reducing the costs of manufacturing with these materials.

- The research from this program, and others like it, highlight a wide range of applications and industries which will spawn further research in materials and processing techniques and provide high reliability, high performance, low cost products.

REFERENCES

1. Rusek, J. J., et al, "Proceedings of the First Annual Advanced Polymer Components Symposium", Phillips Laboratory, Edwards AFB, CA, Technical Report No. PL-TR-92-3018, July 1992

2. Elkins, T. A., Frank, C., "Design and Analysis of a Liquid-Crystal Polymer Rocket Nozzle", *JANNAF Structures and Mechanical Behavior Subcommittee Meeting*, November, 1992

LIQUID CRYSTAL POLYMER AFA BOOSTER MOTOR DEVELOPMENT: PROPELLANT DEVELOPMENT, MOTOR DESIGN AND PRELIMINARY TESTING

Hieu T. Nguyen
Phillips Laboratory
Edwards AFB, CA 93524-7160

ABSTRACT

The Phillips Laboratory is currently testing a new booster rocket motor for the United States Air Force Academy. The original AFA booster motor the Phillips Lab had been manufacturing was labor intensive. The phenolic case and the graphite nozzle had to be individually machined. The new motor being tested has an injection molded liquid crystal polymer (LCP) case and nozzle. The motor is also larger and has almost twice the total impulse.

INTRODUCTION

The original objectives of the task were to 1) develop three non-aluminized propellants with three different burn rates (low (0.25 in/sec), medium (0.35 in/sec) and high (0.5 in/sec)), 2) design a cartridge loaded, neutral burning propellant charge, and 3) test and determine the performance of the motors. Aluminum fuel was not used in the propellants in order lower the throat erosion rate of the LCP nozzles. Three different burn rates were designed to provide three different thrust levels. The cartridge-loaded type propellant grain was selected in order to reduce production time and cost. The AFA motors were static tested to determine thrust vs. time and also total impulse.

PROPELLANT DEVELOPMENT

All three propellants contained hydroxy-terminated polybutadiene (HTPB) binder cured with dimeryl diisocyanate (DDI). This binder also served as the fuel. The plasticizer used to ease processing and improve mechanical properties was dioctylazelate (DOZ). Three different ammonium perchlorate (AP) oxidizer sizes and ratios were used to achieve the three desired burn rates. Iron oxide was used to help increase burn rate and ammonium nitrate (a low burn rate oxidizer) was used to decrease burn rate. Additives such as copper ammonium chlorate, potassium perchlorate and strontium nitrate provided different plume colors. The formulations of the three propellants are shown in Table 1.

The burn rates of all three propellants were characterized. However, only the high burn rate propellant was used in the AFA motors. The low and medium burn rate propellants were abandoned due to processing difficulties. Apparently, the ammonium nitrate in the low burn rate propellant and the boron in the medium burn rate propellant caused extremely high end-of-mix viscosity, which prevented vacuum casting.

INGREDIENT	LOW BURN RATE (%)	MEDIUM BURN RATE (%)	HIGH BURN RATE (%)
HTPB	10.46	10.46	10.46
DOZ	2.15	2.15	2.15
DDI	2.39	2.39	2.39
AP (400 microns)	40.00	27.11	24.93
AP (200 microns)	20.00	27.11	24.93
AP (25 microns)		20.78	24.93
AN	15.00		
Iron Oxide			0.20
Copper Ammonium Chlor	2.00		
Potassium Perchlorate	8.00		
Strontium Nitrate			10.00
Boron		10.00	

Table 1

PROPELLANT GRAIN DESIGN AND INITIAL MOTOR TESTING

The AFA booster motor was originally designed to have three neutral-burning cartridge loaded propellant grains (see Figure 1). However, this design had a variety of problems which were discovered during test firings. A total of 18 motors with the cartridge loaded type grains were tested and all failed due a combination of problems.

After the first three motors failed to overpressurization, it was discovered that following ignition the propellant grain closest to the nozzle was pushed into the nozzle entrance. Apparently the pressure at the forward end of this grain was much higher the pressure at the end facing the nozzle. The pressure difference thus pushed the grain into the nozzle entrance, squeezing the diameter of the grain and center perforation down to the point of choking the flow of the propellant exhaust. This apparently caused overpressurization and motor failure.
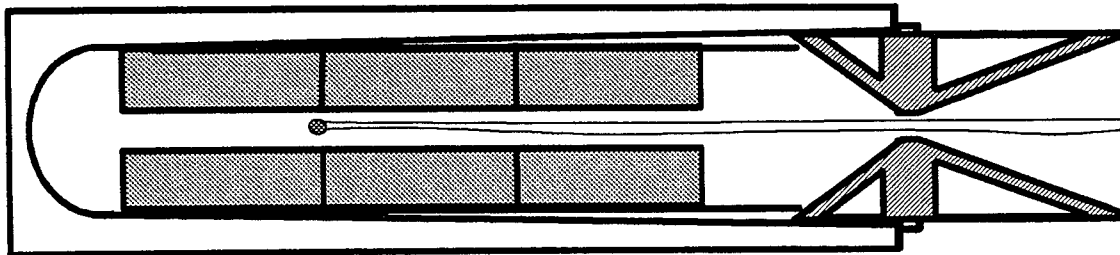

Figure 1. AFA Motor Design with Three Propellant Cartridges

A phenolic spacer was placed between the grain and the nozzle to prevent the grain movement problem (see Figure 2). However, when the motors with this design was test fired, they also overpressured. Inspection of the remains showed that the case as well as the grain segment next to the phenolic spacer had burst. This failure mode was apparently also caused by uneven pressure buildup. Since the inside of the case was tapered and the propellant cartridge was not, there was a significant gap between the grain and the inner wall of the case near the nozzle entrance. During ignition, the pressure difference between the center perforation and the outside of the grain was high enough burst the grain. The extra burn surface area of the damaged grain caused higher gas output and overpressurization.
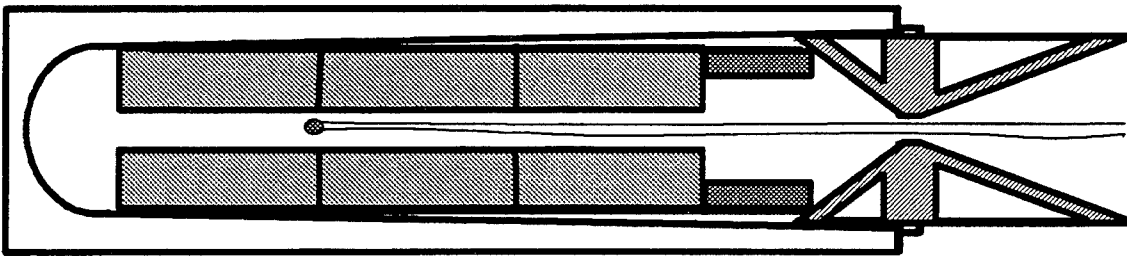

Figure 2. AFA Motor Design with Three Propellant Cartridges and Phenolic Spacer

The cartridge loaded propellant grain design was abandoned and the more conventional case-bonded grain design was used (see Figure 3). When motors with this design were test fired, the grain performed as expected. However, the nozzle throat burned through after about 1.5 seconds into the firing. The nozzle was later fitted with stainless steel throat insert to attempt to delay throat erosion (see Figure 4). This nozzle design also failed, however. The nozzle throat burned through after about 1 second into the firing. The stainless steel throat insert design was also abandoned. The nozzle was later redesigned to be significantly thicker at the throat to take into account the high erosion rate (see Figure 5).
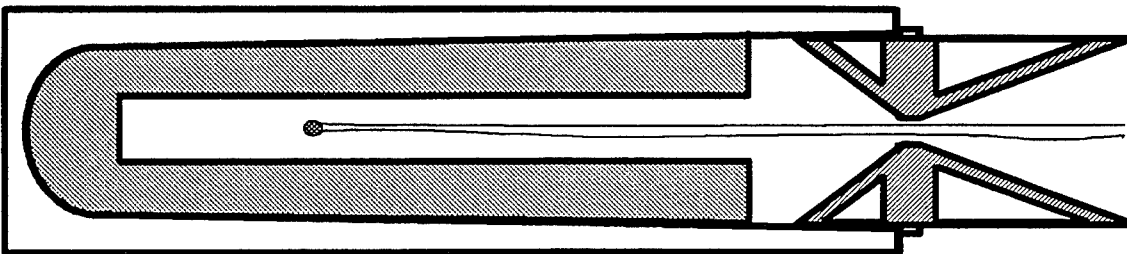

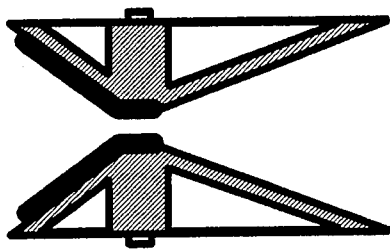**Figure 3. AFA Motor with Case-bonded Propellant Grain**
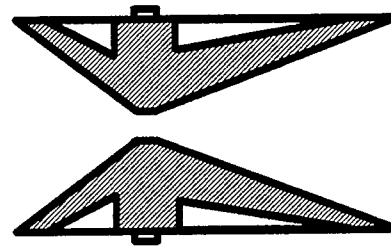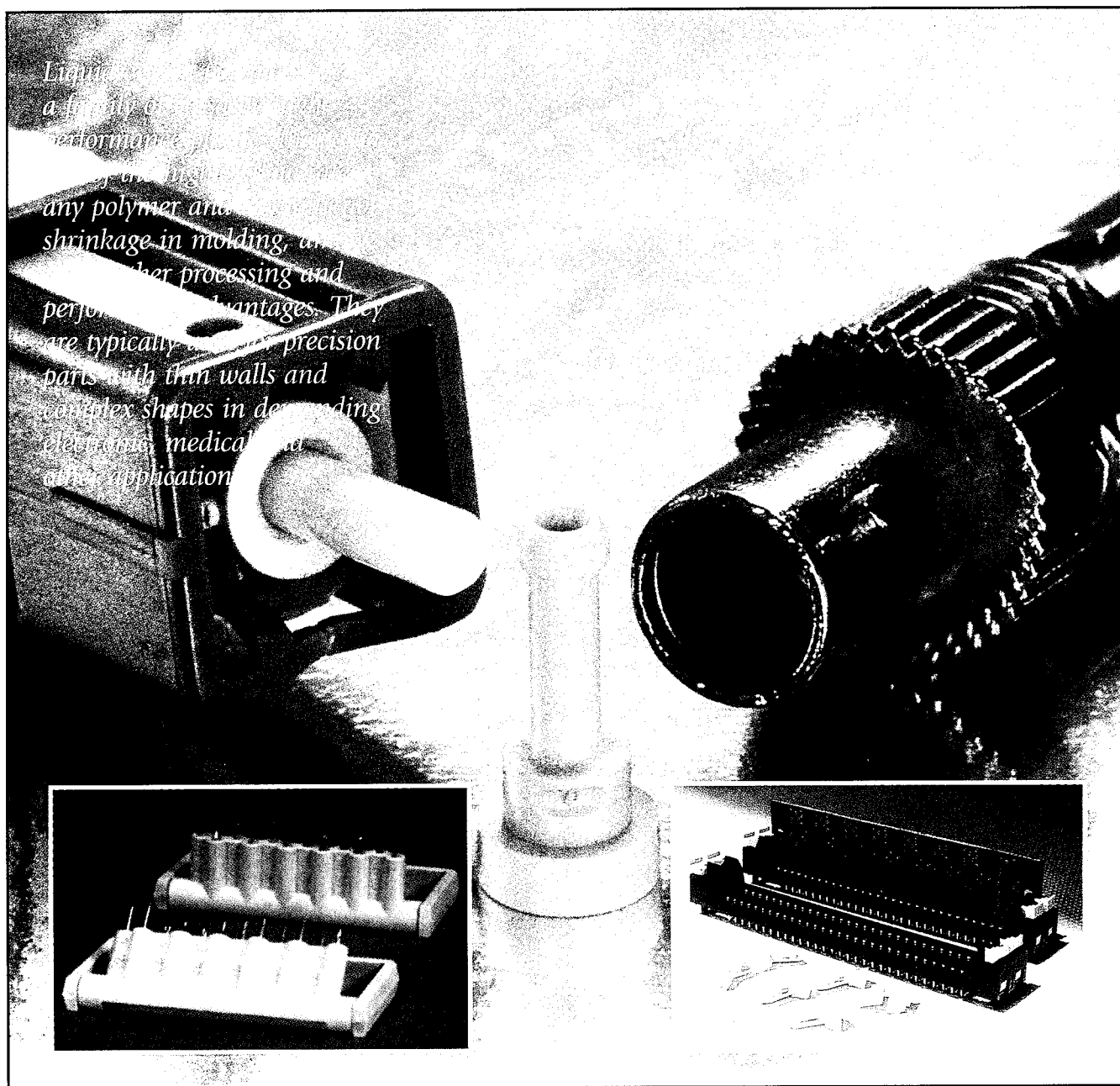
Figure 4. Nozzle with Throat Insert

**Figure 5. Nozzle with Increased
Throat Thickness**

CONCLUSION

The final AFA booster motor design has a conventional case-bonded propellant grain, a non-aluminized propellant, LCP case and nozzle. Four types of LCP's were used: Vectra B420, Vectra B950, Vectra B230 and Vectra A950. A band clamp was also added to the nozzle attachment point for reinforcement. The motor has a total impulse of 110 lb-sec, which is almost double the impulse of the original AFA booster motor. Manufacturing is also much less labor intensive since several hundred cases and nozzles can be injection molded in one day.

Liquid Crystal Polymers: A Primer

Anne Kaslusky

Hoechst Celanese Corporation

Liquid [crystal polymers are] a family of [materials with high-] performance [properties...] [the] [...] high [...] any polymer and [...] shrinkage in molding, a[nd] [ot]her processing and perfo[rmance] [adv]antages. They are typically [used in] precision parts [w]ith thin walls and complex shapes in dem[an]ding elec[tr]onic, medica[l, an]d other application[s].
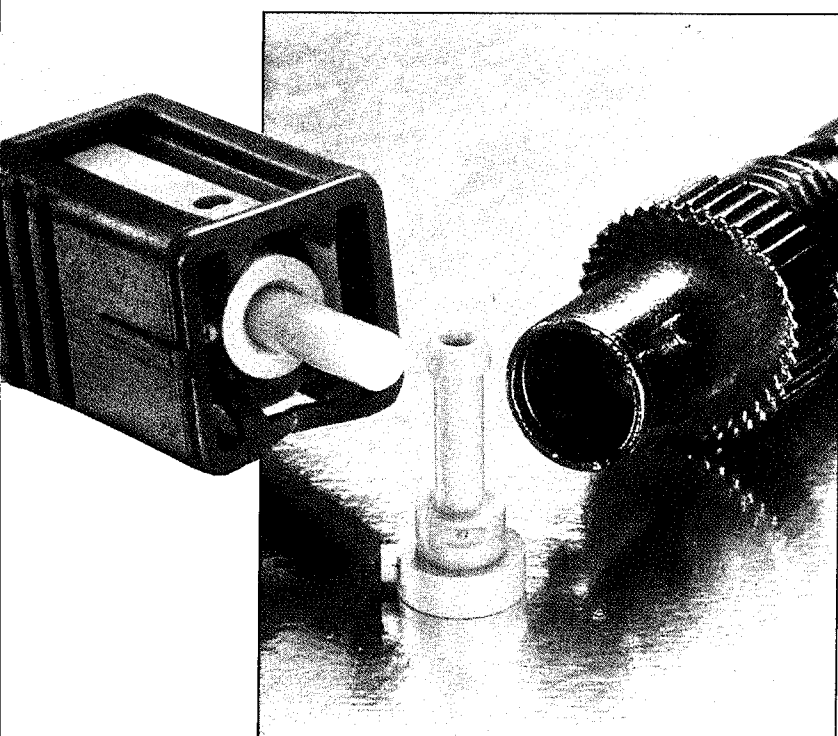
A relatively new family of high-performance plastics offers excellent stability at high temperatures, high rigidity and strength at low temperatures, superior chemical resistance, and little dimensional change with varying temperature and humidity.

LIQUID CRYSTAL POLYMERS

A Primer

Anne Kaslusky
Hoechst Celanese Corporation
Summit, N.J.

L iquid crystal polymers (LCPs) are distinguished from other plastics by their rodlike microstructure in the melt phase. Other resins have randomly oriented molecules in the melt phase, but when LCPs melt, their long, rigid molecules can align into a highly ordered configuration that produces a number of unique features. These include low heat of crystallization, extremely high flow, and significant melt strength. The molecular structure has such a profound effect on properties and processing characteristics that LCPs are best treated as a polymer category separate from amorphous and semi-crystalline resins. In spite of their unique properties, however, LCPs can be processed by all conventional thermoplastic forming techniques.

Liquid crystal polymers may cost as much as $18 to $44/kg ($8 to $20/lb), but they offer processing and performance advantages that often result in lower overall cost than less expensive resins. They can, for instance, easily flow into molds for very thin or highly complex parts, reduce cycle time in molding, produce parts with little molded-in stress, eliminate deflashing and other secondary finishing steps, and reduce part breakage during assembly. These benefits can raise finished assembly or system yields 3% or more, which can more than offset the higher resin cost.

LCPs are especially suited for small-to-medium size parts with complex shapes or thin walls, which must hold tight tolerances during manufacture or end use. In the electronics industry, for example, these benefits plus the resin's resistance to soldering temperatures as high as 230°C (450°F) give it an edge over other high-performance plastics in many surface-mounted interconnect devices, minibobbins, and other components. In the medical equipment industry, the resin is replacing stainless steel in a growing number of surgical instruments and sterilization trays because it can be molded into long, complex shapes, and it can withstand repeated sterilization cycles. LCPs have also been fabricated into a broad range of components in applications such as engine fuel systems, fiber optics, chemical equipment, and photocopiers.

Vectra LCP was selected as the material for the collar of this fiber optic connector because of its ability to fill thin-wall sections, provide dimensional stability at 200°C (400°F), and virtually eliminate shrinkage.

Injection molding LCPs

LCPs suitable for injection molding applications have been commercially available for about eight years, primarily from Hoechst Celanese and Amoco Chemical Co., Chicago, Ill. Parts and tools for injection-molded LCP parts must be carefully designed to control how the resin flows as it fills the mold. To a great extent, the flow pattern determines the mechanical properties, shrinkage, points of weakness, and other key part characteristics.

As an LCP enters a mold tool, its surface molecules line up in the flow direction and form a "skin" that generally is 15 to 30% of the part's thickness (the thinner the part, the greater the percentage). This surface layer reinforces the part, giving it exceptional flexural strength, elastic modulus, and tensile performance. For example, a commonly used Hoechst Celanese LCP (Vectra LCP A130) has 35 to 70 MPa (5 to 10 ksi) greater tensile strength, and about 7 GPa (1 million psi) more stiffness than comparable engineering resins.

The high degree of molecular alignment makes finished parts anisotropic; that is, their mechanical properties depend on both the degree and direction of orientation of the rodlike molecules in the polymer. In most molded LCP parts, strength and stiffness are significantly higher in the flow direction than across the flow. Designers use cavity shape and gate placement to control the filling pattern and "build in" required flexural and tensile properties.

The amount of shrinkage during molding is also affected by the molecular alignment. LCPs have little or no shrinkage in the direction of flow, and hold exceptional tolerances along this axis, but they have a cross-flow shrinkage close to that of conventional polymers. Shrinkage is most dependent on molecular orientation, somewhat less dependent on part thickness, and almost independent of processing conditions. Shrinkage in other polymers, by contrast, is primarily determined by processing conditions. Shrinkage typically ranges from 0 to 0.01 mm/cm (0 to 0.001 in./in.) in the flow direction, compared to about 0.05 mm/cm (0.005 in./in.) across the flow. As shrinkage along the flow de-
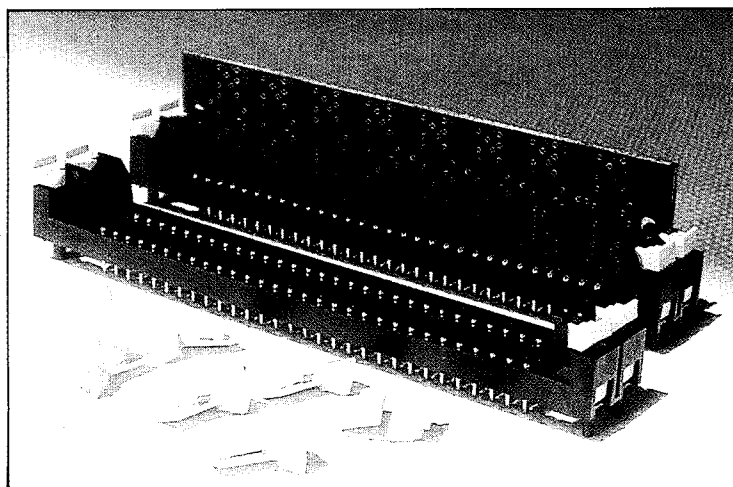
This socket for a computer's single inline memory module (SIMM) has a latch made of Vectra LCP. The material gives the latch optimum flexibility and strength, as well as the ability to withstand soldering temperatures as high as 230°C (450°F).

Metal replacement application

Vectra LCP was the only plastic identified by Altronics Connector Corp., Gardena, Calif., that could replace steel in the latches of a new socket for a computer's single inline memory module (SIMM). Conventional SIMM sockets have a steel latch that holds circuit boards firmly in place in an insulator (usually made of LCP). The latch functions as a stiff spring, flexing to receive the board and hold it firmly in place.

Vectra LCP gave the latch optimum flexibility and strength because it has 12 to 65% higher tensile strength and up to 67% higher flexural modulus than the other resins tested. These included another LCP, polyether sulfone (PES), polyphenylene sulfide (PPS), and a high-temperature polyester (PCT). The LCP also has a heat deflection temperature of 254°C (489°F), so it withstands soldering temperatures as high as 230°C (450°F) when SIMMs are joined to "motherboards." Its low melt viscosity allows it to fill the mold at injection pressures typically half those of comparable semicrystalline resins such as PCT and PPS. It also has half the cycle time of such resins.

In considering alternative materials, Altronics found that the competing LCP was more brittle and intolerant of temperature variations than the Vectra material. PES has good "spring," but it lacks the needed rigidity, and has relatively poor processing characteristics. PPS has a high potential for residual stress problems, and could not meet the high-flow mold-filling requirement, while PCT's disadvantages were residual stress, water absorption, mold filling, and flash.

Comparison of thermoplastics

Amorphous	Semicrystalline	Liquid crystal
Examples: polyarylate, acrylonitrile-butadiene-styrene, polycarbonate, polysulfone, polyetherimide.	**Examples:** polyester, polyphenylene sulfide, polyamide, polyacetal.	**Examples:** wholly aromatic copolyesters.
No sharp melting point. Soften gradually.	Relatively sharp melting point.	Melting range. Low heat of fusion.
Random chain orientation in solid and melt phases.	Ordered arrangement of molecules, and regular recurrence of molecular structure in solid phase.	High chain continuity. Extremely ordered molecular structure in both melt and solid phases.
Do not flow as easily as other two types.	Flow easily above melt temperature.	Flow well under shear or around melting range.
Reinforcement improves load bearing capability only below T_g.*	Reinforcement lowers anisotropy and improves load bearing capability between T_g and T_m.*	Reinforcement improves load bearing capability, esp. in highly crystalline forms between T_g and T_m.*
Can give transparent parts.	Part is usually opaque.	Part is always opaque.

* T_g is the glass transition temperature, above which the polymer is ductile and below which it is brittle. T_m is the melting point.

Polymers are classed as either thermosets or thermoplastics, based on their response to heat. Thermosets cannot be reheated or remolded because they undergo an irreversible two-stage polymerization reaction. In the first stage, the material supplier forms a linear-chain polymer with reactive end groups; in the second, the molder applies heat in the molding press, which cross-links the end groups. Shorter chains with many cross-links form rigid thermosets; longer chains with fewer cross-links form more flexible ones. Exposure to high temperatures for too long a time degrades the plastic by breaking its chains.

Thermoplastics, by contrast, can be remolded because they remelt when heated beyond a certain point. They have linear molecular chains with some branching, but little or no cross-linking. Those with a wide range of chain lengths are easier to process, while those with a narrow range have more uniform properties.

Thermoplastics generally have higher impact resistance, are easier to process, and are better suited to complex designs than thermoset polymers. Thermoplastics are divided into three groups based on molecular structure: amorphous, semicrystalline, and liquid crystalline.

Amorphous polymers have randomly oriented chains in both melt and solid phases. Semicrystalline polymers have randomly oriented chains in the melt phase, but upon cooling can become partially ordered, resulting in a structure consisting of both crystalline and amorphous regions.

Semicrystalline polymers have lower melt viscosities than amorphous polymers. They also have a more compact molecular structure, and have higher shrinkage and warpage in molded parts. Liquid crystal polymers are highly ordered in both liquid and solid states. As a group, LCPs have excellent processability that leads to short cycle times, high flowability in thin sections, and exceptional repeatability of dimensions. Molded parts exhibit very low warpage and shrinkage, along with high dimensional stability, even when heated to 200 to 250°C (390 to 480°F). The rigid-rod nature of LCP molecules results in a microstructure that resembles the physical orientation of the fibers in a reinforced thermoplastic.
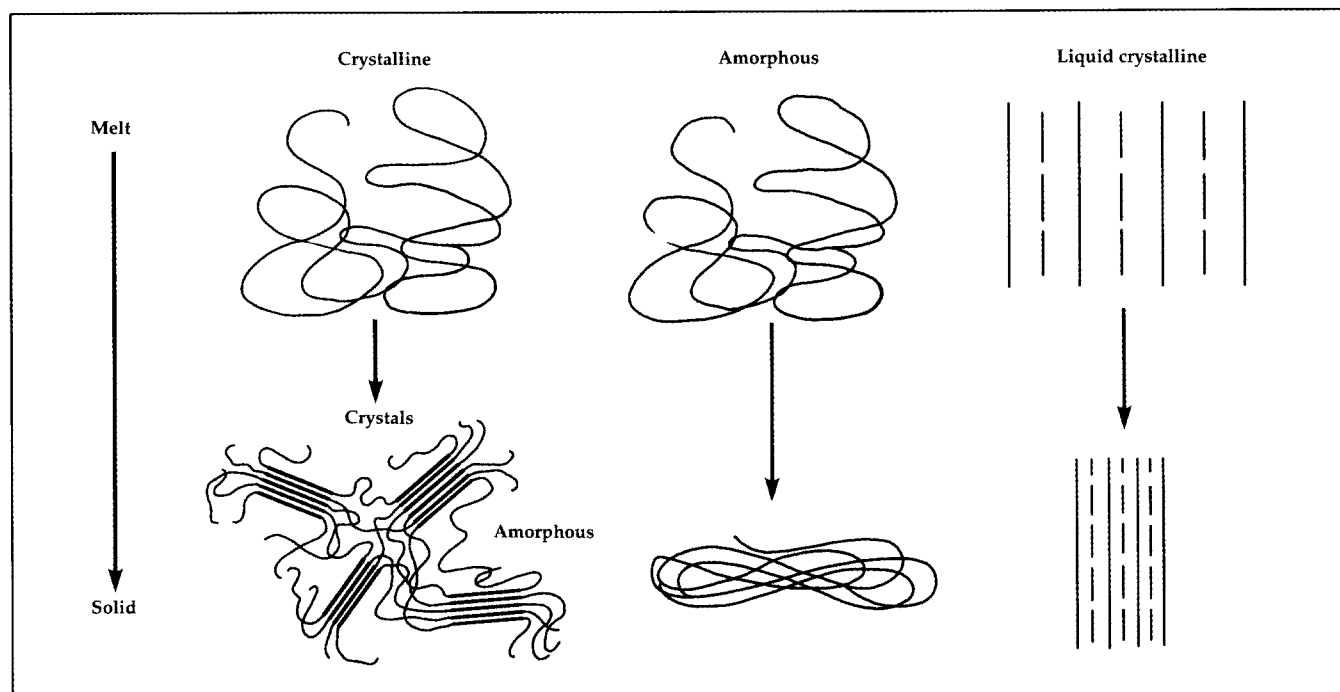
Two-dimensional representations of the structures of crystalline, amorphous, and liquid crystalline thermoplastics.

creases, shrinkage across the flow increases.

If part shrinkage in the flow direction is much less than that across the flow, the part can warp. However, the differential can be controlled by relocating areas of greatest difference to noncritical sections through adjustment of the filling pattern. It can also be controlled by part shape: The shrinkage differential is lowest in a disk filled by diverging, radial flow, and greatest in an end-gated bar.

How resin properties affect molding

LCPs are the easiest to process of all high-performance plastics, in part because they have the highest melt flow and shortest cycle time. They can be processed in conventional equipment by all conventional methods, and can be compounded with most reinforcements and fillers. The resin's unique properties affect processing in several important ways:

Melt viscosity is extremely low because the rigid-rod molecules move past each other easily. The high flow allows the resin to fill intricate parts and thin walls at relatively low injection pressures. Although pressure varies with part design, mold layout, and machine settings, the resin generally needs cavity pressures of only 7 to 35 MPa (1 to 5 ksi), well below those of other

engineering resins. Low pressure reduces molded-in stress, so molders need not extend cooling time to counter warpage from such stress.

Mold cycle time for LCPs is generally half that of other high-performance resins — 10 to 30 seconds for LCPs versus 20 to 60 seconds or more. Exact cycle time for an LCP part depends on parameters such as size, shape, thickness, mold layout, and machine settings.

One reason for the short cycle time is that LCPs can rapidly transition between melt and solid phases because both have a similar ordered structure. The rod-like microstructure in both phases shortens the time needed to melt the resin before injection and the time required for it to solidify in the mold.

Many other factors inherent to LCPs also contribute to the short cycle time. Low viscosity speeds mold fill, and good stiffness at elevated temperatures permits parts to be ejected while still hot. Low molded-in stresses eliminate the need for slow cooling to prevent stress buildup.

Shear thinning is a decrease in melt viscosity as shear increases. LCPs are more sensitive to shear thinning than other engineering plastics, which gives molders a powerful way to alter flow. Molders can improve the resin's ability to fill long, thin, or highly complex parts by increasing injection velocity. With other polymers, molders generally must increase temperature to reduce viscosity, which can degrade the polymer.

Use of regrind lowers material and disposal cost because sprues, runners, and other production scrap can be reground and reused. The reground LCP retains most of the properties of the virgin resin, except that the impact resistance of reground glass-filled grades may decrease because of fiber breakage. In practice, manufacturers mix 50% regrind with virgin resin. Parts should be tested to verify satisfactory performance. ■

Advantages of LCPs

End-use advantages
- Excellent thermal stability: UL (Underwriters Laboratory) relative thermal index up to 240°C (464°F), depending on the grade of LCP.
- High rigidity and strength: typical modulus from 10 to 24 GPa (1.4 to 3.5 million psi), tensile strength from 125 to 255 MPa (18 to 37 ksi), and notched impact energy from 2.2 to 7.5 J (1.6 to 5.5 ft•lbf.
- Little dimensional change as temperature or humidity changes. Coefficient of thermal expansion is less than $10 \times 10^{-6}/°C$ ($6 \times 10^{-6}/°F$) in the flow direction. Moisture absorption is less than 0.03%.
- Retains 70% of its notched impact value down to about −270°C (−450°F). Most other plastics are extremely brittle at these temperatures.
- Inert to acids, bleaches, chlorinated organic solvents, alcohols, and fuels.
- Low gas permeation rates versus commercial packaging films.
- Ionic extractables are well below those needed for corrosion-free environments in integrated-circuit chip applications.
- Inherently flame retardant, low smoke density, and relatively nontoxic products of combustion.

Processing advantages
- Extremely low shrinkage and warpage in molding, and exceptional repeatability of dimensions.
- High melt strength for versatility of fabrication.
- Low melt viscosity for high flow in thin sections and in intricate parts.
- Low heat of fusion for fast melting and rapid cooling, which shortens cycle times in injection molding.
- High stiffness at high temperatures allows ejection from the mold with minimum cooling time.
- Little or no flash because of the low injection pressures and the shear-sensitivity of viscosity.

Hoechst Celanese Locations

Celcon* Acetal Copolymer
Fortron* Polyphenylene Sulfide
Vectra* Liquid Crystal Polymer
Celanese* Nylon 6/6
Celanese* Nylon 6
Celanex* Thermoplastic Polyester
Vandar* Thermoplastic Alloys
Impet* Thermoplastic Polyester
Celstran* Long-Fiber Reinforced Thermoplastics
Hostaflon * Polytetrafluoroethylene
Encore™ Reclaimed Thermoplastic Resins

Hoechst Celanese

Hoechst ▣

Advanced Materials Group
Hoechst Celanese Corporation
26 Main Street
Chatham, New Jersey 07928
(201) 635-2600

Vectra®
Liquid Crystal Polymer

**Short Term
Properties (VC-4)**

Advanced Materials Group

Hoechst Celanese

Hoechst

Vectra® Liquid Crystal Polymer (LCP)

Introduction

Vectra® Liquid Crystal Polymers (LCP) are a family of high performance plastic materials based on patented Hoechst Celanese Corporation technology. A variety of product grades are offered, each with its own unique characteristics tailored to meet demanding thermal and mechanical applications. They are used in place of metals, thermosets and other thermoplastics because of the following set of product advantages that cannot be provided by other materials:

Advantages Over Metal

- Excellent chemical and hydrolytic stability
- Excellent corrosion resistance
- Very high strength to weight ratio - tensile/flex moduli up to 2,500,000 psi
- Concentrates available for color-coding
- Opportunities for parts consolidation
- Eliminates secondary finishing operations
- Space/weight savings possible
- Mold complex parts without machining
- High precision molding
- Similar part dimensional stability and coefficient of thermal expansion

Advantages Over Thermosets

- Processes very easily on both injection molding and extrusion equipment
- Extremely high melt flow under shear - able to fill long and complicated flow paths
- Excellent dimensional stability and very low mold shrinkage
- No deflashing required for molded parts
- Able to use regrind for cost savings

- 100% recyclable
- Fast cycle times, increased productivity
- Most grades have UL 94 V-0 flammability ratings, and low smoke ratings
- Products have extremely low oxygen and moisture permeability

Advantages Over Other Thermoplastics

- Superior thermal stability - UL Relative Thermal Index ratings up to 460°F
- UL 94 V-0 flammability ratings down to 1/64" part thickness
- Heat deflection temperatures as high as 518°F
- Excellent organic solvent resistance
- Low moisture permeability
- Resistant to sterilization by radiation, steam, or chemical processes
- Excellent electrical insulation properties
- Excellent creep resistance at elevated temperature
- Excellent dimensional stability, precision moldability
- Shortest molding cycle times, increased productivity

Additional Features

Extrusion Grades Available

- Specific Vectra LCP grades are recommended for extrusion of rod, profile, film and sheet, pipe, tubing, fiber, and overcoating of optical glass fiber
- Extruded products are highly anisotropic and are very strong in the machine direction
- Products have excellent thermal, chemical, and insulative properties.

Regulatory Listings

Grades are available which have:
- Drug and Device Master files – USP Class VI compliance
- Military and Federal specifications listings
- Underwriters Laboratories listings
- JEDEC Electronic listing

Other Products Available

- Film and Vectran® fiber made from Vectra LCP are available

For more information on these applications or products, contact your local Hoechst Celanese Sales Office, or Product Information Services at (800) 833-4882.

A115 Low glass content reinforced, general purpose grade. Very easy to process; parts have very low notch sensitivity; slightly tougher than A130 but some part configurations may warp slightly more.

A130 General purpose grade with excellent balance of properties including superior thermal stability, mechanical, and electrical properties, good chemical resistance. Inherently flame retardant without additives. Very easy to process; no mold flash. Suitable for vapor phase surface mount electrical and electronic devices. USP Class VI compliant for use in medical devices. Resistant to radiation and steam sterilization.

A150 High glass content reinforced, general purpose grade. Parts exhibit low shrinkage and are highly creep resistant over time. Some part configurations exhibit lower warpage than A130.

A230 General purpose carbon fiber reinforced grade; excellent stiffness, hydrolytic, and chemical stability. Electrically conductive. Recommended for bearings, wear-resistant parts. USP Class VI compliant for use in medical devices.

A410 A glass/mineral filled grade used where minimal warpage is required in molded parts. Slightly more difficult to process than an all glass-reinforced grade.

A420 This grade is similar in properties and processing to A410, but contains graphite flake for improved lubricity and wear resistance.

A422 This grade is similar in properties and processing to A130, but contains graphite flake for improved lubricity and wear resistance.

A430 This grade is similar in properties and processing characteristics to A130, but contains PTFE fluorocarbon for improved lubricity. Molded parts exhibit excellent electrical properties such as arc resistance, even at high frequencies.

A435 This grade is similar in processing characteristics to A430, but is stiffer. It also contains PTFE fluoropolymer for enhanced lubricity. It has excellent electrical properties including the best High Current Arc Ignition values.

A515 This grade has a low level of mineral filler, for a good balance of toughness, hydrolytic stability, and easy processability. Parts made from A515 are in compliance with USP Class VI for medical devices.

A530 The mineral filler in A530 confers excellent surface smoothness and good toughness and hydrolytic stability on molded parts. Products are resistant to radiation and steam sterilization. Parts made from A530 are in compliance with USP Class VI for medical devices.

A540 This grade contains additional mineral filler compared to A530, which increases stiffness at the expense of a slight reduction in processability.

A625 This grade is highly filled with graphite flake for a good balance of toughness, wear resistance, chemical resistance, and hydrolytic stability.

A700 This grade is glass reinforced for good mechanical properties and has electrostatic dissip tive properties as well.

B130 This is a glass reinforced grade based on a polymer with enhanced strength and stiffness compared to A130, with a very low coefficient of thermal expansion and low part shrinkage during molding. It processes less easily than A130.

B230 This grade is reinforced with carbon fiber for metal-like strength and stiffness values, and is electrically conductive. It is highly suitable for metal replacement applications.

B420 This grade is glass/mineral/graphite filled for enhanced strength and stiffness compared to A420. It produces parts with excellent creep resistance and long-term dimensional stability.

C115 C115 is a glass reinforced product similar in mechanical properties to A115 but with higher thermal stability. It processes very well.

C130 This grade has similar properties to A130, but with higher thermal stability and slightly greater dimensional stability, making it useful for parts exposed to vapor phase soldering temperatures.

C150 C150 has excellent strength and stiffness properties, coupled with greater thermal stability compared to A150. Compared to C130, it offers improved creep resistance and long-term dimensional stability. Some part designs show reduced warpage compared to C130.

C550 This grade is highly mineral filled for high temperature applications, especially where cost is a factor.

E130 E130 is a glass reinforced grade having the highest temperature resistance for surface mount technology applications. It processes extremely easily and readily fills thin wall parts.

V140 This product is a unique alloy with processability and dimensional stability comparable to standard LCP products. It provides high heat distortion, superior weld line strength, and low warpage for parts exposed to infra-red and vapor phase reflow soldering conditions.

Vectra® Liquid Crystal Polymer (LCP) – Typical Properties

Property	ASTM Test Method	Units Eng. (S.I.)	A115	A130	A150	A230
Physical						
Specific Gravity	D792	—	1.50	1.61	1.79	1.49
Water Absorption, Immersion to Equilibrium	D570	%	0.02	0.02	0.01	0.03
Mold Shrinkage Flow/Transverse (4" Disk)	D995	%	0.0/0.2	0.1/0.2	0.2/0.2	0.1/0.2
Mechanical @ 73°F (23°C)						
Tensile Strength at Break	D638	10^3 psi (MPa)	28 (195)	30 (207)	26 (180)	28 (193)
Tensile Modulus	D638	10^6 psi (GPa)	1.9 (13.1)	2.4 (16.6)	3.2 (22)	4.5 (31)
Elongation at Break	D638	%	3.0	2.2	1.3	1.1
Flexural Strength	D790	10^3 psi (MPa)	30 (207)	37 (254)	36 (248)	37 (225)
Flexural Modulus	D790	10^6 psi (GPa)	1.6 (11)	2.1 (15)	2.9 (20)	3.5 (24)
Compressive Strength (1% Deflection)	D695	10^3 psi (MPa)	5.9 (41)	20 (140)	22.5 (155)	18 (124)
Compressive Modulus	D695	10^6 psi (GPa)	—	1.7 (12)	2.2 (15)	2.5 (17.2)
Shear Strength	D732	10^3 psi (MPa)	—	17.8 (123)	—	17.5 (121)
Izod Impact Strength, Notched	D256	ft - lb/in (J/m)	5.5 (290)	2.8 (150)	1.7 (90)	1.2 (64)
Tensile Impact Strength	D1822	ft - lb/in² (kJ/m³)	40 (84)	40 (84)	25 (53)	30 (63)
Taber Abrasion	D1044	mg/1000 cycles	—	7.4	—	5.8
Rockwell Hardness	D785	M scale	—	87	93	83 (80)
Coefficient of Friction Against Metal:						
Dynamic	—	—	0.11	0.14	0.19	0.13
Static	—	—	0.11	0.19	0.16	0.16
Thermal						
Heat Deflection Temperature:						
66 psi, 0.46 N/mm²	D648	°F (°C)	—	489 (254)	484 (251)	—
264 psi, 1.82 N/mm²	D648	°F (°C)	430 (220)	446 (230)	449 (232)	430 (221)
Coeff. of Linear Thermal Expansion: (-50°C to 200°C), Flow Direction	D696	cm/cm/°C x 10^{-6}	—	5	5	–2
Transverse to Flow	D696	cm/cm/°C x 10^{-6}	—	65	60	65
Melting Point	—	°F (°C)	536 (280)	536 (280)	536 (280)	536 (280)
Electrical						
Volume Resistivity	D257	ohm-cm	10^{16}	10^{15}	5×10^{15}	—
Dielectric Strength, Short Term, 1.5mm Thickness: 23°C, 50% RH	D149	V/mil (kV/mm)	—	1100 (43)	870 (34)	—
Comparative Tracking Index	D3638	volts	—	175	175	—
Arc Resistance	D495	seconds	—	137	181	—
Dielectric Constant: 1 KHz	D150	—	—	4.1	4.3	—
1 MHz	D150	—	3.2	3.7	3.9	—
1 GHz	D150	—	—	3.7	3.9	—
Dissipation Factor: 1 GHz	—	—	—	0.006	0.006	—
Flammability						
Underwriters Laboratories Ratings, All UL94V0 @ minimum thickness		in. (mm)	0.033 (0.85)	0.018 (0.45)	0.018 (0.45)	0.016 (0.43)
Limiting Oxygen Index, (LOI)	D2863	—	—	37	37	—

	A410	A420	A422	A430	A435	A515	A530	A540	A625	A700
	1.84	1.89	1.68	1.50	1.62	1.52	1.65	1.76	1.54	1.61
	0.02	0.02	0.02	—	—	0.02	—	0.02	0.03	—
	0.2/0.3	0.1/0.2	0.1/0.3	—	—	0.3/0.4	—	0.2/0.4	0.1/0.3	—
	24.5 (169)	21.5 (149)	25 (173)	24.5 (169)	25.1 (173)	27 (185)	27 (186)	27 (145)	23.5 (162)	20 (138)
	3.0 (21)	3.1 (21)	2.4 (16)	1.1 (7.6)	1.6 (11)	1.7 (12)	2.0 (14)	2.5 (17.2)	1.5 (10.3)	2.0 (14)
	1.8	1.4	2.3	5.2	3.0	3.9	4.7	3.5	6.6	1.4
	34 (232)	31 (214)	33.5 (230)	18.5 (128)	29 (200)	23.5 (161)	27 (186)	26 (181)	21 (146)	28 (193)
	2.7 (19)	2.9 (20)	2.2 (15)	1.0 (7.2)	1.4 (9.6)	1.4 (10)	1.7 (11.7)	2.2 (15)	1.5 (10.3)	1.8 (12.7)
	18.5 (127)	20.5 (140)	21 (145)	—	—	11.5 (79)	—	14.5 (100)	10.5 (74)	—
	2.2 (15)	2.8 (20)	2.0 (14)	—	—	1.4 (9.6)	—	2.0 (14)	1.4 (9.6)	—
	—	—	—	—	—	—	—	—	—	
	1.6 (85)	1.9 (100)	2.5 (134)	3.8 (203)	2.1 (112)	6.7 (358)	5.5 (294)	1.3 (70)	1.8 (95)	1.4 (75)
	—	—	—	—	—	36 (76)	—	20 (42)	40 (84)	
	—	—	—	—	—	—	—	—	—	
	76	79	—	—	—	63	—	63	62	
	0.21	0.18	0.17	—	0.11	0.15	0.14	0.12	0.15	—
	0.21	0.20	0.18	—	0.11	0.20	0.13	0.12	0.21	—
	—	—	—	—	—	—	—	—	—	—
	437 (225)	437 (225)	437 (225)	352 (178)	435 (225)	365 (185)	392 (200)	400 (204)	356 (180)	428 (225)
	8	7	6	—	—	—	—	9	6	—
	50	50	55	—	—	—	—	65		
	536 (280)	536 (280)	536 (280)	538 (280)	538 (280)	536 (280)	538 (280)	536 (280)	536 (280)	538 (28...
	10^{15}	—	—	—	—	10^{15}	—	—	—	$10^4\text{-}10...$
	840 (33)	—	—	—	—	890 (35)	570 (22)	—	—	
	175	—	—	—	—	175	175	175	—	—
	163	—	137	—	—	—	100	163	—	
	4.5	—	—	—	—	4.2	—	3.3	—	
	4.2	—	—	—	—	3.8	—	3.9	—	
	4.1	—	—	—	—	3.9	—	—	—	
	0.004	—	—	—	—	0.004	—	—	—	
	0.016 (0.45)	0.035 (0.91)	0.018 (0.45)	—	—	0.125 (3.18)	0.02 (0.46)	0.067 (1.68)	—	—
	37	—	—	—	—	33	—	37	—	

B130	B230	B420	C115	C130	C150	C550	E130	V140
1.61	1.49	1.89	1.50	1.61	1.79	1.89	—	1.67
0.02	0.03	—	—	0.02	0.01	0.02	—	0.02
0.0/0.1	0.0/0.0	—	0.0/0.2	0.1/0.2	0.2/0.2	0.3/0.4	—	1.2/4.5
32 (221)	35 (241)	17 (117)	23 (159)	23 (161)	24 (165)	16.5 (115)	18 (124)	24 (165)
3.5 (24.1)	5.4 (37)	3.0 (20.7)	1.5 (10.3)	2.1 (14.5)	3.0 (20.7)	2.7 (18.6)	2.0 (14)	2.5 (17.3)
1.2	1.0	0.6	2.8	1.7	1.2	2.0	1.7	1.4
43.5 (300)	46 (317)	26 (179)	28.7 (198)	31 (212)	32 (220)	23.5 (163)	25 (174)	36 (248)
2.7 (19)	4.6 (32)	3.0 (20.7)	1.4 (9.6)	1.9 (13.1)	2.8 (19)	2.5 (17.2)	2.0 (14)	2.4 (16.6)
28 (192)	34.5 (238)	—	—	18 (124)	—	—	—	—
2.1 (20)	4.8 (33.1)	—	—	1.7 (20)	—	—	—	—
9.1 (132)	—	—	—	2.9 (20)	—	—	—	—
1.7 (90)	1.4 (75)	0.6 (32)	4.0 (214)	2.4 (125)	1.6 (85)	1.0 (54)	2.0 (107)	1.5
25 (53)	20 (42)	—	—	35 (74)	—	25 (53)	—	—
—	—	—	—	—	—	—	—	—
—	99	93	—	—	—	—	—	—
—	—	—	—	—	—	—	—	—
—	—	—	—	—	—	—	—	—
—	—	—	—	543 (284)	—	—	—	—
446 (230)	440 (227)	410 (210)	455 (235)	469 (243)	485 (252)	429 (221)	518 (270)	265 (510)
2	3	—	—	6	7	12	—	9
50	45	—	—	70	60	65	—	42
536 (280)	536 (280)	536 (280)	620 (327)	620 (327)	620 (327)	620 (327)	670 (355)	580 (305)
—	—	—	—	10^{15}	—	—	10^{15}	10^{16}
—	—	—	—	1110 (43)	—	—	1200 (47)	600 (23)
—	—	—	—	175	—	—	200	175
—	—	—	—	137	—	—	140	160
—	—	—	—	4.1	—	—	3.7	3.7
—	—	—	—	3.7	—	—	—	—
—	—	—	—	3.8	—	—	—	—
—	—	—	—	0.004	—	—	0.006	0.003
0.017 (0.43)	—	—	0.033 (0.81)	0.017 (0.43)	0.018 (0.45)	—	0.033 (0.84)	0.016 (0.40)
—	—	—	—	37	—	37	—	—